Karlsruher Institut für Technologie

# Sterile Neutrino Searches in Neutrino Oscillation Experiments

Dissertation by

by

Álvaro Hernández-Cabezudo

Physics Department

Institute for Nuclear Physics

September 2016 - December 2019

Supervised by
Prof. Dr. T. Schwetz-Mangold

Co-supervised by
Prof. Dr. U. Nierste

June 18, 2020

# Sterile Neutrino Searches in Neutrino Oscillation Experiments

Zur Erlangung des akademischen Grades eines
DOKTORS DER NATURWISSENSCHAFTEN
(Dr. rer. nat.)

von der KIT-Fakultät für Physik des
Karlsruher Instituts für Technologie (KIT)
angenommene

DISSERTATION

von

Álvaro Hernández-Cabezudo

Tag der mündlichen Prüfung: 20.12.2019

1. Referent: Prof. Dr. T. Schwetz-Mangold
2. Korreferent: Prof. Dr. U. Nierste

# Abstract

The main goal of this PhD thesis is the search for new physics in the neutrino sector. In particular the search for eV sterile neutrinos in neutrino oscillation phenomena (a,b) and MeV neutrinos at the MiniBooNE experiment (f). Of equal importance in this thesis, is the contribution of the study of neutrino oscillations for a better understanding of the standard neutrino properties (d,e).

Motivated by the unexpected deficit of $\bar{\nu}_e$ flux observed in reactor experiments, which is known as the reactor anti-neutrino anomaly, a combined analysis of the reactor experiments is performed in the context of active-to-sterile oscillations. In the light of recent measurements that question the reliability of the $\bar{\nu}_e$ flux predictions, we performed reactor data analyses based on the relative comparison of measured spectra, what makes them flux independent: Daya Bay and NEOS analyses. They were used in two publications (a) and (b). In (a) we performed a dedicated study of the active-to-sterile oscillation hypothesis using global reactor data. In (b), a complete study of the active-to-sterile oscillation framework is performed using global data in the $\overset{(-)}{\nu}_e \to \overset{(-)}{\nu}_e$, $\overset{(-)}{\nu}_\mu \to \overset{(-)}{\nu}_e$ and $\overset{(-)}{\nu}_\mu \to \overset{(-)}{\nu}_\mu$ oscillation channels.

We found that the active-to-sterile oscillation hypothesis is compatible with the global reactor data and global $\overset{(-)}{\nu}_e \to \overset{(-)}{\nu}_e$ data. Oscillations are preferred at the $3\sigma$ level with respect to the no oscillation case, with the best fit value at $\Delta m^2_{41} \simeq 1.3\,\mathrm{eV}^2$, $|U_{e4}| \simeq 0.1$. On the other hand, within the active-to-sterile oscillation framework, the anomalous $\overset{(-)}{\nu}_e$ excesses found in LSND and MiniBooNE data in the $\overset{(-)}{\nu}_\mu \to \overset{(-)}{\nu}_e$ oscillation channel are incompatible with the null results from the searches done in the $\overset{(-)}{\nu}_\mu \to \overset{(-)}{\nu}_\mu$ channel. The disagreement is found to be at the level of $5.1\sigma$, excluding the active-to-sterile oscillation hypothesis as an explanation for LSND and MiniBooNE anomalous excesses.

The Daya Bay reactor analysis code was modified in order to study the standard oscillation parameters within the $3\nu$ oscillation framework. A RENO data analysis in the $3\nu$ standard picture was also performed. Both analyses were used in the publications (d) and (e). They are crucial for the determination of the $\theta_{13}$ mixing angle, and they complement the accelerator data analyses in the determination of the $\theta_{23}$ octant and the mass ordering, as it is shown in (d). We also perform an alternative analysis of the current Daya Bay and RENO data combined, which sets an upper limit on $\Delta m^2_{21} \leq 18.3 \times 10^{-5}\,\mathrm{eV}^2$ at the $2\sigma$ level (e).

Given the incompatibility of the MiniBooNE excess with an active-to-sterile oscillation, we have studied an alternative explanation based on a heavy neutrino decaying into a photon. It is found that the excess is compatible with a heavy neutrino, with a mass $m_N \simeq 250\,\mathrm{MeV}$, that is produced in kaon decays via the mixing with the electron or muon flavors. The mixing parameter it is found to lie in the range $10^{-11} \lesssim |U_{\mu 4}|^2 \lesssim 10^{-8}$. The heavy neutrino decays into a photon and a light neutrino through an effective operator me-

diated by new physics at the energy scale $10^4\,\text{TeV} \lesssim \Lambda \lesssim 10^7\,\text{TeV}$.

During the course of the PhD thesis we have also done a study on the complementarity of $\beta$ and $0\nu\beta\beta$ decay processes in order to discern between different low-scale seesaw realizations (c). Since this work is off topic from the main research line of the PhD thesis it was not included in the main text. For its potential use in other studies, a parameterization of the low-scale seesaw realizations that was done in this work is included in an appendix.

---

(a) M. Dentler, Á. Hernández-Cabezudo, J. Kopp, M. Maltoni and T. Schwetz, JHEP 1711 (2017) 099 doi:10.1007/JHEP11(2017)099 [arXiv:1709.04294 [hep-ph]].

(b) M. Dentler, Á. Hernández-Cabezudo, J. Kopp, P. A. N. Machado, M. Maltoni, I. Martinez-Soler and T. Schwetz, JHEP 1808 (2018) 010 doi:10.1007/JHEP08(2018)010 [arXiv:1803.10661 [hep-ph]].

(c) A. Abada, Á. Hernández-Cabezudo and X. Marcano, JHEP 1901 (2019) 041 doi:10.1007/JHEP01(2019)041 [arXiv:1807.01331 [hep-ph]].

(d) I. Esteban, M. C. Gonzalez-Garcia, A. Hernandez-Cabezudo, M. Maltoni and T. Schwetz, JHEP 1901 (2019) 106 doi:10.1007/JHEP01(2019)106 [arXiv:1811.05487 [hep-ph]].

(e) A. Hernandez-Cabezudo, S. J. Parke and S. H. Seo, Phys. Rev. D **100** (2019) no.11, 113008 doi:10.1103/PhysRevD.100.113008 [arXiv:1905.09479 [hep-ex]].

(f) O. Fischer, Á. Hernández-Cabezudo and T. Schwetz, Phys. Rev. D **101** (2020) no.07, 075045 doi:10.1103/PhysRevD.101.075045 [arXiv:1909.09561 [hep-ph]].

# Acknowledgements

I would like to express my special thanks of gratitude to Thomas Schwetz-Mangold for being a great supervisor, for sharing his knowledge with me and for guiding me through my PhD.

I would also like to extend my gratitude to my second supervisor Ulrich Nierste, my office mates Oliver Fischer, Andreas Pagner and Elisa M. Todarello, and my father Eliecer Hernández, for their careful reading of this dissertation an their valuable constructive comments.

For making my stays at CNRS and Fermilab very fruitful and valuable experiences, I would also like to give special thanks to my hosts at these institutions, Asmaa Abada and Stephen Parke. For all the nice research that we did together, which helped me to write this dissertation, I give many thanks to them, together with: Xabier Marcano, Mona Dentler, Joachim Kopp, Pedro A. N. Machado, Michele Maltoni, Ivan Martinez-Soler, Iban Esteban, María Concepción Gonzalez-García, Oliver Fischer and Seon Hee-Seo.

For all the interesting discussions and for creating such a relaxing and enjoyable working environment I would like to thank all my colleagues, who I shared office with, some of them already mentioned: Jonas Enander, Steffen Hahn, Daniel Kramer, Yannick Müller, Albert Zhou, Andreas Pargner, Elisa M. Todarello and Oliver Fischer.

I am also very thankful to Belen Gavela and all the PI's of the Elusives Network for all their work that make this project possible, and for giving me the opportunity to be part of it. It was a total enriching professional and personal experience. And to the Elusive ESR's, I want to say: many thanks for the nice time we spent together at the workshops and schools.

Of course, lots of the most friendly thanks to Alvaro and Arnaud, my special "frudis", my "flat brother" Alberto and all my friends in Karlsruhe: Aayan, Kotryna, Hongye and Rebeca. Thank you for all the nice moments, laughs, and friendship.

Finally, I want to give special thanks, full of love, to my parents, María Teresa and Eliecer, and my sister Inés for their continuous support, help and encouraging cheers during these three years, and also to my love, Sachi, for her strong support and encouragement, and for the wonderful year that we shared together.

This dissertation was possible thanks to all of you.

Thank you.

This project has received funding/support from the European Union Horizon 2020 research and innovation program under the Marie Skłodowska-Curie grant agreement No 674896

# Contents

# List of Figures

# List of Tables

# List of abbreviations

| | |
|---|---|
| **BBN** | Big Bang Nucleosynthesis |
| **CC** | Charged Current |
| **CCQE** | Charged Current Quasielastic |
| **CMB** | Cosmic Microwave Background |
| **EH** | Experimental Hall |
| **EWSB** | Electroweak Symmetry Breaking |
| **IAV** | Inner Acrylic Vessel |
| **IBD** | Inverse Beta Decay |
| **IO** | Inverted Ordering |
| **ISS** | Inverse Seesaw |
| **LBL** | Long Baseline |
| **LISS** | Linear + Inverse Seesaw |
| **LSS** | Linear Seesaw |
| **MBL** | Medium Baseline |
| **NC** | Neutral Current |
| **NO** | Normal Ordering |
| **PG** | Parameter Goodness-of-fit |
| **RAA** | Reactor Anti-neutrino Anomaly |
| **SBL** | Short Baseline |
| **SM** | Standard Model |
| **SBN** | Short-Baseline Neutrino |

# Chapter 1

# Introduction

Neutrinos are the most elusive particles of the Standard Model (SM). They have a tiny mass and neutral electric charge, they only interact through weak interactions, what makes then extremely difficult to be detected. The neutrino was first postulated by Wolfgang Pauli in 1930, as the particle that carries the missing energy measured in beta decays [1]. Its existence was only hypothetical until 1956 when Frederick Reines and Clyde Cowan detected electron anti-neutrinos for the first time [2]. In the SM there are three different types of neutrinos, commonly called flavors: electron, $\nu_e$, muon, $\nu_\mu$ and tau, $\nu_\tau$, flavors. They are named according to the accompanying charged lepton in charged current (CC) interactions.

The neutrino changing flavor in flight, known as neutrino oscillations, was first postulated by Bruno Pontecorvo [3, 4]. Already since 1968 there were some evidences of neutrino oscillations in the solar neutrino experiment Homestake [5] and in the proton decay and neutrino observatory experiments IMB [6] and Kamiokande [7]. But they were not confirmed until 1998, when the Super-Kamiokande reported a strong evidence of neutrino flavor change as a function of the traveled distance and energy in the way it is predicted by the theory [8]. For their contributions on the discovery of neutrino oscillations in the Super-Kamiokande and Sudbury Neutrino Observatory (SNO) experiments, Takaaki Kajita and Arthur B. McDonald were awarded with the Nobel Prize in 2015: "*For the discovery of neutrino oscillations, which shows that neutrinos have mass*".

During the last two decades neutrino oscillations have become a very well established phenomena, which puts into manifest that neutrinos have mass and are mixed among each other. Whitin the SM neutrinos are massless [9, 10]. Therefore, neutrino oscillations is a clear experimental evidence of physics beyond the standard model. Moreover neutrino masses are very small, they lie at a much smaller scale than the rest of the SM particles, what might indicate an alternative origin for the neutrino masses different from the Higgs mechanism, for example the seesaw mechanism [11–14]. This mechanism would imply that the SM is just an effective low energy theory of a more fundamental underlying theory.

The neutrino flavor basis is defined by the neutrinos that interact in weak CC interactions. In a three family neutrino framework, $3\nu$, the flavor and the mass neutrino basis are related by a unitary matrix, called PMNS matrix [3, 4, 15, 16], which depends on 3 mixing angles and one CP violating phase, opening the possibility of CP violation in the lepton sector, which is an important ingredient for the baryogenesis scenarios via leptogenesis [17, 18] and therefore important for the understanding of the matter anti-matter asymmetry in the universe [19].

Deviations from unitarity of the PMNS matrix, would be an indication of extra massive neutrinos mixed with the light active known ones. Measurements of the "invisible" decay width of the $Z$ boson determines very precisely the number of light active neutrinos to be

three [20], so that the hypothetical massive neutrinos have to be mainly sterile, meaning that they do not couple to the SM model particles, except via their mixing with the active flavor neutrinos. Their existence is motivated by scenarios addressing the neutrino mass generation, leptogenesis and they can also be a good dark matter (DM) candidate [21]. The mass scale of these neutrinos could be any, and depending on it, their phenomenology is very diverse. Light sterile neutrinos, at the eV scale, will have an impact in neutrino oscillations [22], heavier neutrinos will be visible in beta and meson decays [23], and much heavier neutrinos could be produced and studied in colliders [24]. Thanks to their mixing with the light neutrinos, their existence can also be confirmed by the non-unitarity of the PMNS matrix [25].

The precise determination of the neutrino masses and the PMNS matrix elements is very important, since they can guide the search for new physics coupled to the neutrino sector and help to discern between the different models that explain the origin of the neutrino masses and hence to find a more complete theory than the SM. The elements of the PMNS matrix can be determined measuring neutrino oscillations. Neutrino oscillations can not determine the absolute neutrino mass, but they are sensitive to the neutrino mass squared differences. During the last two decades neutrino oscillations have been measured in many experiments. Given the large amount of data generated, global fits are a very powerful tool that allows to understand the global data within the same theoretical framework in a consistent way.

Part of the work presented in this disertation is the contribution to the three flavor neutrino ($3\nu$) oscillation global fit [26], done by the NuFit collaboration [27], performing the medium baseline (MBL) reactor data analyses. In the literature, MBL reactor data has not been used for the study of the solar parameters, which drive the solar neutrino phenomena. In this work it is also presented how it can be used to set an upper limit on the solar oscillation frequency [28].

Although the standard $3\nu$ oscillation framework is very well established, there are some anomalous results, found in what are called short baseline (SBL) experiments. The anomalies are: LSND and MiniBooNE, gallium and reactor antineutrino anomaly (RAA). The LSND experiment measured an unexpected excess of $\bar{\nu}_e$ from a $\bar{\nu}_\mu$ beam [29]. With less significance, a similar excess of $\bar{\nu}_e$ was found by the MiniBooNE collaboration [30]. A deficit of $\nu_e$ emitted in strong radioactive sources was found at gallium experiments, seting the gallium anomaly [31,32]. The RAA is set by SBL reactor experiments that measure a deficit of $\bar{\nu}_e$ flux with respect to the theoretical expectations [33]. SBL experiments are located very close to the neutrino source, thus not being sensitive to the standard oscillations in the $3\nu$ framework. The anomalous excesses and deficits can be solved introducing a new neutrino oscillation, usually called active-to-sterile oscillation, caused by a new massive neutrino, mostly sterile, with a mass in the eV scale. This scenario is commonly referred to as the $3+1\nu$ oscillation framework.

In this thesis the active-to-sterile oscillations in the $3+1\nu$ framework is studied, with especial focus on the reactor data. There are two common explanations for the RAA: the introduction of a new massive neutrino with a mass in the eV range that leads to an extra oscillation, and a possible miscalculation of the flux predictions. The latter is motivated by recent measurements that shed doubt on the reliability of the flux predictions [34, 35]. In the present work, after showing that both scenarios are acceptable [36], a global analysis of all the reactor data is performed under the hypothesis of an active-to-sterile oscillation, making especial emphasis on flux independent analyses.

For a complete study of the $3+1\nu$ oscillation framework, global analyses of all the experimental data sensitive to the new hypothetical oscillation are performed in the $\overset{(-)}{\nu}_e$ and

$\overset{(-)}{\nu}_\mu$ disappearance and the $\overset{(-)}{\nu}_e$ appearance channels [1]. The disappearance channel $\overset{(-)}{\nu}_e$ data, which includes reactor data is compatible with an active-to-sterile oscillation above the $3\sigma$ level [37]. In the $\overset{(-)}{\nu}_e$ disappearance channel, LSND and MiniBooNE data is also compatible with an active-to-sterile oscillation, however this explanation is totally inconsistent with the null searches in the $\overset{(-)}{\nu}_\mu$ disappearance data [37], disproving the $3+1\nu$ oscillation framework as the explanation for the LSND and MiniBooNE anomalies.

The MiniBooNE anomalous $\bar{\nu}_e$ excess [30] reported in 2010 was supported with more statistics in 2013 [38], and recently by an unexpected $\nu_e$ excess, $4.5\sigma$ off from the SM predictions [39]. Together, the $\bar{\nu}_e$ and the $\nu_e$ excesses add up to $4.7\sigma$. Motivated by this high significance and being the active-to-sterile oscillation hypothesis, as it was originally considered by the collaboration, ruled out by the null results from the $\overset{(-)}{\nu}_\mu$ disappearance searches, alternative explanations for the excesses are investigated.

In the MininiBooNE detector, $\nu_e/\bar{\nu}_e$ scatter with the nucleons in the medium via charged-current-quasi-elastic (CCQE) interactions producing electrons/positrons. Based on the fact that the MiniBooNE detector can not distinguish between the signal produced by an electron/positron or a photon, in this thesis it is presented an alternative model explaining the MiniBooNE anomaly [40] with a heavy neutrino decaying into a photon.

This work is structured as follows. In chapter 2 we introduce the basic concepts of neutrino mixing and how they can acquire mass. We also explain the heavy neutrino phenomenology in the laboratory, review the status of the standard neutrino parameters and briefly discuss the role of neutrinos in cosmology. In chapter 3 we explain reactor neutrino oscillations, and give details on the studies done in the $3\nu$ and $3+1\nu$ oscillation frameworks using reactor neutrino data. In chapter 4 we study the MiniBooNE excess alternative explanation by a decaying heavy neutrino. Finally, in chapter 5 we summarize and conclude. Details on data analyses, simulations and long calculations are given in the appendices.

[1] The flavor of the emitted and detected neutrino defines what is known as oscillation channel. When the same flavor that is produced is detected, it is called disappearance channel, and when the flavor is different, appearance channel.

# Chapter 2

# Physics of massive neutrinos

Neutrino flavor change in flight can be explained with neutrino oscillations. For that neutrinos must have a non-zero mass and must mix among each other. In this section the basic concepts of massive neutrinos are introduced. In section 2.1, how neutrino mixing arises and how it enters in CC interactions is explained. The current status of the values of the standard neutrino parameters can be found in section 2.2. Section 2.3 is dedicated to the introduction of the neutrino masses in the SM, focusing as a particular example on the type-I mechanism, in which new massive heavy neutrinos are introduced. The phenomenology of the massive neutrinos in the laboratory at different energy scales is summarized in section 2.4. Finally in section 2.5 the role of neutrinos in cosmology and astrophysics is briefly discussed.

## 2.1 Neutrino mixing

In analogy to the quark sector, the flavor neutrino basis $(\nu_e, \nu_\mu, \nu_\tau)$ is related to the mass basis $(\nu_1, \nu_2, \nu_3)$ by a mixing matrix. After EW symmetry breaking, the relevant $\mathcal{L}$agrangian terms for the neutrino phenomenology are:

$$\mathcal{L}_K = i\overline{\nu'_{\alpha\,L}}\not{\partial}\nu'_{\alpha\,L} + i\overline{\ell'_{\alpha\,L}}\not{\partial}\ell'_{\alpha\,L} + i\overline{\ell'_{\alpha\,R}}\not{\partial}\ell'_{\alpha\,R}\,, \tag{2.1.1}$$

$$\mathcal{L}_{CC} = -\frac{g}{\sqrt{2}}\overline{\ell'_{\alpha\,L}}\gamma^\mu P_L \nu'_{\alpha\,L} W^-_\mu + h.c.\,, \tag{2.1.2}$$

$$\mathcal{L}_{NC} = -\frac{g}{2\cos\theta_W}\overline{\nu'_{\alpha\,L}}\gamma^\mu \nu'_{\alpha\,L} Z_\mu + h.c.\,, \tag{2.1.3}$$

$$\mathcal{L}_{\text{mass}} = -m^\ell_{\alpha\beta}\overline{\ell'_{\alpha\,L}}\ell'_{\beta\,R} - \left(\frac{m^\nu_{\alpha\beta}}{2}\nu'^T_{\alpha\,L} C \nu'_{\beta\,L}\right) + h.c.\,. \tag{2.1.4}$$

$\mathcal{L}_K$, $\mathcal{L}_{CC}$, $\mathcal{L}_{NC}$ and $\mathcal{L}_{\text{mass}}$ are the kinetic, CC, neutral currents (NC) and mass terms of the SM $\mathcal{L}$rangian. $\nu'_L$ and $\ell'_L$ are the components of the $SU(2)_L$ doublet $L_L = (\nu_L\ \ell_L)^T$, i.e. the left-handed neutrino and charged lepton fields, and $\ell'_R$ are the right-handed charged lepton fields. $P_L$ projects over the left-handed components of the fields: $P_L\nu = \nu_L = P_L\nu_L$ and $\bar{\nu} \equiv \nu^\dagger\gamma_0$, with $\gamma_0$ the Dirac matrix. There is an implicit sum over the greek indices $\alpha, \beta = e, \mu, \tau$, which label the flavor. $W$ and $Z$ are the massive gauge bosons mediating the charged and neutral current interactions, respectively. $g$ is the $SU(2)_L$ coupling and $\theta_W$ is the weak angle. $C$ is the charged conjugation matrix. $m^\ell$ is the dirac mass matrix of the charged leptons and $m^\nu$ is the neutrino Majorana mass matrix, which here is added by hand. *h.c.* stands for Hermitian conjugated.

### PMNS matrix

The charged lepton mass matrix is a general complex $3\times3$ matrix which can be diagonalized by two unitary transformations, $V_L$ and $V_R$:

$$\left(V^{\ell}\right)^{\dagger}_{L} m^{\ell} V^{\ell}_{R} = m^{\ell}_{d}\,,$$

where $m^{\ell}_{d}$ has real and positive values [41]. Making a rotation of the charged leptons $\ell'_L = V^{\ell}_L \ell_L$ and $\ell'_R = V^{\ell}_R \ell_R$ the kinetic $\mathcal{L}$agrangian (2.1.1) is left invariant and the mass matrix can be diagonalized. The Majorana neutrino mass matrix is a complex symmetric matrix which can be diagonalized by a unitary transformation [41]:

$$(V^{\nu}_L)^T m^{\nu} V^{\nu}_L = m^{\nu}_d\,.$$

This can be done by a rotation of the neutral leptons $\nu'_L = V^{\nu}_L \nu_L$, which leaves the kinetic (2.1.1) and the neutral current (2.1.3) $\mathcal{L}$agrangian terms invariant, while in the charged current term there is a product of two unitary matrices $V^{\nu\,\dagger}_L V^{\ell}_R \equiv U$, being $U$ unitary too:

$$\mathcal{L}_{CC} = -\frac{g}{\sqrt{2}} U_{\alpha j} \overline{\ell_{\alpha\,L}} \gamma^{\mu} \nu_{j\,L} W^{-}_{\mu} + h.c.\,, \tag{2.1.5}$$

where $\alpha = e, \mu, \tau$ and $j = 1, 2, 3$ are the flavor and mass indices, respectively. Note that for the charged leptons the flavor and the mass basis are conveniently chosen to be the same, while for the neutrinos the bases are related by a mixing matrix

$$\nu_{\alpha} = U_{\alpha j} \nu_j\,, \tag{2.1.6}$$

called the PMNS (Pontecorvo–Maki–Nakagawa–Sakata) matrix [3,4,15,16]. For anti-neutrinos, which are right-handed particles $\bar{\nu}_R$, they are related by the conjugate matrix

$$\bar{\nu}_{\alpha} = U^{*}_{\alpha j} \bar{\nu}_j\,.$$

This matrix appears in the charged current interaction (2.1.5), and as an abuse of language it is usually said that neutrinos are mixed with the charged leptons, while in reality the massive neutrinos are mixed with the flavor neutrinos, which couple to charged leptons of the same flavor in the charged current interactions. In this text, both ways of saying are used indistinctly.

### PMNS matrix physical parameters

A unitary $N \times N$ matrix depends on $N^2$ real parameters which can be divided into

$$\frac{N(N-1)}{2} \quad \text{mixing angles}\,,$$

and

$$\frac{N(N+1)}{2} \quad \text{phases}\,.$$

In the case where there are three generations of charged leptons, $N = 3$, this translates into three mixing angles and six phases. Some of these phases are not physical, since all the $\mathcal{L}$agragian terms are invariant under a global rephasing,

$$\ell_{\alpha} \to e^{i\phi_{\alpha}} \ell_{\alpha}\,, \quad \nu_{\beta} \to e^{i\varphi_{\beta}} \nu_{\beta}\,,$$

except the charged current (2.1.2) and the Majorana neutrino mass term. The $U$ mixing matrix can be parameterized in such a way, cf. section 4.3 of reference [42], that the previous

rephasing would allow to absorb five of its six phases if neutrinos were Dirac particles[1] in the following way:

$$\mathcal{L}_{CC} = -\frac{g}{\sqrt{2}}\overline{\ell_{\alpha\,L}}e^{-i\phi_\alpha}U_{\alpha j}\gamma^\mu e^{i\varphi_j}\nu_{j\,L}W^+_\mu = -e^{i(\varphi_2-\phi_\mu)}\frac{g}{\sqrt{2}}\overline{\ell_{\alpha\,L}}e^{-i(\phi_\alpha-\phi_\mu)}U_{\alpha j}\gamma^\mu e^{i(\varphi_j-\varphi_2)}\nu_{j\,L}W^+_\mu\,.$$

In order to keep the Majorana neutrino mass term invariant, the neutrino fields can not be rephased and only three phases of the mixing matrix can be reabsorbed by the rephasing of the charged lepton fields, hence the lepton mixing matrix depends on three mixing parameters and three phases, a Dirac CP violating phase and two Majorana phases, see (2.2.1).

In expression (2.1.5) $j = 1, 2, 3$ and labels the three known light massive neutrinos. In models in which new massive neutrinos are postulated, $j = 1 \ldots n$, the mixing matrix in (2.1.5) becomes a rectangular $3 \times n$ matrix and the $3 \times 3$ sub-matrix that relates the three known flavor neutrinos with the three known light massive neutrinos is not longer unitary. The new elements of $U_{3\times n}$ account for the deviations from unitarity.

For an extended discussion on this topic, see for instance [42].

## 2.2 Status of the standard neutrino parameters

As it has been explained above, neutrinos are massive and the flavor basis and the mass basis are related via the PMNS matrix, which in the $3\nu$ framework depends on 3 angles and 3 phases, whose most common parameterization is given by

$$U = \begin{pmatrix} 1 & 0 & 0 \\ 0 & c_{23} & s_{23} \\ 0 & -s_{23} & c_{23} \end{pmatrix} \begin{pmatrix} c_{13} & 0 & s_{13}e^{-i\delta_{\rm CP}} \\ 0 & 1 & 0 \\ -s_{13}e^{i\delta_{\rm CP}} & 0 & c_{13} \end{pmatrix} \begin{pmatrix} c_{12} & s_{12} & 0 \\ -s_{12} & c_{12} & 0 \\ 0 & 0 & 1 \end{pmatrix} \begin{pmatrix} e^{i\alpha_1} & 0 & 0 \\ 0 & e^{i\alpha_2} & 0 \\ 0 & 0 & 1 \end{pmatrix}, \tag{2.2.1}$$

where $s_{ij} \equiv \sin\theta_{ij}$ and $c_{ij} \equiv \cos\theta_{ij}$; $\theta_{12}$, $\theta_{13}$ and $\theta_{23}$ are the three mixing angles, $\delta_{\rm CP}$ is the CP violating phase and $\alpha_1$ and $\alpha_2$ are the Majorana phases.

Neutrino oscillation phenomena allow to measure many of the standard neutrino properties but the absolute neutrino mass and the Majorana phases, as it will be explained in section 3.1. Apart from the 3 mixing angles and the CP violating phase, neutrino oscillations depend on the two independent mass squared differences which are usually called the solar, $\Delta m^2_{\rm sol}$, and the atmospheric, $\Delta m^2_{\rm atm}$, since they drive the oscillation frequency of the solar and atmospheric neutrino oscillation phenomena, see section 3.1.

The order of the neutrino masses, the mass ordering, can be either normal (NO) i.e. $m_3 > m_2 > m_1$ or inverted (IO) i.e. $m_2 > m_1 > m_3$ as it is depicted in figure 2.2.1. $\Delta m^2_{\rm sol}$ is taken positive for convention, but depending on the ordering, $\Delta m^2_{\rm atm}$ can be either positive or negative. Here the convention from the NuFit collaboration [26, 27] is used:

$$\Delta m^2_{\rm sol} \equiv \Delta m^2_{21} > 0\ ; \quad \Delta m^2_{\rm atm} \equiv \Delta m^2_{3\ell} = \begin{cases} \Delta m^2_{31} > 0 & \text{for NO,} \\ \Delta m^2_{32} < 0 & \text{for IO.} \end{cases} \tag{2.2.2}$$

Given the large amount of experiments measuring neutrino oscillations, global fits are necessary to determine all the oscillation parameters consistently within the same theoretical framework. Oscillation parameters are in general measured by different experiments,

[1] Note that this is what happens in the quark sector and this is why the CKM matrix has only one CP violating phase, see chapter 4 in [42].

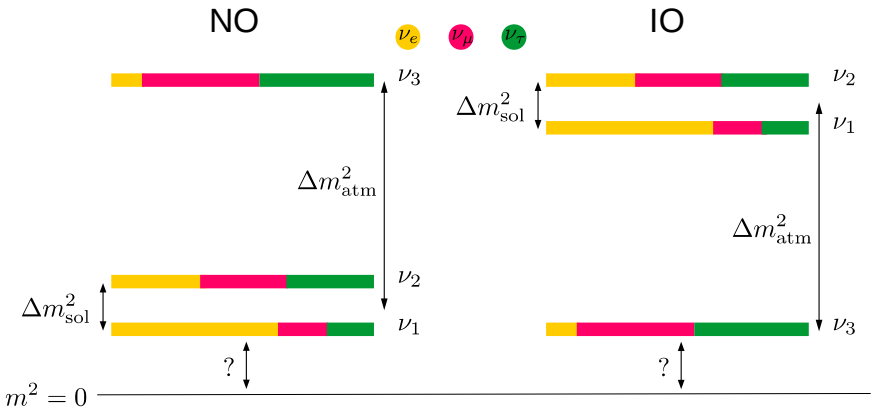


Figure 2.2.1: Neutrino masses for normal (left) and inverted (right) ordering. Yellow, red and green represent a representative fraction of the flavor composition of each massive state, electron, $\nu_e$, muon, $\nu_\mu$, and tau, $\nu_\tau$, flavors respectively.

so a combination of these measurements gives a more precise determination, due to the complementarity of the data sets. Analyzing the global data together also allows to detect inconsistencies and tensions among the experiments.

With current data it is possible to determine accurately most of the oscillation parameters, but the $\theta_{23}$ octant, the $\delta_{CP}$ value and the mass ordering. More on global analysis is discussed in section 3.3.1.

In table 2.1 a summary of the current values of the standard neutrino parameters, obtained in the global analysis by the NuFit collaboration [27], can be found. The relative $3\sigma$ precision of the parameters is given by

$$\begin{aligned}
&\theta_{12} : 14\%\,, \quad \theta_{13} : 8.9\%\,, \quad \theta_{23} : 24\%\,,\\
&\Delta m^2_{21} : 16\%\,, \quad |\Delta m^2_{3\ell}| : 7.6\%\,,\\
&\delta_{\rm CP} : 92\%\,.
\end{aligned}$$

NO is favored over IO by $\Delta\chi^2 = 9.3\,(3\sigma)$.

The absolute neutrino mass can be measured in $\beta$-decay experiments, which are sensitive, depending on their resolution power, to the single neutrino masses $m_i$ or to their weighted sum:

$$m^2_{\nu_e} \equiv \sum_{i=1}^{3} |U_{ei}|^2 m_i^2\,,$$

where $U_{ei}$ are the $1i$ elements of (2.2.1).

The KATRIN experiment set recently the most stringent limit on this mass $m^2_{\nu_e} < 1.1\,\text{eV}^2$ at 90% C.L. [43]. In the extreme case that the lightest neutrino is massless, given the current values of the measured mass squared differences, cf. table 2.1, the smallest value on $m_{\nu_e}$ can be computed, so that for NO(IO)[2]:

$$0.009(0.04) < m_{\nu_e} < 1.05\,\text{eV}\,.$$

$0\nu\beta\beta$ decay can also give direct information on the neutrino masses through the effective electron neutrino Majorana mass, cf. (2.4.5). Cosmological measurements also provide information on the sum of the neutrino masses $\sum m_\nu$, cf. section 2.5.

[2]In the case that the lightest neutrino is massless, for NO: $m_1 = 0$, $m_2 = \sqrt{\Delta m^2_{21}}$ and $m_3 = \sqrt{\Delta m^2_{31}}$; and for IO: $m_1 = \sqrt{-\Delta m^2_{21} - \Delta m^2_{32}}$, $m_2 = \sqrt{-\Delta m^2_{32}}$, $m_3 = 0$.

| Parameters | Normal Ordering (best fit) | | Inverted Ordering ($\Delta\chi^2 = 9.3$) | |
|---|---|---|---|---|
| | bfp $\pm 1\sigma$ | $3\sigma$ range | bfp $\pm 1\sigma$ | $3\sigma$ range |
| $\sin^2\theta_{12}$ | $0.310^{+0.013}_{-0.012}$ | $0.275 \to 0.350$ | $0.310^{+0.013}_{-0.012}$ | $0.275 \to 0.350$ |
| $\theta_{12}/^\circ$ | $33.82^{+0.78}_{-0.76}$ | $31.61 \to 36.27$ | $33.82^{+0.78}_{-0.75}$ | $31.61 \to 36.27$ |
| $\sin^2\theta_{23}$ | $0.563^{+0.018}_{-0.024}$ | $0.433 \to 0.609$ | $0.565^{+0.017}_{-0.022}$ | $0.436 \to 0.610$ |
| $\theta_{23}/^\circ$ | $48.6^{+1.0}_{-1.4}$ | $41.1 \to 51.3$ | $48.8^{+1.0}_{-1.2}$ | $41.4 \to 51.3$ |
| $\sin^2\theta_{13}$ | $0.02237^{+0.00066}_{-0.00065}$ | $0.02044 \to 0.02435$ | $0.02259^{+0.00065}_{-0.00065}$ | $0.02064 \to 0.02457$ |
| $\theta_{13}/^\circ$ | $8.60^{+0.13}_{-0.13}$ | $8.22 \to 8.98$ | $8.64^{+0.12}_{-0.13}$ | $8.26 \to 9.02$ |
| $\delta_{\rm CP}/^\circ$ | $221^{+39}_{-28}$ | $144 \to 357$ | $282^{+23}_{-25}$ | $205 \to 348$ |
| $\frac{\Delta m^2_{21}}{10^{-5}\ \text{eV}^2}$ | $7.39^{+0.21}_{-0.20}$ | $6.79 \to 8.01$ | $7.39^{+0.21}_{-0.20}$ | $6.79 \to 8.01$ |
| $\frac{\Delta m^e_{3\ell}}{10^{-3}\ \text{eV}^2}$ | $+2.528^{+0.029}_{-0.031}$ | $+2.436 \to +2.618$ | $-2.510^{+0.030}_{-0.031}$ | $-2.601 \to -2.419$ |

Table 2.1: Status of the $3\nu$ oscillation parameters, latest update of NuFit collaboration, version 4.1. The two first columns are the values for NO and last two for IO. For all the parameters the best fit point together with its $1\sigma$ uncertainty and their $3\sigma$ C.L. range are shown. NO shows a preference of 9.3 units in $\Delta\chi^2$, but the values of the confidence levels, for both NO and IO, are taken with respect to their respective local minimum. In [26] there is a discussion on the Super-Kamiokande $\Delta\chi^2$ tabulated table, which is included to obtain the values shown here. Table taken from [27], details on the whole data set used for the analysis can also be found in that reference.

Neutrino oscillations are also not sensitive to the Majorana phases, however $0\nu\beta\beta$ decays are. An observation of this process will be a direct measurement of new physics, as explained below. This phenomenon has not been observed so far.

## 2.3 Neutrino masses and the Standard Model

The fact that neutrinos oscillate shows that they are massive and that they mix among each other. But in the SM they are massless. This is why neutrino oscillations is one of the experimental evidences that the SM is not complete and needs an extension in order to include neutrino masses.

Since in the SM there are only left-handed neutrinos (and right-handed anti-neutrinos), they can not have a Dirac mass, so a way to give them mass could be introducing a Majorana mass of the form

$$m^\nu \nu_L^T C \nu_L \,,$$

but it violates $U_{\rm Y}(1)$ symmetry by two units, cf table 2.2. Given the SM gauge symmetries ($SU_{\rm C}(3)\times SU_{\rm L}(2)\times U_{\rm Y}(1)$) and its particle content it is not possible to write a renormalizable four dimensional term in the $\mathcal{L}$agrangian accounting for the neutrino masses.

Using an Effective Field Theory (EFT) approach, with the SM particle content, a five dimensional neutrino mass term can be written, which satisfies the SM gauge symmetries: the Weinberg operator.

| | | $T$ | $T_3$ | $Y$ |
|---|---|---|---|---|
| $L_L$ | $\nu_L$<br>$\ell$ | $\frac{1}{2}$ | $\frac{1}{2}$<br>$-\frac{1}{2}$ | $-1$ |
| $e_R$ | | 0 | 0 | $-2$ |
| $\phi$ | $\phi^+$<br>$\phi^0$ | $\frac{1}{2}$ | $\frac{1}{2}$<br>$-\frac{1}{2}$ | 1 |
| $\tilde{\phi}$ | $\tilde{\phi}^0$<br>$\tilde{\phi}^-$ | $\frac{1}{2}$ | $\frac{1}{2}$<br>$-\frac{1}{2}$ | $-1$ |

Table 2.2: Quantum numbers of the left-handed leptons and higgs doublet under the $SU(2)_L$ ($T_3$) and $U(1)_Y$ (Y) gauge symmetries.

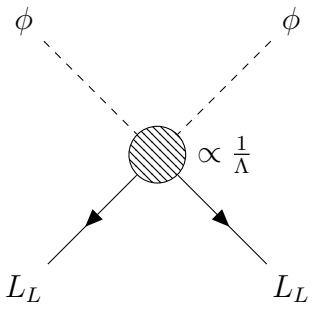


Figure 2.3.1: Feynman diagram of the Weinberg operator.

**Weinberg operator**

The Weinberg operator is given by

$$\mathcal{L}_5 = \frac{1}{\Lambda}\overline{L_L^C}\tilde{\phi}^*\tilde{\phi}^\dagger L_L\,, \tag{2.3.1}$$

where $L_L = (\nu_L\ \ell_L)^T$ is the left-handed lepton doublet and $\overline{L_L^C} = L_L^T C$ with $C$ being the charge conjugation matrix. $\phi = (\phi^+\ \phi^0)^T$ is the Higgs doublet, and $\tilde{\phi} = i\sigma_2\phi^*$ with $\sigma_2$ the second Pauli matrix. $\Lambda$ is a constant with dimension $[\Lambda] = E^1$, its value is related to a new physics energy scale. The corresponding Feynman diagram is depicted in figure 2.3.1.

Although the Weinberg operator (2.3.1) complies with all the SM gauge symmetries, see table 2.2, it is five dimensional, hence not renormalizable. Since it is an effective operator it is not a problem provided that the underlying theory is renormalizable.

After Electro-Weak Symmetry Breaking (EWSB), i.e. $\langle\phi\rangle = \left(v/\sqrt{2}\ \ 0\right)^T$, with $v$ being the Higgs vacuum expectation value, the Weinberg operator takes the form

$$\mathcal{L}_5 = \frac{1}{\Lambda}\frac{v^2}{2}\overline{\nu_L^C}\nu_L\,, \tag{2.3.2}$$

which is a Majoranna mass term for the neutrinos that violates lepton number by two units[3], with the mass given by $m_M = v^2/\Lambda$. Here, the Majorana neutrino mass is suppressed by the new energy scale $\Lambda$, so that the lightness of the neutrino mass can be explained when it lies at very high energies.

The fact that neutrino masses are so small compared with the masses of the rest of the SM particles, suggests that there must be an alternative mechanism that give them mass, different from the Higgs mechanism. Of the most common ones are the type-I, II

[3]Lepton number is an accidental symmetry of the SM $\mathcal{L}$agrangian.

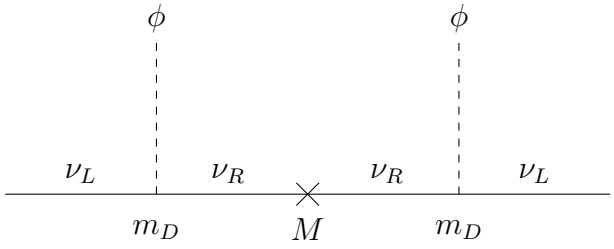


Figure 2.3.2: Type-I seesaw mechanism for the neutrino mass generation.

and III seesaw mechanisms [11–14, 44], in which the SM particle content is extended with a right-handed singlet, scalar $SU_{\rm L}(2)$ triplet and a $SU_{\rm L}(2)$ fermion triplet, respectively. The neutrino mass can also be generated radiatively at one or more loops level depending on the extension of the particle content of the SM, like for example in the Zee-Babu model [45]. As an illustrative example, the type-I seesaw mechanism for one neutrino family is explained below.

**Type-1 seesaw**

A straight forward way of extending the SM particle content is adding right-handed neutrinos $\nu_R$ which are singlets of all the SM gauge symmetries, usually called sterile neutrinos. So that the most general $\mathcal{L}$agrangian is given by

$$\mathcal{L} = \mathcal{L}_{\rm SM} + i\bar{\nu}_R \not{\partial} \nu_R - \left( Y_\nu \overline{L_L} \tilde{\phi} \nu_R + \frac{1}{2} \overline{\nu_R^C} M \nu_R + h.c. \right) . \tag{2.3.3}$$

$\tilde{\phi}$ is introduced in order to make the Dirac mass term invariant under $SU_{\rm L}(2) \times U_{\rm Y}(1)$. Since $\nu_R$ are singlets under the SM gauge symmetries, the Majorana mass term is allowed[4], where $\overline{\nu_R^C} = \nu_R^T C$. Then the neutrinos acquire mass through the tree level diagram depicted in figure 2.3.2.

After EWSB the full neutrino mass term can be written in the following form:

$$n^T C \mathcal{M} n = \begin{pmatrix} \nu_L^T & \left(\nu_R^C\right)^T \end{pmatrix} C \begin{pmatrix} 0 & m_D \\ m_D^T & M \end{pmatrix} \begin{pmatrix} \nu_L \\ \nu_R^C \end{pmatrix} , \tag{2.3.4}$$

where $m_D = Y_\nu \frac{v}{2}$ and $v$ is the Higgs v.e.v.. The first entry in the matrix is 0, since a Majorana mass term for the $\nu_L$ would violate hypercharge by two units. In general there are three $\nu_L$ and in principle there could be any number, $m$, of $\nu_R$, so that $m_D$ is a $3 \times m$ matrix and $M$ a $m \times m$ matrix. For simplicity these indices do not appear explicitly.

In order to see how the light neutrinos can acquire a small mass through this mechanism, let us considered the particular example of one single $\nu_L$ and one single $\nu_R$ with a Majorana mass $M \gg m_D$. Then,

$$\mathcal{M} = \begin{pmatrix} 0 & m_D \\ m_D & M \end{pmatrix} ,$$

is a $2 \times 2$ matrix. It is expressed in the neutrino "flavor" basis $\{\nu_L, \nu_R^C\}$. Since $\mathcal{M}$ is symmetric it can be diagonalized by a unitary matrix $\mathcal{U}$:

$$\mathcal{U}^T \mathcal{M} \mathcal{U} = \text{diag}\left\{ m_{\rm light}, m_{\rm heavy} \right\} .$$

[4]Note that in order to conserve lepton number in the Dirac mass term, $\nu_R$ must have lepton number +1, so that the Majorana mass term violates it by two units.

In the approximation $M \gg m_D$ the masses are given by

$$m_{\text{light}} = \frac{m_D^2}{M} + \mathcal{O}\left(\frac{m_D^2}{M}\right)^2 \; ; \quad m_{\text{heavy}} = M + \mathcal{O}\left(\frac{m_D^2}{M}\right) \tag{2.3.5}$$

and the mixing matrix by

$$\mathcal{U} = \begin{pmatrix} \cos\theta & \sin\theta \\ -\sin\theta & \cos\theta \end{pmatrix} = \begin{pmatrix} 1 & \frac{m_D}{M} \\ -\frac{m_D}{M} & 1 \end{pmatrix} + \mathcal{O}\left(\frac{m_D}{M}\right)^2 . \tag{2.3.6}$$

So that the light neutrino mass can be expressed as:

$$m_{\text{light}} \simeq \theta^2 M \, , \tag{2.3.7}$$

where $\theta$ is approximately the mixing of the active neutrino with the heavy mass eigenstate.

From (2.3.5) it can be seen that in the limit $M \gg m_D$ the spectrum of masses consist of a light and a heavy neutrino. This way the light neutrinos acquire a small mass, suppressed by the large right-handed neutrino Majorana mass. From (2.3.6) it can be seen how the "flavor" basis mixes with the massive eigenstates. In the limit considered here:

$$\begin{aligned} \nu_L &\simeq \nu_l - \tfrac{m_D}{M}\nu_h \, , \\ \nu_R^C &\simeq \tfrac{m_D}{M}\nu_l + \nu_h \, . \end{aligned} \tag{2.3.8}$$

where $\nu_{l,h}$ are the light and heavy mass eigenstates. Note that the light mass eigenstate, $\nu_l$, is mainly an active neutrino, $\nu_L$, and the heavy, $\nu_h$, a sterile neutrino $\nu_R^C$. As an abuse of language heavy and sterile neutrinos are named indistinctly, also here in this work.

The same can be generalized in a three light neutrino family scenario, when the scale of the Dirac mass matrix, $m_D$, is much smaller than the scale of the Majorana mass matrix, $M$. In that scenario, taking into account that the deviations from unitarity of the PMNS matrix are very small, it is obtained that the light neutrinos are related to the active flavor neutrinos by

$$\tilde{U} = U\left(\mathbb{1} + \mathcal{O}\left(\Theta\right)^2\right) \, , \tag{2.3.9}$$

where $U$ is the unitary PMNS matrix and $\Theta$ is a matrix that accounts for its deviations from unitarity that is precisely the mixing between the known flavor neutrinos, $\nu_L$, and the heavy neutrinos $N$, i.e.

$$\nu_{L,\alpha} \simeq \tilde{U}_{\alpha i}\nu_i + \Theta_{\alpha J} N_J \, , \tag{2.3.10}$$

whit $\alpha = e, \mu, \tau$ and $J = 1 \ldots m$, in analogy to the one $\nu_L$ family case (2.3.8). See appendix D.

## 2.4 Phenomenology with massive neutrinos

Massive neutrinos have a rich phenomenology. This work is not limited to the study of the three known light neutrinos, but also scenarios where a heavier neutrino is coupled to the known neutrinos are studied. Those scenarios are effective, in the sense that they should be embedded in a more general theoretical framework, which for instance can provide mass to the light neutrinos via the seesaw mechanism as it was discussed above.

In the same way as light neutrinos are mixed among each other, i.e. the flavor basis is a linear combination of the massive eigenstates, the heavy neutrinos talk to the active known ones via mixing as well. Depending on the mass scale of the extra neutrino its effects are going to be visible in different physical phenomena. A summary of the heavy neutrino phenomenology and its constraints are shown in [46]. In the following, some of the laboratory searches for heavy neutrinos, from the eV to the TeV scale, are explained.

### eV neutrinos and neutrino oscillations

An eV scale heavy neutrino can be studied in neutrino oscillation experiments. Its existence would give rise to new oscillation frequencies, the heavier the neutrino the higher the frequency, changing the expected patterns of the standard $3\nu$ framework oscillation probability, see section 3.1. The new oscillation frequencies would cause an excess or deficit of neutrinos of a given flavor, with respect to the expectations, through what is called active-to-sterile oscillations. Depending on the mass and mixing with the active neutrinos, it can be tested in different neutrino oscillation experiments: solar, reactor, atmospheric or accelerator experiments.

It is worth to highlight that those experiments measuring at a short distance from the neutrino source, are sensitive to high oscillation frequencies, being crucial in the study of eV neutrino as it will be explain in section 3.

Neutrino detection via NC interactions also provides very valuable information in the search for these sterile neutrinos. Through NC interactions all the neutrino flavors of a given flux, e.g. solar or an accelerator neutrino flux, can be detected indistinctly. Then the measurement is proportional to the total neutrino flux regardless of the neutrino flavor change in the oscillations. Therefore any suppression of the total expected neutrino flux would be a clear probe of active neutrinos oscillating into sterile states that are not measurable in NC interactions.

A gobal search for the eV sterile neutrino through neutrino oscillations, focusing on the contribution from reactor neutrino experiments, is described in section 3.4, based on the work done in reference [37].

### KeV neutrinos and $\beta$-decay

Heavier neutrinos, in the KeV scale, are interesting in the context of cosmology and astrophysics since they are candidates of warm dark matter (WDM)[5]. However, within the simplest neutrino model and not considering exotic cosmological frameworks, many astrophysical and cosmological observations constrain the parameter space for these heavy neutrinos, see references [47, 48] for a detailed review.

Different probes for KeV neutrinos can be achieved in laboratory searches, for example in $\beta$-decay experiments. In a $\beta$-decay both and electron and an electron anti-neutrino are produced

$$A(Z,N) \to A(Z+1, N-1)\, e^- \, \bar{\nu}_e \,,$$

where $A$ is a nucleus with $Z$ protons and $N$ neutrons. In this process there is a probability of producing a heavy neutrino weighted by its mixing with the electron neutrino, $U_{e4}$, as long as it is kinematically allowed, i.e. provided it is lighter than the available energy in the process.

In this way a heavy neutrino of mass $m_4$ and mixing $|U_{e4}|^2$ would contribute to the electron $\beta$-decay spectrum, since in that scenario the total spectrum would be a superposition of the light and heavy neutrino contributions [23]:

$$\begin{aligned} \frac{\mathrm{d}\Gamma}{\mathrm{d}E}(E) &= \Theta\left(E_0 - E - m_{\text{light}}\right)\left(1 - |U_{e4}|^2\right)\frac{\mathrm{d}\Gamma}{\mathrm{d}E}\left(E, m_{\text{light}}\right) \\ &\quad + \Theta\left(E_0 - E - m_4\right)|U_{e4}|^2\,\frac{\mathrm{d}\Gamma}{\mathrm{d}E}\left(E, m_4\right) \quad , \end{aligned} \tag{2.4.1}$$

[5] A review of the cosmological and astrophysical motivation for the sterile neutrinos can be found in references [47–49].

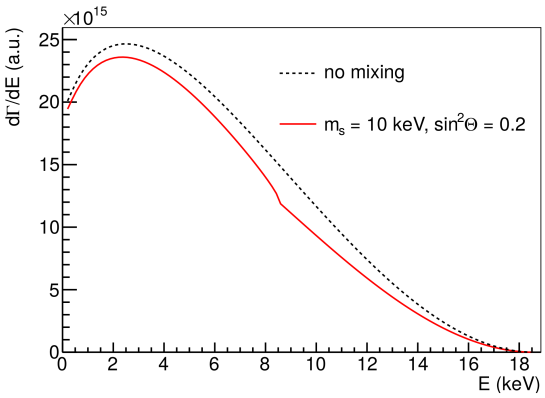


Figure 2.4.1: Figure taken from figure 1 in reference [50]. Tritium $\beta$-decay spectrum (2.4.1) for a light neutrino only (dashed black) and introducing a heavy neutrino mass $m_s \equiv m_4 = 10\,\mathrm{KeV}$ and mixing $\sin^2\Theta \equiv |U_{e4}|^2 = 0.2$ (red). Here the mixing is exaggerated so that the kink like feature, at an energy $E = E_0 - m_4$, is visible.

where $m_{\text{light}}$ is the effective mass of the light neutrino, $E$ is the electron kinetic energy and $E_0$ is the available energy of $\beta$-decay the process. $\mathrm{d}\Gamma/\mathrm{d}E(E,m)$ is the $\beta$-decay spectrum as a function of the neutrino mass [50,51]. The $\Theta$ function accounts for the energy conservation, which leads to a step like feature in the $\beta$-decay spectrum proportional to $|U_{e4}|^2$, at an energy given by the difference $E_0 - m_4$. An example of this feature is represented in figure 2.4.1.

From $\beta$-decays, the light neutrino mass can be determined measuring at the very end point of the spectrum, as the KATRIN experiment is aiming to do [43], while scanning the entire $\beta$-decay energy spectrum there is a potential of discovery of new particles that couple to the electron in a wide range of energies, from the eV to the tenths of KeV scale, in particular KeV heavy neutrinos [50].

### MeV neutrinos and meson decays

Heavier neutrinos are not kinematically allowed in $\beta$-decay processes but they are in meson decays.

MeV neutrinos that couple to the charged leptons, can be searched for in meson decays [23,52]. Of particular interest are the pure leptonic decays of charged pseudoscalar mesons, $M \to \ell\nu$, where $\ell$ is a charge lepton and $\nu$ a light active neutrino. In these decays the charged leptons show a characteristic signal consisting of a monochromatic energy peak at an energy given by:

$$E_\ell = \frac{m_M^2 + m_\ell^2 - m_\nu^2}{2m_M}\,. \tag{2.4.2}$$

Due to the neutrino mixing, mesons could also decay into a heavy neutrino and a charged lepton, $M \to \ell N$. In this decay the lepton energy (2.4.2) would be shifted by $-m_N^2/2m_M$. The relation between the decay rates into a light and heavy neutrino is given by [23,52]:

$$\frac{\mathrm{Br}(M \to \ell N)}{\mathrm{Br}(M \to \ell\nu)} = \frac{|U_{\ell 4}|^2 \bar{\rho}(m_N)}{1 - |U_{\ell 4}|^2}\,, \tag{2.4.3}$$

where

$$\bar{\rho}(m_N) = \frac{(x_N^2 + x_\ell^2 - (x_N^2 - x_\ell^2)^2)\,\sqrt{(1-(x_N+x_\ell)^2)(1-(x_N-x_\ell)^2)}}{x_\ell^2(1-x_\ell^2)^2}\,, \tag{2.4.4}$$

with $x_i \equiv m_i/m_M$; $i = \ell, N$. The $\bar{\rho}(m_N)$ factor is a kinematic enhancement of the decay rate into heavy neutrinos with respect to the decay rate into light neutrinos. It accounts for two effects: a helicity enhancement and a phase space suppression [23]. The helicity enhancement arises from the decay matrix element. Pseudoscalar mesons have spin 0, light neutrinos and anti-neutrinos have a definite chirality and since they are essentially massless their helicity coincides with their chirality. Thus the charged lepton helicity has to be the opposite in order to conserve angular momentum. The heavy neutrino helicity do not coincide with its chirality, hence any helicity is allowed, also for the charged lepton. This leads to an enhancement with respect to the decay into light neutrino that depends on the neutrino mass. See [23] for further details. The phase space suppression arises when computing the decay rate, because the heavier the neutrino the less kinetic energy for the final states is left, leading to a mass dependent suppression.

For small mixing the branching ratio relation (2.4.3) is proportional to $|U_{\ell 4}|^2$, hence so is the sensitivity to the heavy neutrino.

The range of energies at which the new particles that couple to the charged leptons can be found, depends on the energy available in the given process. This is given by the difference between the meson mass and the rest of the daughter particle masses in the decay: $m_N \leq m_M - \sum_{i\neq N}^{\text{daughters}} m_i$. In the particular case of the two body decay $M \to \ell\nu$, it is $m_N \leq m_M - m_\ell$.

In beam dump experiments these meson decays can be searched for, where a beam of protons is dumped into a target, producing many particles, in particular many pions, kaons and even D mesons, depending on the original energy of the proton beam. These mesons subsequently decay into lighter particles, neutrinos among them. Mesons can also be stopped before decaying, producing charged leptons with definite energy (2.4.2), being possible to search for heavy neutrinos as it is here described, as for example in the NA62 [53] and E949 [54] experiments.

### GeV neutrinos at colliders

Heavy neutrinos with masses at the GeV-TeV scale, have to be studied at high energy colliders where the heavy neutrino can be produced as long as its mass is below the center of mass energy. Such heavy Majorana neutrinos can be searched for via lepton number violation processes from meson decays, as for example it is done at the B factories, LHCb [55–57] and Belle [58], and generated via the CC Drell-Yan processes [59]. They can also be long lived and thus leave displaced vertex signals in the detector [60, 61]. For a complete review of heavy neutrino signatures at colliders with lepton number violation see for instance references [24,62,63]. A complete overview of lepton number-conserving signatures and their prospects at running and future colliders can be found in [64].

### Heavy neutrinos and non-unitarity

The mixing between active and sterile neutrinos (2.3.10) gives rise to deviations of the PMNS matrix from unitarity. Non unitarity has been studied in the literature as a viable way of searching for sterile neutrinos, at different energy scales [64–66]. With high enough precision, hints of much heavier neutrinos, with masses at an energy scale much larger than what is achievable in current and near future experiments, can still be obtained studying the deviations of the PMNS matrix from unitarity.

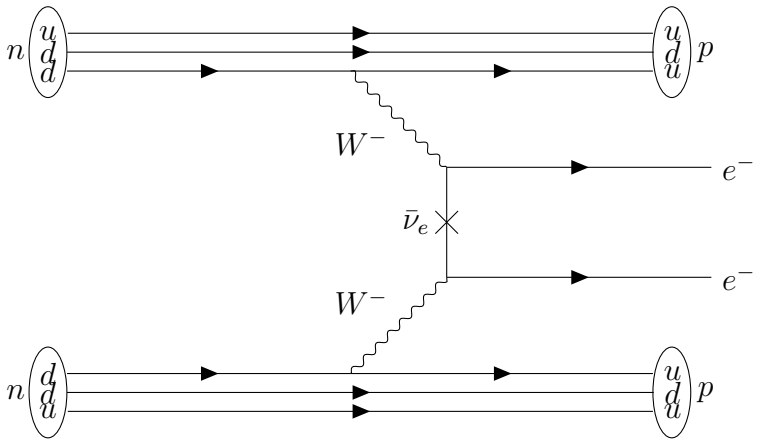


Figure 2.4.2: Feynman diagram of a $0\nu\beta\beta$ decay. A nucleus $A$ with $Z$ protons and $N$ nucleus decay without emitting neutrinos $A(Z,N) \to A(Z+2, N-2)\, e^- e^-$. Here the decay is represented being mediated by Majorana neutrinos.

### Heavy neutrinos and $0\nu\beta\beta$

If neutrinos are Majorana particles, they will have an impact in $0\nu\beta\beta$ decay processes, which can also provide information on the mass and the mixing of heavy neutrinos at any mass scale.

In $0\nu\beta\beta$ decays

$$A(Z,N) \to A(Z+2, N-2)\, e^- e^- \,,$$

lepton number is violated by two units. Its observation could be understood as being mediated by Majorana neutrinos, see figure 2.4.2, where the mass insertion could be a heavy neutrino exchange at tree level (2.3.2). However this process could be also casued by other particles and interactions from new physics models that violates lepton number by two units [67–71].

The $0\nu\beta\beta$ decay amplitude is proportional to what is called effective electron neutrino Majorana mass:

$$m_{ee} \simeq \left| \sum_{i=1}^{3} U_{ei}^2 m_i \right| . \tag{2.4.5}$$

Being $0\nu\beta\beta$ decays sensitive to the Majorana phases (2.2.1). So far this process has not been measured. The limit on $m_{ee}$ is currently given by $m_{ee} \lesssim 0.06 - 0.200\,\text{eV}$ at the 90% C.L. [72, 73].

A heavy neutrino that mixes with the electron neutrino would have an impact on $m_{ee}$ with respect to the SM model case [74, 75]:

$$m_{ee} \simeq \left| \sum_{i}^{3+N} U_{ei}^2 p^2 \frac{m_i}{p^2 - m_i^2} \right| . \tag{2.4.6}$$

Here $p$ is the exchange of virtual momentum in the nucleus decay, with a typical value of $p^2 \simeq -(125\,\text{MeV})^2$. In the case of the three light neutrino masses $m_i$, the expression (2.4.5) is recovered. For a discussion on how the heavy neutrino affects the nuclear matrix element, which are omitted here, see reference [75].

As can be seen in (2.4.6), regardless of the mass of the heavy neutrinos they will have an impact in the effective electron neutrino mass [46], making $0\nu\beta\beta$ decay studies complementary to other searches for heavy neutrinos. In [76] we performed a study on the

complementarity of heavy neutrino searches in $\beta$ and $0\nu\beta\beta$ decays in the context of low-scale seesaw realizations [77–80].

## 2.5 Neutrinos and cosmology

Neutrinos contribute to the energy density of the universe, taking part on the dynamics of the cosmos and hence its evolution, see for instance references [42,81]. In the early universe they are relativistic particles, so they contribute to the energy density as relativistic degrees of freedom. The effective number of relativistic neutrino species, $N_{\text{eff}}$, have an impact in the Big Bang nucleosynthesis (BBN) [82] and cosmic microwave background (CMB) [83] observables. The CMB and structre formation also depend on the sum of the neutrino masses $\sum m_\nu$ [84,85]. Precise measurements on these observables set $N_{\text{eff}} = 2.99 \pm 017$ and $\sum m_\nu \lesssim 0.12\, eV$ [83].

In the standard picture, sterile neutrinos are produced in collisions in the in the early universe through active-to-sterile transitions, knwon as the Dodelson-Widrow production mechanism [21]. The amount of sterile neutrinos produced depends on their mixing with the active ones. For a large enough mixing they can even reach thermal equilibrium with the primordial bath before neutrino decoupling [86]. Depending on their mass and mixing, heavy neutrinos will contribute to $N_{\text{eff}}$, and to the sum of the neutrino masses. Therefore BBN, CMB and structure formation observables can be used to set bounds on the sterile neutrino parameters [87].

Detailes on the role of the sterile neutrino in cosmology and its constraints from cosmological and astrophysical observables can be found in the review articles [22, 48, 49]. Of special interest in this work are the constraints on the eV and MeV mass scale sterile neutrinos.

The BBN, CMB and structure formation bounds on $N_{\text{eff}}$ and $\sum m_\nu$ constrain the mass and mixing of an extra sterile neutrino in the eV range [83, 86]. In the eV sterile neutrino searches performed in this work cosmological constraints are not applied, since they are model dependent and in non-minimal frameworks they can be weakened or even vanished. For example, including new interactions in the sterile neutrino sector, usually called secret interactions [88].

MeV neutrinos will have an impact on BBN observables depending on their life time [89], its bounds restrict MeV neutrinos to have a lifetime less than 1s [90]. The supernova SN1987A also set bounds on neutrinos at this mass scale since they work as a cooling mechanism, thus reducing the observed time of the neutrino burst [89]. As it will be explained in chapter 4, the MeV neutrino required to explain the MiniBooNE anomalous excess, is compatible with both BBN and SN1987A constraints.

Cosmological bounds are model dependent and modifications of the standard scenario can relax them, see for example [87,91]. Therefore even though some of the sterile neutrino constrains, coming from cosmology, are more stringent than the current sensitivity of laboratory searches, where measurements can be repeated under the same circumstances, the latter are always a good check for consistency and will have the last word on the determination of the standard and non-standard neutrino parameters.

# Chapter 3

# Oscillation studies with reactor neutrinos

Studies on neutrino oscillations in the $3\nu$ standard framework as well as in the $3+1\nu$ are discussed in this chapter, based on references [26, 28, 36, 37].

Section 2.1 is an introduction to neutrino oscillations in the $3\nu$ framework and how to extend then to a $3+1\nu$ framework. In section 2.2 the basics of reactor neutrinos are introduced, also it is explained how the analyses of their data are performed. In section 2.3 and 2.4 studies using the reactor neutrino data in the $3\nu$ and $3+1\nu$ frameworks are presented.

## 3.1 Neutrino oscillations

In this section, basic concepts of neutrino oscillations, useful for this work, are briefly discussed.

#### Oscillation probability in vacuum

The neutrino flavor states can be expressed as a linear combination of the mass eigenstates, weighted by the conjugate PMNS mixing matrix[1] (2.2.1):

$$|\nu_\alpha\rangle = U^*_{\alpha j}|\nu_j\rangle \,.$$

The index $\alpha$ labels the flavor and $j$ the mass eigenstate, i.e. $\alpha = e, \mu, \tau$ and $j = 1, 2, 3$. In the case of anti-neutrinos $U^*$ has to be replaced by $U$. Since the neutrino masses are different, each of the mass eigenstates evolves differently in time, $t$. In vacuum they evolve as follows:

$$|\nu_j(t)\rangle = e^{-iE_j t}|\nu_j\rangle \,,$$

where $E_j = \sqrt{m_j^2 + p^2}$ is the neutrino energy, which depends on its mass $m_j$ and momentum $p$. Then, the evolution of the flavor state can be written as

$$|\nu_\alpha(t)\rangle = U^*_{\alpha j} e^{-iE_j t}|\nu_j\rangle \,.$$

[1] Note that the flavor and mass eigenstates are related by the conjugate PMNS matrix, $U^*$, while this relation for the neutrino fields (2.1.6) is given by $U$. The conjugate PMNS matrix arises because the neutrino state, $|\nu_\alpha\rangle$, is created when the anti-neutrino filed, $\bar{\nu}_\alpha$, containing the creator opperator, $a^\dagger_{\nu_\alpha}(p)$, acts on the vacuum [42, 92].

Writing the mass eigenstate as a combination of the flavor eigenstates, $|\nu_j\rangle = U_{\beta j}|\nu_\beta\rangle$, the probability of finding a flavor neutrino $\beta$ when a flavor neutrino $\alpha$ was produced and propagated through vacuum a distance $L$, is given by the oscillating probability

$$\begin{aligned} P_{\nu_\alpha\to\nu_\beta} &= |\langle\nu_\beta|\nu_\alpha(t)\rangle|^2 = \left|U^*_{\alpha j}e^{-iE_j t}U_{\beta j}\right|^2 \\ &= \sum_{j,k} U^*_{\alpha j}U_{\beta j}U_{\alpha k}U^*_{\beta k}\exp\left\{i\frac{\Delta m^2_{kj}L}{2E}\right\}, \end{aligned} \tag{3.1.1}$$

where $\Delta m^2_{kj} \equiv m^2_k - m^2_j$. Here it is assumed that the light neutrinos are highly relativistic, so that $t = L$ in natural units, and that the neutrinos have definite momentum, so

$$E_k - E_j \simeq \frac{\Delta m^2_{kj}}{2E} + \mathcal{O}\left(\frac{m^4}{E^3}\right).$$

This way of obtaining the oscillation probability is ilustrative but it is not rigorous, since neither neutirnos are plane waves nor have definite momentum. For rigorous derivations of the neutrino oscillation probability, see for instance [42, 93, 94]. The result obtained here (3.1.1) is valid as long a neutrinos are highly relativistic.

From (3.1.1) it can be seen that the amplitudes of the oscillations are driven by the mixing matrix elements and the frequencies by the mass squared differences. Expression (3.1.1) can be rewritten in the following way [42]:

$$\begin{aligned} P_{\nu_\alpha\to\nu_\beta} = \delta_{\alpha\beta} &- 4\sum_{k>j}\Re\mathfrak{e}\left[U^*_{\alpha j}U_{\beta j}U_{\alpha k}U^*_{\beta k}\right]\sin^2\left(\frac{\Delta m^2_{kj}L}{4E}\right) \\ &- 2\sum_{k>j}\Im\mathfrak{m}\left[U^*_{\alpha j}U_{\beta j}U_{\alpha k}U^*_{\beta k}\right]\sin\left(\frac{\Delta m^2_{kj}L}{2E}\right). \end{aligned} \tag{3.1.2}$$

As can be seen in expression (3.1.2) taking a matrix element and a conjugate of the same column cancels the Majorana phases, cf. (2.2.1), playing no role in neutrino oscillations.

The oscillation probability (3.1.2) depends on the produced and detected neutrino flavors, $\alpha$ and $\beta$ , determining what is called an oscillation channel. When the same neutrino flavor that was produced is measured, $\nu_\alpha \to \nu_\alpha$, it is called disappearance channel, and when the flavor is different, $\nu_\alpha \to \nu_\beta$, appearance channel.

As it is clear from (3.1.2), in neutrino oscillation phenomena the absolute mass can not be measured, but only mass squared differences, in the $3\nu$ framework $\Delta m^2_{21}$ and $\Delta m^2_{\text{atm}}$. These two parameters along with the three mixing angles, the CP violating phase, $\delta_{\text{CP}}$, and the mass ordering discrete parameter are the measurable parameters in neutrino oscillation experiments. In table 2.1 the status of these parameters is summarized.

### Oscillation regimes

Depending on the neutrino energy, $E$, and the distance traveled from the source to the detector, commonly called baseline, $L$, neutrino oscillation experiments are sensitive to different parameters. In order to discuss the different oscillation regimes, the illustrative example of the two family approximation is very suitable, for which equation (3.1.2) reduces to

$$\begin{aligned} P_{\nu_\alpha\to\nu_\beta} &= \sin^2 2\theta\sin^2\left(\frac{\Delta m^2}{4E}L\right) \\ &\simeq \sin^2 2\theta\sin^2\left(1.27\frac{\Delta m^2[\text{eV}^2]}{E[\text{MeV}]}L[\text{m}]\right). \end{aligned} \tag{3.1.3}$$

In this case there is only one mass squared difference and one mixing angle[2]. As can be seen in equation (3.1.3), apart from the size of the mixing angle, which determines the amplitude of the oscillation, the mass squared difference determines at which regime of baseline and energy an experiment has to run in order to be sensitive to the oscillation. The optimal regime is when ratio $L/E$ is such that $1.27\Delta m^2 L/E$ is close to $\pi/2$, i.e. close to the maximum of the oscillation. That means that an experiment with an $L/E \sim 1\,\mathrm{Km/MeV}$ will be sensitive to an oscillation frequency driven by $\Delta m^2 \simeq 10^{-3}\mathrm{eV}^2$.

In a three family framework, as can be seen in (3.1.2), different oscillation regimes change the mixing parameters that an experiment is sensitive to. This is because only the oscillating terms in which the $\sin(\dots)$ is not negligible are going to have measurable effects. And this depends on the oscillation frequency, the larger the oscillation frequency the faster the oscillation term develops and the faster it becomes non negligible[3].

For instance, experiments with an $L/E \sim 1\,\mathrm{Km/MeV}$ are sensitive only to oscillating terms depending on the atmospheric mass splitting $\Delta m^2_{\mathrm{atm}} \sim 10^{-3}\mathrm{eV}^2$. The solar frequency, $\Delta m^2_{21} \sim 10^{-5}\,\mathrm{eV}^2$, is much smaller and hence the oscillating terms depending on it are not developed. In this case the experiment is sensitive to the amplitudes $U^*_{\alpha 3}U_{\beta 3}U_{\alpha(1,2)}U^*_{\beta(1,2)}$, but not $U^*_{\alpha 2}U_{\beta 2}U_{\alpha 1}U^*_{\beta 1}$. Increasing $L/E$ the experiment would start being sensitive to both atmospheric and solar oscillations.

For very big $L/E$ the oscillations average out:

$$\sin^2\left(\frac{\Delta m^2 L}{4E}\right) \to \frac{1}{2}\,.$$

The averaging out effect is produced by the finite energy resolution of an experiment, $\sigma_E$. In this case, it defines the precision of determining the true energy of a detected neutrino, $E_\nu^{\mathrm{true}}$. The energy resolution gives a certain probability of measuring a neutrino energy, $E_\nu^{\mathrm{mes}}$, given a certain $E_\nu^{\mathrm{true}}$. It can be modeled as a gaussian distribution centered at the measured neutrino energy, $E_\nu^{\mathrm{mes}}$, with width $\sigma_E$. It averages the oscillation probability as follows:

$$\langle P(L, E_\nu^{\mathrm{mes}})\rangle = \frac{1}{\sqrt{2\pi}\sigma_E}\int_{-\infty}^{\infty} \mathrm{d}E_\nu^{\mathrm{true}} P(L, E_\nu^{\mathrm{true}}) \exp\left\{\frac{\left(E_\nu^{\mathrm{true}} - E_\nu^{\mathrm{mes}}\right)^2}{2\sigma_E^2}\right\}.$$

The more peaked is the gaussian, i.e. the finer is the energy resolution, the more precise will $E_\nu^{\mathrm{true}}$ be measured. The argument of the sines in (3.1.2) depends on $L$ and $E$ such that the larger the baseline $L$, the more oscillations are contained in small intervals of $E$. Then the averaging effect of the energy resolution will have a larger impact, averaging out completely the oscillations for sufficiently large $L$, as is depicted in figure 3.2.2.

### Matter effects

Neutrinos traveling through matter can interact coherently with matter, without changing their momentum, via CC ($\nu_e\, e \to e\, \nu_e$) and NC ($\nu_\alpha\, \ell_\alpha \to \ell_\alpha\, \nu_\alpha$) interactions, depicted in figure 3.1.1. These interactions give rise to an effective matter potential affecting their evolution in time.

For certain regimes of energy, baseline and matter density, matter effects can not be neglected, like for example in LBL and atmospheric experiments, where neutrinos can travel through the Earth for long distances, or neutrinos propagating inside the sun and supernovae, which are very dense mediums. Matter effects have an impact on the neutrino

[2]The mixing matrix in a two neutrino scenario is just a rotation depending on one mixing angle.

[3]The function is oscillating, so at some point it will decrease become negligible again.

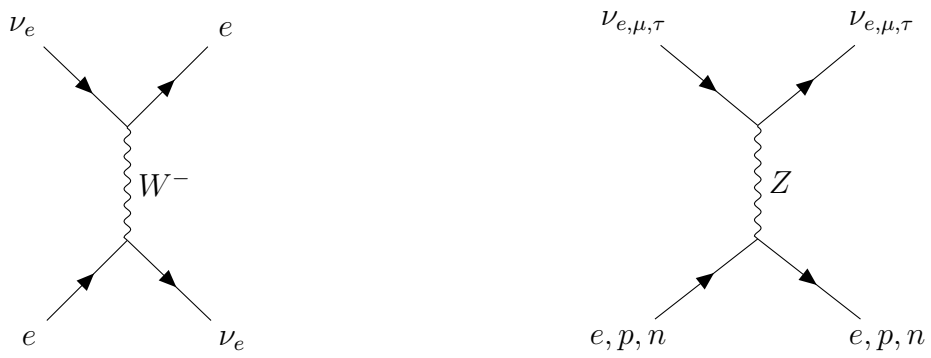


Figure 3.1.1: Feynman diagrams of the elastic CC and NC neutrino scattering.

oscillation probability, modifying the mixing angle and oscillation frequency. The most important effects are the Mikheyev-Smirnov-Wolfenstein (MSW) resonant effect [95, 96], for which the mixing angle is resonantly enhanced; and the introduction of a CP asymmetry. The latter is due to the fact that neutrinos or anti-neutrinos propagate through a medium made out of matter and never anti-matter. The matter CP violating effect adds to the intrinsic CP violating effect, due to $\delta_{\rm CP}$, in a non-trivial way.

Complete lectures on neutrino matter effects can be found, for example, in references [42, 97].

### $3 + 1\nu$ framework

The $3\nu$ oscillation paradigm is very well tested, however there are some experimental results that do not agree with it. As it be explained below, they point into the direction of a new oscillation frequency driven by a new massive eigenstate, which mixes with the flavor neutrinos as the three known ones do. In this scenario, known as the $3 + 1\nu$ oscillation framework, the PMNS matrix have to be extended to a $4 \times 4$ unitary matrix

$$U = \begin{pmatrix} U_{e1} & U_{e2} & U_{e3} & U_{e4} \\ U_{\mu 1} & U_{\mu 2} & U_{\mu 3} & U_{\mu 4} \\ U_{\tau 1} & U_{\tau 2} & U_{\tau 3} & U_{\tau 4} \\ U_{s1} & U_{s2} & U_{s3} & U_{s4} \end{pmatrix} , \tag{3.1.4}$$

being now the $3 \times 3$ PMNS matrix no longer unitary.

In the $3\nu$ oscillation framework the PMNS matrix is considered to be unitary and deviations from unitarity would be directly related to the new matrix elements $U_{e4}$, $U_{\mu 4}$, $U_{\tau 4}$. Within the current uncertainties on the elements of the $3\times3$ mixing matrix, the hypothetical deviations are expected to be small and so the new matrix elements, depicted in figure 3.1.2. The last row of the $U$ matrix is added by hand in order to make it unitary. The elements $U_{si}$ are the mixings of a new hypothetical flavor neutrino $s$ with the massive eigenstates. This new flavor, which is commonly called sterile, does not couple to the charged and neutral current interactions.

In the $3 + 1\nu$ oscillation framework, there are also three new mass squared differences $\Delta m^2_{41}$, $\Delta m^2_{42}$ and $\Delta m^2_{43}$, which will drive three new oscillations. Current anomalies are compatible with a new oscillation driven by a $\Delta m^2_{\rm new} \simeq 1{\rm eV}^2$. In this case, there is only one new effective oscillation frequency, since $\Delta m^2_{\rm sol}$, $\Delta m^2_{\rm atm} \ll \Delta m^2_{41} \simeq \Delta m^2_{42} \simeq \Delta m^2_{43} \equiv \Delta m^2_{\rm new}$, depicted in figure 3.1.2.

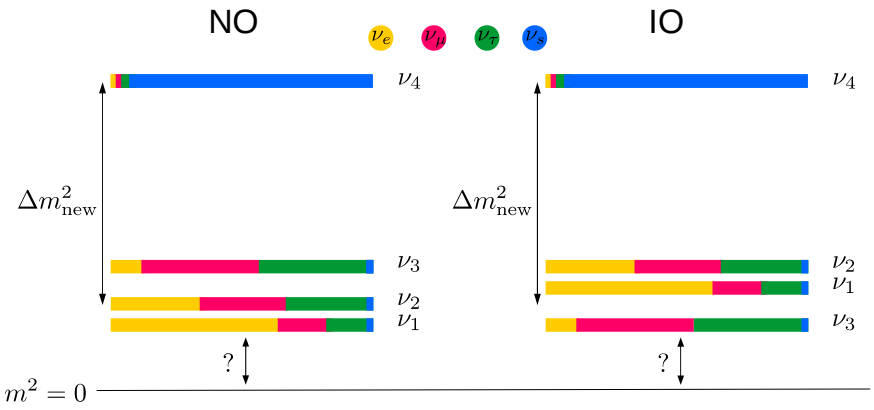


Figure 3.1.2: Neutrino masses in a $3+1\nu$ framework, for normal (left) and inverted (right) ordering. Yellow, red and green represent a representative fraction of the flavor composition of each massive state and blue represent the fraction of sterile neutrino.

## 3.2 Basics on reactor neutrinos

Reactor power plants are a very powerful source of electron anti-neutrinos, $\bar{\nu}_e$. A pure $\bar{\nu}_e$ flux with a typical energy of MeV is produced in long chain $\beta$-decay reactions of unstable isotopes [98–101]. The predominant[4] contributions to the flux come from four isotopes: $^{235}$U, $^{239}$Pu, $^{238}$U and $^{241}$Pu, whose proportions vary in time. A recalculation of the reactor anti-neutrino fluxes by P. Huber and Th. A. Mueller [102, 103] led to the RAA [33], which consists of a deficit of measured anti-neutrinos with respect to the expectations[5]. As it will be shown below in this chapter, this anomaly is at the level of $3\sigma$ away from the SM predictions, and data, up to spring 2018, is compatible with an active-to-sterile neutrino oscillation.

In this section we review the different oscillation regimes in reactor neutrino experiments and describe the basic principle on how do they detect neutrinos. We also present a general way of predicting reactor anti-neutrino events and of analyzing reactor data independently of the $\bar{\nu}_e$ flux predictions.

### Long, medium and short baseline reactor experiments

Reactor experiments search for $\bar{\nu}_e$ events via inverse beta decay (IBD), $\bar{\nu}_e\, p \to n\, e^+$, so they measure in the disappearance oscillation channel $\overline{\nu}_e \to \overline{\nu}_e$, whose oscillation probability is given by

$$P_{\overline{\nu}_e \to \overline{\nu}_e} = 1 - 4 \sum_{j=1}^{N} \sum_{k>j} |U_{ek}|^2 \, |U_{ej}|^2 \sin^2 \left( \Delta m^2_{kj} \frac{L}{4E} \right) , \tag{3.2.1}$$

As discussed above in this chapter, different oscillation regimes will be sensitive to different oscillation parameters.

Long baseline (LBL) reactor experiments, working in an oscillation regime of $L \sim 100\,\text{km}$ and $E \sim$ MeV, are sensitive to the solar frequency. That is the case of KamLAND [105] experiment, which together with solar experiments determines what are called the solar parameters $\theta_{12}$ and $\Delta m^2_{21}$. The KamLAND experiment consists of a single detector, which is located underground at the Kamioka Observatory in Japan, measuring $\bar{\nu}_e$ produced in the nuclear power plants in Japan, with a typical baseline of 180 Km.

[4] More than 99% of the total reactor $\bar{\nu}_e$ [102].

[5] A revaluation of the RAA with updated flux predictions was recently done in [104].

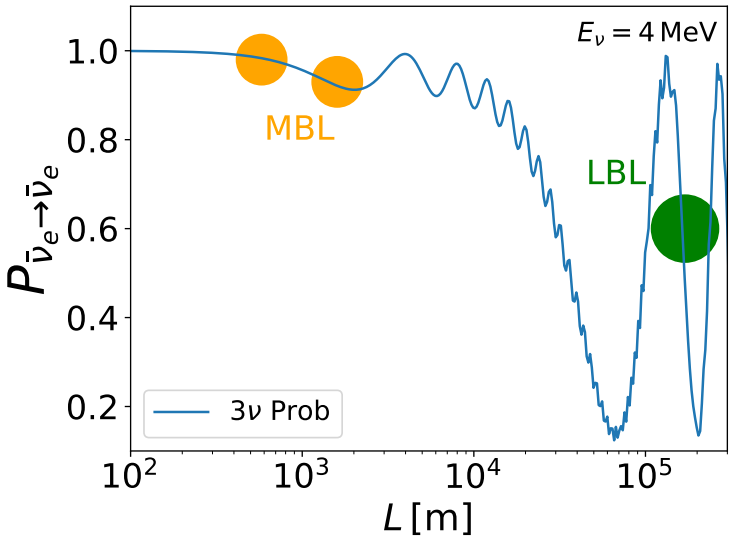


Figure 3.2.1: Electron appearance oscillation probability in the $3\nu$ framework (3.2.1). Both oscillation frequencies atmospheric (short oscillation) and solar (long oscillation) are included. The oscillation parameters are taken from NuFit 4.1. In this example the neutrino energy is set to 4 MeV. The orange regions represent typical baselines for the far and near detector sites of the MBL reactor experiments and in green a representative baseline of the KamLAND experiment.

MBL reactor experiments, as Daya Bay [106], RENO [107] and Double Chooz [108], work in a regime of $L \sim 1$ Km and $E \sim$ MeV, being sensitive to the atmospheric oscillation frequency and to $\theta_{13}$, which was first measured by the Daya Bay collaboration in 2012 [109]. Double Chooz is based in France. It consist of 2 detectors that measure $\bar{\nu}_e$ from two reactors. One of the detectors is closer to the reactors, called near detector, with an averaged baseline of $\langle L \rangle \simeq 400$ m, and the other one further, far detector, with $\langle L \rangle \simeq 1050$ m. The RENO experiment is based in South Korea, it consist of 2 detectors, near ($\langle L \rangle \simeq 430$ m) and far ($\langle L \rangle = 1445$ m) detectors, which measure $\bar{\nu}_e$ from 6 nuclear reactors. Daya Bay is based in China, closed to Hong Kong, it consists of 8 detectors placed in three different locations, called experimental halls (EH), which measure $\bar{\nu}_e$ produced at 6 powerful reactors. The EH are placed such that two of them work as near detectors ($\langle L \rangle \sim 575$ m) and the other one as a far detector ($\langle L \rangle = 1640$ m). All three experiments measure energy spectral information.

In figure 3.2.1 it can be seen how MBL reactor experiments can be sensitive to the atmospheric oscillation frequency and the LBL to the solar one, given the baseline at which the detectors are placed.

Short baseline (SBL) reactor experiments are located very close to the source, $L \sim 10$ m, so that they are not sensitive to the solar and atmospheric frequencies, but they would be sensitive to a frequency driven by a hypothetical $\Delta m^2 \sim$ eV. ILL [111], Gösgen [112], Krasnoyarks [113–115], ROVNO [116,117], Bugey-4 [118] and SPR [119] experiments, measure a deficit of total $\bar{\nu}_e$ with respect to the theoretical expectations, setting the RAA [33]. This suggests either a miscalculation of the flux predictions or an extra oscillation, usually called active-to-sterile oscillation. As can be seen in figure 3.2.2 a fast oscillation, which averages out due to the finite energy resolution can cause a suppression of the flux solving the RAA. Added to the possible overestimation of the flux predictions found by Daya Bay and RENO [34,35], experiments measuring energy spectra (Daya Bay, RENO and Double Chooz) found a spectral distortion in the energy range $4-6$ MeV [108,110,120,121], which is commonly referred as the 5 MeV "bump". Possible origins of these bumps have been

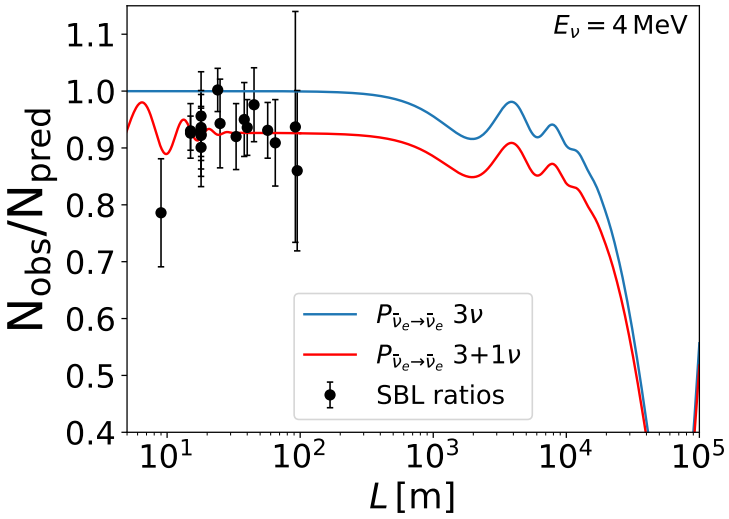


Figure 3.2.2: Ratio of number of observed over predicted $\bar{\nu}_e$ events in the SBL experiments (black dots) and electron appearance oscillation probability with energy resolution effects added, for the standard $3\nu$ (blue line) and the $3+1\nu$ (red line) oscillation frameworks (3.2.1). The three oscillation frequencies are included: atmospheric, solar and the extra one. The standard oscillation parameters are taken from NuFit 4.1 and the new ones $(|U_{e4}|^2, \Delta m^2_{\mathrm{new}})$ are set to $\left(0.01, 1.3\,\mathrm{eV}^2\right)$. In this example the energy is set to 4 MeV. The resolution effects are simulated performing an integral of the oscillation probability weighted by a gaussian distribution with a variance $\sigma = 0.5\,\mathrm{MeV}$. The ratios[1] of the SBL experiments are taken from table 11 of reference [110]. [1]The ratios shown are from the experiments: Buyey-4, ROVNO91, Bugey-3-I, Bugey-3-II, Bugey-3-III, Goesgen-I, Goesgen-II, Goesgen-III, ILL, Krasn. I, Krasn. II, Krasn. III, SRP-I, SRP-II, ROVNO88-1I, ROVNO88-2I, ROVNO88-1S, ROVNO88-2S and ROVNO88-3S.

studied [122–124] but it is still under debate. The bump's presence questions the reliability of the flux predictions. These two reasons make it necessary to consider flux mismodeling as another possibility to explain the RAA.

Recent SBL reactor experiments like NEOS [121], DANSS [125], STEREO [126] and PROSPECT [127], measure energy spectral information at different baselines, which allows them to make neutrino oscillation analyses independent of the flux shape and normalization predictions, being crucial in order to study sterile oscillations in a $3+1\nu$ framework. This is discussed below in detail in section 3.4.2. The NEOS experiment is based in Korea at 23.7 m from a commercial reactor core, it measures $\bar{\nu}_e$ energy spectral information at a fixed baseline. DANSS is located at ∼11 m from a nuclear reactor core in Russia. The detector is movable allowing it to measure $\bar{\nu}_e$ spectral information at two different baselines, 10.7 m and 12.7 m. STEREO is in France, installed at a distance of 9.4 m from a reactor core, being the back of the detector at 11.1 m. The detector is modulated in 6 separate cells, allowing it to measure $\bar{\nu}_e$ spectral information at 6 different baselines. PROSPECT detector is installed at 6.7 m from from a reactor core in the US. It measures $\bar{\nu}_e$ spectral information at different baselines within its segmented detector (6.7-7.1 m, 7.1-7.5 m, 7.5-8.0 m, 8.0-8.4 m, 8.4-8.8 m, 8.8-9.2 m).

Note that in this work SBL, MBL and LBL experiments, refers to experiments placed at ∼10 m (like NEOS), ∼1 Km (like Daya Bay) and ∼180 Km (like KamLAND) from the reactor core. In the literature it can be also found that experiments at ∼10 m and ∼1 Km from the reactor core are called very short baseline (VSBL) and SBL experiments, while MBL refer to experiments placed at ∼50 Km from the source like JUNO [128]. The JUNO experiment is a future experiment, which is under construction. It will be placed at

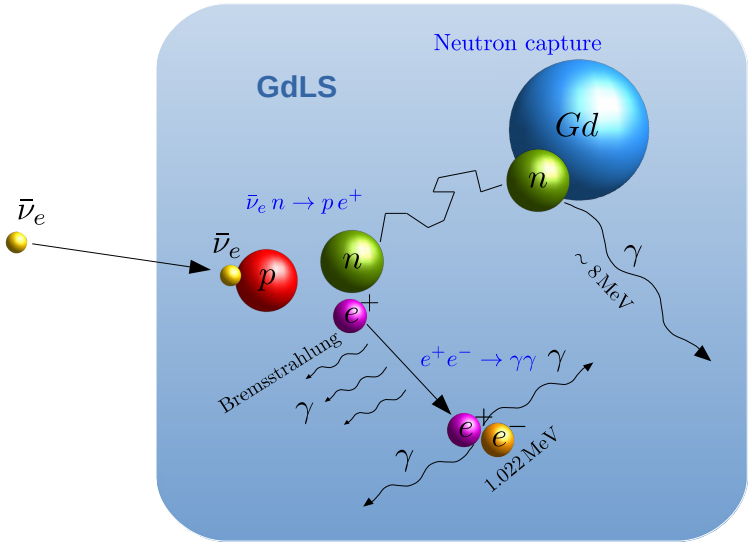


Figure 3.2.3: IBD process followed by the electron positron annihilation and the later neutron capture. An electron anti-neutrino comes into the detector and interacts via IBD with one proton in the medium, being gadolinium-doped liquid scintillator (GdLS) commonly used. The produced positron is slowed down emitting Bremstrahlung radiation, which along with the two photons coming from the subsequent annihilation with an electron in the medium constitute the deposited prompt energy signal. The produced neutron, eventually gets captured around 30 $\mu s$ later, emitting a delayed signal of 8 MeV. This signal is characteristic of the IBD process and is crucial in its identification.

a distance of ∼53 Km from a reactor source in China. At this baseline it will be sensitive to both atmospheric and solar oscillations.

### Reactor anti-neutrino events

In the detection process in reactor experiments, the electron anti-neutrino enters the detector and interacts via IBD.

In a neutrino event, the signal measured by reactor experiments are photons coming from the Bremsstrahlung radiation of the positron emitted in the IBD process, $\bar{\nu}_e\, p \to n\, e^+$, when it slows down and from its subsequent annihilation with an electron in the medium $e^+\, e^- \to \gamma\, \gamma$. The energy deposited in the slowing down process is given by the positron kinetic energy, $T_e$, and the energy of the two photons produced in the annihilation is twice the electron mass, $m_e$. So that the energy of the signal, which is called deposited prompt energy, is given by $E_{\text{dep}} = T_e + 2m_e$. The neutron produced in the IBD process is eventually captured in the medium emitting a signal of around 8 MeV about 30$\mu s$ later[6]. This delayed neutron capture signal is characteristic from IBD processes and it is a key feature for the signal selection and background rejection. The process is depicted in figure 3.2.3.

The cross section of the IBD process has a threshold given by $E_{\bar{\nu}_e} > m_n - m_p + m_e \simeq 1.8$ MeV, below which the process is not kinematically possible. Here $m_p$ and $m_n$ are the proton and neutron masses. The kinetic energy of the positron which turns into Bremsstrahlung radiation is given by

$$T_{e^+} = E_{\bar{\nu}_e} + m_p - m_n - T_n - m_e\,,$$

where $T_n$ is the neutron kinetic energy. Then, the relation between the deposited prompt

[6]The energy depends on the medium, in Gadolinium (Gd) $E_\gamma^{\text{delay}} \sim 8$ MeV.

energy and the neutrino energy is given by

$$\begin{aligned} E_{\text{dep}} &= E_{\bar{\nu}_e} + m_p - m_n - T_n + m_e \\ &\simeq E_{\bar{\nu}_e} - 0.78\,\text{MeV} - T_n\,. \end{aligned} \tag{3.2.2}$$

The neutron kinetic energy gives a small correction that is of order $\sim 10\,\text{KeV}$ for reactor experiments, which we always neglect.

### IBD cross section

The IBD cross section, $\sigma_{IBD}$, up to corrections $\mathcal{O}\left(1/m^2\right)$, were $m$ is the nucleon mass, is given by:

$$\begin{aligned} \frac{\sigma_{IBD}(E_{\bar{\nu}_e})}{\sigma_0} &= \left(f^2+3g^2\right)\left[E_{e,0}p_{e,0} - \frac{E_{e,0}}{m}\left(\frac{E_{e,0}}{p_{e,0}}+\frac{p_{e,0}}{E_{e,0}}\right)\left(E_{e,0}E_{\bar{\nu}_e}+y^2\right)\right] \\ &\quad + \frac{E_{e,0}}{m}p_{e,0}\left[2(f+f_2)y\left((2E_{e,0}+\Delta)-\frac{m_e^2}{E_{e,0}}\right)+(f^2+3g^2)E_{e,0}\right. \\ &\qquad \left. +(f^2+g^2)\left(\Delta+\frac{m_e^2}{E_{e,0}}\right)-(f^2-g^2)\frac{1}{3}(E_{e,0}+\Delta)\right] \\ &\quad + \frac{2}{3}\left(f^2-g^2\right)\frac{E_{e,0}}{m}E_{\bar{\nu}_e}p_{e,0}\,. \end{aligned} \tag{3.2.3}$$

It has been obtained performing the $\text{dcos}\,\theta$ integral of the angular distribution given in reference [129], where

$$\begin{aligned} &E_{e,0} = E_{\bar{\nu}_e} - \Delta\,, \quad \Delta = m_n - m_p\,, \quad m = \frac{m_n+m_p}{2}\,, \\ &y^2 = \frac{(\Delta^2-m_e^2)}{2}\,, \quad \sigma_0 = \frac{G_F^2\cos^2\theta_C}{\pi}\left(1+\Delta^R_{\text{inner}}\right)\,, \end{aligned}$$

with $m_e$, $m_p$ and $m_n$ the electron, proton and neutron masses. $\cos\theta_C$ is the Cabibbo angle, and $f=1$ and $g=1.26$ are the vector and axial-vector coupling constants, respectively. $f_2 = \mu_p - \mu_n = 3.706$ is the difference between the anomalous magnetic moments of the proton and the neutron, $G_F$ is the Fermi constant and $\Delta_{\text{inner}} \simeq 0.024$ is the inner radiative correction. See [129] for more details. $\sigma_{\text{IBD}}$ is plotted in red in the left panel of figure 3.2.4.

### Reactor anti-neutrino flux

The total $\bar{\nu}_e$ flux, $\phi$, has four different components coming from the successive $\beta$-decays of the isotopes: $^{235}$U, $^{239}$Pu, $^{238}$U and $^{241}$Pu. In this work we use the Huber-Mueller flux predictions for each isotope contribution, $\phi^{\text{iso}}$, taken from [102, 103]. We construct the flux function linear-interpolating the tabulated flux values for $E_{\bar{\nu}_e} \in [2,8]$ MeV; from the energy threshold 1.8 to 2 MeV the flux is taken constant, extrapolating its value at 2 MeV; and for energies $E_{\bar{\nu}_e} > 8$ MeV we take the exponential of a fifth order polynomial [102]:

$$\phi(E_{\bar{\nu}_e}) = \exp\left(\sum_i^6 \alpha_i E_{\bar{\nu}_e}^{i-1}\right)\,, \tag{3.2.4}$$

where the coefficients $\alpha_i$ are taken from [102] for the $\phi^{235}$, $\phi^{239}$ and $\phi^{241}$ flux components and from [103] for the $\phi^{238}$ one.

In the reactor core, the isotopes are present in different relative proportions, called fission fractions, $f_c^{\text{iso}}$, that vary in time. The usual information given by the experimental

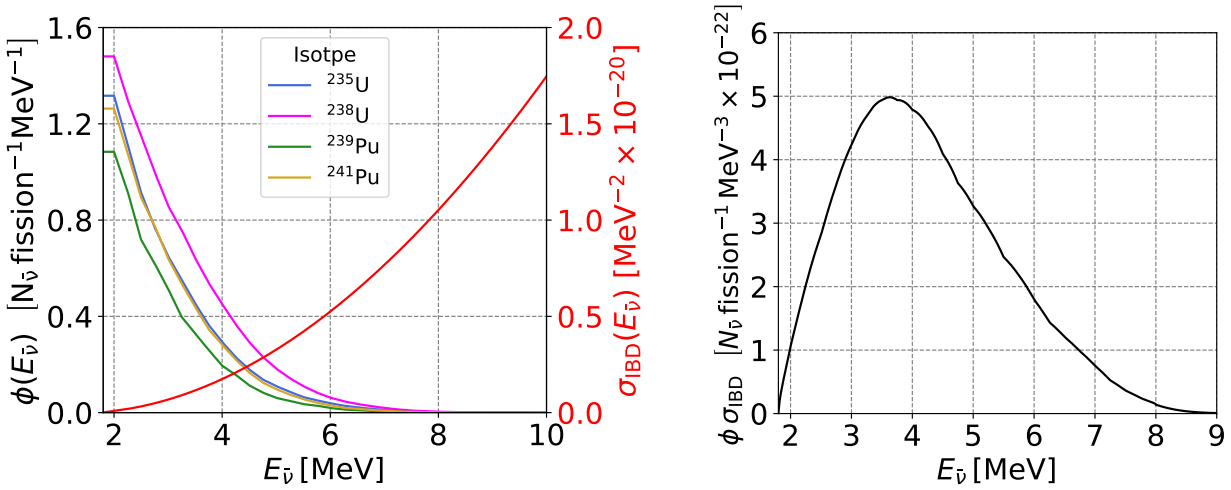


Figure 3.2.4: Left: The four different components of the reactor anti-neutrino flux coming from the four different isotopes (left y-axis) and the IBD cross section represented in red (right y-axis). Both are given as a function of the anti-neutrino energy. Right: total reactor anti-neutrino flux weighted by the IBD cross section. In this example, the fission fractions $f_c^{235} = 0.564$, $f_c^{238} = 0.076$, $f_c^{239} = 0.303$, $f_c^{241} = 0.056$ are used.

collaborations are the averaged-in-time relative amount of an isotope seen at the detectors, $f^{\rm iso}$, called effective fission fractions. The total flux is given by $\phi = \sum_{\rm iso} f_{(c)}^{\rm iso}\phi^{\rm iso}$. In the left panel of figure 3.2.4 the different contributions $\phi^{\rm iso}$ are plotted as a function of the anti-neutrino energy.

The amount of IBD events as a function of the anti-neutrino energy is proportional to the total flux weighted by the cross section, $\phi(E_{\bar{\nu}_e})\,\sigma_{IBD}(E_{\bar{\nu}_e})$. The latter is plotted in the right panel of figure 3.2.4. The dominant contribution of the weighted flux appears at energies $\sim$4 MeV. This is why in figures 3.2.1 and 3.2.2 the neutrino energy is set to 4 MeV.

The amount of IBD events also depends on the oscillation probability (3.2.1). Since the reactor anti-neutrino flux is isotropic, the number of IBD events in a detector is also proportional to the solid angle weighting factor $A/4\pi L^2$:

$$\frac{A}{4\pi L^2}\phi(E_{\bar{\nu}_e})\,\sigma_{IBD}(E_{\bar{\nu}_e})P_{\bar{\nu}_e\to\bar{\nu}_e}(E_{\bar{\nu}_e}, L)\,, \tag{3.2.5}$$

where $A$ is the area of the detector and $L$ the baseline. Ideally, these are all the ingredients to predict the number of neutrino events, but in reality detector and detection effects also have to be taken into account.

### Detector response

Due to detector characteristics and detection effects, namely the inner acrylic vessel (IAV), non linearity and energy resolution effects; the prompt energy deposited by the positron, $E_{\rm dep}$ (3.2.2), is not the same as the prompt reconstructed energy, $E^{\rm rec}$. All these effects have to be taken into account in order to trace the $E^{\rm rec}$ back to the neutrino energy $E_{\bar{\nu}_e}$. The IAV effect accounts for the probability that a positron is produced and starts depositing energy outside the detection region. Non linearity takes into account non linear effects in the light emission and detection. The energy resolution is the probability of reconstructing a different energy than the given true energy, which is usually modeled by a gaussian distribution centered at the true energy. The function that relates the anti-neutrino energy $E_{\bar{\nu}_e}$ and the reconstructed energy $E_{\rm rec}$ is called detector response function, $R(E_{\bar{\nu}_e}, E_{\rm rec})$, which takes

into account all the above mentioned reconstruction and detection effects and the energy shift given by the IBD process (3.2.2). A detailed example of the event detection and reconstruction performed by the Daya Bay collaboration can be found in [110, 130].

### Event predictions

In order to perform a neutrino oscillation analysis, neutrino event predictions have to be compared with data. In the reactor neutrino experiments measuring energy spectral information the predicted number of signal events in the detector $d$ and reconstructed energy bin $i$ is computed as follows:

$$\begin{aligned} X_i^d(\boldsymbol{\theta}) &= \mathcal{N} \sum_r \sum_{\text{iso}} \frac{\varepsilon_{ff}}{L_{rd}^2} \int_{E_i^{\text{rec}}}^{E_{i+1}^{rec}} \mathrm{d}E^{\text{rec}} \\ &\quad \times \int_0^\infty \mathrm{d}E_{\bar{\nu}_e}\, \sigma_{\text{IBD}}(E_{\bar{\nu}_e}) f^{\text{iso}} \phi^{\text{iso}}(E_{\bar{\nu}_e}) P_{\bar{\nu}_e \to \bar{\nu}_e}(E_{\bar{\nu}_e}, L_{rd}, \boldsymbol{\theta}) R(E^{\text{rec}}, E_{\bar{\nu}_e}) \,, \end{aligned} \tag{3.2.6}$$

where the indices $r$ and iso refers to the $r^{\text{th}}$ reactor, in the case that there is more than one reactor and to the iso$^{\text{th}}$ fissionable isotope ($^{235}$U, $^{239}$Pu, $^{238}$U or $^{241}$Pu). $L_{rd}$ is the distance between the reactor $r$ and detector $d$ and $\varepsilon_{ff}$ is the relative detector efficiency. As explained above $E_{\bar{\nu}_e}$ and $E^{\text{rec}}$ are the true incoming neutrino energy and the measured prompt reconstructed energy, related by the detector response function $R(E^{\text{rec}}, E_{\bar{\nu}_e})$. $\sigma_{\text{IBD}}(E_{\bar{\nu}_e})$ is the IBD cross section (3.2.3), $f^{\text{iso}}$ are the effective fission fractions[7], and $\phi^{\text{iso}}$ are the different flux contributions from each isotope. As it is done and explained in section 2.6 of [110], non-equilibrium relative corrections taken from table VII of [103] are applied to the Huber-Mueller fluxes [102, 103]. $P_{\bar{\nu}_e \to \bar{\nu}_e}(E_{\bar{\nu}_e}, L_{rd}, \boldsymbol{\theta})$ is the electron anti-neutrino disappearance oscillation probability as a function of the neutrino energy, reactor-detector distance and oscillation parameters $\boldsymbol{\theta}$ (3.2.1). $\mathcal{N}$ is the common input to all the identical detectors of an experiment, like the total reactor power or the total number of protons inside the detectors[8].

### Far-to-near ratio analysis

Modern reactor experiments like Daya Bay, RENO, Double Chooz, NEOS, DANSS, STEREO and PROSPECT, measure energy spectral information at two different sites. This allows them to perform an analysis based on a far-to-near ratio, which is a powerful tool that makes the oscillation analysis independent of the predicted flux shape, avoiding problems like the unexplained "5 MeV" bump, and of global flux normalization, hence independent of the RAA [33]. Ratios of measured spectra at different baselines are only sensitive to relative shape distortions which is a crucial point to the results presented in this chapter. Taking ratios also makes predictions (3.2.6) independent of the common input $\mathcal{N}$, with only relative differences being important.

A general flux independent analysis recipe for the reactor neutrino experiments, using a least-squares statistic method, reads as follows:

$$\chi^2 = \sum_{ij} \left( \frac{O_i^F}{O_i^N} - \frac{X_i^F(\boldsymbol{\theta})}{X_i^N(\boldsymbol{\theta})} \right) V_{ij}^{-1} \left( \frac{O_j^F}{O_j^N} - \frac{X_j^F(\boldsymbol{\theta})}{X_j^N(\boldsymbol{\theta})} \right) , \tag{3.2.7}$$

where $O_i^S$ is the observed number of events in the energy bin $i$ and experimental site $S = N(\text{near}), F(\text{far})$; $X_i^S(\boldsymbol{\theta})$ are the predictions (3.2.6), which depend on the oscillation

[7] Ideally we would have information on the fission factions as a function of time in each reactor, $f_c^{\text{iso}}$. Instead we usually have effective time-averaged values for each detector, $f^{\text{iso}}$.

[8] Daya Bay, RENO and Double Chooz near and far detectors are identical.

parameters $\boldsymbol{\theta}$ of the model, and $V$ is the covariance matrix which accounts for the statistical, and systematic uncertainties as well as their correlations. Depending on the available data and the available experimental details given by the collaborations, such as systematic uncertainties and their correlations, in what follows we will use different variations of (3.2.7) in order to reproduce analyses of different data sets, see appendix A.

Note that the predicted ratios in (3.2.7) are not fully independent of the flux predictions, since the flux function is convoluted in an energy bin $E_i^{\rm rec}$ along with other energy dependent functions (3.2.6). However, flux independence is a good approximation for a small $E_i^{\rm rec}$ bin size and smooth functions.

## 3.3 $3\nu$ Oscillation framework

In this section we study reactor neutrino experiments in the $3\nu$ standard oscillation framework and we show two applications: their role in a global $3\nu$ oscillation fit in section 3.3.1 and their power to constrain the solar $\Delta m^2_{21}$ parameter in section 3.3.2.

#### $\bar{\nu}_e \to \bar{\nu}_e$ oscillation probability

As it was introduced before, the oscillation probability (3.1.2) in the $3\nu$ oscillation framework depends on six parameters and the mass ordering. Using the PMNS parameterization in (2.2.1), the $\bar{\nu}_e$ disappearance oscillation probability takes the explicit form

$$\begin{aligned} P_{\bar{\nu}_e\to\bar{\nu}_e} &= 1 - \cos^4\theta_{13}\sin^2 2\theta_{12}\sin^2\left(\Delta m^2_{21}\frac{L}{4E}\right) \\ &\quad - \sin^2 2\theta_{13}\left(\cos^2\theta_{12}\sin^2\left(\Delta m^2_{31}\frac{L}{4E}\right) + \sin^2\theta_{12}\sin^2\left(\Delta m^2_{32}\frac{L}{4E}\right)\right), \end{aligned} \tag{3.3.1}$$

which depends on the independent parameters: $\theta_{12}$, $\theta_{13}$, $\Delta m^2_{21}$ and $\Delta m^2_{31}$.

For the discussion it is convenient to define the solar and the atmospheric oscillating terms as follows:

$$\begin{aligned} P_{12} &\equiv \sin^2 2\theta_{12}\cos^4\theta_{13}\sin^2\Delta_{21}\,, \\ P_{13} &\equiv \sin^2 2\theta_{13}\left(\cos^2\theta_{12}\sin^2\Delta_{31} + \sin^2\theta_{12}\sin^2\Delta_{32}\right)\,, \end{aligned}$$

where $\Delta_{ij} \equiv \Delta m^2_{ij} L/4E$. Given the current values of the oscillation parameters, cf. table 2.1, they are given by

$$P_{12} \simeq 0.8\sin^2\left(\frac{\pi}{2}\left(\frac{L/E}{17\,\text{Km/MeV}}\right)\right) \tag{3.3.2}$$

$$P_{13} \simeq 0.08\sin^2\left(\frac{\pi}{2}\left(\frac{L/E}{0.5\,\text{Km/MeV}}\right)\right)\,. \tag{3.3.3}$$

Here we can see how the atmospheric frequency has a maximum of oscillation at $L/E \simeq 0.5\,\text{Km/MeV}$ while the solar one has it at $L/E \simeq 17\,\text{Km/MeV}$. For a given energy it is clear that the atmospheric oscillating term becomes relevant at much shorter baselines than the solar one, which takes more time to develop.

The LBL reactor experiment, KamLAND, with a typical baseline of $L \sim 180\,\text{Km}$ is sensitive to the solar oscillation. However the atmospheric one is averaged out due to finite energy resolution effects. Therefore its oscillation probability is given by

$$P_{\bar{\nu}_e\to\bar{\nu}_e,\text{LBL}} = \sin^4\theta_{13} + \cos^4\theta_{13}\left\{1 - \frac{1}{2}\sin^2 2\theta_{12}\sin^2\left(\frac{\Delta m^2_{21}L}{2E}\right)\right\}\,, \tag{3.3.4}$$

being KamLAND mainly sensitive to the solar parameters $\theta_{12}$ and $\Delta m^2_{21}$ and marginally to $\theta_{13}$.

The MBL reactor experiments (Daya Bay, RENO and Double Chooz) measure at two different baselines, near and far, with identical detectors. From atmospheric and accelerator measurements it is known that in order to be sensitive to $\Delta m^2_{\rm atm}$ (2.2.2) the far detector has to be placed at a baseline $\sim 1\,\text{Km}$. At that baseline the oscillation probability (3.3.1) is dominated by $P_{13}$ since the solar oscillation does not have time to develop, i.e. $P_{12}$ is negligible. This can be seen approximating $\sin x \sim x$ in equation (3.3.2), and writing it as

$$P_{12} \simeq 0.002 \left( \frac{L/E}{0.5\,\text{Km/MeV}} \right)^2 , \tag{3.3.5}$$

From (3.3.5) and (3.3.3) it is clear that for the MBL oscillation regime, the solar term $P_{12}$ is much smaller than $P_{13}$.

It will be shown later in section 3.3.2 that the determination of $\Delta m^2_{\rm atm}$ with MBL data depends very little on the specific value of $\Delta m^2_{21}$, as long as it is of the order $\Delta m^2_{21} \sim 10^{-5}\,\text{eV}^2$.

### Effective atmospheric frequency

For MBL reactor experiments it is very useful to consider the atmospheric frequencies $\Delta m^2_{31}$ and $\Delta m^2_{32} \equiv \Delta m^2_{31} - \Delta m^2_{21}$ as an effective one $\Delta m^2_{ee}$, turning (3.3.1) into an approximated oscillation probability

$$P_{\overline{\nu}_e \to \overline{\nu}_e} = 1 - \cos^4\theta_{13} \sin^2 2\theta_{12} \sin^2\left(\Delta m^2_{21} \frac{L}{4E}\right) - \sin^2 2\theta_{13} \sin^2\left(\Delta m^2_{ee} \frac{L}{4E}\right) , \tag{3.3.6}$$

where

$$\Delta m^2_{ee} \equiv \cos^2\theta_{12} \Delta m^2_{31} + \sin^2\theta_{12} \Delta m^2_{32} \, . \tag{3.3.7}$$

Using that $\Delta m^2_{21}/\Delta m^2_{31} \ll 1$, in [131, 132] an expansion in $\Delta m^2_{21}$ of the atmospheric oscillation term of the complete probability (3.3.1) is performed reaching the expression (3.3.6) in which terms $\mathcal{O}(\Delta m^2_{21} L/(4E))^2$ are neglected, while the effective mass squared difference (3.3.7) contains the first order effect in $\Delta m^2_{21}$. This approximation holds to a very good accuracy in the oscillation regime in which MBL reactor experiments work, $L/E \lesssim 1\,\text{Km/MeV}$ [133]. The oscillation probability (3.3.7) is used in the data analyses performed by the collaborations, Daya Bay, RENO and Double Chooz.

### Validations of the reactor analyses

In order to use the available reactor data for the studies presented in this work the first thing to do is making sure that the collaboration results are reproduced under the same assumptions. In this work, Daya Bay and RENO analyses have been reproduced at a very good accuracy, see figure 3.3.1[9]. In appendix A we describe in detail how to perform these data analyses. For other reactor data analyses that are based on far-to-near ratios a similar procedure could be done, accounting for differences between different experiments and the available information on the systematic uncertainties.

In what follows applications of these MBL reactor analyses are discussed: their role in global neutrino oscillation data analyses and their current capability to constrain $\Delta m^2_{\rm sol}$, as a way of checking the robustness of the 3ν oscillation framework.

[9]For these validation analyses the approximated oscillation probability is used (3.3.6) but for the rest of the analyses performed in this work using this data the complete oscillation probability (3.3.1) is used.

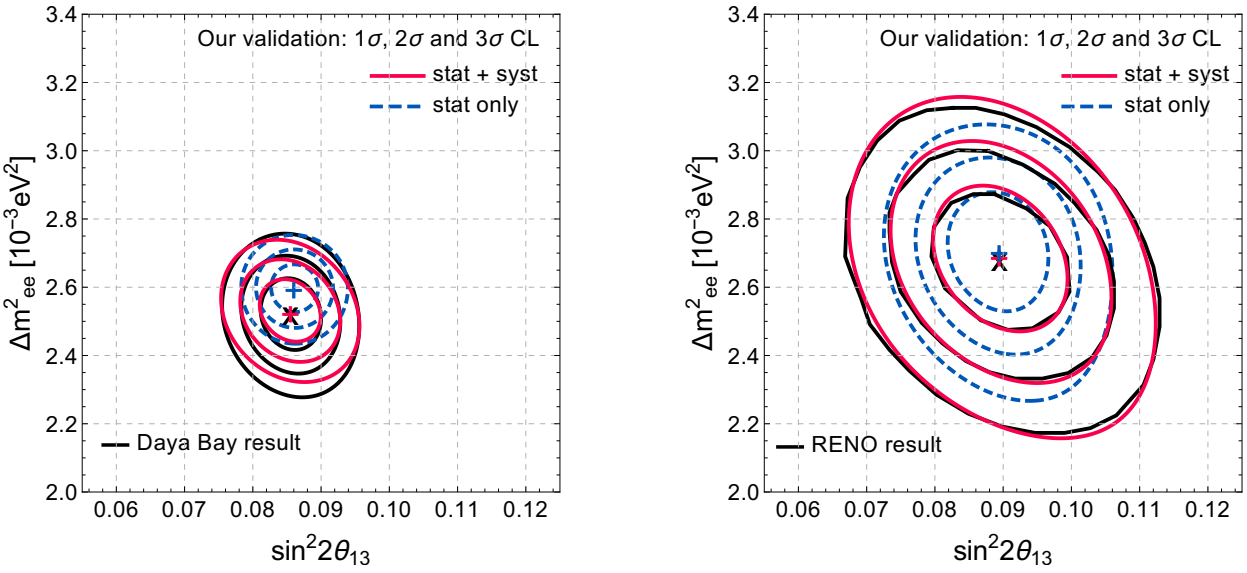


Figure 3.3.1: Comparision of our results, in red and blue-dashed including and not including systematic uncertainties respectively, with Daya Bay (left) and RENO (right) collaboration analyses, in black, of the data sets [106] and [107] respectively. The best fit value together with the 1, 2 and 3 $\sigma$ C.L. are shown. Plots are taken from [28].

### 3.3.1 Global analysis

This section is based on the global analysis performed by the NuFit collaboration [26]. Main results and figures are also taken from this reference. A list of the experimental data used in the global analysis cited here can be found in [26, 27].

Currently there are a large amount of neutrino oscillation data, in different oscillation channels and different oscillation regimes, being sensitive to different oscillation parameters. In this present situation, global analyses are very important in order to measure all the oscillation parameters consistently within the same theoretical framework. With current global data, a global fit is able to determine most of the oscillation parameters in the standard $3\nu$ oscillation framework, but still some of them are unknown: $\delta_{CP}$, the mass ordering and the octant of $\theta_{23}$. The present status of the global picture is summarized in section 2.2.

#### MBL reactor data

The MBL reactors experiments (Daya Bay, RENO and Double Chooz) enter into the global fit as key input in the determination of $\theta_{13}$ mixing angle. As it was explained before these experiments work in a regime in which the solar oscillation term in the oscillation probability (3.3.1) plays a marginal role compared to the atmospheric oscillation term. In figure 3.3.2 it is shown the 1, 2 and 3$\sigma$ C.L. regions in the $\Delta m^2_{\text{atm}}$ vs $\sin^2\theta_{13}$ space determined by Daya Bay, RENO and Double Chooz and their combination, for the NO case[10], fixing the values for the solar parameters $(\Delta m^2_{21}, \sin^2\theta_{12}) = (7.39 \times 10^{-5}\,\text{eV}^2, 0.310)$ set by the solar and KamLAND experiments. The combined best fit value is given at $\Delta m^2_{31} = 2.58 \times 10^{-3}\,\text{eV}^2$ and $\sin^2\theta_{13} = 0.0223$. From figure 3.3.2 it can be seen that the combined fit is dominated by Daya Bay, followed by a significant contribution from RENO, being Dooble Chooz only marginally relevant. The Daya Bay and RENO data sets [106,107] are analyzed as described

[10]For the NO case $\Delta m^2_{\text{atm}} = \Delta m^2_{31}$, cf. (2.2.2).

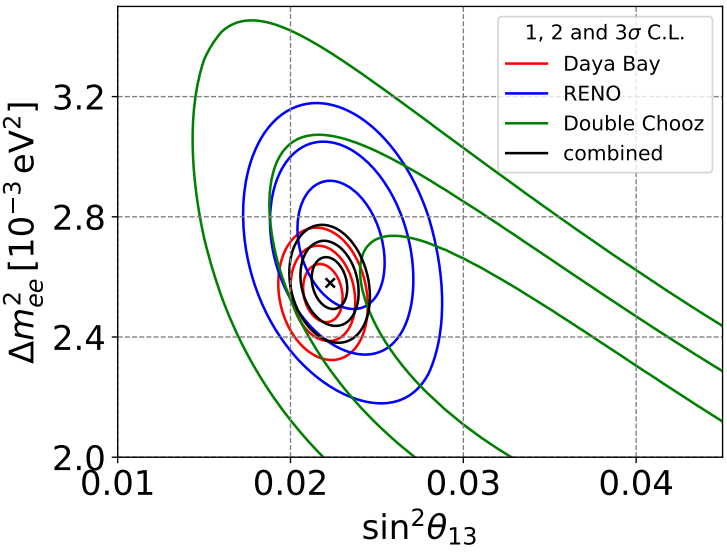


Figure 3.3.2: 1, 2 and 3 $\sigma$ C.L. regions in the $\Delta m^2_{\text{atm}}$ vs $\sin^2\theta_{13}$ parameter space, determined by the MBL reactor experiments in normal ordering: Daya Bay (red), RENO (blue) and Double Chooz (green) from the data sets [106, 107, 134] respectively. The combined fit is represented in black. The black cross represents the global best fit value $(\Delta m^2_{31},\, \sin^2\theta_{13}) = (2.58 \times 10^{-3}\,\text{eV}^2, 0.0223)$. The solar parameters are fixed to $(\Delta m^2_{21},\, \sin^2\theta_{12}) = (7.39 \times 10^{-5}\,\text{eV}^2, 0.310)$.

in appendix A[11]. The Double Chooz data set [134] analysis is performed following a similar procedure.

$\theta_{13}$ is determined by the MBL reactor experiments with high precision. Marginalizing over $\Delta m^2_{31}$, it is found that $\sin^2\theta_{13} = 0.0223^{+0.0006}_{-0.0007}$. Comparing this result with the one obtained in the global fit, cf. table 2.1, it can be seen that $\theta_{13}$ determination is totally dominated by the MBL reactor data contribution.

### Global neutrino oscillation data

In order to perform a consistent combined fit of all the neutrino data, a least-squares statistics, $\chi^2$, including all the data, which depends on all the oscillation parameters has to be built. In [26] reactor, solar, LBL accelerator and atmospheric data is included.

As it was said above, MBL reactor experiments, measure neutrinos in the $\bar{\nu}_e \to \bar{\nu}_e$ oscillation channel, whose oscillation probability is given by (3.3.1). Its $\chi^2$ contribution depends on the same oscillation parameters that its oscillation probability depends on, hence:

$$\chi^2_{\text{reactor}}\left(\theta_{12}, \Delta m^2_{21}, \theta_{13}, \Delta m^2_{31}\right) .$$

The KamLAND experiment [105] also measured in the $\bar{\nu}_e \to \bar{\nu}_e$ channel and its oscillation probability is given by (3.3.4).

The solar experiments, Gallex [135], SAGE [136], Super-Kamiokande [137], SNO [138] and Borexino [139], measure $\nu_e$ neutrinos coming from the sun. The sun is a very dense medium, and its density is considered to slowly decrease in the direction from the core towards the surface, what is called the adiabatic approximation. Due to these strong matter effects inside the sun, the $\nu_e$ states are basically produced and leave the sun as $\nu_2$ massive

[11] In [26] Daya Bay analysis is done implementing an older version for $\chi^2$ than the one described in the appendix A, which is the newest an more rigorous one, used in [28].

eigenstates, see reference [97] for details. Then, they propagate in vacuum to the Earth and solar experiments detect approximately $\nu_2$ mass eigenstates. If they are detected via CC interactions, due to their low energy, ∼MeV, only the electron neutrino component can be measured and the experiment is sensitive to the mixing $|U_{e2}|^2 = \sin^2\theta_{12}\cos^2\theta_{13}$, cf. (2.2.1).

Then the $\chi^2$ contribution from KamLAND and solar data depends on the three parameters:

$$\chi^2_{\text{sol+KamLAND}}\left(\theta_{12}, \Delta m^2_{21}, \theta_{13}\right)$$

LBL accelerator experiments T2K [140], NO$\nu$A [141] and MINOS [142] measure a neutrino beam produced in an accelerator source that travel through the Earth for long distances. Neutrinos are produced in meson decays after the mesons are produced in a proton beam-target interaction. The T2K experiment is based in Japan, the neutrinos are produced at Tokai and measured at the Super-Kamiokande detector, which is located at the Kamioka mine, at a baseline $L = 295\,\text{Km}$. NO$\nu$A and MINOS detectors are based in the US at a baseline $L = 734$ and 810 Km from the NuMI beam at Fermilab.

Atmospheric experiments like Super-Kamiokande [143,144] and Ice Cube [145,146] measure neutrinos produced as a result of cosmic ray interactions with particles in the atmosphere. These neutrinos, depending on the zenith angle with which they face the detector, travel for long distances through the Earth. In the extreme case of being produced at the other side of the globe, i.e. zenith angle $0^o$, the neutrinos go through the entire Earth, twice its radius.

Both atmospheric and LBL experiments measure neutrino oscillations in the $\overset{(-)}{\nu}_\mu \to \overset{(-)}{\nu}_\mu$ disappearance and $\overset{(-)}{\nu}_\mu \to \overset{(-)}{\nu}_e$ appearance oscillation channels, whose corresponding oscillation probabilities depend on all the oscillation parameters and matter effects. A series expansion of these oscillation probabilities taking into account matter effects can be found in reference [147].

The LBL experiments work in a regime that allows to approximate the $\overset{(-)}{\nu}_\mu$ disappearance oscillation probability as being driven by an effective mass squared difference: $\Delta m_{\mu\mu}$ [131]. Analogous to the $\bar{\nu}_e$ disappearance probability (3.3.6), it can be written as

$$P_{\overset{(-)}{\nu}_\mu \to \overset{(-)}{\nu}_\mu} \simeq 1 - \sin 2\theta_{\mu\mu}\sin^2\left(\frac{\Delta m^2_{\mu\mu}}{4E_\nu}\right), \tag{3.3.8}$$

where

$$\begin{aligned}
&\sin^2\theta_{\mu\mu} = \cos^2\theta_{13}\sin^2\theta_{23}\,,\\
&\Delta m^2_{\mu\mu} = \sin^2\theta_{12}\Delta m^2_{31} + \cos^2\theta_{12}\Delta m^2_{32} + \cos\delta_{\text{CP}}\sin\theta_{13}\sin 2\theta_{12}\tan\theta_{23}\Delta m^2_{21}\,.
\end{aligned} \tag{3.3.9}$$

Approximately, the $\overset{(-)}{\nu}_\mu \to \overset{(-)}{\nu}_e$ appearance probability can be written as follows:

$$\begin{aligned}
P_{\overset{(-)}{\nu}_\mu \to \overset{(-)}{\nu}_e} \simeq\ & \sin^2\theta_{23}\sin^2 2\theta_{13}\left(\frac{\Delta_{13}}{\pm A - \Delta_{31}}\right)^2\sin^2\left(\frac{\pm A - \Delta_{31}}{2}L\right)\\
&+\cos^2\theta_{23}\sin^2 2\theta_{12}\left(\frac{\Delta_{12}}{A}\right)^2\sin^2\left(\frac{AL}{2}\right)\\
&+\tilde{J}\frac{\Delta_{21}}{A}\frac{\Delta_{31}}{\pm A - \Delta_{31}}\sin\left(\frac{AL}{2}\right)\sin\left(\frac{\pm A - \Delta_{31}}{2}L\right)\cos\left(\pm\delta + \frac{\Delta_{31}L}{2}\right),
\end{aligned} \tag{3.3.10}$$

where $\tilde{J} \equiv \cos\theta_{13}\sin 2\theta_{12}\sin 2\theta_{13}\sin 2\theta_{23}$ is proportional to the Jarlskog invariant [148], $A$ is a constant matter potential and $\Delta_{ij} \equiv \frac{\Delta m^2_{ij}}{2E}$.

As can be seen from equations (3.3.9) and (3.3.10), in LBL and atmospheric experiments, the oscillation probabilities depend on all the oscillation parameters, hence their contribution to the global $\chi^2$ is:

$$\chi^2_{\text{LBL}}\left(\theta_{12}, \Delta m^2_{21}, \theta_{13}, \Delta m^2_{31}, \theta_{23}, \delta_{CP}\right)$$
$$\chi^2_{\text{atmospheric}}\left(\theta_{12}, \Delta m^2_{21}, \theta_{13}, \Delta m^2_{31}, \theta_{23}, \delta_{CP}\right)$$

Moreover, due to matter effects, which both LBL and atmospheric experiments experience, they are sensitive to the mass ordering. In equation (3.3.10), it can be seen how the matter potential $A$ affects differently the oscillation probability for normal or inverted ordering, i.e. sing of $\Delta_{31}$.

A fully consistent combination of all the data gives rise to a total $\chi^2$ given by

$$\begin{aligned}\chi^2_{\text{global}}\left(\theta_{12}, \Delta m^2_{21}, \theta_{13}, \Delta m^2_{31}, \theta_{23}, \delta_{CP}\right) &= \chi^2_{\text{sol+KamLAND}}\left(\theta_{12}, \Delta m^2_{21}, \theta_{13}\right) \\ &+ \chi^2_{\text{reactor}}\left(\theta_{12}, \Delta m^2_{21}, \theta_{13}, \Delta m^2_{31}\right) \\ &+ \chi^2_{\text{atmospheric}}\left(\theta_{12}, \Delta m^2_{21}, \theta_{13}, \Delta m^2_{31}, \theta_{23}, \delta_{CP}\right) \\ &+ \chi^2_{\text{LBL}}\left(\theta_{12}, \Delta m^2_{21}, \theta_{13}, \Delta m^2_{31}, \theta_{23}, \delta_{CP}\right) . \quad (3.3.11)\end{aligned}$$

In order to get the $\chi^2$ profile for one specific parameter, $\chi^2_{\text{global}}$ has to be marginalized, i.e. minimized over the rest of the parameters. For instance, for the $\theta_{12}$ profile:

$$\chi^2_{\text{global}}(\theta_{12}) = \min_{\Delta m^2_{21}, \theta_{13}, \Delta m^2_{31}, \theta_{23}, \delta_{CP}} \chi^2_{\text{global}}\left(\theta_{12}, \Delta m^2_{21}, \theta_{13}, \Delta m^2_{31}, \theta_{23}, \delta_{CP}\right) .$$

Since not all the experiments are equally sensitive to the parameters that their oscillation probability depends on, it is valid and cheaper in computational time to fix some parameters that are well determined by certain experiments. For example the solar parameters, whose determination is essentially driven by KamLAND and solar experiments.

In the work performed by the NuFit collaboration [27], the MBL reactor analyses were included in the global fit, fixing the solar parameters to the best fit values determined by the solar and KamLAND experiments. Obtaining then a $\chi^2_{\text{reactor}}(\Delta m^2_{\text{atm}}, \sin^2\theta_{13})$ function. This function is added consistently to the $\chi^2$ contributions from LBL accelerator and atmospheric experiments, which depend on the remaining oscillation parameters $\Delta m^2_{\text{atm}}$, $\sin^2\theta_{13}$, $\sin^2\theta_{23}$ and $\delta_{CP}$.

In what follows it is shown how the interplay between the current reactor and LBL data can be useful for the determination of the $\theta_{23}$ octant and the mass hierarchy. All the references of the data used by the NuFit collaboration can be found in [26].

### Reactor and LBL complementarity for the $\theta_{23}$ octant determination

Figure 3.3.3 illustrates how both reactor and LBL data complement each other for the determination of $\Delta m^2_{\text{atm}}$. The right panels show the MBL reactor allowed regions and their combination in the $\Delta m^2_{\text{atm}}$ vs $\sin^2\theta_{13}$ parameter plane, for both normal (upper panel) and inverted (lower panel) ordering. While the left panels show the LBL allowed regions in the plane $\Delta m^2_{\text{atm}}$ vs $\sin^2\theta_{23}$, for normal (upper panel) and inverted (lower panel) ordering.

The LBL experiments (T2K, NO$\nu$A and MINOS) allowed regions in the $\Delta m^2_{\text{atm}}$ vs $\sin^2\theta_{23}$ plane present a non trivial correlation between the two parameters. Smaller values of the atmospheric mass splitting prefer maximal mixing, i.e. $\sin^2\theta_{23} = 0.5$, while larger values deviate from it. The preferred $\Delta m^2_{\text{atm}}$ value by the MBL reactor experiment is somewhat larger than the one preferred by the LBL experiments, so that a combined fit will push the preferred value for $\Delta m^2_{\text{atm}}$ such that $\sin^2\theta_{23}$ will be pushed to non-maximality. In [26] it is shown how in this way a combined fit of LBL and reactor data gives a slight preference for non maximal mixing, with respect to LBL data alone.

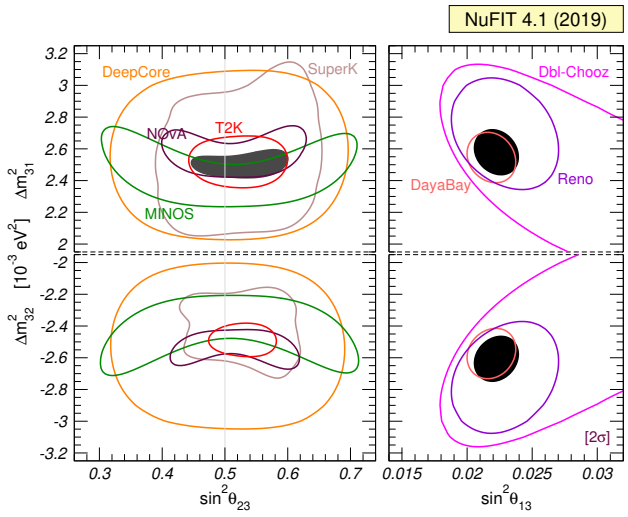


Figure 3.3.3: Figure taken from reference [26]. Determination of $\Delta m^2_{\text{atm}}$ at $2\sigma$ CL for NO (upper pannels) and IO (lower pannels). For each experiment, contours are defined with respect to global minimum of the two orderings. Left: Appearance and disappearance data from MINOS (green), T2K (red), NO$\nu$A (brown) as well as IceCube/DeepCore (orange) and Super-Kamiokande atmospheric (maroon) and their combination (black regions) in the parameter space $\Delta m^2_{\text{atm}}$ vs $\sin^2\theta_{23}$. $\sin^2\theta_{13}$ is minimized over and constrained using the global best fit value. Right: MBL reactor data from Daya Bay (red), RENO (violet) and Double Chooz (magenta) and their combination (balck region) in the parameter space $\Delta m^2_{\text{atm}}$ vs $\sin^2\theta_{13}$. In all panels the solar parameters $\Delta m^2_{21}$ and $\sin^2\theta_{12}$ are fixed to the best fit values.

### Reactor and LBL complementarity for the ordering determination

From equation (3.3.10) it can be seen that LBL experiments are sensitive to the mass ordering thanks to matter effects. LBL data make an important contribution to the mass ordering determination. But also the interplay between MBL reactor experiments measuring in the $\bar{\nu}_e$ disappearance channel and LBL experiments measuring in the $\overset{(-)}{\nu}_\mu$ disappearance channels contributes significantly, [131,149]. The $\bar{\nu}_e$ disappearance probability is symmetric with respect to the sign of the effective mass squared difference $\Delta m^2_{ee}$ (3.3.6) and $\overset{(-)}{\nu}_\mu$ disappearance probability is also symmetric with respect to the sign of $\Delta m^2_{\mu\mu}$, i.e. the probabilities depend on their absolute value. The difference between them is given by [131]

$$|\Delta m^2_{ee}| = |\Delta m^2_{\mu\mu}| \pm \cos 2\theta_{12}\Delta m^2_{21} \mp \cos\delta_{CP}\sin\theta_{13}\sin 2\theta_{12}\tan\theta_{23}\Delta m^2_{21}\,, \tag{3.3.12}$$

where the different upper(lower) signs are for normal(inverted) ordering [131]. Then a precise determination of both $\Delta m^2_{ee}$ and $\Delta m^2_{\mu\mu}$ is sensitive to the mass ordering.

In figure 3.3.4 the $\Delta\chi^2$ profile of the atmospheric mass squared difference is shown, for IO (left panel) and for NO (right panel), following convention (2.2.2). The agreement on the determination of $\Delta m^2_{\text{atm}}$ between the reactor and LBL data is better for NO ordering, which makes this ordering to be preferred. In the upper plots, the long baseline analysis is performed constraining $\theta_{13}$ using a prior given by its precise determination from reactor data, while in the lower panels, LBL and reactor data are consistently combined. The combined LBL fit (blue line) for NO has a smaller $\chi^2$ for both types of analysis, i.e. NO is preferred. But the analysis in which T2K, NO$\nu$A and MINOS data is consistently combined with MBL reactor data, increases the preference for NO by two units of $\Delta\chi^2$ with respect to the case in which $\theta_{13}$ is constrained.

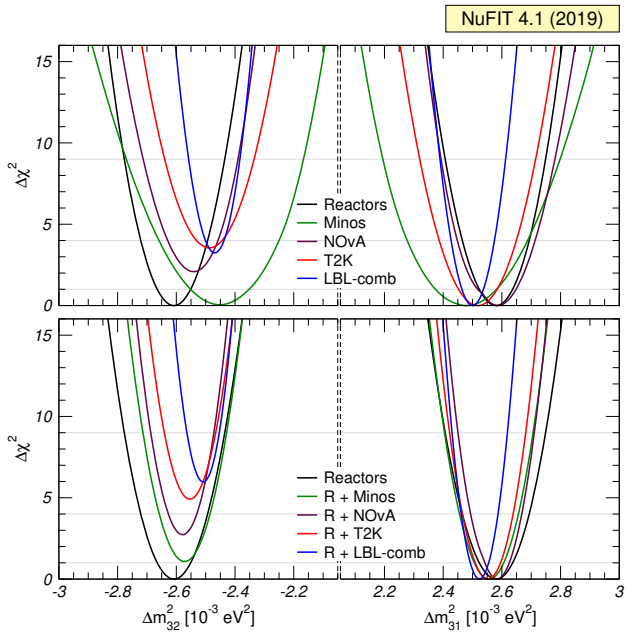


Figure 3.3.4: Figure taken from reference [26]. $\Delta m^2_{\rm atm}$ determination from LBL accelerator and MBL reactor experiments, for IO (left panels) and NO (right panels). For each experiment $\Delta\chi^2$ is defined with respect to the minimum of the two orderings. The upper panels show the $\chi^2$ projection over $\Delta m^2_{\rm atm}$ constraining $\theta_{13}$ from reactor data and the lower panels show the $\chi^2$ projection when LBL and reactor data is combined consistently. In all panels the solar parameters $\Delta m^2_{21}$ and $\sin^2\theta_{12}$ are fixed to the best fit values.

**Summary**

In this section it has been shown that MBL reactor data constitutes the main contribution to the determination of the $\theta_{13}$ mixing angle, and that a consistent combination of reactor and LBL data push into the direction of preference for non-maximal $\theta_{23}$ mixing and increases the preference for NO over IO by two units in $\Delta\chi^2$ with respect to the case in which both data sets are analyzed independently.

### 3.3.2 Constrains on $\Delta m^2_{\rm sol}$ using reactor data

This section is based on reference [28] and contains numerical results and figures from that reference.

As it has been pointed out in the previous section, the 3$\nu$ framework is a very well tested framework but there are still some parameters to be measured, $\theta_{23}$ octant, $\delta_{CP}$ and the mass ordering. LBL experiments are sensitive to $\delta_{\rm CP}$ through the $\overset{(-)}{\nu}_\mu \to \overset{(-)}{\nu}_e$ channel, cf. (3.3.10) and the size of the CP violation oscillating term is proportional to $\Delta m^2_{21}$. Therefore, for the determination of $\delta_{CP}$ in current (NO$\nu$A and T2K) and future LBL experiments (T2HK [150], DUNE [151] and T2HKK [152]), it is crucial to have a precise value for $\Delta m^2_{21}$.

**$\Delta m^2_{21}$ tension**

The determination of $\Delta m^2_{21}$ is driven by the solar and KamLAND experiments, measuring solar and reactor neutrino oscillations in the oscillation channels $\nu_e \to \nu_e$ and $\bar\nu_e \to \bar\nu_e$ respectively. If CPT is a good symmetry of nature, both measurements should give the same value for $\Delta m^2_{21}$, but a $2\sigma$ tension is found between the two determinations [26]. Solar

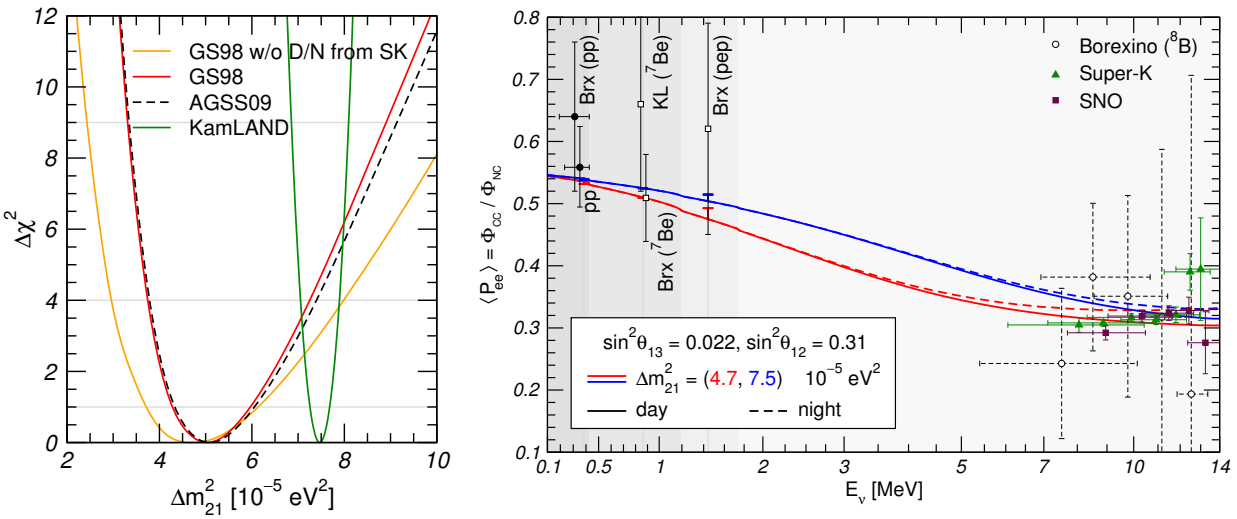


Figure 3.3.5: Left panel: figure taken from [26]. $\Delta\chi^2$ profile of the $\Delta m^2_{21}$ parameter, determined by KamLAND (green) and solar experiments: using the GS98 (red) and the AGSS09 (dashed black) solar models, and removing the day-night data from SuperKamiokande. Right panel: figure taken from reference [153]. Solar oscillation probability vs the neutrino energy. For the fixed parameters $\sin^2\theta_{13} = 0.022$ and $\sin^2\theta_{12} = 0.31$, the predicted red (blue) curve corresponds to the $\Delta m^2_{21}$ value preferred by solar experiments (KamLAND). Solid (dashed) lines correspond to the day (night) predictions. The data points in the low end of the spectrum correspond to the Borexino, Super-Kamiokande and SNO data, see text for details. The abbreviations "Brx" and "KL" are used for Borexino and KamLAND.

experiments prefer a somewhat smaller value $\Delta m^2_{21} \simeq 5.1 \times 10^{-5}\text{eV}^2$ than the one preferred by KamLAND[12] $\Delta m^2_{21} \simeq 7.5 \times 10^{-5}\text{eV}^2$. The tension is shown in the left panel of figure 3.3.5, where it can be seen that it does not depend on the assumed solar flux model. This tension is driven by the non-observation of the low energy up turn in the SNO [138], Super-Kamiokande [137, 154, 155] and Borexino [156] $^8$B data, and by the day-night asymmetry observed in Super-Kamiokande [157], with respect to the predictions based on KamLAND $\Delta m^2_{21}$ measurement, cf. right panel of figure 3.3.5. The tension could be caused by a statistical fluctuation or new physics, but with only the KamLAND measurement from reactor neutrinos it is difficult to make a strong statement and new experiments and checks are needed to address this issue.

As it was demonstrated with simulated data in [133], Daya Bay and RENO experiments are capable of setting an upper limit, and potentially a lower one, on $\Delta m^2_{21}$ to be less than 3 times the measured value by KamLAND. Although they can not address the $2\sigma$ tension, this upper limit measured at much smaller baseline compared to KamLAND, would contribute as a consistency check of the $3\nu$ standard framework. Future experiments, JUNO [128] measuring reactor neutrinos at a baseline $L \sim 50\,\text{Km}$ and Hyper-K [158] and DUNE [159] measuring $^8$B solar neutrinos, will determine this parameter very precisely.

### MBL reactor oscillation probability as a function of $\Delta m^2_{21}$

Given the current values of the oscillation parameters, cf. table 2.1, in MBL reactor experiments the electron disappearance oscillation probability (3.3.1) is dominated by the atmospheric oscillation term over the solar one, cf. equations (3.3.3) and (3.3.5). As can be seen in figure 3.3.6 for a larger value of $\Delta m^2_{21}$ the solar oscillation term becomes more

[12] The global fit [26] sets $\Delta m^2_{21} \simeq 7.39 \times 10^{-5}\,\text{eV}^2$, being KamLAND measurement the main contribution.

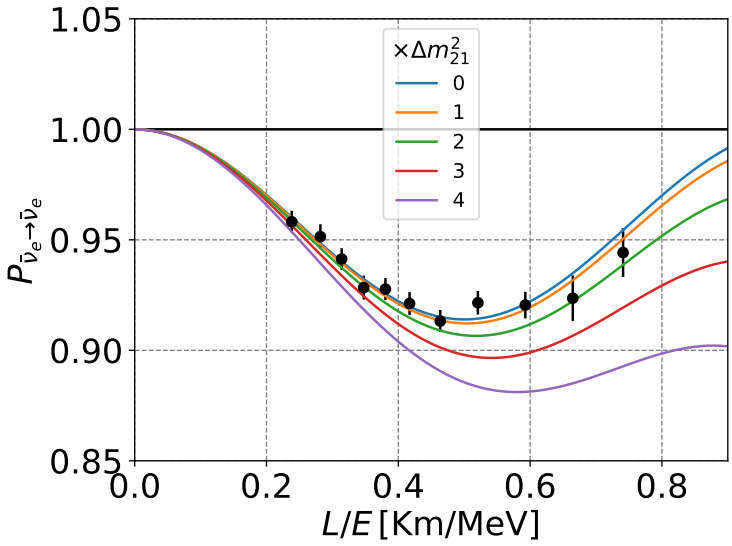


Figure 3.3.6: Disappearance oscillation probability vs $L_{\text{eff}}/E$. Black dots are Daya Bay EH3 data, taken from figure 40 in [130], the curves are the electron neutrino disappearance oscillation probability for $\Delta m^2_{21} = (0, 1, 2, 3, 4) \times 7.4 \times 10^{-5}\,\text{eV}^2$. The rest of the oscillation parameters are fixed to their global best fit values [26].

important and comparable to the atmospheric one. This can be seen rewriting (3.3.2) as

$$P_{12} \simeq 0.002 \left(\frac{L/E}{0.5\,\text{Km/MeV}}\right)^2 \left(\frac{\Delta m^2_{21}}{7.5 \times 10^{-5}\,\text{eV}^2}\right)^2 ,$$

which is a good approximation of (3.3.2) provided $\Delta m^2_{21} \lesssim 4 \times 7.5 \times 10^{-5}\,\text{eV}^2$. For a value $\Delta m^2_{21} = 3 \times 7.5 \times 10^{-5}\,\text{eV}^2$, $P_{12}$ and $P_{13}$ are already of comparable size. Therefore a sufficiently large $\Delta m^2_{21}$ would have an impact in the MBL reactor experiments analyses, such that the data can be used to set an upper limit. Note that after the atmospheric oscillation maximum at $L/E \sim 0.5\,\text{Km/MeV}$, $P_{12}$ keeps on increasing while $P_{13}$ starts decreasing, hence the constraint on $\Delta m^2_{21}$ will come predominantly from the data with large $L/E$, cf. figure 3.3.6.

### Daya Bay and RENO analysis

Following the study done in [133], current available data by Daya Bay [106] and RENO [107] are used to set an upper limit on $\Delta m^2_{21}$. The data analysis is performed as explained in Appendix A. For this analysis the free parameters are $\Delta m^2_{21}$ and $\sin^2\theta_{13}$. $\theta_{12}$ is kept fixed to the value $\sin^2\theta_{12} = 0.310$ and $\Delta m^2_{ee}$ is constrained to the value set by the LBL experiments, including an additional penalizing term to the $\chi^2$-function:

$$\frac{\left(\Delta m^2_{ee,\,\text{LBL}} - \Delta m^2_{ee}\right)^2}{\sigma^2_{ee}} .$$

$\Delta m^2_{ee,\,\text{LBL}}$ and its uncertainty, $\sigma_{ee}$, are inferred from the measurement of $\Delta m^2_{\mu\mu}$ by LBL experiments [26]. The relation between $\Delta m^2_{ee}$ and $\Delta m^2_{\mu\mu}$ is given by (3.3.12). Although in the analysis $\Delta m^2_{21}$ is left to vary up to $3 \times 10^{-4}\,\text{eV}^2$, since $\theta_{13}$ is very small, the product $\sin\theta_{13}\Delta m^2_{21}$ suppresses the second term over the first, so that [131]

$$|\Delta m^2_{ee}| \simeq |\Delta m^2_{\mu\mu}| \pm \cos 2\theta_{12}\Delta m^2_{21} ,$$

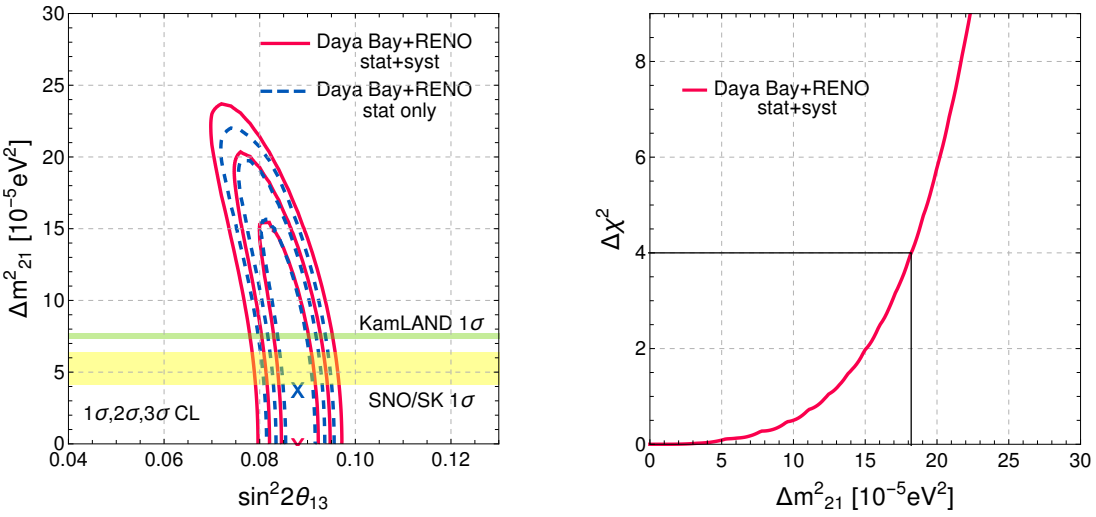


Figure 3.3.7: Daya Bay and RENO combined analysis for the $\Delta m^2_{21}$ constraint. The $\theta_{12}$ parameter is set to $\sin^2\theta_{12} = 0.310$ and $\Delta m^2_{ee}$ is constrained by the LBL experiments measured value. Left: 1, 2 and 3 $\sigma$ contours in the $\Delta m^2_{21}$ vs $\sin^2 2\theta_{13}$ parameter space, including (not including) systematic uncertainties in red (dashed-blue), best fit values are marked with an $\times$. For comparison, the KamLAND and SNO combined with SK $\Delta m^2_{21}$ values are shown. Right: $\chi^2$ projection over $\Delta m^2_{21}$, minimizing with respect to $\sin^2 2\theta_{13}$, systematic uncertainties included. Plots are taken from [28].

is a good approximation. The "+" and "−" signs are for NO and IO cases.

Since $\Delta m^2_{21}$ is a free parameter in this study and the hierarchy is unknown, the second term acts as an uncertainty on $|\Delta m^2_{ee}|$:

$$|\Delta m^2_{ee}| \;=\; |\Delta m^2_{\mu\mu}| \pm \sigma_{e\mu}\,.$$

$\Delta m^2_{\mu\mu}$ is computed taking the best fit value of $\Delta m^2_{\rm atm}$ from the LBL combined analysis in [26] and the global best fit values for $\theta_{12}$ and $\Delta m^2_{21}$, ignoring the term proportional to $\sin\theta_{13}\Delta m^2_{21}$ in (3.3.9). The uncertainty, $\sigma_{e\mu}$, is estimated considering small variations of $\sin^2\theta_{12}$ and $\Delta m^2_{21} < 4\times 7.5\times 10^{-5}\,\mathrm{eV}^2$, which translates into a 4% relative uncertainty. The uncertainty on $\Delta m^2_{\mu\mu}$, about 4%, is computed propagating the $1\sigma$ uncertainty on $\Delta m^2_{\rm atm}$ determined by the combined LBL analysis. Adding both, the total relative uncertainty on $\Delta m^2_{ee}$ becomes 6%:

$$|\Delta m^2_{ee}| = (2.45 \pm 0.15)\times 10^{-5}\,\mathrm{eV}^2\ .$$

The data analysis is performed using the complete oscillation probability (3.3.1), meaning that $\Delta m^2_{31}$ and $\Delta m^2_{32}$ are computed according to (3.3.7) for each value of the parameters $\theta_{12}$, $\Delta m^2_{21}$ and $\Delta m^2_{ee}$ that we scan over.

### Results

The best fit of the Daya Bay and RENO combined data analysis, together with the 1,2 and $3\sigma$ confidence regions in the plane $\Delta m^2_{21}$ vs $\sin^2\theta_{13}$ are shown in the left panel of figure 3.3.7, including systematic uncertainties in red solid lines and including only statistical uncertainties in dashed blue. The right panel of figure 3.3.7 shows the $\chi^2$ projection over $\Delta m^2_{21}$, computed minimizing over $\sin^2 2\theta_{13}$. The upper bound on $\Delta m^2_{21}$ at the $2\sigma$ confidence level is $18.3\times 10^{-5}\,\mathrm{eV}^2$.

We also performed a more conservative analysis, in which no assumptions for $\Delta m^2_{ee}$ are taken, fitting it together with $\Delta m^2_{21}$ and $\sin^2\theta_{13}$, fixing $\sin^2\theta_{12} = 0.310$. In figure 3.3.8 the

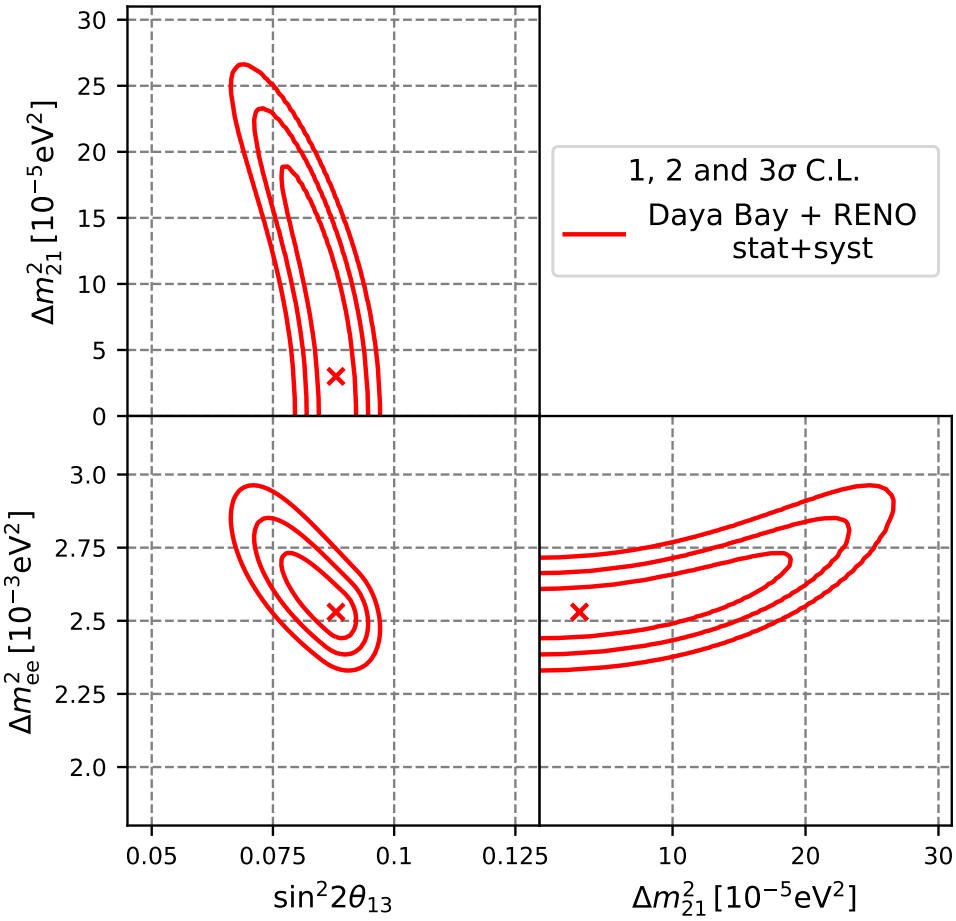


Figure 3.3.8: 1, 2 and 3 $\sigma$ contours of the $\chi^2$ projection over the $\Delta m^2_{21}$ vs $\sin^2 2\theta_{13}$ (upper), $\Delta m^2_{ee}$ vs $\sin^2 2\theta_{13}$ (lower left) and $\Delta m^2_{ee}$ vs $\Delta m^2_{21}$ (lower right) planes, from the simultaneous 3 parameter combined fit, $\Delta m^2_{21}$, $\sin^2 2\theta_{13}$ and $\Delta m^2_{ee}$ of Daya Bay and RENO data sets, systematic uncertainties included. $\theta_{12}$ parameter is set to $\sin^2\theta_{12} = 0.310$. Plots are taken from [28].

three different projections of the fit including both statistical and systematic uncertainties are shown. The best fit value is found at $\Delta m^2_{21} = 3.3 \times 10^{-5}\,\text{eV}^2$, $\Delta m^2_{ee} = 2.5 \times 10^{-3}\,\text{eV}^2$ and $\sin^2 2\theta_{13} = 0.088$.

Comparing figure 3.3.7 left panel and figure 3.3.8 upper panel, it can be seen how constraining $\Delta m^2_{ee}$ with complementary information from LBL experiments helps to set a stronger upper limit on $\Delta m^2_{21}$.

Note that the solar and KamLAND experiments determine at the same time both $\Delta m^2_{21}$ and $\sin^2\theta_{12}$. Then, in order to be independent of their measurements, no assumption on $\sin^2\theta_{12}$ should be taken. In our analysis, in which $\Delta m^2_{21}$ is varied up to $30 \times 10^{-5}\,\text{eV}^2$, the approximated oscillation probability (3.3.6) holds to a good accuracy[13], so that the MBL reactor experiments are sensitive to the combination $\sin^2 2\theta_{12}\Delta m^2_{21}$. Which can be seen approximating $\sin^2\Delta_{21} \simeq \Delta^2_{21}$ in (3.3.1) for small $\Delta_{21} = \Delta m^2_{21}L/(4E)$. That means that $\Delta m^2_{21}$ in these analyses can be reinterpreted as $\Delta m^2_{21}\sin^2 2\theta_{12}/0.92$, where 0.92 is the value taken for $\sin^2 2\theta_{12}$ in the analyses. [133] discusses the little impact of varying $\sin^2\theta_{12}$ on these analyses.

[13]For $\Delta m^2_{21} = 30 \times 10^{-5}\,\text{eV}^2$ in the MBL regime: $\Delta m^2_{21}\frac{L}{4E} < 0.5$, so the approximation holds to a good acuracy, [133].

**Summary**

A precise determination of $\Delta m^2_{21}$ is needed in order to measure $\delta_{CP}$ in future LBL experiments. The current sensitivity of MBL reactor experiments is far from addressing the $2\sigma$ tension in the determination of $\Delta m^2_{21}$ between solar and KamLAND experiments. So far the upper limit on $\Delta m^2_{21}$ is set to be less than $18.3\,\mathrm{eV}^2$ at the $2\sigma$ C.L. As can be seen in figure 3.3.7, current bounds are limited by statistics so are still to be improved with more data and with a possible improvement of the systematic uncertainties. In the near future, a precise determination of $\Delta m^2_{21}$ by JUNO, Hyper-K and DUNE will solve the present $2\sigma$ tension, until then the limit set by MBL reactor experiments, Daya Bay and RENO, works as a consistency check of the $3\nu$ oscillation framework.

## 3.4 $3+1\nu$ Oscillation Framework

In this section, reactor data compatible with active-to-sterile oscillations in the context of $3+1\nu$ framework is studied. In spite of the success of the $3\nu$ standard scenario, in the last decade this framework has been actively under research driven by anomalies in neutrino oscillation data, in particular in SBL experiments. This section starts with an overview on the SBL anomalies, section 3.4.1. Then we perform a detailed study on the reactor anti-neutrino flux in section 3.4.2. Finally, in sections 3.4.3 and 3.4.4 the current status of the global picture of the active-to-sterile oscillations is discussed.

### 3.4.1 Overview on short baseline anomalies

As discussed in the previous section, the $3\nu$ framework, although some of the oscillation parameters are unknown, is a very well tested and consistent framework. However there are a number of experimental results that disagree with this picture: LSND [29], MiniBooNE [38], reactor [33] and intense radioactive source [31,32] anomalous results. The LSND experiment measures an excess of $\nu_e$ like events in the oscillation channel $\nu_\mu \to \nu_e$, also the MiniBooNE experiment measures an excess of $\overset{(-)}{\nu}_e$ like events in the oscillation channels $\overset{(-)}{\nu}_\mu \to \overset{(-)}{\nu}_e$. Reactor experiments, measuring in the $\bar{\nu}_e \to \bar{\nu}_e$ channel, after a recalculation of the theoretical $\bar{\nu}_e$ predictions [102, 103], found a deficit in the ratio of measured vs the predicted events. This deficit is supported by a similar deficit found in gallium-based radiochemical detectors in the oscillation channel $\nu_e \to \nu_e$, using an intense radioactive source as the source of $\nu_e$. These anomalous results, the LSND, reactor and gallium anomalies, occur at a very short baseline, so they are commonly referred as the SBL anomalies. As it was explained before, at a SBL regime, the $3\nu$ standard framework oscillations do not have time to develop, being not measurable. Since the $3\nu$ standard picture is well established and compatible with a lot of different data sets, the excesses and deficits of events setting these anomalies must come from another source. The existence of a hypothetical eV scale sterile neutrino, which would drive active-to-sterile oscillations, could cause an excess of $\nu_e$ like events in the $\overset{(-)}{\nu}_\mu \to \overset{(-)}{\nu}_e$ channel and a deficit of events in the $\overset{(-)}{\nu}_e \to \overset{(-)}{\nu}_e$ channel. In figure 3.2.2 it can be seen how the oscillation probability $P_{\bar{\nu}_e \to \bar{\nu}_e}$ can fit the measured deficit of $\bar{\nu}_e$ events when an active-to-sterile oscillation is included.

In this scenario, which is called $3+1\nu$ oscillation framework, the LSND, reactor and gallium anomalies have to be contrasted with all the constraints on the eV active-to-sterile neutrino oscillation searches, set by the null results from the experiments that would be sensitive to this new hypothetical oscillation, measuring in the channels $\overset{(-)}{\nu}_\mu \to \overset{(-)}{\nu}_e$, $\overset{(-)}{\nu}_e \to \overset{(-)}{\nu}_e$ and $\overset{(-)}{\nu}_\mu \to \overset{(-)}{\nu}_\mu$. This is discussed in section 3.4.5. Apart from existing constrains, concerning

the reactor data, there is experimental evidence that sheds doubt into the reliability of the reactor $\bar{\nu}_e$ flux predictions, indicating that a miscalculation of the $\bar{\nu}_e$ fluxes could be the origin of the RAA. This is discussed in detail in section 3.4.2. Given this situation, experimental data based on ratios of reactor spectral information is of high importance, since those experiments are insensitive to reactor $\bar{\nu}_e$ flux shape and normalization.

In the short baseline regime only the oscillating terms in (3.1.2) driven by the new mass squared difference, $\Delta m^2_{\text{new}}$, have time to evolve and have a measurable effect. Since the mass of the new massive eigenstate considered is at the eV scale, $\Delta m^2_{\text{new}} \equiv \Delta m^2_{41} \simeq \Delta m^2_{42} \simeq \Delta m^2_{43}$ the appearance and disappearance oscillation probabilities are given by:

$$\begin{aligned} P^{\text{SBL}}_{\nu_\alpha \to \nu_\alpha} &= 1 - 4\,|U_{\alpha 4}|^2 \left(1 - |U_{\alpha 4}|^2\right) \sin^2\left(\frac{\Delta m^2_{41} L}{4E}\right) \\ P^{\text{SBL}}_{\nu_\alpha \to \nu_\beta} &= 4\,|U_{\alpha 4}|^2\,|U_{\beta 4}|^2 \sin^2\left(\frac{\Delta m^2_{41} L}{4E}\right) . \end{aligned} \tag{3.4.1}$$

In these expressions it can be clearly seen that the active-to-sterile oscillation cause a deficit of $\alpha$ favor neutrinos in the disappearance channel and an excess of $\beta$ flavor neutrinos in the appearance channel. Here $U_{\alpha 4}$ are the elements of the $4 \times 4$ lepton mixing matrix (3.1.4). According to [37], here we use the following parameterization:

$$U \equiv R_{34}(\theta_{34}) R_{24}(\theta_{24}, \delta_{24}) R_{14}(\theta_{14}) R_{23}(\theta_{23}) R_{13}(\theta_{13}, \delta_{13}) R_{12}(\theta_{12}, \delta_{12}) ,$$

where $R_{ij}(\theta_{ij})$ denotes a real rotation of $\theta_{ij}$ in the $ij-$plane and $R_{ij}(\theta_{ij}, \delta_{ij})$ includes complex phases, e.g.:

$$R_{14} = \begin{pmatrix} \cos\theta_{14} & 0 & 0 & \sin\theta_{14} \\ 0 & 1 & 0 & 0 \\ 0 & 0 & 1 & 0 \\ -\sin^2\theta_{14} & 0 & 0 & \cos\theta_{14} \end{pmatrix} ; \quad R_{24} = \begin{pmatrix} 1 & 0 & 0 & 0 \\ 0 & \cos\theta_{24} & 0 & \sin\theta_{24} e^{-i\delta_{24}} \\ 0 & 0 & 1 & 0 \\ 0 & -\sin^2 e^{i\delta_{24}} & 0 & \cos\theta_{24} \end{pmatrix} .$$

Here the Majorana phases are omitted[14].

In this parameterization $U_{14} \equiv U_{e4} = \sin\theta_{14}$. Then, in a SBL regime, the reactor neutrino oscillation probability is given by

$$P_{\overline{\nu}_e \to \overline{\nu}_e} = 1 - \sin^2 2\theta_{14} \sin^2\left(\Delta m^2_{41} \frac{L}{4E}\right) . \tag{3.4.2}$$

### 3.4.2 Flux predictions vs. sterile neutrino oscillations

This section is based on the study done in reference [36]. Expressions and figures are taken or based on the ones from that reference.

The RAA relies on the theoretical $\bar{\nu}_e$ flux predictions and the magnitude on their predicted uncertainties [102, 103]. Recent experimental data, as the unpredicted 5 MeV bump in the measured spectrum and the measurements of the individual flux components by Daya Bay [34] and RENO [35], suggest that the predictions should not be trusted at face value and that the source of the anomaly can be a mismodelling of the flux predictions.

[14] Following this notation, (2.2.1) is parameterized as $R_{23}(\theta_{23}) R_{13}(\theta_{13}, \delta_{13}) R_{12}(\theta_{12}) \text{diag}\{e^{i\alpha_1}, e^{i\alpha_2}, 1\}$.

### Daya Bay measurement

The Daya Bay collaboration measured for the first time the contributions to the $\bar{\nu}_e$ flux coming from the four different isotopes $^{235}$U, $^{239}$Pu, $^{238}$U and $^{241}$Pu, by using the measured IBD yield per fission, $\sigma$, and the effective fission fractions, $F^{\rm iso}$, as a function of time at the near site detectors, EH1 and EH2 [34]. $F^{\rm iso}$ are the relative amount of a given isotope *iso* that is effectively seen at the near site detectors[15]. The IBD yield per fission is proportional to the neutrino flux normalization, it is given by the convolution of the neutrino flux per fission, $\phi(E_\nu)$, and the IBD cross section, $\sigma_{\rm IBD}(E_\nu)$:

$$\sigma = \sum_{\rm iso} F_{\rm iso}\sigma_{\rm iso} = \sum_{\rm iso} F_{\rm iso} \int \phi^{\rm iso}(E_\nu)\sigma_{\rm IBD}(E_\nu){\rm d}E_\nu \,.$$

$\sigma^{\rm iso}$ is the contribution from each isotope. The effective fission fractions of each isotope were measured as a function of time using information on the isotope composition of the reactor fuel and the total power generated in each reactor together with their time dependence [34].

The collaboration reported a 7.8% deficit between the observed and predicted IBD yield from $^{235}$U, $\sigma_{235}$, while the rest $\sigma_{239}$, $\sigma_{238}$ and $\sigma_{241}$ are consistent within the uncertainties. This suggests that an over estimation of the $^{235}$U flux predictions is the main source of the RAA.

### Active-to-sterile $\nu$ oscillations

Daya Bay data in [34] favours the $^{235}$U overestimation hypothesis over the global suppression of the four components at the level of $2.8\sigma$. The global suppression is identical to the effect that an active-to-sterile neutrino oscillation would cause with a new mass squared difference of $\sim$ 1eV. For this value the oscillation probability (3.4.2) is completely averaged out[16] at the Daya Bay near detectors baseline, acting then as a global suppression factor

$$P_{\bar{\nu}_e\to\bar{\nu}_e} = 1 - \frac{1}{2}\sin^2 2\theta_{14}\,. \tag{3.4.3}$$

In the light of these results, before performing an analysis of the SBL reactor data under the active-to-sterile neutrino oscillation hypothesis, it is worth to check how well this hypothesis fits to the Daya Bay flux measurement. To do that, the goodness of fit for this hypothesis is computed using [34] data.

### Analyses: flux free and flux fixed hypotheses

Since there is basically a 1 to 1 correspondence between the time evolution of the effective fission fraction $F_{239}$ and the other $F_{\rm iso}$, c.f. figure 1 in [34], the time dependent total IBD yield measurements and effective fission fractions $F_{\rm iso}$ are expressed as a function of $F_{239}$ in 8 different bins. The IBD yields are given in units of cm$^2$ per fission. The predictions of the total IBD yields, $\sigma_{\rm pred}$, in each $F_{239}$ bin $a$ are computed as

$$\sigma^a_{\rm pred} = \sum_{\rm iso} P^{\rm iso}_{\rm osc}\xi_{\rm iso}F^a_{\rm iso}\sigma^{\rm HM}_{\rm iso}\,, \tag{3.4.4}$$

where $P^{\rm iso}_{\rm osc}$ is the oscillation probability (3.4.3)[17]. $F^a_{\rm iso}$ are the effective fission fractions for each isotope iso in each $F_{239}$ bin ($a = 1,\ldots,8$). $\sigma^{\rm HM}_{\rm iso}$ are the Huber-Mueller IBD yield

[15] The difference between $F^{\rm iso}$ and $f^{\rm iso}$ in (3.2.6), is that the latter are averaged in time.

[16] The average $\lim_{\Delta\to\infty}\frac{1}{2\Delta}\int_{-\Delta}^{\Delta}{\rm d}x\,\sin^2 x = \frac{1}{2}$.

[17] $P^{\rm iso}_{\rm osc}$ depends on the oscillation frequency, energy and baseline, so it depends on the Daya Bay near detector configuration. Also, the different energy spectra of each isotope introduces a small dependence on them. For $\Delta m^2_{41} \gtrsim 0.05\,{\rm eV}^2$ the probability is completely averaged out in the Daya Bay near detectors, therefore independent of the isotope, energy and baseline.

predictions, for the $^{235}$U, $^{239}$Pu and $^{241}$Pu isotopes [102] and for $^{238}$U [103]. $\xi_{\rm iso}$ are the pull parameters that allow each IBD yield to be rescaled from their predictions.

The analysis is performed using a least-squares statistic method as follows:

$$\chi^2 = \sum_{a,b=1}^{8} (\sigma^a_{\rm obs} - \sigma^a_{\rm pred}) V^{-1}_{ab} (\sigma^b_{\rm obs} - \sigma^b_{\rm pred}) + \chi^2_{\rm flux}(\hat{\boldsymbol{\sigma}}) \,. \tag{3.4.5}$$

Here the measured IBD yields $\sigma_{\rm obs}$ as well as the covariance matrix $V$, which includes statistical and systematic uncertainties and their correlations, are taken from the complementary material provided in [34]. Depending on the assumptions taken for the analysis, different expressions are taken for $\chi^2_{\rm flux}(\xi_i)$ which accounts for the constrains over the pull parameters.

Here we performed two different analyses: one in which no active-to-sterile oscillation is considered and the flux normalizations are left free and fitted to the data, called "flux free (no $\nu$)" analysis, and the second one in which active-to-sterile oscillations are included and the flux normalizations are constrained to the predicted values within their predicted uncertainties, called "flux fixed ($\nu$)". In the "flux fixed ($\nu$)" case, $\chi^2_{\rm flux}(\xi_i)$ includes the systematic uncertainties of the IBD yields [102, 103]:

$$\chi^2_{\rm flux}(\hat{\boldsymbol{\sigma}}) = (\hat{\sigma}_i - \sigma_i^{HM}) V^{-1}_{\sigma_{\rm ij}} (\hat{\sigma}_j - \sigma_j^{HM}) \,, \tag{3.4.6}$$

where $V^{-1}_{\sigma_{\rm ij}}$ is the covariance matrix with the uncertainties of predicted IBD yields and their correlations, taken from table 3 in reference [160]. $\hat{\sigma}_i \equiv \sigma_i^{\rm HM} \xi_i$ (no summed indices). In the "flux free (no $\nu$)" analysis, these penalizing terms are not considered, but since the $^{238}$U and $^{241}$Pu contributions to the total flux are subdominant, a $1\sigma$ constraint of 10% uncertainty is imposed to the IBD yields of theses two isotopes in order to avoid unphysical results. In the "flux free (no $\nu$)" analysis, $\chi^2_{\rm min}$ is expected to follow a $\chi^2$ distribution with $8-2$ degrees of freedom, since there are 8 data bins and 2 main fit parameters, $\sigma_{235}$ and $\sigma_{239}$, whereas in the "flux fixed ($\nu$)" case, $8-1$ degrees of freedom are expected, coming from the $\theta_{14}$ mixing angle that causes the global suppression. We checked by a Monte Carlo simulation that the $\chi^2_{\rm min}$ in both analyses follow a $\chi^2$ distribution with 6 and 7 degrees of freedom. In appendix B details on the Monte Carlo study are provided.

**Results**

The goodness of fit, computed assuming $\chi^2$ distributions with 7 and 6 degrees of freedom, can be found in table 3.1. The "flux free (no $\nu$)" hypothesis fits better to the data with a p-value of 73%, but the "flux fixed ($\nu$)" hypothesis can not be rejected at a high enough confidence level since it has a reasonably good p-value of 17%. In the latter case, it is found that active-to-sterile oscillations are preferred with respect to no oscillations at the level of 4.0 units in $\Delta\chi^2$ ($\sim 2\sigma$ for a $\chi$ distribution of 1 dof), with the best fit value at $\sin^2 2\theta_{14} = 0.13$.

In order to quantify how disfavored the "flux fixed ($\nu$)" is with respect to the "flux free (no $\nu$)" hypothesis, denoted as $H_0$ and $H_1$ respectively, a test statistic $T$ is built as follows

$$T = \chi^2_{\rm min}(H_0) - \chi^2_{\rm min}(H_1) \,. \tag{3.4.7}$$

$T$ is expected to follow a $\chi^2$ distribution with one degree of freedom, since $H_0$ is a subset of $H_1$, a particular case in which all the fluxes are rescaled with the same factor. It was checked by a Monte Carlo study that this approximation is good, cf. appendix B.

$$T_{\rm DB\,flux} = 6.8 \,, \quad p\text{-value} = \begin{cases} 0.7\% \ (2.7\sigma) & \text{(Monte Carlo)}, \\ 0.9\% \ (2.6\sigma) & (\chi^2 \text{ approximation}). \end{cases}$$

| Analysis | $\chi^2_{\text{min}}$/dof | gof | $\sin^2 2\theta_{14}$ | $\Delta\chi^2$(no osc) |
|---|---|---|---|---|
| flux fixed ($\nu$) | 10.4/7 | 0.17 | 0.13 | 4.0 |
| flux free (no $\nu$) | 3.6/6 | 0.73 | - | - |

Table 3.1: Analysis of the Daya Bay IBD yields per fission measurements [34] for two different hypothesis: keeping the fluxes normalization to the predictions including an active-to-sterile oscillation, "flux fixed ($\nu$)", and leaving the fluxes normalization free and fitting them to the data without considering the oscillation, "flux free (no $\nu$)". The goodness of fit are computed under the assumption that the $\chi^2_{\text{min}}$ follow a $\chi^2$ distribution with 7 and 6 degrees of freedom respectively.

Here the sterile neutrino hypothesis $H_0$ is disfavored with respect to $H_1$ at 99.3% confidence level. This is in agreement with [34] in which it is found that $H_0$ is disfavored with respect to $H_1$ at the $2.8\sigma$ level. The number here obtained is smaller since the "flux fixed ($\nu$)" hypothesis includes the predicted uncertainties of the IBD yields, which was not taken into account in [34]. Whit the latter assumption, the $p$-values found for $\chi^2_{(\nu),\text{min}}$ and $T_{\text{DB flux}}$ are 12% and 0.5%($2.8\sigma$) respectively. In appendix B, details on the $p$-values for the different assumptions and the verification that the least square statistics quantities follow $\chi^2$ distributions are shown.

**Conclusions**

Although Daya Bay data on the different flux contributions [34] prefers the "flux free (no $\nu$)" with respect to the "flux fixed ($\nu$)"hypothesis, we have shown in this section that it is worth to perform an analysis of the reactor data in the $3+1\nu$ oscillation framework, since this hypotheses fits good enough to the Daya Bay flux data, with a goodness of fit of 17%. Moreover, as it will be shown in the next section when including all the reactor data available up to February 2018, the test statistic $T_{\text{reactors}} = -1.3$ do not longer disfavor active-to-sterile neutrino oscillations, being both hypothesis equally compatible.

### 3.4.3 Global reactor analysis

This section is based on results from reference [37]. Numerical results and some of the plots are taken from that reference.

As it was shown in the previous section, despite the problems with the $\bar{\nu}_e$ flux predictions, it is licit to consider the reactor data analysis within the $3+1\nu$ oscillation framework. Therefore we perform a global analysis of all the reactor data sensitive to the hypothetical active-to-sterile oscillation.

**Data sets**

Two sets of experiments are studied, the one that set the reactor anomaly [33] together with the Double Chooz [161] and RENO [162] near detector rate measurements, called "old", and all the available data up to February 2018 called "all", summarized in table 3.2. The "old" data set was used in the analysis performed in [167], here we do a follow up of this analysis including new data, the "all" data set, and implementing the new codes.

Besides the Daya Bay flux data [34], there are two types of data: total rates and ratios of measured spectra. The latter is independent of the flux shape and normalization, as it was explained in section 3.2. The total rate measurements consists of the integrated spectrum and depend on the normalization of the flux predictions. But it is worth to highlight that

| | | Experiment | References | $L$ [m] | Data type |
|---|---|---|---|---|---|
| all | old | ILL | [111] | 9 | total rate |
| | | Gösgen | [112] | 38, 45, 65 | total rate |
| | | Krasnoyarks | [113–115] | 33, 92, 57 | total rate |
| | | ROVNO | [116, 117] | 18, 25 | total rate |
| | | Bugey-3 | [163] | 15, 40, 95 | spectra at 3 different sites |
| | | Bugey-4 | [118] | 15 | total rate |
| | | SRP | [119] | 18, 24 | total rate |
| | | Double Chooz | [161] | 400 | near detector total rate |
| | | RENO | [162, 164] | 430 | near detector total rate |
| | | KamLAND | [165] | 180000 | spectral data |
| | | Daya Bay | [130] | 570, 1640 | 2 ratios of spectral data |
| | | Daya Bay flux | [34] | 570 | flux contributions from each isotope |
| | | NEOS | [110, 121] | 24 | ratio of NEOS and Daya Bay spectral data |
| | | DANSS | [166] | 11 | ratio of spectral data |

Table 3.2: "Old" and "all" data sets included in the global reactor analysis. Details on the baseline $L$ and data type are given in the third and fourth columns.

no direct comparison of spectral predictions to measurements is done, being the whole data set insensitive to the 5 MeV bump.

The "old" data set basically consists of total ratios between the predictions and expectations, except the Bugey-3 data, whereas in the data set "all", spectral information at different short baselines and direct information on the normalization of the four individual fluxes [34] is added.

Experiments of special importance are NEOS [121] and DANSS [125], which perform analyses based on far-to-near spectral ratios which are flux shape and normalization independent, allowing to study the active-to-sterile oscillations independently of the flux predictions, which is crucial given the current situation. NEOS data is based on a ratio between the observed energy spectrum, at a basline $L = 24\,\mathrm{m}$ and a no-oscillation prediction based on the unfolded Daya Bay $\bar{\nu}_e$ spectrum [110], such that Daya Bay works as a far detector for NEOS. The Daya Bay unfolded spectrum is the measured spectrum decoupled from the $3\nu$ oscillations, which can be used as a model independent $\bar{\nu}_e$ flux input in other experiments. DANSS data is given as a ratio of measured spectra at two different baselines, $L = 12.7\,\mathrm{m}$ (down) and $L = 10.9\,\mathrm{m}$ (up), from the center of the reactor core.

In figure 3.4.1 the NEOS and DANSS spectral data is shown, together with the theoretical predictions for the best fit values of the NEOS and DANSS single analysis and the global analysis described below. As it can be seen, the spectral data show distortions that are compatible with active-to-sterile oscillations, with NEOS and DANSS being compatible for the same oscillation parameters. Details on NEOS and DANSS analyses can be found in sections A.2 and A.3.

The Daya Bay oscillation data analysis is also based on a ratio between two measured spectra at two different baselines, as it was done for the $3\nu$ standard analysis. Daya Bay operates at a much larger baseline than NEOS and DANSS, so it is sensitive to much smaller mass squared differences, cf. discussion on oscillation regimes in section 3.1. Out of the three MBL reactor experiments, only the Daya Bay [130] spectral information is included in the analyses. Double Chooz and RENO spectral information [107, 168] is not included since their statistical power is much inferior than the Daya Bay one.

The Daya Bay flux data [34] is also taken into account in the analysis and provides very valuable information on the flux normalizations, constraining the flux predictions in

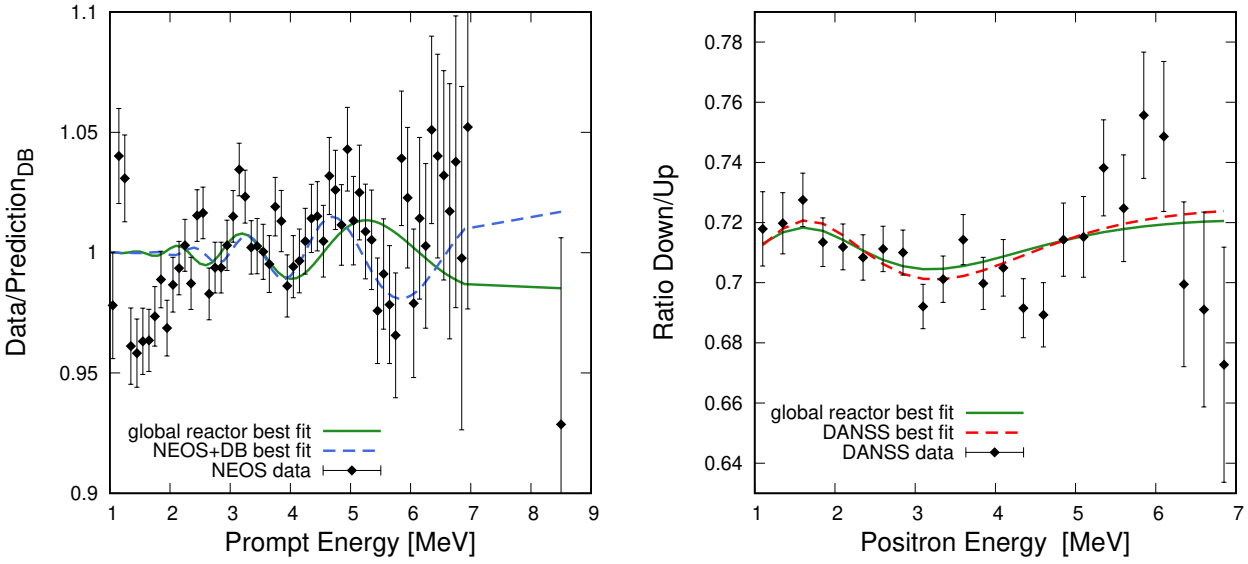


Figure 3.4.1: Observed and predicted energy spectra of the NEOS (left panel) and DANSS (right panel) experiments. DANSS data shows the ratio between the down and up detector position spectra and NEOS data the ratio between the observed spectrum and the predicted one without oscillations, based on the Daya Bay unfolded spectrum. Data are denoted with black dots and error bars, which account for the statistical uncertainties. The best fit parameters for NEOS (blue dashed) and DANSS (red dashed) are $\Delta m^2_{41} = 1.78\,\mathrm{eV}^2$, $\sin^2 = 0.013$ and $\Delta m^2_{41} = 1.32\,\mathrm{eV}^2$, $\sin^2 = 0.012$ respectively. The global best fit (green line) is at $\Delta m^2_{41} = 1.29\,\mathrm{eV}^2$, $\sin^2\theta_{14} = 0.0089$. Plots are taken from [37], error bars of the plot on the right have been corrected.

a consistent way for all the experiments. Its contribution to the total $\chi^2$-function is given in equation (3.4.5), where the complete dependence of the oscillation probability on baseline and isotopes is considered in the predictions. The penalizing term (3.4.6) is included in a consistent way, such that the pull parameters affect the flux predictions of all the experiments.

### Analyses

Given the situation of the flux predictions, two analyses of the active-to-sterile oscillation are performed, one in which the fluxes and their uncertainties are fixed to the Huber-Mueller predictions, called "flux fixed" analysis, and one in which the flux normalization from each isotope are left free and are fitted to the data together with the oscillation parameters, the "flux free" analysis. As explained in the previous section, depending on the analysis performed, the explicit form of (3.4.6) varies. In the latter case, an additional weak constraint of 20% is added to the subleading isotope flux contributions, $^{238}$U and $^{241}$Pu, in order to avoid unphysical results. Note that all the experimental data based on ratios of spectral information are flux shape and normalization independent, so that they contribute in the same way to both "flux free" and "fixed" analyses.

In SBL experiments, the oscillation probability depends on $\theta_{14}$ and $\Delta m^2_{41}$ (3.4.2), so that their contribution to the total $\chi^2$ depends as well on those parameters:

$$\chi^2_{\mathrm{SBL}}(\theta_{14}, \Delta m^2_{41})\,.$$

In the $3+1\nu$ oscillation framework, the Daya Bay oscillation probability depends on $\theta_{12}$, $\Delta m^2_{21}$, $\theta_{13}$, $\Delta m^2_{31}$, $\theta_{14}$ and $\Delta m^2_{41}$, and so does its $\chi^2$ contribution:

$$\chi^2_{\mathrm{DB}}\left(\theta_{12}, \Delta m^2_{21}, \theta_{13}, \Delta m^2_{31}, \theta_{14}, \Delta m^2_{41}\right)\,.$$

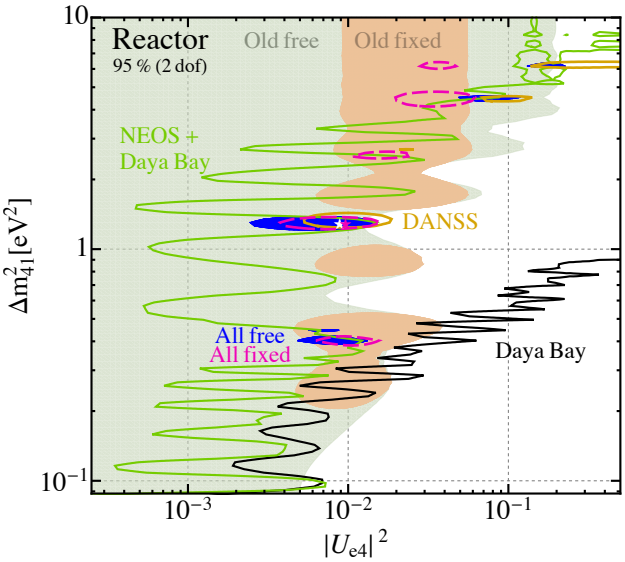


Figure 3.4.2: Allowed regions at 95% CL ($2\sigma$) in the parameter space $\Delta m^2_{41}$ vs $|U_{e4}|^2$ from different reactor data sets. The light-shaded regions correspond to the "old" data set for the flux fixed (orange) and free (green) analyses. Solid lines correspond the data based on ratios of measured spectra: Daya Bay (black), NEOS+Daya Bay (green), DANSS (brown); independent of the analysis performed. The results of the global analyses, "all" data set, are shown for the flux fixed (dashed pink) and free (shaded blue). The pink and white stars corresponds to the best fit values $\Delta m^2_{41} = 1.29\,\mathrm{eV}^2$ vs $|U_{e4}|^2 = 0.0096$ and $\Delta m^2_{41} = 1.29\,\mathrm{eV}^2$ vs $|U_{e4}|^2 = 0.0089$, for the flux fixed and free analyses. Figure taken from reference [37].

The analysis were performed scanning over the oscillation parameters $\Delta m^2_{41}$, $\theta_{14}$, fixing the solar parameters, $\theta_{12}$ and $\Delta m^2_{21}$, and the atmospheric mass squared difference, $\Delta m^2_{\mathrm{atm}}$, to their best fit values, cf. table 2.1. Finally, a marginalization over $\theta_{13}$ is performed in order to get a $\chi^2$ map depending on the two new oscillation parameters:

$$\chi^2_{\mathrm{marginalized}}(\theta_{14}, \Delta m^2_{41}) = \min_{\theta_{13}} \chi^2(\theta_{14}, \Delta m^2_{41}, \theta_{13})\,.$$

### Results

The results of both analyses, "flux fixed" and "free", are shown in figure 3.4.2, which shows the allowed regions of different data sets in the parameter space $\Delta m^2_{41}$ vs $|U_{e4}|^2$. The "old" data set, represented by the light-shaded regions, shows a preference for active-to-sterile oscillation in the "flux fixed" analysis with $|U_{e4}|^2 \simeq 0.01$, while it loses all the sensitivity to the active-to-sterile oscillation in the "flux free" analysis, i.e. it is compatible with no mixing. This is because the active-to-sterile oscillation global suppression effect (3.4.3) can be also caused by the rescaling of the flux predictions, so that for $|U_{e4}|^2 = \sin^2\theta_{14} = 0$ data can be equally fitted as when $|U_{e4}|^2 \simeq 0.01$ with an extra rescaling of the flux normalizations.

On the other hand, NEOS along with DANSS and "all" data sets favor active-to-sterile neutrino oscillations at the level of around $3\sigma$, for very similar best fit values. These results are driven by ratios of spectral data, which is independent of the flux predictions, being the best fit value dominated by the remarkable agreement between NEOS and DANSS data. In the "flux fixed" analysis there is a minor tension between the "old" data set and the new spectral information, which exclude the "old" data set preferred region. Adding this to the uncertainty on the reliability of the flux predictions, a "flux free" analysis should be considered as the representative one.

In table 3.3, the results of the "all" data set "flux free" and "fixed" analyses as well as

| Analysis | $\Delta m^2_{41}$ [eV$^2$] | $\lvert U_{e4}\rvert^2$ | $\chi^2_{\text{min}}$/dof | $\Delta\chi^2_{\text{no-osc}}$ |
|---|---|---|---|---|
| "all" data set (flux fixed) | 1.3 | 0.00964 | 196.0/(233-3) | 15.5(3.5$\sigma$) |
| "all" data set (flux free) | 1.3 | 0.00887 | 185.8/(233-5) | 11.5(2.9$\sigma$) |
| DANSS + NEOS | 1.3 | 0.00964 | 74.4/(84-2) | 13.6(3.3$\sigma$) |

Table 3.3: Results of the analyses from the "all" data set for the "flux fixed" and "flux free" analyses, and from the DANSS + NEOS data set. The best fit values for $\Delta m^2_{41}$, $|U_{e4}|^2$, $\chi^2$ and the $\Delta\chi^2$ between the no active-to-sterile oscillation hypothesis and the best fit, along with its significance assuming a $\chi^2$ distribution with 2 degrees of freedom.

the single analysis of NEOS together with DANSS are shown. The number of degrees of freedom of $\chi^2_{\text{min}}$ is given by the number of data points minus the number of free parameters of the model: two parameters $\Delta m^2_{41}$ and $\theta_{14}$ for NEOS and DANSS analysis, being $\theta_{13}$ fixed to the best fit value and being independent of the flux predictions; three parameters, the free parameter $\theta_{13}$ enters in the "flux fixed" analysis when including Daya Bay data; and finally two extra free parameters coming from the main flux contributions in the "flux free" analysis makes then five parameters. In table 3.3 it can be seen that $\chi^2_{\text{min}}/\text{dof} \simeq 1$, so that the fits have a good goodness of fit.

The result of the "all" data set analysis is mainly driven by the remarkable agreement between NEOS and DANSS, cf. figure 3.4.2. So it can be said that reactor data is compatible with a "new" reactor anomaly, which is independent of the flux predictions, than can be explained with an active-to-sterile neutrino oscillation within the $3+1\nu$ framework and the oscillation parameters $(\Delta m^2_{41}, |U_{14}|^2) \simeq (1.3\,\text{eV}^2, 0.01)$.

Coming back to the question of the model preferred by the fits to the data, "flux fixed ($\nu$)" ($H_0$) or "flux free (no $\nu$)" ($H_1$), the test statistic (3.4.7) is built using the "all" data set, from table 3.3:

$$T_{\text{all}} = \chi^2_{\text{min, free}} - \left(\chi^2_{\text{min, fixed}} + \Delta\chi^2_{\text{no-osc,fixed}}\right) = -1.3\,.$$

This result tells that the $H_1$ hypothesis is no longer favoured over $H_0$, once all the reactor data is considered, and that both hypotheses are equally compatible, even a slight preference for $H_0$ shows up, since $\chi^2_{H_0} < \chi^2_{H_1}$. This statement is just qualitative, but valid since $T_{\text{all}} = 0$ would mean that both hypothesis are equally compatible. A translation of $T_{\text{all}}$ into a $p$-value needs a full Monte Carlo study, which was not performed in this work.

**New data**

Note that in this study the data used is up to February 2018. The latest data from DANSS [169] is not included, RENO flux data [35] is not used, and neither are the STEREO [170] and PROSPECT [171] results, which are also based on a ratio of measured spectra independent of flux predictions. Their limits [170,171], depicted in figure 3.4.3 together with the allowed regions of the global analyses, already exclude the region of the "old" data set RAA, the orange shaded region in figure 3.4.2, but are still not sensitive to the new interesting region driven by NEOS and DANSS data. So it could be said that the "new" reactor anomaly independent of flux predictions, set by NEOS and DANSS experiments, is compatible with all the experiments with flux shape information. Note that in figure 3.4.3, the PROSPECT limit is shown at 90 % C.L. while the rest are shown at a 95 % C.L., not being consistently plotted, but shown for comparison and to contextualize their current sensitivity, which will increase as they collect more data. Neutrino-4 [172] results are also not included. The best fit value of their analysis is shown as a read star. This result has been very controversial because the way the analysis was performed and its best fit value is already excluded by

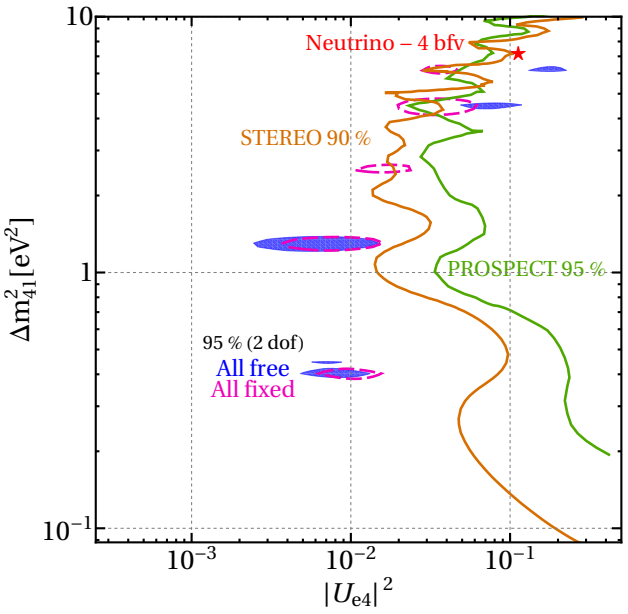


Figure 3.4.3: Limits from the STEREO (orange) and PROSPECT (green) experiments in the $\Delta m^2_{41}$ vs $\sin^2\theta_{14}$ parameter space, taken from references [170,171], along with the global reactor data allowed regions, as comparison. Neutrino-4 best fit value is also shown as a red star. Note that the allowed regions and PROSPECT limit are given at 95% CL while the STEREO is given at 90% CL.

STEREO and PROSPECT current limits, and by solar bounds, see figure 3.4.4. From the SoLid experiment [173], also designed to measure spectral information, there is still no available information.

In the near future, as more data is collected and the analyses are refined, the experiments measuring spectral information (NEOS, DANSS, STEREO, PROSPECT, Neutrino-4 and SoLid) are going to be able to test the interesting region of the parameter space preferred by NEOS and DANSS $(\Delta m^2_{41}, |U_{14}|^2) \simeq (1.3\,\text{eV}^2, 0.01)$, and say something conclusive about the RAA.

### 3.4.4 Global $\bar{\nu}_e/\nu_e$ disappearance analysis

This section is based on reference [37]. Figures and numerical results are taken from that reference.

Reactor experiments measure in the $\bar{\nu}_e$ disappearance channel. As long as CPT is a good symmetry of nature, experiments measuring in the $\nu_e$ disappearance channel are sensitive to the same oscillation parameters. Then it makes sense to combine all those experiments and check in a consistent way if the RAA explanation in terms of an active-to-sterile oscillation is compatible with existing bounds and the Gallium anomaly.

#### Experiments

In [37], on top of the reactor experiments listed in table 3.2, solar, atmospheric, $\nu_e$ scattering on carbon and radioactive source experiments are used in the global $\overset{(-)}{\nu}_e$ disappearance study.

The solar experiments Chlorine [174], GALLEX and GNO [135], SAGE [136], Super-Kamiokande (solar) [137, 154, 155, 157], SNO [175–177] and Borexino [139, 156, 178] were used. The explicit dependence of their oscillation probability can be found in appendix C

or reference [167]. This experiments set a bound on $|U_{e4}|^2$, which depends on how well the normalization of the solar neutrino flux is known.

The intense radioactive source measurements in the Gallium solar experiments GALLEX [135, 179] and SAGE [180, 181] are also included. These measurements where done during the calibration of these experiments introducing intense radioactive sources, $^{37}$Ar and $^{51}$Cr, inside the detectors. The measurements done during the calibration observed a deficit of $\nu_e$ with respect to the expectations, setting the Gallium anomaly. This deficit can be explained by the hypothesis of the $\nu_e$ disappearance due to active-to-sterile neutrino oscillations, with a new frequency set by a new mass squared difference of $\sim 1\,\mathrm{eV}^2$. This supports the active-to-sterile neutrino oscillation explanation of the RAA in a totally independent way, since the production of the $\nu_e$ flux has a different origin than the $\bar{\nu}_e$ flux produced in nuclear power plants. Since the $\nu_e$ source is inside the detector, the experiments measure $\nu_e$ disappearance at a very short baseline, so that the oscillation probability is given by (3.4.2).

The $^{12}$C experiments LSND [182, 183] and KARMEN [183–185] measured $\nu_e$ from the decay at rest of $\mu^+$. They are beam dump experiments that produce a stream of particles colliding protons into a wall. Among the out-coming particles, there are charged pions which decay into leptons $\pi^+ \to \mu^+ \nu_\mu$. The decay of negative particles is suppressed by the high probability of nuclear capture. The muons produced in pion decays are then stopped and subsequently decay at rest $\mu^+ \to e^+ \nu_e \bar{\nu}_\mu$, producing a flux of $\nu_e$. The $\nu_e$ are detected by the scattering onto $^{12}$C, $\nu_e\, ^{12}C \to e^-\, ^{12}N$, producing an electron signal. Then, the Nitrogen decays back, $N^{12} \to ^{12} C\, e^+ \nu_e$, producing a positron delayed signal, which allows for precise identification of the signal events and background rejection. These experiments did not find a discrepancy between the measured numbers of events and the expectations, so they set bounds on the active-to-sterile oscillation parameters. Since the muons are stopped very close to the detector, the experiments operate at a short baseline, so for a $3+1\nu$ analysis the oscillation probability is given by the appearance probability (3.4.1).

In [37], also the atmospheric experiments Super-Kamiokande, IceCube and DeepCore are included, which set a bound in the $\Delta m^2_{41}$ vs $\theta_{14}$ parameter space. In reference [186] the impact of a sterile neutrino on low-energy atmospheric data is studied.

### Analysis

In the global reactor data analysis, it was checked that the $\theta_{13}$ measurement is very well determined by Daya Bay measurement and that its best fit does not depend on the introduction of an active-to-sterile neutrino oscillation, so then the $\chi^2$ contribution of all the experiments depends on 6 parameters, see [37]:

$$\chi^2_{\overset{(-)}{\nu}_e,\,\mathrm{disapp}}(\Delta m^2_{31}, \Delta m^2_{41}, \theta_{12}, \theta_{14}, \theta_{24}, \theta_{34})\,. \tag{3.4.8}$$

When combining with reactor data under the "flux free" assumption, the two extra free parameters coming from the two main contributions of the $\bar{\nu}_e$ reactor flux add up to 8 free parameters, cf. table 3.4. A marginalization over all the parameters but $\Delta m^2_{41}$ and $\theta_{14}$ gives the $\chi^2$ allowed regions shown in figure 3.4.4.

### Results

In figure 3.4.4, it can be seen how the "flux free" analysis of the reactor data, which is taken as the representative one, is compatible with bounds from solar, atmospheric and $\nu_e$ scattering on $^{12}$C data. There is a minor tension between the preferred region by the radioactive source data that set the Gallium anomaly, denoted by the yellow region, and the global data allowed regions, which are driven by the reactor data. This tension can

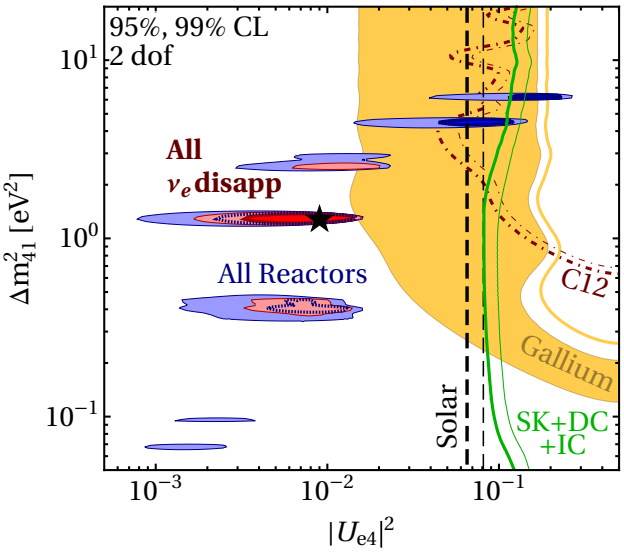


Figure 3.4.4: Allowed regions and limits in the parameter space $\Delta m^2_{41}$ vs $|U_{e4}|^2$, minimizing over the rest, at 90 and 95% CL ($2\sigma$) from different $\nu_e/\bar{\nu}_e$ appearance data sets: flux free global reactor analysis (blue), gallium anomaly (yellow), solar bounds (dashed black), $^{12}$C limits (dashed brown), atmospheric limits (green), and the combination of all (red). Figure taken from reference [37].

| Analysis | $\Delta m^2_{41}$ [eV$^2$] | $\lvert U_{e4}\rvert^2$ | $\chi^2_{\text{min}}$/dof | $\Delta\chi^2_{\text{no-osc}}$ |
|---|---|---|---|---|
| $\overset{(-)}{\nu}_e$ disappearance (flux free) | 1.3 | 0.00901 | 542.9/(594-8) | 13.4($3.2\sigma$) |

Table 3.4: Results of the analyses from the whole $\nu_e/\bar{\nu}_e$ disappearance data set: the best fit values for $\Delta m^2_{41}$, $|U_{e4}|^2$, $\chi^2$ and the $\Delta\chi^2$ between the no active-to-sterile oscillation hypothesis and the best fit, along with its significance assuming a $\chi^2$ distribution with 2 degrees of freedom.

be quantified performing a parameter goodness of fit test statistic, explained below in this section. Since the best fit value of the combined fit, reactor and radioactive source experiments, lies in a region excluded by the solar and $\nu_e$ scattering on $^{12}$C experiments, the PG test is computed comparing the $\chi^2_{\text{min,reactors}}$ and $\chi^2_{\text{min,radioactive}}$, with the global $\chi^2_{\text{min},\overset{(-)}{\nu}_e}$ and it is found that the tension between the reactor and radioactive source data, at the global best fit value, is given by $\Delta\chi^2_{\text{PG}} = 7.2$, translating into a $p$-value of 2.8%. This indicates some tension between the two data sets, but minor. Here "flux free" hypothesis for the reactor data analysis was considered. Recently, it has been pointed out that the predictions in the radioactive source experiments might be over estimated, being the revisited allowed parameter space compatible with the preferred region by reactor experiments [187].

In table 3.4, the best fit value of the global $\overset{(-)}{\nu}_e$ disappearance data set analysis is given, leaving the reactor flux free, shown also as a black star in figure 3.4.4. Despite the small tension, the significance of rejecting the no active-to-sterile oscillation hypothesis is disfavoured at the level of $3.2\sigma$, two more units in $\Delta\chi^2$ with respect to the global reactor analysis.

### Summary

The global $\overset{(-)}{\nu}_e$ disappearance data favours the active-to-sterile oscillation hypothesis at the level of $3\sigma$ with respect to the no oscillation hypothesis, i.e. $|U_{e4}|^2 = 0$. This result is mainly driven by the reactor data as can be seen comparing the results from reactor data alone, cf.

table 3.3, with the global $\overset{(-)}{\nu}_e$ disappearance results, cf. table 3.4.

**Parameter goodness of fit test statistic**

The parameter goodness of fit (PG) test statistic [188] quantifies the compatibility of statistically independent sub-sets of data $A$ and $B$ of a data set $C$. $A, B \subset C$. The quantity

$$\chi^2_{\rm PG} \equiv \chi^2_{{\rm min},C} - \chi^2_{{\rm min},A} - \chi^2_{{\rm min},B} = \Delta\chi^2_A + \Delta\chi^2_B \,, \tag{3.4.9}$$

where $\chi^2_{{\rm min},X}$ are the minimum $\chi^2$ value of the data set $X$, measures by how much the fit gets worse when the two data sets are combined. If $\chi^2_{A,B,C}$ depend on $P_A$, $P_B$ and $P_C$ free parameters ($P_A, P_B \leq P_C$), respectively, it was shown in reference [188] that $\chi^2_{\rm PG}$ follows a $\chi^2$ distribution with $N_{\rm PG} \equiv P_A + P_B - P_C$ degrees of freedom. $N_{\rm PG}$ accounts for the "join" free parameters of the sub-sets $A$ and $B$. Then the $p$-value can be computed as

$$p = \int_{\chi^2_{\rm PG}}^{\infty} {\rm d}x \, f_{\chi^2}(x; N_{\rm PG}) \,,$$

where $f_{\chi^2}(x; {\rm N_{PG}})$ is the probability density function of a $\chi^2$ distribution with $N_{\rm PG}$ degrees of freedom.

### 3.4.5 Global picture and tensions

This section is based on reference [37]. Figures and numerical results are taken from that reference.

In order to perform a complete analysis of the active-to-sterile oscillation, other oscillation channels have to be investigated: $\overset{(-)}{\nu}_\mu$ disappearance and $\overset{(-)}{\nu}_\mu \to \overset{(-)}{\nu}_e$ appearance channels. In the $\overset{(-)}{\nu}_\mu \to \overset{(-)}{\nu}_e$ appearance data, there is an allowed region in the parameter space $\Delta m^2_{41}$ vs $|U_{\mu 4}U_{e4}|^2$, which is driven by LSND [29] and MiniBooNE [38, 189] $\overset{(-)}{\nu}_e$ excesses, compatible with the bounds set by the other experiments measuring in the same appearance channel, cf. left panel of figure 3.4.5; while from the $\overset{(-)}{\nu}_\mu$ disappearance global data, only bounds on the mixing parameter $|U_{\mu 4}|^2$ are obtained, cf. right panel of figure 3.4.5.

**Appearance data**

In [37], a combined fit of the experiments measuring in the $\overset{(-)}{\nu}_\mu \to \overset{(-)}{\nu}_e$ appearance channel was performed: LSND [29], MiniBooNE [38, 189], KARMEN [190], NOMAD [191], E776 [192], ICARUS [193, 194] and OPERA [195].

LSND and KARMEN experiments measured oscillations of $\bar{\nu}_\mu$, produced in muon decays at rest $\mu^+ \to e^+ \nu_e \bar{\nu}_\mu$, into $\bar{\nu}_e$. The detectors were located at an averaged distance of 30 and 17.7 m from the beam stop neutrino source. LSND also has a contribution to the $\bar{\nu}_\mu$ flux from pions decaying in flight. The MiniBooNE experiment measures an anomalous $\overset{(-)}{\nu}_e$ appearance from $\overset{(-)}{\nu}_\mu$ produced at the Booster neutrino beam at Fermilab, after a flight of 540 m. The NOMAD experiment measured neutrinos from the SPS wide-band neutrino beam at CERN, consisting predominantly of $\nu_\mu$, produced in pion an kaon decays, which are originated in the collision of high energy (450 GeV) protons into a beryllium target. The detector was located at an average distance of 620 m from the source. The E776 experiment, with a baseline of 1 Km, measured $\nu_\mu$ from a high energy beam at Brookhaven. E776 was fitted together with solar data in order to constrain the $\overset{(-)}{\nu}_e$ background. The ICARUS and

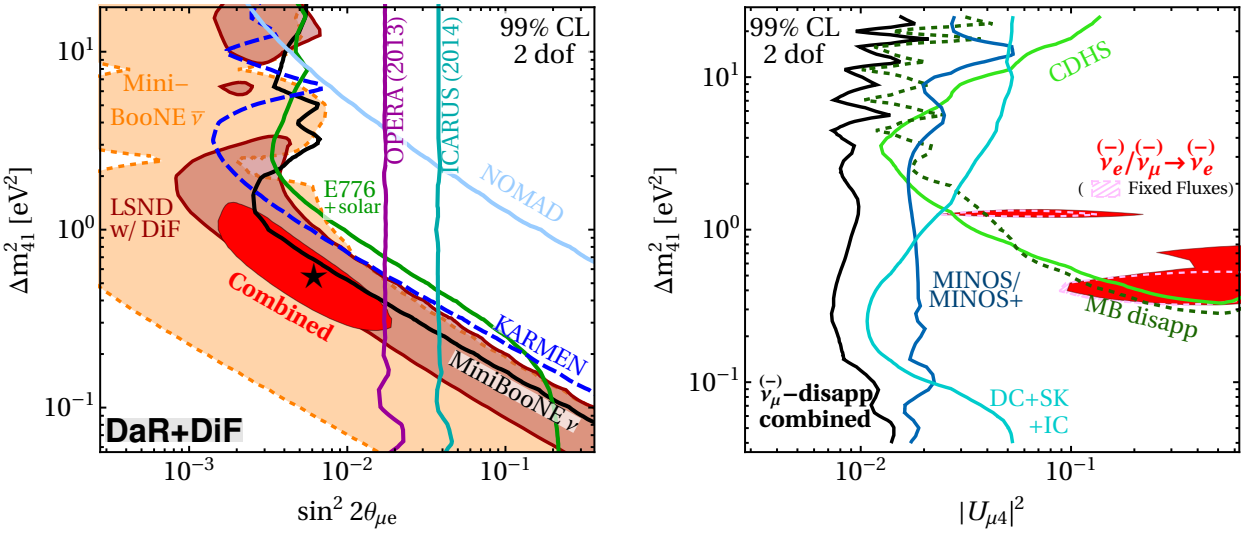


Figure 3.4.5: $\nu_e/\bar{\nu}_e$ appearance (left panel) and $\nu_\mu/\bar{\nu}_\mu$ disappearance (right panel) combined analyses. Left: Allowed regions on the parameter space $\Delta m^2_{41}$ vs $\sin^2 2\theta_{\mu e}$ set by the LNSD and MiniBooNE anomalous $\bar{\nu}_\mu \to \bar{\nu}_e$ appearance, together with the constraints set by the null results on the active-to-sterile oscillation searches by KARMEN, NOMAD, E776+solar, ICARUS and OPERA experiments. Right: constraints from $\nu_\mu/\bar{\nu}_\mu$ disappearance data in the parameter space $\Delta m^2_{41}$ vs $|U_{\mu 4}|^2$. Constraints from IceCube (IC), DeepCore (DC), Super-Kamiokande (SK), NO$\nu$A, MINOS and MINOS+, CDHS and MiniBooNE are shown. In black it is shown the combined limit. The red shaded region is the projected allowed parameter region from the combined $\nu_e/\bar{\nu}_e$ appearance and disappearance data. Figures are taken from reference [37].

OPERA experiments searched for $\nu_e$ appearance from the high energy $\nu_\mu$ flux of the CNGS beam at CERN. $\nu_\mu$ are produced in pions and kaons decays originated in collisions of high energy protons (400 GeV) into a graphite target. The detectors were located at 730 Km from the source, at the Gran Sasso Laboratory.

When studying this data within a $3+1\nu$ oscillation framework, the appearance oscillation probability in the SBL given in (3.4.1) is used, which depends on the oscillation frequency $\Delta m^2_{41}$ and the effective mixing angle $|U_{e4}U_{\mu 4}|^2 \equiv \sin^2 2\theta_{\mu e}$. For ICARUS and OPERA, which have longer baselines than the rest of the experiments, the oscillation probability depends on more oscillation parameters. However the extra parameters do not play a role neither for the global nor for the appearance best fit points.

Of all these experiments, only LNSD and MiniBooNE[18] data present an excess in the $\bar{\nu}_\mu \to \bar{\nu}_e$ channel with respect to the SM expectations. The rest have found no evidence for an anomalous $\overset{(-)}{\nu}_e$ appearance, setting strong bounds in the parameter space $\Delta m^2_{41}$ vs $\sin^2 2\theta_{\mu e}$. In the right panel of figure 3.4.5 the combined analysis is shown. The red shaded region shows the preferred region, compatible with all the constraints, which is driven by LSND and MiniBooNE anomalous appearance data.

The preferred new mass square difference is of the order of the one that explains the RAA, but the value of the effective mixing parameter $\sin^2\theta_{\mu e}$ is in contradiction with the limits set by the $\overset{(-)}{\nu}_e$ and $\overset{(-)}{\nu}_\mu$ disappearance limits. We discuss this below.

[18]Recently MiniBooNE has reported a new excess in the $\nu_\mu \to \nu_e$ channel [39] after [37] was done.

**Disappearance data**

In [37], a combined fit of the experiments measuring in the $\overset{(-)}{\nu}_\mu \to \overset{(-)}{\nu}_\mu$ disappearance channel was performed: IceCube [196–198], DeepCore [145, 146], Super-Kamiokande (atmospheric) [199,200], NO$\nu$A [201], MINOS and MINOS+ [202], CDHS [203] and MiniBooNE [204–206].

The IceCube experiment is a neutrino telescope based at the South Pole. It measures neutrinos coming from space and atmospheric neutrinos as a function of the zenith angle of incidence and energy. In the search of $\bar{\nu}_\mu$ appearance, given the energy range, from 320 GeV to 20 TeV, and distances traveled through matter, the MSW resonance effect has a huge impact on the oscillation probability. DeepCore is a sub-detector based in the inner part of the IceCube detector, which is more compact and thus can measure lower energy neutrinos, of tens of GeV. Super-Kamiokande, is a tank of water based in the Kamioka mine under the Japanese Alps mountains, it also measures low energy atmospheric neutrinos as DeepCore. NO$\nu$A measures neutrinos with energies 1-10 GeV from the NuMI beam in Fermilab at a baseline of 810 Km. It searches for the mixing of a light new massive eigenstate with the flavor neutrinos from a reduction of the expected NC interactions. MINOS and its upgrade MINOS+ measure $\nu_\mu$ neutrinos from the NuMI beam in Fermilab. They consist of two detector located at 1.04 Km and 735 Km from the source, being sensitive to a wide range of oscillation frequencies. Given the energy range of the neutrino beam, 1-10 GeV, and baselines, for $\Delta m^2_{41} \sim 10^{-3} - 10^{-1}\,\text{eV}^2$ oscillations are expected only in the far detector. Increasing $\Delta m^2_{41}$, the oscillations would start averaging out in the far detector and showing up in the near detector. For $\Delta m^2_{41} \sim 1 - 100\,\text{eV}^2$ oscillations are expected at the near detector. They search for active-to-sterile oscillations through CC and NC neutrino interactions. CDHS was a short baseline experiment measuring $\nu_\mu$ from a neutrino beam produced by a proton beam from the CERN Proton Synchrotron, it consist of two detectors located at 130 and 885 m from the source. CDHS searched for $\nu_\mu$ oscillations comparing the CC neutrino interaction rates at the two detectors. The MiniBooNE experiment, apart from the anomalous appearance searches, also performed searches in the $\overset{(-)}{\nu}_\mu$ disappearance channel.

NC interactions are of high importance in the search of active-to-sterile mixing, since they are sensitive to the mixing of a fourth neutrino mass eigenstate with any of the flavor neutrinos.

Except for the SBL experiments, CDHS and MiniBooNE, matter effects have to be taken into account in the oscillation probability, specially in the atmospheric experiments, IceCube, DeepCore and Super-Kamiokande, since, depending on the zenith angle of incidence, neutrinos can travel for long distances through the Earth. The oscillation probability depends mainly on 6 free paraemters $\Delta m^2_{31}, \Delta m^2_{41}, \theta_{12}, \theta_{14}, \theta_{24}, \theta_{34}$ and so does their $\chi^2$-function. In order to get the $\chi^2$ profile in the $\Delta m^2_{41}$ vs $|U_{\mu 4}|$ plane, a marginalization over the rest of the parameters has to be performed.

None of these experiments found evidence for active-to-sterile oscillations, so that they set limits on the new mass squared difference and mixing, plotted in the right panel of figure 3.4.5. The combined limit is plotted in black, which sets a strong bound $|U_{\mu 4}|^2 < 0.01$ for the whole interesting range of $\Delta m^2_{41}$.

For comparison, in figure 3.4.5 the allowed region of the combined $\overset{(-)}{\nu}_e$ appearance and disappearance data is plotted, for the "flux fixed" and "free" analyses of the reactor anti-neutrino data. This region is obtained embedding the appearance $\chi^2$ contribution into the three parameter space:

$$\chi^2_{\overset{(-)}{\nu}_\mu,\text{app}}\left(|U_{e4}U_{\mu 4}|^2, \Delta m^2_{41}\right) \longrightarrow \chi^2_{\overset{(-)}{\nu}_\mu,\text{app}}\left(|U_{e4}|^2, |U_{\mu 4}|^2, \Delta m^2_{41}\right) .$$

So that the total $\chi^2$ function is given adding the disappearance and appearance contribu-

tions:

$$\chi^2_{\overset{(-)}{\nu}_\mu,\text{app/dis}}\left(|U_{e4}|^2,|U_{\mu4}|^2,\Delta m^2_{41}\right)=\chi^2_{\overset{(-)}{\nu}_\mu,\text{dis}}\left(|U_{e4}|^2,\Delta m^2_{41}\right)+\chi^2_{\overset{(-)}{\nu}_\mu,\text{app}}\left(|U_{e4}|^2,|U_{\mu4}|^2,\Delta m^2_{41}\right).$$

Finally a marginalization over $|U_{e4}|$ gives the $\chi^2$ profile over the parameter space $\Delta m^2_{41}$ vs $|U_{\mu4}|^2$.

**Tension**

The oscillation probabilities for the three above mentioned channels in the SBL regime can be written in terms of effective mixings as follows:

$$\begin{aligned}
P_{\overset{(-)}{\nu}_e\to\overset{(-)}{\nu}_e}&=1-\sin^2 2\theta_{ee}\sin^2\left(\frac{\Delta m^2_{41}E}{4L}\right)\\
P_{\overset{(-)}{\nu}_\mu\to\overset{(-)}{\nu}_\mu}&=1-\sin^2 2\theta_{\mu\mu}\sin^2\left(\frac{\Delta m^2_{41}E}{4L}\right)\\
P_{\overset{(-)}{\nu}_\mu\to\overset{(-)}{\nu}_e}&=\sin^2 2\theta_{e\mu}\sin^2\left(\frac{\Delta m^2_{41}E}{4L}\right),
\end{aligned}$$

where $\sin^2 2\theta_{ee}\equiv 4|U_{e4}|^2\left(1-|U_{e4}|^2\right)$, $\sin^2 2\theta_{\mu\mu}\equiv 4|U_{\mu4}|^2\left(1-|U_{\mu4}|^2\right)$ and $\sin^2 2\theta_{e\mu}\equiv 4|U_{e4}U_{\mu4}|^2$. Then in the approximation of small mixings it follows that:

$$\sin^2 2\theta_{e\mu}\simeq\frac{1}{4}\sin^2 2\theta_{ee}\sin^2 2\theta_{\mu\mu}\,. \tag{3.4.10}$$

This equation shows how a lack of evidence for active-to-sterile oscillation in any of the disappearance channels is going to suppress the effective mixing in the appearance channel. Then, since no signal in favor of active-to-sterile oscillation is found in the $\overset{(-)}{\nu}_\mu$ disappearance data, the limits from the whole $\overset{(-)}{\nu}_e/\overset{(-)}{\nu}_\mu$ disappearance data set on the effective mixing $\sin^2 2\theta_{e\mu}$ are very stringent, as can be seen in figure 3.4.6. In order to project the $\overset{(-)}{\nu}_e/\overset{(-)}{\nu}_\mu$ disappearance limits onto the $\Delta m^2_{41}$ vs $\sin^2 2\theta_{e\mu}$ plane, first the contributions from each channel are combined

$$\chi^2_{\text{dis}}(|U_{e4}|,|U_{\mu4}|,\Delta m^2_{41})=\chi^2_{\overset{(-)}{\nu}_e,\text{dis}}(|U_{e4}|,\Delta m^2_{41})+\chi^2_{\overset{(-)}{\nu}_\mu,\text{dis}}(|U_{\mu4}|,\Delta m^2_{41}),$$

and then the projection over $\sin^2 2\theta_{e\mu}$ is performed minimizing $\chi^2_{\text{dis}}$ keeping the product $|U_{e4}||U_{\mu4}|$ constant.

This disappearance/appearance tension is quantified performing a PG test, explained at the end of the previous section, dividing the global data into two subsets: appearance and disappearance, cf. reference [37]. In table 3.5, the results of the PG test for two different global data sets are shown: global data and global without reactor data. For the complete set of active-to-sterile oscillation data, appearance and disappearance data are incompatible at the level of $5\sigma$. Being sceptical about the RAA, it was proven that removing the reactor data from the disappearance data set does not alleviate the tension, which remains at the level of $4\sigma$. In the latter case, the bounds on $|U_{e4}|^2$ from solar and atmospheric experiments, cf. figure 3.4.4, together with the bounds on $|U_{\mu4}|^2$, cf. right panel in figure 3.4.5, are sufficient to have a large suppression in their product $|U_{e4}U_{\mu4}|^2$, so that the tension between the two data sets is strong.

In [37], it was shown that the tension is independent of any particular constraint in the $\overset{(-)}{\nu}_\mu$ disappearance channel, neither on the MiniBooNE and gallium data sets. This was done removing these particular data sets one by one and computing the PG test. Only when

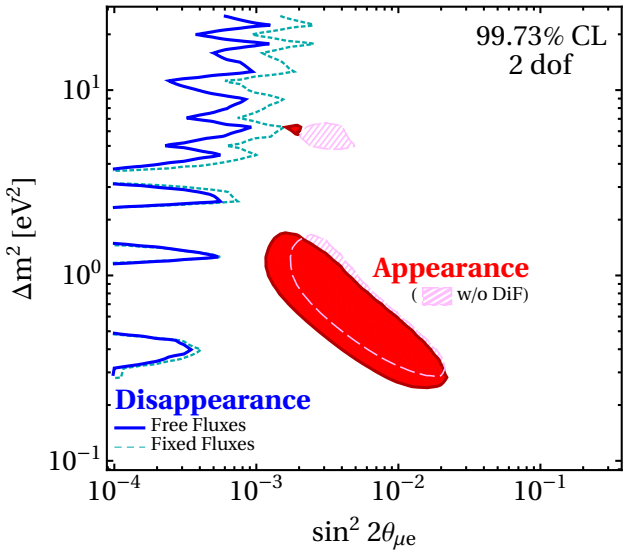


Figure 3.4.6: Allowed region (red) by the appearance data set together with the projected limits (blue) from the disappearance data set in the parameter space $\Delta m^2_{41}$ vs $\sin^2 2\theta_{e\mu}$ plane, at the 99.73% CL for 2 dof. The pink region is obtained by not including the LSND decay in flight data set into the appearance data. The dark blue and light blue limits correspond to the "flux free" and "fixed" reactor analysis. Figure taken from reference [37].

| Analysis | $\chi^2_{\rm PG}$/dof | $p$-value |
|---|---|---|
| Global | 29.6/2 | $3.7 \times 10^{-7} (5.1\sigma)$ |
| Without reactors | 20.3/2 | $3.9 \times 10^{-5} (4.1\sigma)$ |

Table 3.5: Results of the PG test, comparing appearance and disappearance data, for the global data set and the global data set without reactor data, together with its $p$-value and significance.

removing the LSND data from the appearance data set, the tension decreases, being the tension at the level of $3\sigma$ ($p$-value $= 1.6 \times 10^{-30}$). Note however that the latest MiniBooNE results, reported in [39], were not included in these analyses. From a qualitative point of view, it is clear that they would make the tension even stronger, since the new MiniBooNE excess data would favor the allowed region from the $\overset{(-)}{\nu}_\mu \to \overset{(-)}{\nu}_e$ data. Then, it is expected that the PG test performed in [37] removing the LSND data would give a strong disagreement, even when removing the LSND data set.

Given the incompatibility between the appearance and disappearance data sets, it does not make sense to considered LSND and MiniBooNE data within an active-to-sterile oscillation framework and alternative explanations for those anomalies have to be pursued. In chapter 4, an alternative explanation [40] for the latest MiniBooNE excess [39], is studied.

### $3 + 2\nu$ oscillation framework

The study described above is done within a $3 + 1\nu$ framework. Driven by the appearance/disappearance tension, there is room for questioning if a $3 + 2\nu$ framework would alleviate the tension. In this framework, another massive eigenstate is considered, so that there is more than one new oscillation frequency. It could happen that one frequency explains the RAA and another one the anomalous $\overset{(-)}{\nu}_e$ appearance.

In reference [167], a $3 + 2\nu$ oscillation framework is considered and it is found that this

framework does not help to get a better fit to the data. Moreover, it does not help to solve the tension, since the suppression on the effective mixings driving the appearance channel is going to be suppressed in an analogous way as it was described in (3.4.10) by the strong constrains on the effective mixings driving the $\overset{(-)}{\nu}_\mu$ disappearance oscillations.

In a $3+2\nu$ oscillation framework, the disappearance oscillation probabilities in the SBL and LBL regimes are given by [167]:

$$\begin{aligned} P^{\text{SBL},3+2\nu}_{\overset{(-)}{\nu}_\alpha \to \overset{(-)}{\nu}_\alpha} &= 1 - 4\left(1 - \sum_{i=4,5} |U_{\alpha i}|^2\right) \sum_{i=4,5} |U_{\alpha i}|^2 \sin^2\left(\frac{\Delta m^2_{i1} L}{4E}\right) \\ &\quad -4|U_{\alpha 4}U_{\alpha 5}|^2 \sin^2\left(\frac{\Delta m^2_{54} L}{4E}\right) \end{aligned} \tag{3.4.11}$$

$$\begin{aligned} P^{\text{LBL},3+2\nu}_{\overset{(-)}{\nu}_\alpha \to \overset{(-)}{\nu}_\alpha} &= \left(1 - \sum_{i=3}^{5} |U_{\alpha i}|^2\right)^2 + \sum_{i=3}^{5} |U_{\alpha i}|^4 \\ &\quad +2\left(1 - \sum_{i=3}^{5} |U_{\alpha i}|^2\right) |U_{\alpha 3}|^2 \cos\left(2\frac{\Delta m^2_{31} L}{4E}\right) \end{aligned} \tag{3.4.12}$$

where in the long baseline regime, the frequencies driven by $\Delta m^2_{4i}$ and $\Delta m^2_{5i}$ are considered to be infinite and the oscillation driven by the solar frequency to be averaged out.

In this framework, the SBL regime appearance oscillation is given by [167]:

$$\begin{aligned} P^{\text{SBL},3+2\nu}_{\overset{(-)}{\nu}_\alpha \to \overset{(-)}{\nu}_\beta} &= 4|U_{\alpha 4}|^2|U_{\beta 4}|^2 \sin^2\left(\frac{\Delta m^2_{41} L}{4E}\right) + 4|U_{\alpha 5}|^2|U_{\beta 5}|^2 \sin^2\left(\frac{\Delta m^2_{51} L}{4E}\right) \\ &\quad +8|U_{\alpha 4}U_{\beta 4}U_{\alpha 5}U_{\beta 5}| \sin\left(\frac{\Delta m^2_{41} L}{4E}\right) \sin\left(\frac{\Delta m^2_{51} L}{4E}\right) \\ &\quad \times \cos\left(\frac{\Delta m^2_{54} L}{4E} - \arg\left\{U^*_{\alpha 4}U_{\alpha 5}U_{\beta 4}U^*_{\beta 5}\right\}\right) \end{aligned} \tag{3.4.13}$$

Expressions (3.4.11) and (3.4.12) show that a null disappearance observed in the $\overset{(-)}{\nu}_\mu$ disappearance channel indicates that both $|U_{\mu 4}|^2$ and $|U_{\mu 5}|^2$ are negligible, suppressing the appearance oscillation probability (3.4.13) quadratically. So the tension would still persist in this scenario.

# Chapter 4

# An alternative MiniBooNE explanation

This chapter is based on the study and results from reference [40]. Numerical results and some of the figures are taken from that reference.

The MiniBooNE experiment, based at Fermilab, was designed to test the LSND anomalous $\nu_e$ appearance [29]. A beam of protons with an energy up to 8 GeV are dumped into a beryllium target, producing a stream of secondary particles that subsequently decay into light neutrinos along a 50 m long decay pipe, resulting in a neutrino beam that travels another 500 m through the Earth before reaching the detector. In the detector, the $\nu_e$ and $\bar{\nu}_e$ interact with the medium via a CCQE scattering producing an electron or positron that emits a shower of radiation that is measured in the photomultipliers.

In summer 2018, the MiniBooNE collaboration reported an excess of $\nu_e$ appearance events of $381.2 \pm 85.2$ over the SM predictions [39], which combined with a previous measured excess of $\bar{\nu}_e$ appearance, adds up to a total excess of $460.5 \pm 95.8$ events, which translates into a $4.8\sigma$ deviation with respect to the SM predictions. This supports the LSND anomaly with a significance of the combined excess of $6.0\sigma$.

The excess of events was interpreted as a $\overset{(-)}{\nu}_e$ appearance due to neutrino oscillations in the $\overset{(-)}{\nu}_\mu \to \overset{(-)}{\nu}_e$ channel [39]. In order to comply with the standard $3\nu$ oscillation measured parameters, the excess has to be caused by a new active-to-sterile oscillation. As it was explained in section 3.4.5, this interpretation is not consistent with many bounds set by null active-to-sterile oscillation searches in the $\overset{(-)}{\nu}_\mu$ disappearance channel at the level of $4 - 5\sigma$, and this tension is robust regardless of any particular constraint. This makes clear that the excess can not be interpreted as an active-to-sterile oscillation within a $3 + 1\nu$ oscillation framework and alternative explanations have to be studied.

The electron like signal measured at MiniBooNE can be mimicked by the signal produced by a photon or a collimated electron-positron pair. Based on that, recent models have been proposed in which a heavy neutrino, produced by $\nu_\mu$ scattering with nuclei inside the detector, decays into a photon [207, 208] or an electron-positron pair [209, 210]. Different models are studied in [211,212], in which heavy neutrinos are produced and decay radiatively. Recently it has been proposed in [213,214] that the excess can be caused by a fourth heavy neutrino decaying into a light electron neutrino and light boson. See also [215].

In this work, an alternative explanation based on a decay of a heavy neutrino, of around 250 MeV, into a photon and a light neutrino is proposed as the cause of the excess [40]. Note that the model here presented can not explain the LSND excess, since the heavy neutrino

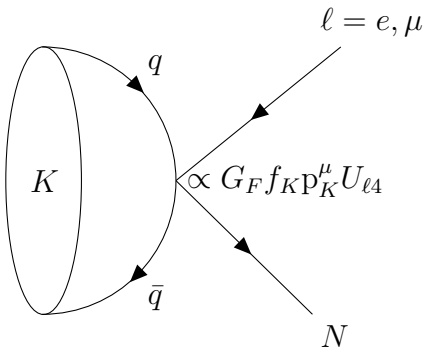


Figure 4.1.1: Effective kaon decay into a heavy neutrino $N$ and an electron or muon.

is too heavy to be produced at LSND[1]. The decay of a lighter neutrino give a too much forward peaked signal, inconsistent with MiniBooNE data [216].

The heavy neutrino is produced in Kaon decays via mixing with the charged leptons, $|U_{4\ell}|$. It travels through the Earth as the light neutrinos do and decays into the detector via an effective interaction mediated by new unknown physics. The emitted high energy photon interacts inside the detector producing an electromagnetic shower mimicking the electron like signal. The heavy neutrinos in general travel more slowly towards the detector than the light neutrinos, so that some of them will decay outside the time window in which the light neutrinos are expected to reach the detector. This timing signal can be the ultimate proof of this model or can rule it out, and any other model in which a heavy particle is produced at the proton beam-target interaction.

This chapter is organized as follows: In section 4.1 the heavy neutrino production and decay mechanisms are described. In section 4.2 we compute the predictions of the model: total number of signal events, energy and angular spectra and the time distribution of the signal events. The data analysis is done in section 4.3. In section 4.4 the results of the analysis are presented as well as the constraints from other searches. Finally in section 4.5 the conclusions and further searches are summarized.

## 4.1 Effective model

A Dirac heavy neutrino with mass at around 250 MeV is introduced. It is produced, after the proton beam is dumped into the target, in kaon decays, via a mixing with the charged leptons through the effective operator:

$$\mathcal{O}_{K\ell N} = G_F f_K \mathrm{p}_K^\mu U_{\ell 4} \bar{\ell} \gamma_\mu P_L N \,, \tag{4.1.1}$$

where $f_K$ is the kaon decay constant, $\mathrm{p}_K$ the kaon four-momentum, $G_F$ the Fermi constant, $P_L \equiv (\mathbb{1} - \gamma_5)/2$ is the left-handed projection operator and $U_{\ell 4}$ the mixing matrix element between the heavy neutrino $N$ and the charged lepton[2] $\ell = e, \mu$; depicted in figure 4.1.1. Then the heavy neutrino travels towards the detector and there decays into a photon and a

[1]The neutrino flux in LSND is produced in $\pi^+$ decays, so that $m_N < m_\pi$.

[2]The accompanying charged lepton can not be a tau, since its mass is larger than the kaon mass.

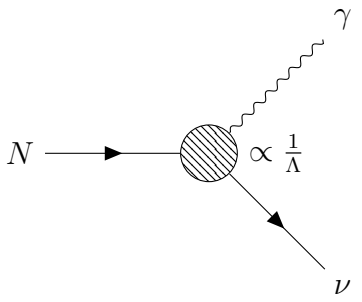


Figure 4.1.2: Effective $\mathcal{O}_{N\gamma\nu}$ operator (4.1.2) that mediates the heavy neutrino $N$ decay into a photon and a light neutrino.

light neutrino via its magnetic moment, $N \to \gamma\nu$, through the effective operator[3]:

$$\mathcal{O}_{N\gamma\nu} = \frac{1}{\Lambda}\bar{N}\sigma^{\alpha\beta}\nu_L F_{\alpha\beta}\,, \tag{4.1.2}$$

where $\nu_L$ is a light neutrino, $F_{\mu\nu} = \partial_\mu A_\nu - \partial_\nu A_\mu$ is the electromagnetic field strength tensor, $\sigma^{\mu\nu} = \frac{i}{2}(\gamma^\mu\gamma^\nu - \gamma^\nu\gamma^\mu)$ is an anti-symmetric tensor, and $\Lambda$ is an unknown energy scale. The Feynman diagram is depicted in figure 4.1.2. The operator (4.1.2) is not $SU_{\rm L}(2)$ gauge invariant, so it must be originated after the EWSB from a dimension-6 operator, so that $1/\Lambda \equiv v/\Lambda'^2$, where $v$ is the Higgs v.e.v.

The differential decay width in the laboratory frame, neglecting the light neutrino mass, is given by:

$$\mathrm{d}\Gamma^{\rm lab}_{N\to\nu\gamma} = \frac{1}{2E_N}|\mathcal{M}|^2(2\pi)^4\delta^4(\mathrm{p}_N - \mathrm{p}_\gamma - \mathrm{p}_\nu)\frac{\mathrm{d}^3p_\gamma}{(2\pi)^3 2p_\gamma}\frac{\mathrm{d}^3p_\nu}{(2\pi)^3 2p_\nu}\,. \tag{4.1.3}$$

where $E_N$ the heavy neutrino energy. The four-momenta are denoted as p and the three-momenta as $p$. $N$, $\gamma$ and $\nu$ label the heavy neutrino, the photon and the light neutrino respectively. The matrix element $|\mathcal{M}|^2$ is computed as follows:

$$|\mathcal{M}|^2 = \frac{1}{2}\sum_{s,s',r}\left[\bar{u}_\nu(s',p_\nu)\left(\frac{\mathbb{1}+\gamma_5}{2}\right)\sigma_{\lambda\rho}\,2\mathrm{p}_\gamma^\rho\,\varepsilon_r^{*\lambda}\,u_N(s,p_N)\right]\left[\bar{u}_N(s,p_N)\left(\frac{\mathbb{1}-\gamma_5}{2}\right)\sigma_{\beta\alpha}\,2\mathrm{p}_\gamma^\beta\,\varepsilon_r^{\alpha}\,u_\nu(s',p_\nu)\right],$$

where $u_N$, $u_\nu$ and $\varepsilon$ are the heavy and light neutrino spinors and the photon polarization, respectively; $\mathrm{p}_\gamma$ is the photon four-momentum; $s$, $s'$ and $r$ label the heavy and light neutrino helicities and the photon polarization and $\lambda$, $\rho$, $\alpha$ and $\beta$ are Lorentz indices. The factors of 2 written before the photon four-momenta come from the contraction of the anti-symmetric electromagnetic field strength tensor with the anti-symmetric tensor $\sigma$. The factor 1/2 averages over the initial polarizations of the heavy neutrino. Using the completeness relations,

$$\sum_s u(s,p)\bar{u}(s,p) = (\not{p} + m) \quad ; \quad \sum_r \varepsilon_r^{*\lambda}\varepsilon_r^{\alpha} = -g^{\lambda\alpha}\,,$$

and the four-momentum Dirac delta, we find,

$$|\mathcal{M}|^2 = 4\frac{m_N^4}{\Lambda^2}\,.$$

[3]The operator $\mathcal{O}_{N\nu\gamma}$ could be generated at loop level, such that $1/\Lambda$ is a combination of a typical loop suppression factor, the inverse of the new physics mass scale, $M_{\rm NP}$, and unknown coupling constants, $g$:

$$\frac{1}{\Lambda} \sim \frac{g}{16\pi^2}\frac{1}{M_{\rm NP}}$$

Using the dirac delta in (4.1.3), $\mathrm{d}p_\nu$ can be integrated. Since the experiment configuration has an axial symmetry, $\mathrm{d}\varphi$ from $\mathrm{d}^3p_\gamma$ can be also integrated, leaving the differential decay rate as a function of the photon momentum and its angle with respect to the beam line:

$$\mathrm{d}\Gamma^{\mathrm{lab}}_{N\to\nu\gamma} = \frac{1}{4\pi\Lambda^2}\frac{m_N^4}{E_N p_\nu}\delta(E_N - p_\gamma - p_\nu)p_\gamma \mathrm{d}p_\gamma \mathrm{d}\cos\theta\,,$$

where

$$p_\nu = \sqrt{p_N^2 + p_\gamma^2 - 2p_N p_\gamma\cos\theta}\,.$$

Performing the change of variables for the dirac delta:

$$y \equiv E_N - p_\gamma - \sqrt{p_N^2 + p_\gamma^2 - 2p_N p_\gamma\cos\theta}\,,$$

and differentiating it with respect to $p_\gamma$ and $\cos\theta$, allows to perform the integral over $\mathrm{d}\cos\theta$ and $\mathrm{d}p_\gamma$, so that the differential decay rates with respect to $p_\gamma$ and $\mathrm{d}\cos\theta$ are:

$$\frac{\mathrm{d}\Gamma^{\mathrm{lab}}_{N\to\nu\gamma}}{\mathrm{d}p_\gamma} = \frac{1}{4\pi\Lambda^2}\frac{m_N^4}{E_N p_N}\,, \tag{4.1.4}$$

$$\frac{\mathrm{d}\Gamma^{\mathrm{lab}}_{N\to\nu\gamma}}{\mathrm{d}\cos\theta} = \frac{1}{8\pi\Lambda^2}\frac{m_N^6}{E_N(E_N - p_N\cos\theta)^2}\,. \tag{4.1.5}$$

Where we have used that the Dirac delta sets $y = 0$, which solved for $p_\gamma$ gives:

$$p_\gamma = \frac{m_N^2}{2(E_N - p_N\cos\theta)}\,. \tag{4.1.6}$$

Hence the minimum value of $p_\gamma$ is for the backward direction $\cos\theta = -1$, $p_{\gamma,\,\mathrm{min}} = (E_N - p_N)/2$, and the maximum for the forward direction $\cos\theta = 1$, $p_{\gamma,\,\mathrm{max}} = (E_N + p_N)/2$. The total decay rate, in the lab frame, is obtained either integrating the differential the decay rate (4.1.4) or (4.1.5):

$$\Gamma^{\mathrm{lab}}_{N\to\nu\gamma} = \frac{m_N^4}{4\pi\Lambda^2 E_N}\,.$$

The decay rate is the inverse of the life time and it Lorentz transforms as $\Gamma^{\mathrm{lab}} = \gamma\Gamma$, where $\gamma = E_N/m_N$. Hence the decay rate in the proper frame is:

$$\Gamma_{N\to\nu\gamma} = \frac{m_N^3}{4\pi\Lambda^2} \approx 1.2\times10^{-16}\,\mathrm{MeV}\left(\frac{10^5\,\mathrm{TeV}}{\Lambda}\right)^2\left(\frac{m_N}{250\,\mathrm{MeV}}\right)^3\,. \tag{4.1.7}$$

Since the heavy neutrino is mixed with the charged leptons, it is allowed to decay via a $W$ boson exchange. For the masses of interest in this work, $m_\pi < m_N < m_K$, the dominant decay modes via mixing are $N \to \ell^\mp\pi^\pm$ and $N \to \nu\pi^0$ [24, 63], whose decay rates are estimated as:

$$\begin{aligned}\Gamma_\pi \equiv \Gamma_{N\to\mathrm{lept}\pi} &= \frac{G_F^2 f_\pi^2 m_N^3}{32\pi}|U_{\ell 4}|^2 g(m_\pi, m_{\mathrm{lept}}, m_N) \\ &\approx 3\times10^{-13}\,\mathrm{MeV}\,|U_{\ell 4}|^2\left(\frac{m_N}{250\,\mathrm{MeV}}\right)^3 g(m_\pi, m_{\mathrm{lept}}, m_N)\,,\end{aligned} \tag{4.1.8}$$

where $f_\pi \simeq 130\,\mathrm{MeV}$ is the pion decay constant and $g(m_\pi, m_{\mathrm{lept}}, m_N)$ is a dimensionless kinematical function that depends on the decay channel [63], "lept" can be either a light neutrino or an electron or muon.

Under the assumption that $\Gamma_{N\to\nu\gamma}$ is much bigger than $\Gamma_\pi$, the branching ratio $\mathrm{Br}(N \to \gamma\nu) = \Gamma_{N\to\nu\gamma}/\Gamma_{\mathrm{tot}} \simeq 1$, with $\Gamma_{\mathrm{tot}}$, the total decay width. Anticipating the results below, a wide range of values of $|U_{\mu 4}|^2$, for which the MiniBooNE excess can be explained, make $N \to \gamma\nu$ the dominant decay channel.

It is worth to note that at the target, in the processes following the protons collision with the beryllium wall, a huge amount of high energy photons is expected, producing heavy neutrinos via the operator introduced in (4.1.2). Reinterpreting figure 1 of reference [212], which considers this effective interaction as the production and decay mechanism, it can be concluded that the production mechanism through (4.1.2) is subleading with respect to the process (4.1.1), as it will be explained below.

## 4.2 Predictions

In this section the predicted number of events and the energy and angular spectra inside the MiniBooNE detector are computed, as well as the time spectral shape of the signal.

### 4.2.1 Total number of events

The number of heavy neutrinos that decay inside the detector is obtained by integrating over the heavy neutrino flux $\phi_N(p_N)$, together with the decay probability inside the detector, $P_{\mathrm{dec}}$:

$$N_{\mathrm{decay}} = \mathrm{POT}\ \mathrm{Br}_{\nu\gamma}\, A_{\mathrm{MB}} \int dp_N\, \phi_N(p_N)\hat{\epsilon}(p_N) P_{\mathrm{dec}}(p_N)\omega_{\mathrm{time}}(p_N, m_N)\,. \tag{4.2.1}$$

Here, POT denotes the number of protons on target, which is $12.84\,(11.27) \times 10^{20}$ for the neutrino (anti-neutrino) mode. $\mathrm{Br}_{\gamma\nu} = \Gamma_{N\to\gamma\nu}/\Gamma_{\mathrm{tot}}$ is the decay branching ratio and $A_{\mathrm{MB}} = \pi(5\,\mathrm{m})^2$ is the effective area of the MiniBooNE detector. An effective area is considered, since the geometry of the detector is a sphere and then the area varies as a function of the longitudinal distance at which the heavy neutrino decays. The decay probability is given by

$$P_{\mathrm{dec}}(p_N) = e^{-t_1\Gamma^{\mathrm{lab}}_{\mathrm{tot}}} - e^{-t_2\Gamma^{\mathrm{lab}}_{\mathrm{tot}}}\,,$$

where $t_1$ and $t_2$ are the times at which the heavy neutrino reaches the beginning and the end of the detector. The decay rate can be expressed in the rest frame $\Gamma_{\mathrm{tot}} = \Gamma^{\mathrm{lab}}_{\mathrm{tot}}/\gamma$, and the time can be converted into the length from the source to the beginning and end of the detector $t\beta = L$, where $\beta \equiv v/c = p_N/E_N$ is the heavy neutrino velocity for $c = 1$. Then, the probability can be rewritten as

$$\begin{aligned} P_{\mathrm{dec}}(p_N) &= e^{-L_1\Gamma_{\mathrm{tot}}\frac{m_N}{p_N}} - e^{-L_2\Gamma_{\mathrm{tot}}\frac{m_N}{p_N}} && (4.2.2)\\ &\simeq \Gamma_{\mathrm{tot}}\frac{m_N}{p_N}\Delta L\,, && (4.2.3)\end{aligned}$$

with $\Delta L = 12\,\mathrm{m}$. For the MiniBooNE baseline, $L = 540\,\mathrm{m}$, the approximation (4.2.3) holds provided $\Gamma_{\mathrm{tot}} \lesssim 10^{-15}\,\mathrm{MeV}$ and $p_N \gtrsim 50\,\mathrm{MeV}$. $\hat{\epsilon}(p_N)$ is the integrated detection efficiency, which imposes an energy threshold to the heavy neutrino momentum as a function of the signal energy, in this case the photon energy. It is computed integrating the detection efficiency $\epsilon(p_\gamma)$ weighted by the photon momentum distribution:

$$\hat{\epsilon}(p_N) = \int_{p_{\gamma,\min}}^{p_{\gamma,\max}} dp_\gamma \epsilon(p_\gamma) \frac{1}{\Gamma^{\mathrm{lab}}_{N\to\nu\gamma}} \frac{\mathrm{d}\Gamma^{\mathrm{lab}}_{N\to\nu\gamma}}{\mathrm{d}p_\gamma}\,.$$

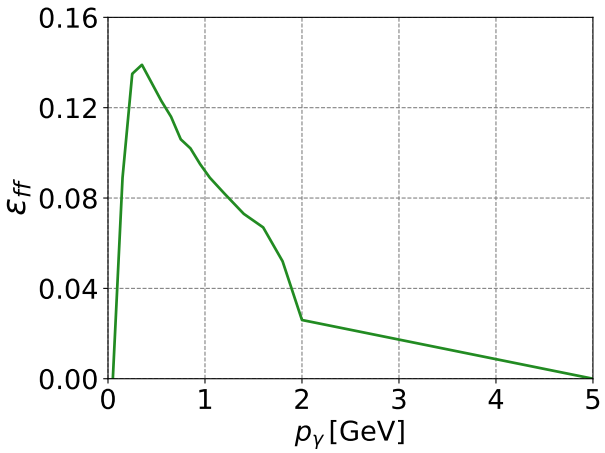


Figure 4.2.1: MiniBooNE detection efficiency as a function of the photon energy. Obtained by private communication, see reference [40].

$\epsilon(p_\gamma)$, figure 4.2.1, was obtained via private communication, see reference [40]. $\omega_{\text{time}}(p_N, m_N)$ is a weight related to the arrival time of the heavy neutrinos into the detector. Here we assume that the proton beam pulse produces step-like neutrino pulses of $\delta t = 1.6\,\mu s$. Then, the light neutrino signal is expected in a time window $\delta t$, after the expected arrival time from the source to the detector, i.e. $t_0 = L/c$. The heavy neutrinos in general arrive later at the detector than the light ones, and only those that arrive between $t_0$ and $t_0 + \delta t$ are expected to have been considered in the original MiniBooNE analysis. Then, taking into account the beam pulse structure and the heavy neutrino arrival time $t_N = L/v_N = t_0/\beta$, the weight is given by

$$\omega_{\text{time}}(p_N, m_N) = \begin{cases} \frac{t_0+\delta t-t_N}{\delta t} & \text{for } t_N < \delta t + t_0\,, \\ 0 & \text{for } t_N \geq \delta t + t_0\,. \end{cases}$$

The time window $\omega_{\text{time}}$ cuts the slow neutrino pulses that arrive completely out of the time window, while the ones that are fast enough are weighted by the relative amount of heavy neutrinos that actually make it to the detector in time, depicted in figure 4.2.2. This results in a suppression of the heavy neutrino flux for low momentum. Finally, $\phi_N(p_N)$ is the heavy neutrino flux which is constructed from the $\phi_{\nu_\mu}$ produced in kaon decays, obtained from reference [217], assuming only the two body decay channel $K \to N\ell$. In appendix C, the complete process of constructing $\phi_N(p_N)$ from the kaon induced $\phi_{\nu_\mu}$ is explained. As a general observation, it can be said that the flux components with lower momentum are going to be suppressed by the timing window and angular acceptance[4], see figure C.3.3.

MiniBooNE runs in two modes, neutrino and anti-neutrino modes, depending on the horn polarization that focus either mainly the positive charged mesons or the negative ones, respectively. The relative ratio of number of events between the anti-neutrino and neutrino modes is given by

$$R_{\text{pred}} = \frac{N_{\bar{\nu}}}{N_\nu}\,. \tag{4.2.4}$$

This ratio can be predicted in this model, given as a function of the mass, figure 4.2.3. The difference in the number of events, between the different modes, comes from the different POT and the light neutrino predicted fluxes [217] induced from kaon decays. The ratio depends on the heavy neutrino mass because the heavy neutrino flux depends on it, see appendix C.

[4]This ensures that $p_N \gtrsim 50\,\text{MeV}$, necessary for the approximation (4.2.3).

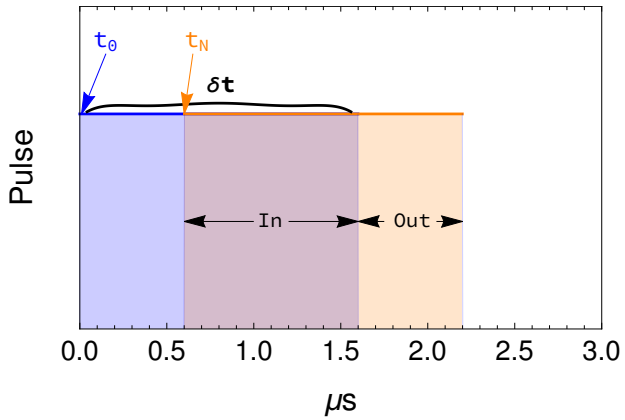


Figure 4.2.2: Time pulse for a light neutrino $\nu$ (blue) and a heavy neutrino $N$ (orange), both of size $\delta t$. The origin of the x axis is taken at the arrival time of the light neutrinos to the detector, $t_0$. When the time window function, $\omega_{\text{time}}$, is applied, only the fraction of the heavy neutrino pulse that overlaps with the light neutrino pulse is included in the MiniBooNE analysis.

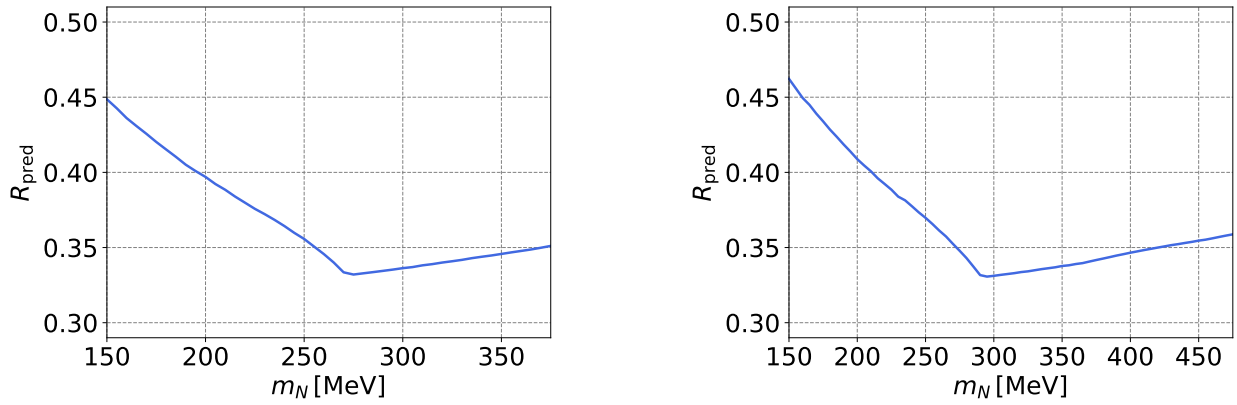


Figure 4.2.3: Predicted ratio of the total number of events between the anti-neutrino and neutrino modes, considering the production of the heavy neutrino from kaon decays together with a muon (left panel) and with an electron (right panel). The time window function, $\omega_{\text{time}}$, is applied.

### 4.2.2 Spectral predictions

The spectral shape predictions are computed convoluting, in each energy and angular bin, the detection efficiency with the photon momentum and angular distributions:

$$\frac{1}{\Gamma^{\text{lab}}_{N\to\gamma\nu}}\frac{\mathrm{d}\Gamma^{\text{lab}}_{N\to\gamma\nu}}{\mathrm{d}p_\gamma}(p_\gamma)\,; \qquad \frac{1}{\Gamma^{\text{lab}}_{N\to\gamma\nu}}\frac{\mathrm{d}\Gamma^{\text{lab}}_{N\to\gamma\nu}}{\mathrm{d}\cos\theta}(\cos\theta)\,.$$

The angular spectrum is given by:

$$\begin{aligned}\mathcal{A}_i(z) \;=\; & \text{POT}\,\text{Br}_{\nu\gamma}\,A_{\text{MB}}\int dp_N\,\phi_N(p_N)P_{\text{dec}}(p_N)\omega_{\text{time}}(p_N,m_N) \\ & \times\int_{p_{\gamma,i}}^{p_{\gamma,i+1}}\mathrm{d}p_\gamma\;\epsilon(p_\gamma)\frac{1}{\Gamma^{\text{lab}}_{N\to\nu\gamma}}\frac{\mathrm{d}\Gamma^{\text{lab}}_{N\to\nu\gamma}}{\mathrm{d}p_\gamma}S_{tp}(p_\gamma)\,. \qquad (4.2.5)\end{aligned}$$

And the energy spectrum by:

$$\begin{aligned}\mathcal{E}_i(p_\gamma) &= \mathrm{POT}\,\mathrm{Br}_{\nu\gamma}\,A_{\mathrm{MB}}\int dp_N\,\phi_N(p_N)P_{\mathrm{dec}}(p_N)\omega_{\mathrm{time}}(p_N,m_N)\\ &\quad\times\int_{z_i}^{z_{i+1}}\mathrm{d}z\;\epsilon(p_\gamma(z))\frac{1}{\Gamma^{\mathrm{lab}}_{N\to\nu\gamma}}\frac{\mathrm{d}\Gamma^{\mathrm{lab}}_{N\to\nu\gamma}}{\mathrm{d}z}\,.\end{aligned}\tag{4.2.6}$$

$z\equiv\cos\theta$ is related to $p_\gamma$ by (4.1.6) and $S_{tp}(p_\gamma)$ is a step function that prevents the $p_\gamma$ from being larger or smaller than the values allowed for a given $p_N$:

$$S_{tp}(p_\gamma)\equiv\theta(p_\gamma-p_{\gamma,\mathrm{min}})-\theta(p_\gamma-p_{\gamma,\mathrm{max}})\,,$$

where $p_{\gamma,\mathrm{min}}=(E_N-p_N)/2$ and $p_{\gamma,\mathrm{max}}=(E_N+p_N)/2$.

As explained before, the MiniBooNE detector does not distinguish between the signal produced by a photon and an electron/positron emitted in the interaction of a $\overset{(-)}{\nu}_e$ via CCQE. The MiniBooNE collaboration interprets the signal of the excess as being produced by an electron/positron. In the predictions described here, the energy and angular distributions of the photon are identified with the visible energy and angular distributions of the electromagnetic shower produced by that electron/positron, originally considered by the MiniBooNE collaboration.

### 4.2.3 Time shape

As mentioned above, heavy neutrinos arrive in general later at the detector than light neutrinos, so only those ones that are very relativistic would make it into the detector within the time window at which the light neutrinos are expected to arrive. Here it is explained how to predict the time distribution of the signal produced by the heavy neutrino.

Given the arrival time of the expected neutrinos

$$t_N=t_0\frac{E_N}{p_N}\,,\tag{4.2.7}$$

see section 4.2.1, the heavy neutrino flux $\phi_N(p_N,m_N)$, computed in appendix C, can be written as a function of time:

$$\phi_N(t,m_N)=\phi_N(p_N,m_N)\left|\frac{\mathrm{d}p_N}{\mathrm{d}t}\right|\,,$$

with the variable transformation $|\mathrm{d}p_N/\mathrm{d}t|=p_Nt/(t^2-t_0^2)$, which follows from (4.2.7).

In order to predict the time signal, the heavy neutrino decay probability has to be taken into account, here the linear approximation (4.2.3) is used, so that the flux is weighted by the factor $m_N/p_N$. As it was explained above in section 4.2.1, a step-like feature of width $\delta t$ is assumed for the neutrino beam pulse, so that the time distribution of the signal is obtained from a cumulative integral in the beam pulse structure at each time $t$:

$$T(t)\propto\int_{t-\delta t}^{t}\mathrm{d}t'\phi_N(t,m_N)\frac{m_N}{p_N}\,.\tag{4.2.8}$$

Since only the timing signal shape is important for the discussion, global factors, like the POT, effective area or $\mathrm{Br}(\mathrm{N}\to\gamma\nu)$, are not taken into account. In figure 4.2.4, the time distributions of the signal events of the heavy neutrino with a mass of 260 MeV for the neutrino and anti-neutrino modes are shown. The fractions of events that lie inside the time window are 41% and 34% for the neutrino and anti-neutrino modes, respectively.

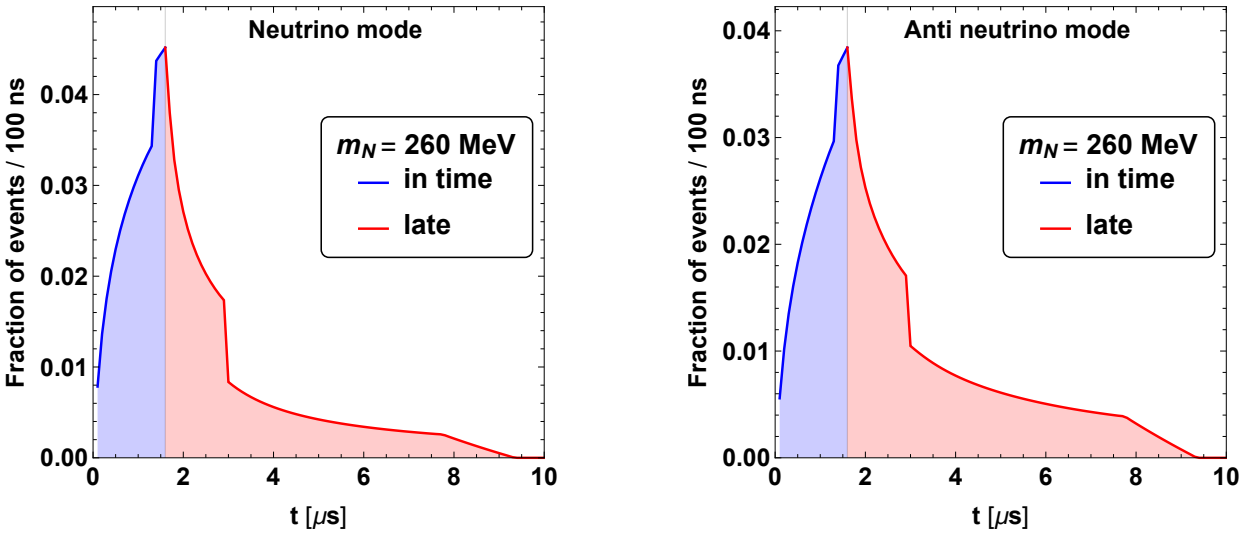


Figure 4.2.4: Time distribution of signal events for a heavy neutrino of 260 MeV assuming a step-like neutrino pulse of $\delta t = 1.6\mu s$, for the neutrino (left panel) and antineutrino mode (right panel). The origin of the x axis corresponds to the arrival time of the light neutrinos $t_0$. See text for details. The blue region corresponds to the fraction of events that lie inside the time window $[t_0, t_0 + \delta t]$, while the red region corresponds to those that lie outside it. Figures are taken from [40].

In figure 4.2.4, the effect of the monochromatic peak can be seen as a steep rise inside the timing window (in the blue region) corresponding to the first neutrinos of the monochromatic peak pulse arriving to the detector, and a steep decrease outside the timing window (in the red region) corresponding to the last neutrinos of the pulse. The tail after the monochromatic peak corresponds to the neutrinos emitted backwards in the kaon rest frame, which in the laboratory frame are slower than the neutrinos from the monochromatic peak, produced from kaon decays at rest with a fixed momentum, $p_{N,0}$, see appendix C.

As it has been shown, the time signal is very characteristic of heavy neutrinos and it would work as an ultimate test of the model. Actually, any model in which heavy particles are produced at the proton beam-target interaction and later decay or scatter in the detector can be tested via the time distribution of the signal events. Searches for heavy neutrinos in this way were also suggested in reference [218].

## 4.3 Analysis

Given the MiniBooNE data, taken from figure 14 of reference [39], the model can be tested fitting both the energy and the angular spectra of the excess. Since no correlation information is provided between the energy and angular spectral data, the fits are performed independently. In each of the fits, data from both neutrino and anti-neutrino modes are considered.

The free parameters of the fit are the total normalization, $N_{\text{total}}$, i.e. total number of excess events, and the heavy neutrino mass, $m_N$. Then the spectral predictions in each bin are given by $N_\nu f_i^\nu(m_N)$ and $N_{\bar{\nu}} f_i^{\bar{\nu}}(m_N)$ for the neutrino and anti-neutrino mode, respectively, where $f_i$ are the spectral shapes normalized to one, given by (4.2.5) and (4.2.6), and

$$N_\nu = \frac{N_{\text{total}}}{1 + R_{\text{pred}}(m_N)} \qquad \text{and} \qquad N_{\bar{\nu}} = N_{\text{total}} \frac{R_{\text{pred}}(m_N)}{1 + R_{\text{pred}}(m_N)}$$

are the respective normalizations for each mode. $R_{\text{pred}}$ is the predicted total number of

| Bkg contribution | $\nu$ mode | $\bar{\nu}$ mode |
|---|---|---|
| $\nu_e$ from $\mu$ | 0.24 | 0.3 |
| $\nu_e$ from $K^{\pm}$ | 0.22 | 0.21 |
| $\nu_e$ from $K^0$ | 0.38 | 0.35 |
| $\pi^0$ miss | 0.13 | 0.10 |
| $\Delta \to N\gamma$ | 0.14 | 0.16 |
| dirt | 0.25 | 0.25 |
| other | 0.25 | 0.25 |

Table 4.1: Relative uncertainties $\sigma_a$ and $\bar{\sigma}_a$ for the different background contributions in the neutrino and anti-neutrino modes, taken from table 1 of reference [39]. Uncertainties for "dirt" and "other" contributions are estimates. Table taken from [40].

events ratio (4.2.4), which depends only on the mass, shown in figure 4.2.3.

The fit to the data is done by the following least squares statistics:

$$\begin{aligned}\chi^2(N_\nu, m_N) &= \sum_i \frac{\left(O_i^\nu - b_a B_i^a - N_\nu f_i^\nu(m_N)\right)^2}{(\sigma_i^{\text{stat}})^2 + (\sigma_i^{\text{syst}})^2} \\ &+ \sum_i \frac{\left(O^{\bar{\nu}_i} - \bar{b}_a \bar{B}_i^a - R_{\text{pred}} N_\nu f_i^{\bar{\nu}}(m_N)\right)^2}{(\bar{\sigma}_i^{\text{stat}})^2 + (\bar{\sigma}_i^{\text{syst}})^2} \\ &+ \sum_a \left(\frac{b_a - 1}{\sigma_a}\right)^2 + \sum_a \left(\frac{\bar{b}_a - 1}{\bar{\sigma}_a}\right)^2 . \end{aligned} \tag{4.3.1}$$

$O^{(-)}_{\nu}$ are the observed number of events in each energy or angular bin $i$ for the neutrino and anti-neutrino modes, $B_i^a$ is the contribution from background $a$ in each bin $i$. $\sigma_i^{\text{stat}}$ and $\sigma_i^{\text{syst}}$ are the statistical and systematic uncertainties. The latter ones are a 20% uncertainty on the spectral shape, given by:

$$\begin{aligned}\sigma_i^{\text{syst}}(m_N) &= 0.2 N_\nu f_i^\nu(m_N)\,, \\ \sigma_i^{\text{syst}}(m_N) &= 0.2 N_{\bar{\nu}} f_i^{\bar{\nu}}(m_N)\,. \end{aligned}$$

They are added by hand due to the fact that the heavy neutrino flux is an estimate only, see appendix C. $\overset{(-)}{b}_a$ are the pull parameters accounting for the background component $a$ uncertainty, $\sigma_a$, which can be found in table 4.1. Since no information is found in the original publication [39] all the background uncertainties are assumed to be uncorrelated. These pull parameters are going to give different weights to the different background contributions, resulting in a rescaled background shape.

## 4.4 Results

### 4.4.1 Spectral fits

The timing window $\omega_{\text{time}}$ plays a crucial role in the angular spectral analysis. This is because the signal coming from slow heavy neutrinos[5], which is less forward-peaked distributed, is cut from the analysis.

[5]Slow heavy neutrinos come mainly from neutrinos emitted in the backward direction in the kaon rest frame and from the monochromatic peak contribution, cf. appendix C.

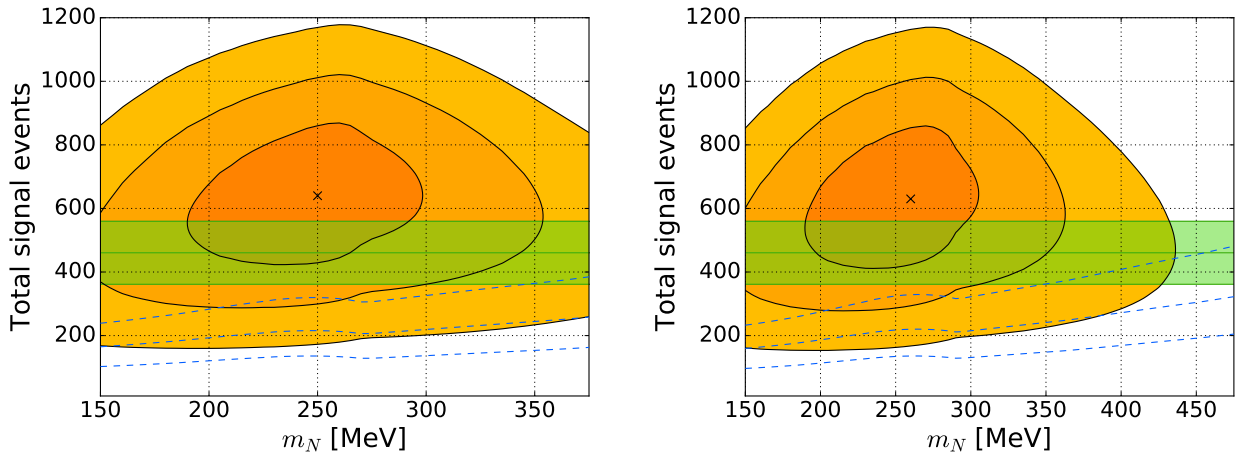


Figure 4.4.1: 1, 2 and $3\sigma$ contours for the energy (orange) and the angular spectral fits (dashed blue) in the $N_{\text{total}}$ vs $m_N$ parameter space. In the left (right) panel the heavy neutrino is assumed to be produced in kaon decays together with a muon (electron). The black crosses correspond to the energy best fit value. The green band shows the reported excess [39] together with the $1\sigma$ uncertainty. The left figure is taken from reference [40].

The analysis performed here is done under certain assumptions, which might not be fully correct, since it is not clear whether the time cut is applied or not in the original analysis from the MiniBooNE collaboration. Therefore here we study the two extreme cases: in which the timing window function is and is not applied.

### Applying timing cut

Results of the energy and angular fit preformed according to (4.3.1) are shown in figure 4.4.1, where both cases, a heavy neutrino produced together with a muon or an electron in kaon decays, are considered.

For the muon and electron cases, the energy spectral fit gives preferred regions in the parameter space with a best fit value at $(m_N, N_{\text{total}}) = (250\,\text{MeV}, 640)$ and $(260\,\text{MeV}, 640)$, respectively, while the angular fit sets only an upper limit, being both fits in tension. The goodness of fit of the energy fit $\chi^2_{\text{min}}/\text{dof} = 58.1/36$, translates to a $p$-value of 1%.

In figure 4.4.2, both spectral fits are shown for a benchmark point, for the muon case, compatible with the reported excess and the energy fit at $(m_N, N_{\text{total}}) = (250\,\text{MeV}, 400)$.

Although the energy fit seems by eye that it fits very well the data, the $\chi^2_{\text{min}}/\text{dof} = 61/36$ is rather high. This can be understood from considering the lower panels of figure 4.4.2, where it can be seen how a large contribution to the $\chi^2$ comes from the high energy bins, where an excess is neither predicted nor observed.

On the other hand, in the neutrino mode the angular fit is too much forward-peaked compared to the data. While the anti-neutrino mode seems to fit well the spectra, in the neutrino mode there is a large contribution to the $\chi^2$ coming from three scattered bins around $\cos\theta = 0$, especially the negative one, which could not be fitted by any smooth curve predicted by a model. This gives a total $\chi^2_{\text{min}}/\text{dof} = 52/18$, with a very poor $p$-value. As it was studied in detail in reference [216], models in which new physics is produced at the proton beam-target interaction and later decays at the detector always produce a very forward-peaked spectrum. As explained before, an energy and angular fit has to be performed consistently at the same time. Such a fit together with a time signal analysis would provide the definitive fit to accept or exclude this model.

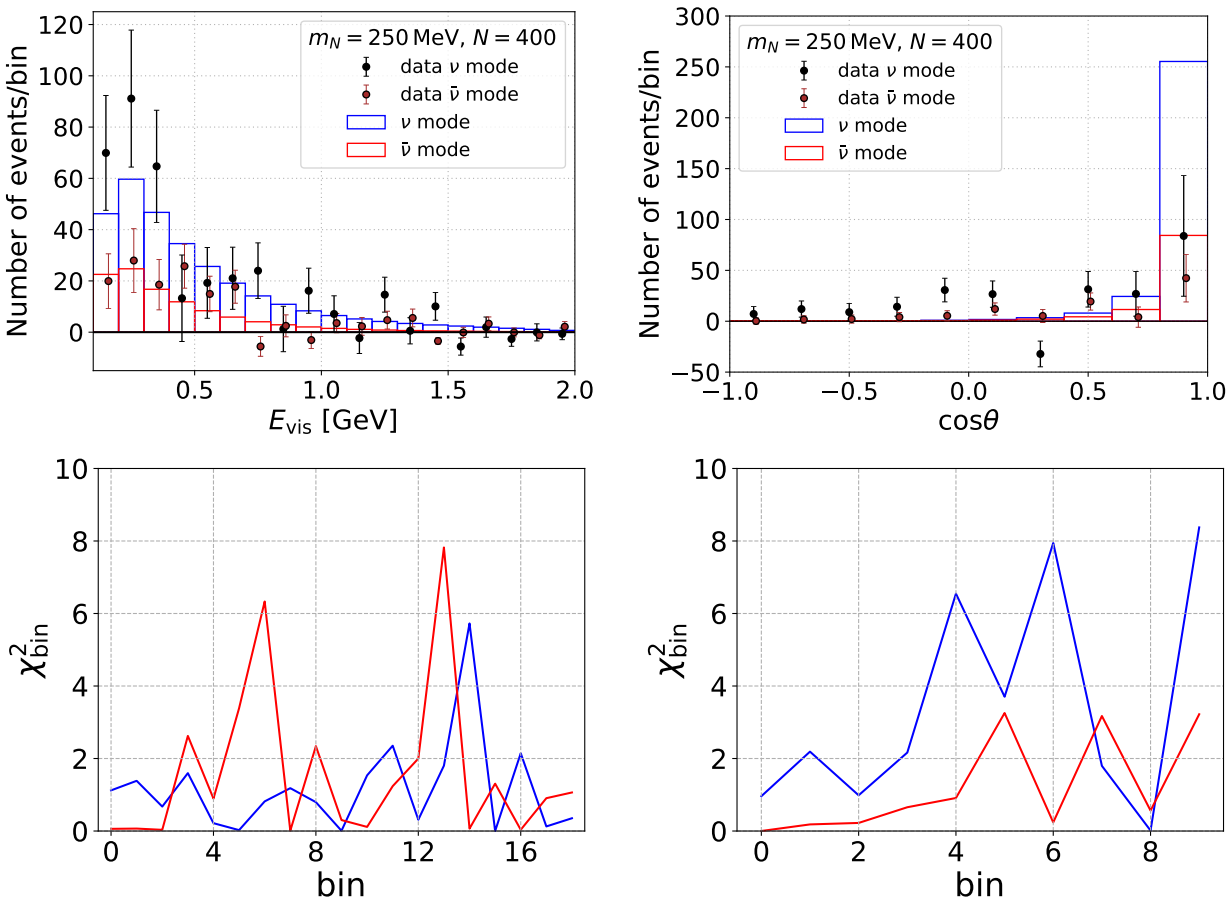


Figure 4.4.2: Visible energy (left panels) and angular (right panels) spectral fits (upper panels) and $\chi^2$ contribution per bin (lower panels), at the benchmark point $(m_N, N_{\rm total}) = (250\,{\rm MeV}, 400)$. The black (brown) dots are the observed number of events with the rescaled background subtracted, for the neutrino (anti-neutrino) mode. The error bars represent the statistical and systematic uncertainties. The blue (red) histogram is the predicted excess for the neutrino (anti-neutrino) mode. The heavy neutrino is assumed to be produced together with a muon in kaon decays. The upper plots are taken from reference [40]. In the lower plots the blue (red) lines corresponds to the neutrino (anti-neutrino) mode.

### Not applying the timing cut

In figure 4.4.3 it is shown, for the muon case, how the same fit looks like if the timing window is removed from the fit, i.e. the complete heavy neutrino flux, $\phi_N(p_N)$, is considered. The spectral fits are shown for the benchmark point $(m_N, N_{\rm total}) = (370\,{\rm MeV}, 400)$. This point now is compatible at the $1\sigma$ level with the best fit values for the energy and angular spectral fits. In the right lower panel it can be clearly seen how the angular spectrum improves, because now it is not so much forward-peaked. The fit is reasonable with a $\chi^2_{\rm min}/{\rm dof} = 33/18$. The energy fit, with $\chi^2_{\rm min}/{\rm dof} = 63/36$, shown in the left lower panel, is as good as it was when the timing cut was applied.

## 4.4.2 Allowed parameters of the model

In what follows, the timing cut analysis is considered.

Using the expression of the total number of predicted events (4.2.1), the allowed regions obtained in the energy fit, cf. figure 4.4.1, can be translated to allowed regions in the model parameters: the mixing $|U_{\ell 4}|^2$, the heavy neutrino mass $m_N$ and the decay rate $\Gamma_{N\to\gamma\nu}$,

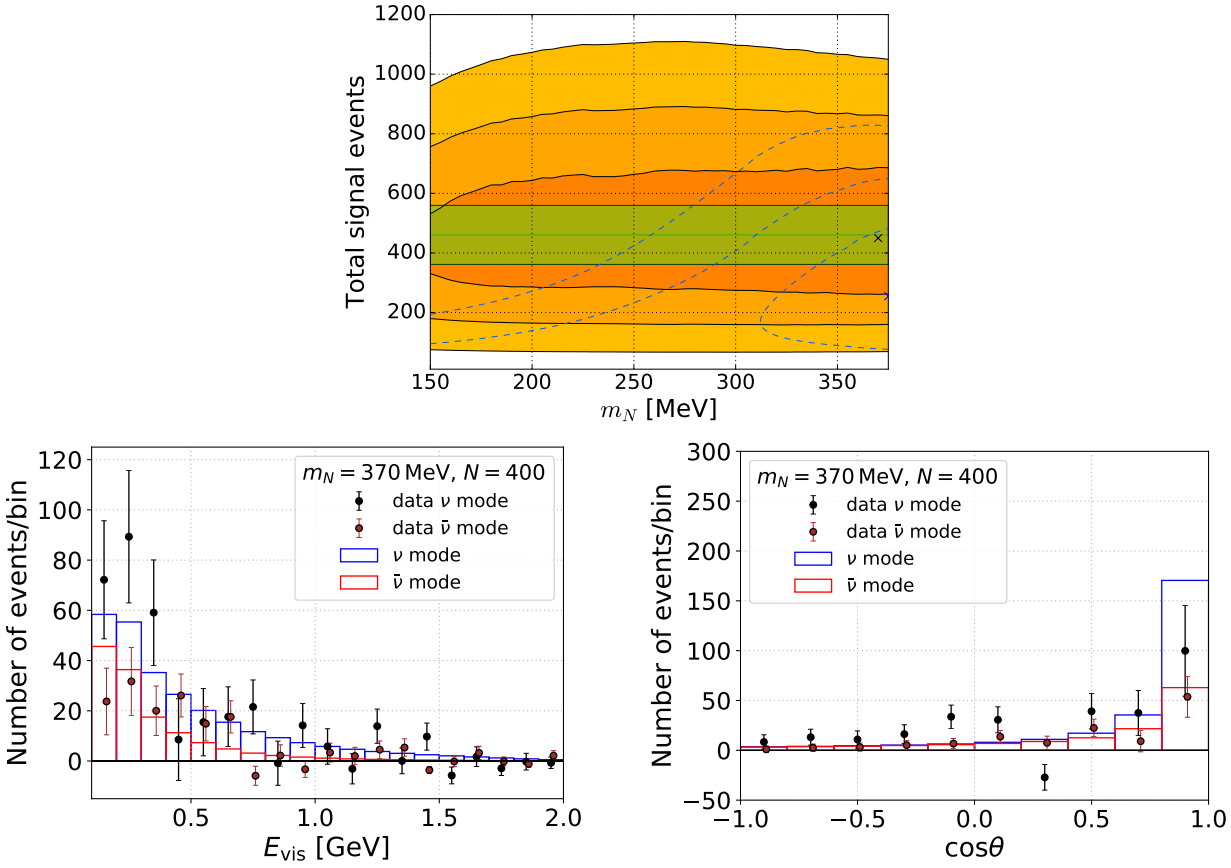


Figure 4.4.3: Upper plot: allowed 1,2 and 3$\sigma$ regions for the energy (orange) and angular (dashed blue) spectral fits, not applying the timing cut, in the parameter space $N_{\text{total}}$ vs $m_N$. The green band correspond to the reported excess in reference [39] and its 1$\sigma$ uncertainty. Lower plots: visible energy (left) and angular (right) spectral fits not applying the timing cut. The black (brown) dots are the observed number of events with the rescaled background subtracted, for the neutrino (anti-neutrino) mode. The error bars represent the statistical and systematic uncertainties. The blue (red) histogram is the predicted excess for the neutrino (anti-neutrino) mode. A heavy neutrino produced together with a muon in kaon decays is assumed. Figures are taken from reference [40].

which is directly related to the energy scale $\Lambda$ (4.1.7).

In figure 4.4.4, the 1 and 2$\sigma$ allowed regions in the parameter space $|U_{\ell 4}|^2$ vs $\Gamma_{N\to\gamma\nu}$ for a fixed mass, are shown as red and orange bands. The linear behavior on the left of the figures corresponds to the parameters for which the decaying probability can be linearly approximated. In this regime[6] $N_{\text{decay}} \propto |U_{\ell\nu}|^2\Gamma_{N\to\gamma\nu}$. This linear approximation breaks down at the "knee" before the upwards turn, which corresponds to the parameters for which the heavy neutrino decays before reaching the detector.

In 4.4.5, a projection onto the $|U_{\ell 4}|^2$ vs $m_N$ parameter space is performed minimizing over $\Gamma_{N\to\gamma\nu}$. The lower limit of the allowed 1 and 2$\sigma$ regions that explains MiniBooNE, red and orange shaded regions, is set by the lowest part of the knee in 4.4.4, where the decay probability linear approximation does not hold.

For an excess of 400 events, fitting the mass dependence of the number of events to a power law and choosing the regime in which the decay probability can be linearly approxi-

[6]Note that in (4.2.1) in the linear approximation $\text{Br}(N\to\gamma\nu)\Gamma_{\text{total}} = \Gamma_{N\to\gamma\nu}$.

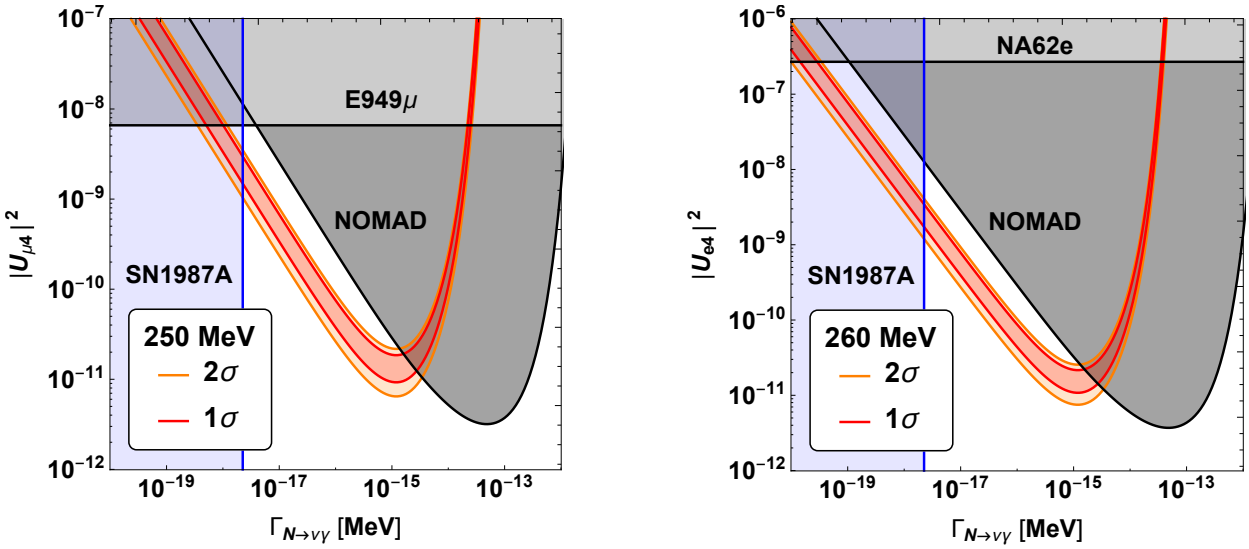


Figure 4.4.4: 1 and $2\sigma$ allowed regions in the parameter space $|U_{\ell 4}|^2$ vs $\Gamma_{N\to\ell\nu}$ (red and orange regions) for the neutrino mass fixed at the best fit value. The left (right) plot assumes that the heavy neutrino is produced from a kaon decay together with a muon (electron). Also the upper limits on $|U_{\ell 4}|^2$ from NA62 and E949 direct searches (light gray) and the region excluded by NOMAD (dark gray), as well as the region for $\Gamma_{N\to\gamma\nu}$ disfavoured by the supernova bound SN1987A (blue) are shown. Figures are taken from [40].

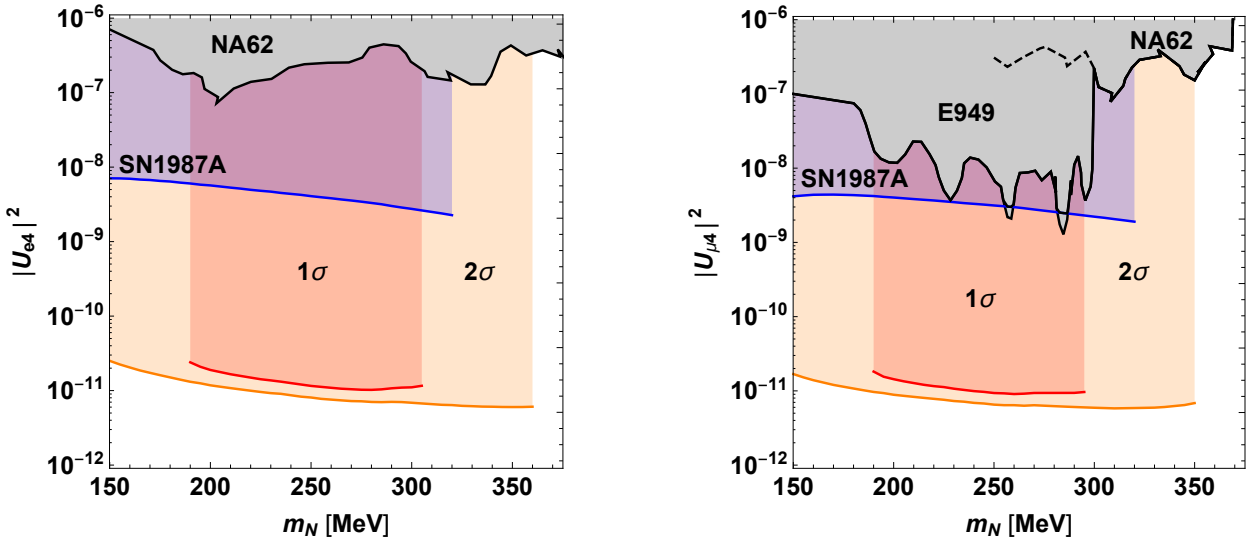


Figure 4.4.5: 1 and $2\sigma$ allowed regions projected in the parameter space $|U_{\ell 4}|^2$ vs $m_N$ (red and orange regions). The projection is done minimizing the $\chi^2$ over $\Gamma_{N\to\gamma\nu}$. For the left (right) panel the heavy neutrino is produced by $K\to\mu N(eN)$. Excluded parameter space from peak searches in the kaon decay spectra of electron and muon from the NA62 and E949 experiments are shown as gray shaded regions. The regions disfavoured by SN1987A constraints are shown as blue shaded regions. Figures are taken from [40].

mated (4.2.3), i.e. $N_{\rm decay} \propto \Gamma_{N\to\gamma\nu}|U_{\ell 4}|^2$, the following relation is obtained:

$$\Gamma_{N\to\gamma\nu} \simeq 3\times 10^{-17}\,{\rm MeV}\left(\frac{10^{-10}}{|U_{\ell 4}|^2}\right)\left(\frac{250\,{\rm MeV}}{m_N}\right)^{2.3}\left(\frac{N_{\rm decay}}{400}\right)\,. \tag{4.4.1}$$

Comparing it with the decay rate via mixing (4.1.8), it is found that in order for $\Gamma_{N\to\gamma\nu}$ to dominate over $\Gamma_{N\to{\rm lept}\pi}$, the mixing has to be

$$|U_{\ell 4}|^2 \ll 10^{-7}\left(\frac{250\,{\rm MeV}}{m_N}\right)^{2.65}\left(\frac{N_{\rm decay}}{400}\right)^{-1/2}\,.$$

For larger values of the mixing extra signals from the decay channels (4.1.8) are expected. When the linear approximation of the decay probability breaks, $|U_{\ell 4}|^2$ is small so that the $N\to\gamma\nu$ is the dominant decay channel. Then, as it was anticipated in section 4.1, for a large range of the values of the parameters that explain the MiniBooNE excess, the leading signal comes from the decay channel $N\to\gamma\nu$.

As it was stated in section 4.2.1, for the allowed regions of the parameters that explain MiniBooNE, the production mechanism through (4.1.2) is subleading with respect to the process (4.1.1). This can be seen plotting the allowed regions of the parameters obtained here against figure 1 of reference [212]. This region would lie below the allowed region derived in that work, for which the production and decay mechanisms considered are through the effective operator (4.1.2). This means that the production mechanism considered here is stronger, not requiring a small value $\Lambda$ (4.1.7) that enhances the heavy neutrino decays at the detector in order to have the excess.

### 4.4.3 Constraints

Constrains on the model come from direct searches experiments as NA62 [53] and E949 [54], setting limits on the mixings $|U_{e4}|^2$ and $|U_{\mu 4}|^2$ respectively. Those experiments search for peaks in the charged lepton spectra coming from the kaon decays, as it is described in section 2.4. In figures 4.4.4 and 4.4.5 their limits at the 90% C.L. are shown as grey shaded regions.

A null search for single photon events performed by the NOMAD experiment [219] can be reinterpreted within this model to set a bound in the parameter space. The NOMAD experiment is also a beam dump experiment, with an original proton beam of 450 GeV. Predictions can be done using the expression (4.1.7). The heavy neutrino flux is constructed as explained in section C from the kaon-induced muon neutrino flux given in reference [220]. The POT is $2.2\times 10^{19}$, the average baseline $L = 620\,{\rm m}$, and the dimensions of the detector are 7.5 m in the beam line direction and $3.5\times 3.5$ m$^2$ in the transverse direction. A constant reconstruction efficiency of 90%, an analysis efficiency of 8%, and a trigger efficiency of 30% [219] are included. In order to take into account a cut on the observed energy, only heavy neutrinos with momentum greater than 1.5 GeV are considered. No information on the timing window was found, so no time window cut is applied for the events prediction. The limit at 90% C.L. shown in figures 4.4.4 and 4.4.5 is set for a total number of predicted events of 18[7]. Given its similar baseline and higher neutrino energies compared to MiniBooNE, the linear behavior starts breaking at larger values of $\Gamma_{N\to\gamma\nu}$ (4.2.2).

Heavy neutrinos are subject to supernova constraints, since they could work as a cooling mechanism. This translates into a bound on the decay rate, so that it is large enough to keep the neutrinos trapped inside the supernova. The bounds set by SN1987A can be

[7]The NOMAD collaboration excludes $N_{\rm events} \geq 18$ at 90% C.L..

approximately extracted from figure 1 of reference [212] in the parameter space $1/\Lambda$ vs $m_N$, for $50 \lesssim m_N \lesssim 320\,\text{MeV}$:

$$\Gamma_{N\to\nu\gamma} > 2.4\times 10^{-18}\,\text{MeV}\left(\frac{250\,\text{MeV}}{m_N}\right).$$

For larger values of the masses, the neutrinos are gravitationally bound inside the supernova [221]. In figure 4.4.4, the bound on the decay rate can be seen, which translates into a bound on the mixing in figure 4.4.5.

For the allowed parameters of the model that explain the MiniBooNE excess (4.4.1), the heavy neutrino life time is below 1 millisecond, so that BBN bounds do not apply [48, 90].

## 4.5 Conclusions and further searches

Taking the constraints into account it can be seen, for the analysis in which the timing window is included, how the model is compatible with the MiniBooNE excess in a large range of the model parameters: $10^{-11} \lesssim |U_{\mu 4}|^2 \lesssim 10^{-8}$, $m_N \sim 250\,\text{MeV}$ and the new physics scale[8] $10^4\,\text{TeV} \lesssim \Lambda \lesssim 10^7\,\text{TeV}$.

If the heavy neutrino were Majorana, it would contribute to the mass of the light neutrinos through the seesaw mechanism, figure 2.3.2. For some of the allowed parameters, e.g. $m_N \simeq 250\,\text{MeV}$ and $|U_{\ell 4}|^2 \simeq 10^{-10}$, the seesaw contribution to the light neutrino mass is $m_\nu \simeq 0.025\,\text{eV}$ (2.3.7), of the order expected for the light neutrino masses. On top of that contribution, the operator (4.1.2) gives a loop level contribution to the light neutrino masses, cf. figure 3 of [212], whose size depends on the ultra violet completion of the operator.

Apart from the constraints mentioned above, further present and future experiments can search for this type of signal and test this model, like the NO$\nu$A and T2K near detectors, Minerva [222] and the experiments of the Fermilab short-baseline neutrino (SBN) program: MiniBooNE, SBND, MicroBooNE and Icarus [223,224]. In particular, T2K made an analysis searching for single photon events, cf. reference [225], and no excess was found. We have estimated that the limit from this null search is weaker than the one set by NOMAD, so we do not include it.

Of great interest are the Fermilab SBN program experiments since they are based at the same neutrino beam as MiniBooNE. Moreover, the SBND, MicroBooNE and Icarus detectors, which are filled with liquid argon, are very suitable for this kind of searches, since they would not misidentify a photon and an electron signal. Assuming that the angular size of all the detectors are smaller than the angular size of the beam spread and that the linear approximation of the decay probability (4.2.3) holds for all the detector baselines, we can do a rough estimation of the number of events in each detector by scaling with the proportionality factor

$$\text{POT}\times V/L^2\,, \tag{4.5.1}$$

where $L$ is the baseline and $V$ is the detector volume. In table 4.2, the benchmark characteristics of each detector are shown together with the relative ratio of expected events with respect to MiniBooNE. As can be seen in the last row, assuming 400 signal events in MiniBooNE, the three SBN program detectors expect a significant number of heavy neutrino decay events, so that they will be able to test this model in the near future.

Apart from these tests, the MiniBooNE experiment can perform a direct test of the model by measuring the time distribution of the signal events, which we have shown that is very characteristic of this model.

[8] The new physics scale can be obtained from the limits on $\Gamma_{N\to\gamma\nu}$ in figure 4.4.5 with $\Lambda = \sqrt{\frac{1}{4\pi}\frac{m_N^3}{\Gamma_{N\to\gamma\nu}}}$.

| | MiniBooNE | SBND | MicroBooNE | Icarus |
|---|---|---|---|---|
| POT / $10^{20}$ | 24 | 6.6 | 13.2 | 6.6 |
| Volume / $m^3$ | 520 | 80 | 62 | 340 |
| Baseline / m | 540 | 110 | 470 | 600 |
| Ratio | | 1 | 0.09 | 0.15 |
| Events | 400 | 400 | 35 | 58 |

Table 4.2: Benchmark characteristics of the three SBN program detectors [223, 224]. We use the number of POT quoted in [218]. For MiniBooNE we sum the POT in neutrino and antineutrino modes. In the row "Ratio" we show the ratio of heavy neutrino events relative to MiniBooNE, based on the scaling with the proportionality factor (4.5.1). In the row "Events" the expected number of events assuming 400 signal events in MiniBooNE are given. Table taken from [40].

# Chapter 5

# Summary and conclusions

In this thesis we have shown applications of the reactor neutrino data to neutrino oscillation studies in the $3\nu$ standard and $3+1\nu$ oscillation frameworks. We have also presented an alternative explanation of the MiniBooNE excess, different from the active-to-sterile oscillation, in terms of a heavy neutrino decaying into a photon and a light neutrino.

## $3\nu$ oscillations

In this work the MBL reactor data from the Daya Bay, RENO and Double Chooz experiments has been analyzed in the $3\nu$ standard oscillation framework. It has been shown that in a global fit the determination of the mixing angle $\theta_{13}$ is dominated by MBL reactor experiments. Daya Bay, RENO and Double Chooz combined analysis determines $\theta_{13}$ with high precision: $\sin^2\theta_{13} = 0.0223^{+0.0006}_{-0.0007}$; and also provide information on the oscillation parameter $\Delta m^2_{\text{atm}}$, complementary to its determination by LBL accelerator experiments. In this work we have summarized two relevant implications of the consistent combination of MBL reactor and LBL accelerator data: the preference for non-maximality of the $\theta_{23}$ mixing angle improves slightly and the preference for NO over IO increases by two units in $\Delta\chi^2$; both with respect to the LBL accelerator independent data analysis using a constraint on $\theta_{13}$ given by the MBL reactor data.

The Daya Bay and RENO data has also been used to get information on the solar parameter $\Delta m^2_{21}$. A combined analysis of Daya Bay and RENO data set the upper limit $\Delta m^2_{21} \leq 18.3 \times 10^{-3}\,\text{eV}^2$ at the $2\sigma$ C.L., constraining the $\Delta m^2_{\text{atm}}$ parameter using independent information from LBL experiments. This measurement is far from solving the $2\sigma$ tension between the solar and the KamLAND measurements, but it gives a consistent result in a complete different oscillation regime that shows the robustness of the $3\nu$ oscillation framework. The limit can be lowered as statistics increases, but the tension is not expected to be solved until the JUNO experiment provides additional information on $\Delta m^2_{21}$.

## $3+1\nu$ oscillations

The study of the $3+1\nu$ oscillation framework with reactor data has been affected by recent measurements in reactor anti-neutrino experiments, as the discovery of the "5 MeV bump" and the determination of the independent contributions to the neutrino flux by Daya Bay. Both shed doubt on the reliability of the flux predictions, on which the RAA depends on. Based on these measurements, in this work the Daya Bay flux data was analyzed under two hypothesis: "flux free (no $\nu$)" and "flux fixed ($\nu$)". We confirm the Daya Bay result, which favors the first over the latter at the level of $2.8\sigma$, however we also found that the "flux fixed ($\nu$)" hypothesis gives a reasonable goodness of fit to the data, with a $p$-value $= 17\%$. Thus the explanation of the RAA based on an active-to-sterile oscillation can not be rejected.

Therefore, a global analysis of all the reactor data within the $3+1\nu$ framework is performed, in which no assumptions for the anti-neutrino fluxes are taken, i.e. their normalizations are left free and fitted to data together with the oscillation parameters. Reactor data shows to be compatible with the active-to-sterile oscillation, which is preferred over the no oscillation hypothesis at the level of $2.9\sigma$ with the best fit value at $(\Delta m^2_{41}, |U_{14}|^2) \simeq (1.3\,\mathrm{eV}^2, 0.01)$. This result is mainly driven by the remarkable agreement between NEOS and DANSS data, whose analyses, based on a comparison of measured spectra, are independent of the flux predictions.

The combined analysis of all the experiments, sensitive to the hypothetical active-to-sterile oscillations in the disappearance oscillation channel $\overset{(-)}{\nu}_e \to \overset{(-)}{\nu}_e$, gives a preference for the oscillation over $3\sigma$, also at the best fit value $(\Delta m^2_{41}, |U_{14}|^2) \simeq (1.3\,\mathrm{eV}^2, 0.01)$. This result is mainly driven by the reactor data.

Although an active-to-sterile oscillation is compatible with the reactor and the global $\overset{(-)}{\nu}_e$ disappearance data, it has been shown that it is not a good explanation for the $\overset{(-)}{\nu}_e$ appearance anomalies, namely the LSND and MiniBooNE anomalies. A study of the oscillation global data, within the $3+1\nu$ framework, shows that the constraints set by the null results in the $\overset{(-)}{\nu}_\mu$ disappearance channel searches lead to a strong tension between the $\overset{(-)}{\nu}_e$ appearance and the $\overset{(-)}{\nu}_e/\overset{(-)}{\nu}_\mu$ disappearance data sets. A PG test-statics shows that the $p$-value measuring their incompatibility is at the $5.1\sigma$ level, using the whole global data set. The tension does not rely on any particular $\overset{(-)}{\nu}_\mu$ disappearance experiment, and it is very strong even when removing the reactor data set, remaining at the level of $4.1\sigma$. This result excludes the active-to-sterile oscillation as an explanation for the LSND and MiniBooNE anomalies, so that alternative explanations are needed.

**MiniBooNE alternative explanation**

In the present work an alternative explanation for the MiniBooNE excess is shown by introducing a heavy neutrino that decays radiatively into a photon and a light neutrino through an effective magnetic moment interaction.

The heavy neutrinos are produced in kaon decays via mixing with the light neutrinos, $U_{\ell 4}$ ($\ell = e, \mu$), after the kaons are originated in the proton beam-target collisions. They travel through the Earth and decay in the detector into a photon and a light neutrino. Based on the fact that the MiniBooNE detector can not distinguish between an electron/positron and a photon, in this model the excess is produced by the photon signal.

Both the energy and angular spectra, as well as the time distribution of the signal events, can be predicted with the model. The angular spectral fit is in tension with the energy fit which gives a reasonable goodness of fit to the data. This tension can be alleviated with different assumptions for the event selection applying a timing cut. Ideally a joined fit of the energy and angular spectral data have to be performed, but no information for this kind of fit is provided by the collaboration. Based on the energy spectral fit, the excess can be explained for a wide range of the model parameters: $m_N \simeq 250\,\mathrm{MeV}$, $10^{-11} \lesssim |U_{\ell 4}|^2 \lesssim 10^{-8}$, and the scale $10^4\,\mathrm{TeV} \lesssim \Lambda \lesssim 10^7\,\mathrm{TeV}$ of the new physics that mediates the decay of the heavy neutrino.

Since heavy neutrinos travel more slowly to the detector than the light ones, 60% of the events are predicted to lie outside the expected time of the signal produced by light neutrinos. So that a study of the time distribution of the signal events measured at MiniBooNE will provide an ultimate test of the model, and not only this model but any model in which heavy particles are produced at the proton beam-target interaction and either decay or scatter at the detector.

# Appendix A

# Reactor data analyses

In this appendix it is explained how Daya Bay, RENO, NEOS and DANSS data analyses are performed. This appendix is an extension on the details given in [26, 28, 36].

## A.1 Daya Bay and RENO

Daya Bay and RENO predictions are computed according to (3.2.6) and their data analyses are performed using the least-squares statistic method (3.2.7) which is based on an a far-to-near ratio, thus become flux shape and normalization independent and the flux systematic uncertainties are reduced. In both analyses the systematic effects are included in a pull parameter approach. Systematic uncertainties on the relative detection efficiency, relative energy scale and the main background contributions are taken into account, summarized in table A.1.

| | Daya Bay<br>EH1,EH2 - EH3 | RENO<br>Near,Far |
|---|---|---|
| **Source** | **Uncertainty %** | |
| Relative detection efficiency | 0.13 | 0.21 |
| Energy scale | 0.2 | 0.15 |
| Li-He background | 30 | 5-8 |
| Fast neutron background | 13-17 | – |
| Accidental background | 1 | – |

Table A.1: Relative systematic uncertainties in each detector used for the Daya Bay and RENO analyses, taken from [106, 107] respectively.

The validation of Daya Bay and RENO analyses can be seen in figure 3.3.1.

### A.1.1 Daya Bay data analysis

Daya Bay data, background estimation, energy response function, and systematic uncertainties are taken from the supplementary material in [106]. The efficiencies $\varepsilon^d$ include $\varepsilon_\mu \times \varepsilon_m \times \text{life time days}$, obtained from table 1 in [106], and the relative difference of target protons $\Delta N_p$ of each detector, taken from [130]. The baselines $L_{rd}$ are also taken from [130]. For each isotope, $f^{\text{iso}}$ is computed as the average of the fission fractions in table 9 of [110]. The detector response function is given in the complementary material of [106] as a $2 \times 2$ array $R\left(E^{\text{rec}}, E_{\text{dep}}\right)$ relating both $E^{\text{rec}}$ and $E_{\text{dep}}$. In order to perform the integral over $\mathrm{d}E^{\text{rec}}$, for every $E_{\text{dep}}$ column of the matrix, a trapezoidal integral is performed over the $E^{\text{rec}}$ rows contained in each $E_i^{\text{rec}}$ bin. The result is a detector response function depending only on $E_{\text{dep}}$

for each bin $i$ of $E^{\rm rec}$, $\widehat{R}_i(E_\nu)$, which will be linear-interpolated over $E_\nu$ when performing the integral over $\mathrm{d}E_\nu$. The relation between $E_\nu$ and $E_{\rm dep}$ is just an energy shift (3.2.2).

The Daya Bay experimental set up has two near detector sites, called experimental halls (EH1 and EH2) and a far one (EH3). For the Daya Bay analysis two pairs of far-to-near ratios, EH3/EH1 and EH3/EH2, are considered

$$\begin{aligned}\chi^2(\boldsymbol{\theta}) &= \sum_{i,j}^{2\mathrm{N_{bins}}} \left(\frac{O_i^F - B_i^F}{O_i^N - B_i^N} - \frac{X_i^F(\boldsymbol{\theta})}{X_i^N(\boldsymbol{\theta})}\right) V^{-1}_{\mathrm{stat},ij} \left(\frac{O_j^F - B_j^F}{O_j^N - B_j^N} - \frac{X_j^F(\boldsymbol{\theta})}{X_j^N(\boldsymbol{\theta})}\right) \\ &\quad + \sum_{\alpha}^{\mathrm{N_{pull}}} \frac{(\xi_\alpha - 1)^2}{\sigma_\alpha^2}\,, \end{aligned} \tag{A.1.1}$$

where the superscripts $F(N)$ and the indices $i$ ($j$) represent the Far (Near) detector and $i^{th}$ ($j^{th}$) prompt energy bin, respectively. Being $O$ the observed number of IBD candidate events and $B$ the estimated background number of events taken from the complementary material of [106], $X$ are the expected number of events for a given value of the oscillation parameters $\boldsymbol{\theta}$ (3.2.6). The total number of bins is taken to be $2\mathrm{N_{bins}}$ in order to include in a compact notation the two ratios considered. For $1 \leqslant i \leqslant \mathrm{N_{bins}}$, $F$ =EH3 and $N$ =EH1, and for $\mathrm{N_{bins}} + 1 \leqslant i \leqslant 2\mathrm{N_{bins}}$, $F$ =EH3 and $N$ =EH2. The reason why the background is subtracted from the observed events and not added to the predictions is because in this way the normalization of the total number of events is not needed, only the relative normalization matters. $V^{-1}_{\mathrm{stat},ij}$ accounts for the statistical uncertainties and its correlations[1],

$$V_{\mathrm{stat},ij} = \sum_{\alpha=1}^{2\mathrm{N_{bins}}} \sum_{\beta=F,N} \frac{\partial D_i^{FN}}{\partial O_\alpha^\beta} \frac{\partial D_j^{FN}}{\partial O_\alpha^\beta} \left(\sqrt{O_\alpha^\beta}\right)^2\,, \tag{A.1.2}$$

where $D_i^{FN} \equiv \frac{O_i^F - B_i^F}{O_i^N - B_i^N}$. The statistical correlations come into the expression since EH3 is being used in the two ratios. The relative systematic uncertainties $\sigma_\alpha$, cf. table A.1, are included with pull parameters $\xi_\alpha$. Since the detectors are identical, the relative uncertainty in each experimental hall is obtained dividing the detector systematic uncertainties by $\sqrt{2}$ in EH1 and EH2 and by 2 in EH3, since there are 2 and 4 detectors, respectively. In order to reproduce as good as possible the Daya Bay collaboration result [106] with the available information, a 1.3 fudge factor is added to the relative energy scale and Li-He background uncertainties. The pull parameters accounting for detection efficiency ($\epsilon^d$) and relative energy scale ($\eta^d$) are included in the number of expected events (3.2.6) as follows:

$$X_i^d(\epsilon^d, \eta^d) = \epsilon^d \sum_r \sum_{\rm iso} \frac{\varepsilon^d}{L_{rd}^2} \int_{\eta^d E_i^{\rm rec}}^{\eta^d E_{i+1}^{rec}} \mathrm{d}E^{\rm rec} \int_0^\infty \mathrm{d}E_\nu\; \sigma(E_\nu) f^{\rm iso} \phi^{\rm iso}(E_\nu) P^{rd}_{\bar{\nu}_e \to \bar{\nu}_e}(E_\nu) R(E^{\rm rec}, E_\nu)\,.$$

The background pull parameters are included in background events $B_i^d$ used in $D_i^{F/N}$ as follows:

$$B_i^d(b_{\rm LH}^d, b_{\rm acc}^d, b_{\rm n}^d) = B_i^d + (b_{\rm LH}^d - 1) B_{{\rm LH},i}^d + (b_{\rm acc}^d - 1) B_{{\rm acc},i}^d + (b_{\rm n}^d - 1) B_{{\rm n},i}^d\,.$$

Here $B_i^d$ ($B_{{\rm LH},i}^d$, $B_{{\rm acc},i}^d$ and $B_{{\rm n},i}^d$) represents the number of total (Li-He, accidental and fast neutron) background events in the $i^{th}$ prompt energy bin in the $d^{th}$ detector, and $b$ represents the corresponding pull parameters.

[1]The $\chi^2$ defined in this section was used in [28], older versions in which the statistical correlations were not considered, where used in [26, 36, 37]

As explained above, the predicted number of events (3.2.6) is computed taking the same effective fission fractions $f^{\rm iso}$ in all the detectors, so that if any uncertainty on the flux normalizations were considered, it will cancel when taking the ratios of predicted events.

The data analysis is performed scanning over the oscillation parameters of the model, $\boldsymbol{\theta}$, minimizing over the pull parameters at each value of the model parameters. For that, a linear expansion over the pull parameters in (A.1.1) is performed. This way, it is possible to minimize with respect the $n$ pull parameters solving a linear system of $n$ equations:

$$\frac{\partial\chi^2(\alpha_1,\cdots,\alpha_n)}{\partial\alpha_j}=0\,,\ j=1,\cdots,n\,. \tag{A.1.3}$$

As an example, the explicit linearization of one of the components of (A.1.1) reads

$$\begin{aligned}\frac{O_i^3-B_i^3(b^3_{\rm LH},b^3_{\rm acc},b^3_{\rm n})}{O_i^1-B_i^1(b^1_{\rm LH},b^1_{\rm acc},b^1_{\rm n})}-\frac{X_i^3(\epsilon^3,\eta^3)}{X_i^1(\epsilon^1,\eta^1)} &= \frac{O_i^3-B_i^3(\mathbf{1})}{O_i^1-B_i^1(\mathbf{1})}-\sum_{\alpha={\rm LH,acc,n}}\frac{B^3_{\alpha i}}{O_i^1-B_i^1}\bigg|_{b^3_\alpha=1}(b^3_\alpha-1)\\ &+\frac{O_i^3-B_i^3}{(O_i^1-B_i^1)^2}\bigg|_{b^1_\alpha=1}B^1_{\alpha i}(b^1_\alpha-1)\\ &+\frac{X_i^3(\mathbf{1})}{X_i^1(\mathbf{1})}+\frac{X_i^3}{X_i^1}\bigg|_{\epsilon^3=1}(\epsilon^3-1)-\frac{X_i^3}{X_i^1}\bigg|_{\epsilon^1=1}(\epsilon^1-1)\\ &+\frac{1}{X_i^1}\,\frac{\partial}{\partial\eta}X_i^3\bigg|_{\eta^3=1}(\eta^3-1)-\frac{X_i^3}{(X_i^1)^2}\,\frac{\partial}{\partial\eta}X_i^1\bigg|_{\eta^1=1}(\eta^1-1)\,.\end{aligned}$$

In order to linearize with respect to the energy scale pull parameter, which appear in the limits of the $\mathrm{d}E^{\rm rec}$ integral

$$\int_{\eta E_i^{\rm rec}}^{\eta E_{i+1}^{\rm rec}}\mathrm{d}E^{\rm rec}R(E^{\rm rec},E_\nu)\,,$$

the Leibniz integral rule is applied

$$\begin{aligned}\frac{\partial}{\partial\eta}X_i\bigg|_{\eta=1} &= \int_0^\infty \mathrm{d}E_{\bar\nu_e}\cdots\frac{\partial}{\partial\eta}\int_{\eta E_i^{\rm rec}}^{\eta E_{i+1}^{\rm rec}}\mathrm{d}E^{\rm rec}R(E^{\rm rec},E_\nu)\bigg|_{\eta=1}\\ &= \int_0^\infty \mathrm{d}E_{\bar\nu_e}\cdots\left(R(E^{\rm rec}_{i+1},E_\nu)E^{\rm rec}_{i+1}-R(E^{\rm rec}_i,E_\nu)E^{\rm rec}_i\right)\,.\end{aligned}$$

In works [26, 36, 37] Daya Bay predictions are different from what it is described in this appendix, a different pair of ratios was used, EH3/EH1 and EH2/EH1, and the statistical correlations were not considered. In this case the statistical correlations are on the observed events at EH1 (near detector), so they are not so relevant since they are proportional to the squared relative uncertainty on the observed events in EH1 (A.1.2), which is the EH with more statistics, while in the analysis here described, statistical correlations are proportional to the relative uncertainty at EH3 (far detector), which has the least statistics. In [28] the here described more sophisticated analysis was performed.

### A.1.2 RENO data analysis

RENO data and background estimation are extracted from FIG.1 in [107], the systematic uncertainties are also taken from [107]. The baselines are taken from [226], the averaged fission fractions from [35] and the life times can be found in [107]. For the detector response

function the on from Daya Bay is used. The relative far to near normalization is computed normalizing to the total number of expected events in the far detector without oscillations

$$\varepsilon = \frac{\sum_i P^F_{Ri}}{\sum_i O^N_{Ri} \frac{P^F_i}{P^N_i}} ,$$

where for each energy bin $i$, $P^F_{Ri}$ are the predictions performed by the RENO collaboration at the far detector without oscillations, $O^N_{Ri}$ are the observed number of events measured at the near detector, $P^F_i$ and $P^N_i$ are the predicted events at the far and near detectors.

The RENO $\chi^2$ is based on the far to near ratio implemented as follows

$$\chi^2 = \sum_i \frac{\left(\frac{O'^F_i}{O'^N_i} - \frac{X^F_i(\boldsymbol{\theta})}{X^N_i(\boldsymbol{\theta})}\right)^2}{\left(\sigma^{\text{stat}}_i\right)^2} + \sum_\alpha \frac{\left(\xi_\alpha - 1\right)^2}{\sigma^2_\alpha} .$$

Here $O'^D_i$, are the observed number of events, background subtracted, at the $D = F, N$ detector in the energy bin $i$. $O'^D_i = O^D_i - B^D_i$, with $O$ the total number of observed events and $B$ the estimated background, so that the statistical uncertainties are computed as:

$$\sigma^{\text{stat}}_i = \sum_{\alpha=N,F} \frac{\partial \frac{O'^F_i}{O'^N_i}}{\partial O^\alpha_i} \left(\sqrt{O^\alpha_i}\right)^2 .$$

Both $O'^D_i$ and the estimated background contributions are obtained from fig. 1 of [107], $X^D_i$ are the predictions as a function of the oscillation parameters $\boldsymbol{\theta}$ and $\xi_\alpha$ are the pull parameters accounting for the systematic uncertainties $\sigma_\alpha$. The most relevant systematic uncertainties used are summarized in table A.1, which are included in the same way as it is done in the Daya Bay analysis, but the detection efficiency pull parameter is included in the far-to-near ratio, instead of in each detector.

Following this method and with the available information, in order to match as good as possible the RENO collaboration result [107] an extra factor of 0.984 to the relative far to near efficiency has to be included and the relative detection efficiency uncertainty has to be increased by a factor of 1.4.

## A.2 NEOS data analysis

In this section it is explained how NEOS data [121] is analyzed in order to reproduce the collaboration result.

The number of events in every energy bin is computed following equation (3.2.6). Since the NEOS detector is very close to the source and both the source and detector finite sizes can not be neglected, an average of the probability over the size of the source and detector, $\Delta L$, is performed:

$$\frac{1}{\Delta L} \int_{L-\Delta L/2}^{L+\Delta L/2} dl \; \frac{\sin^2\left(\Delta m^2 \frac{l}{4E}\right)}{l^2} , \tag{A.2.1}$$

with $\Delta L = 3$m and $L = 24$m. Since no response function $R(E^{\text{rec}}, E_p)$ is provided by the NEOS collaboration, following reference [123] a renormalized gaussian centered in $E^{\text{rec}} = E_p$ ($E_p \equiv E_{\text{dep}} \simeq E_\nu - 0.8$MeV) plus a constant value for $E^{\text{rec}} < E_p$ accounting for the IAV

effect is considered:

$$R(E^{\text{rec}}, E_p) = \frac{1}{\sqrt{2\pi}\sigma(E_p)} \exp\left\{-\frac{(E^{\text{rec}} - E_p)^2}{2\sigma^2(E_p)}\right\} \Theta\left(E^{\text{rec}} - E_p\right) + \left(Z + \frac{1 - \sqrt{2\pi}\sigma(E_p)Z}{\sqrt{2\pi}\sigma(E_p)} \exp\left\{-\frac{(E^{\text{rec}} - E_p)^2}{2\sigma^2(E_p)}\right\}\right) \Theta\left(E_p - E^{\text{rec}}\right) ,$$

where the width of the gaussian is the energy resolution given in equation (1) in reference [123], $\sigma(E_p) = (0.05\sqrt{E_p} + 0.12)\,\text{MeV}$, and $Z = 0.022$. In order to reproduce the NEOS spectrum of figure 3(b) in [121] as good as possible, an energy rescale factor of 0.935 was included as well as the non-linearity effect, $E'_p = E_p f(E_p)$, for the energy deposited, for which the non-linearity function provided by Daya Bay in the complementary material of [130] is used, which was found to work properly in this case.

The NEOS analysis is done minimizing the least-squares statistic:

$$\chi^2(\theta_{14}, \Delta m^2_{41}) = \sum_{i,j} \left[O_i - P_{\text{red},\,i}(\theta_{14}, \Delta m^2_{41})\right] V^{-1}_{ij} \left[O_j - P_{\text{red},\,j}(\theta_{14}, \Delta m^2_{41})\right]$$

where $O_i$ is the NEOS data in every energy bin $i$, extracted from figure 3(c) of reference [121]. It is presented as a ratio of the NEOS spectrum and a NEOS prediction in the $3\nu$ framework based on the Daya Bay unfolded spectrum [110], $P_{\text{red}}$ are the predictions and $V$ is the covariance matrix accounting for the statistical and systematic uncertainties. Since Daya Bay unfolded spectrum is computed in the $3\nu$ framework, it is only unfolded from the $3\nu$ oscillations but not from the active-to-sterile one, hence the NEOS predictions in the $3\nu$ framework have to take the information from the active-to-sterile oscillations from Daya Bay. As a good approximation this is done bin per bin in the following way:

$$P_{\text{red},\,i} = \frac{P^{\text{NEOS}}_{4\nu,\,i}}{P^{\text{NEOS}}_{3\nu,\,i} \frac{P^{\text{DB}}_{4\nu,\,i}}{P^{\text{DB}}_{3\nu,\,i}}} ,$$

where $P^{\text{NEOS(DB)}}_{3(4)\nu,\,i}$ are the predicted energy spectrum for NEOS (Daya Bay) in the $3(4)\nu$ framework, computed as described in (3.2.6). Here Daya Bay predictions are computed with the NEOS bin size, which is different from the one used in Daya Bay.

The covariance matrix $V$ includes the statistical uncertainties, extracted from figure 3(c) in reference [110] and the relative covariance matrix of the Daya Bay unfolded spectrum, which is obtained dividing the covariance matrix of table 13 of reference [110] by the corresponding components of the flux, table 12 of reference [110], in each bin, and then rebinning it to match the NEOS binning.

## A.3 DANSS data analysis

The DANSS data, taken from slide 10 in reference [166], is analyzed using the least-squared statistics defined in (A.2.2). The DANSS detector is movable an measures at two different positions from the detector, $L = 12.7\,\text{m}$ (down position) and $L = 10.7\,\text{m}$ (up position). $O_i$ is the data at each energy bin $i$, which is given as a ratio of measured events at the two different baselines, down/up. The measured spectrum is given as a function of the kinetic energy of the positron emitted in the IBD process. $P_{\text{red},i}$ are the predictions, computed as in (3.2.6). For the detector response function an energy resolution modeled as a gaussian with a width given by figure 5 in reference [227] is used. The detection efficiency here cancels in the

ratio since measurements come from the same detector. The covariance matrix $V$ contains statistical uncertainties and a 2% systematic uncertainty on the down/up ratios. As in the NEOS analysis, the DANSS detector and reactor core can not be considered punctual, so an average over $L = 12.85 \pm 4.0\,\mathrm{m}$ of the oscillation probability weighted by the geometrical factor $1/L^2$ (A.2.1) have to be performed.

# Appendix B

# Monte Carlo study on the Daya Bay flux data

A Monte Carlo study is performed in order to determine the $p$-values of different hypotheses for the analysis of the Daya Bay data [34] and to verify that the minimum of their least square statistics follows $\chi^2$ distributions.

### Simulated data

The simulated IBD yield data $\sigma_i^{\rm MC}$ is generated, for a given "true" $\theta_{14}$, using a random number generator following a multivariate gaussian distribution

$$f(\boldsymbol{x}) = \frac{1}{\sqrt{(2\pi)^4|V|}} \exp\left\{-\frac{1}{2}(x_i - \sigma_i^{\rm HM})V_{ij}^{-1}(x_j - \sigma_j^{\rm HM})\right\} ,$$

where the means $\sigma_i^{\rm HM}$ and the covariance matrix $V$, with running indices $i, j = 1, ..., 8$ labelling the $F_i^{239}$ bins, are computed as follows

$$\begin{aligned} \sigma_i^{\rm HM} &= P_{\rm osc} \sum_{\rm iso} F_i^{\rm iso} \sigma_{\rm iso}^{\rm HM} \\ V_{ij} &= V_{ij}^{\rm stat} + V_{ij}^{\rm syst} \sigma_i^{\rm HM} \sigma_j^{\rm HM} \quad \text{(no summed indices)} , \end{aligned}$$

here $F_k^{\rm iso}$ are the effective fission fractions, in each $F_k^{239}$ bin, for each isotope iso, $P_{\rm osc}$ is the averaged out[1] oscillation probability (3.4.3) determined by the "true" $\theta_{14}$. $V^{\rm stat}$ and $V^{\rm syst}$ are the statistical uncertainties and the systematic correlation matrix respectively, taken from the complementary material in [34]. The IBD yield contributions, $\sigma_{\rm iso}^{\rm HM}$, are Huber and Mueller predictions [102, 103].

### Analyses

Given the mote carlo generated data, their analysis is performed using the following least-squares statistic:

$$\chi^2(\theta_{14}, \hat{\boldsymbol{\sigma}}) = \sum_{a,b=1}^{8} (\sigma_{\rm obs}^a - \sigma_{\rm pred}^a) V_{ab}^{-1} (\sigma_{\rm obs}^b - \sigma_{\rm pred}^b) + \chi^2_{\rm flux}(\hat{\boldsymbol{\sigma}}) .$$

Where $\sigma_{\rm pred}^a \equiv P_{\rm osc} \sum_{\rm iso} \xi_{\rm iso} F_{\rm iso}^a \sigma_{\rm iso}^{\rm HM}$ and $\sigma_{\rm pred}^a \equiv \sum_{\rm iso} \xi_{\rm iso} F_{\rm iso}^a \sigma_{\rm iso}^{\rm HM}$, for the "flux fixed ($\nu$)" (hypothesis $H_0$) and the "flux free (no $\nu$)" (hypothesis $H_1$) analyses, respectively. $\hat{\sigma}_{\rm iso} \equiv$

[1] The averaged out regime is valid for $\Delta m^2_{41} > 0.05\,{\rm eV}^2$.

$\xi_{\rm iso}\sigma^{\rm HM}_{\rm iso}$ (no summed indices). The covariance matrix is given by $V_{ij} = V^{\rm stat}_{ij} + V^{\rm syst}_{ij}\sigma^{i}_{\rm obs}\sigma^{j}_{\rm obs}$ (no summed indices). For the "flux fixed ($\nu$)" analysis, two different cases are considered, what is called Huber-Mueller (HM) analysis in which the uncertainties of the flux predictions are taken into account, and the Daya Bay (DB) analysis in which they are fixed to their predicted value. In the HM case the penalizing term takes the form

$$\chi^2_{\rm flux}(\hat{\boldsymbol{\sigma}}) = (\hat{\sigma}_i - \sigma_i^{HM})V^{-1}_{\sigma_{\rm ij}}(\hat{\sigma}_j - \sigma_j^{HM})\,,$$

where $V_\sigma$ is the covariance matrix with the uncertainties of predicted IBD yields and their correlations, taken from table 3 in reference [160]. While in the DB case the penalizing term is not considered. For the "flux free (no $\nu$) analysis a constraint of a 10% is added to the two least contributions to the flux $\sigma^{HM}_{238}$ and $\sigma^{HM}_{241}$ in order to avoid unphysical results, hence the penalizing term takes the form

$$\chi^2_{\rm flux}(\hat{\boldsymbol{\sigma}}) = \left(\frac{\hat{\sigma}_{238} - \sigma^{\rm HM}_{238}}{0.1\sigma^{\rm HM}_{238}}\right)^2 + \left(\frac{\hat{\sigma}_{241} - \sigma^{\rm HM}_{241}}{0.1\sigma^{\rm HM}_{241}}\right)^2 .$$

The parameters $\hat{\sigma}_{\rm iso}$ are minimized solving a linear system of equations

$$\frac{\partial\chi^2(\hat{\boldsymbol{\sigma}})}{\partial\hat{\sigma}_{\rm iso}} = 0\,. \tag{B.0.1}$$

In the "flux fixed ($\nu$)" analysis, as a double check, two ways of minimizing with respect to $P_{\rm osc}(\theta_{14})$ are performed: finding the minimum scanning over $P_{\rm osc}$ and including it analytically into the linear system of equations (B.0.1). Using the second method, first the predictions have to be linearized with respect to the parameters the $\chi^2$ is minimized over, $P_{\rm osc}$ and $\hat{\boldsymbol{\sigma}}$:

$$\sigma^a_{\rm pred} = P_{\rm osc}\sum_{\rm iso} F^a_{\rm iso}\sigma^{\rm HM}_{\rm iso} + \sum_{\rm iso} F^a_{\rm iso}\hat{\sigma}_{\rm iso} - \sum_{\rm iso} F^a_{\rm iso}\sigma^{\rm HM}_{\rm iso} \tag{B.0.2}$$

**Results**

Distributions of the quantities $\chi^2_{\rm min}(H_0)$, $\chi^2_{\rm min}(H_1)$ and $T \equiv \chi^2_{\rm min}(H_0) - \chi^2_{\rm min}(H_1)$ are obtained generating ten thousand of simulated data for each "true" $\theta_{14}$. These distributions coincide with $\chi^2$ distributions with 7, 6 and 1 degree of freedom, respectively, see figure B.0.1. The goodness of fit of $H_0$ and $H_1$, and the $p$-value of the test statistic $T$ for each $\theta^{\rm true}_{14}$, shown in figure B.0.2, are given by the relative area enclosed under the distributions on the right of the measured values: $\chi^2_{\rm DB\,flux,\,min}$ and $T_{\rm DB\,flux,\,min}$; computed with the actual measured data, table 3.1.

The $p$-values of $H_0$ are 18 and 12 % for the HM and DB analyses, respectively, of the $H_1$ hypothesis is 73 %, and of the test statistic $T$ is 0.7 and 0.5 % for the HM and DB analyses, respectively. The two different cases for the $H_0$ hypothesis analysis, HM and DB, give a different gof, being smaller the DB one, as expected, since it does not consider an uncertainty to the Huber-Mueller predictions. This difference is also visible in the $p$-value of the test statistic $T$.

**Remarks**

The $p$-values show a systematic up-turn feature for $\sin^2 2\theta_{14}$ small and close to 1 when minimizing the $\chi^2$ scanning over $P_{\rm osc}$, specially in the $H_0$ and $T$ cases, lower left and right panels. These features are understood, they appear because in the scanning over $P_{\rm osc}$, the physical boundary $0 \leq \sin^2 2\theta_{14} \leq 1$ is imposed, but the random generated data for $\sin^2 2\theta^{\rm true}_{14}$ close to 0 and 1, due to the random fluctuations, can generate data out of the

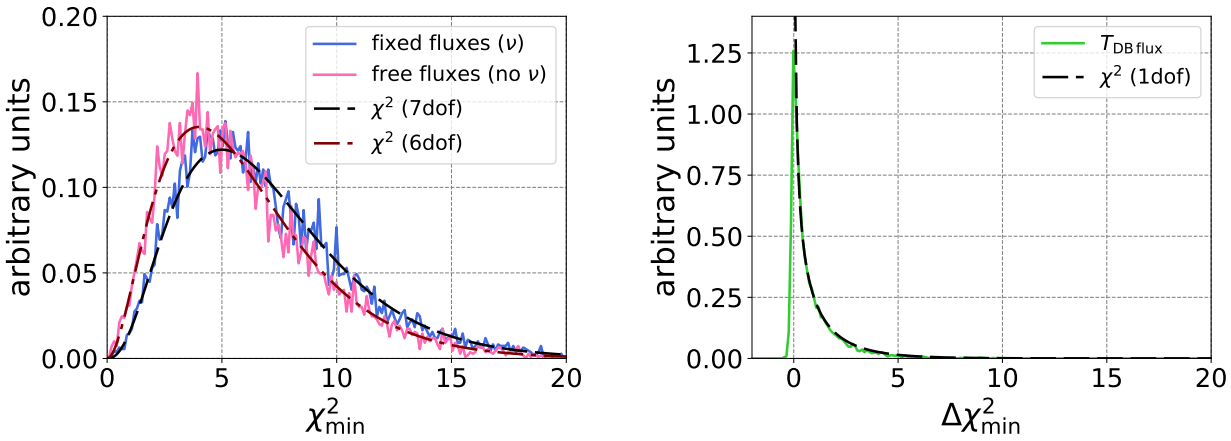


Figure B.0.1: Distributions of statistical quantities for the Daya Bay data [34] analysis. Left: $\chi^2_{\text{min}}$ distributions for the "flux fixed ($\nu$)" and "flux free (no $\nu$)" analyses, blue an pink solid lines, and $\chi$ distributions for 7 and 6 degrees of freedom, black and red dashed lines, for comparison. Right: test statistic $T$ (3.4.7) distribution, green solid line, and $\chi^2$ distribution for one degree of freedom in dark green dashed lines.

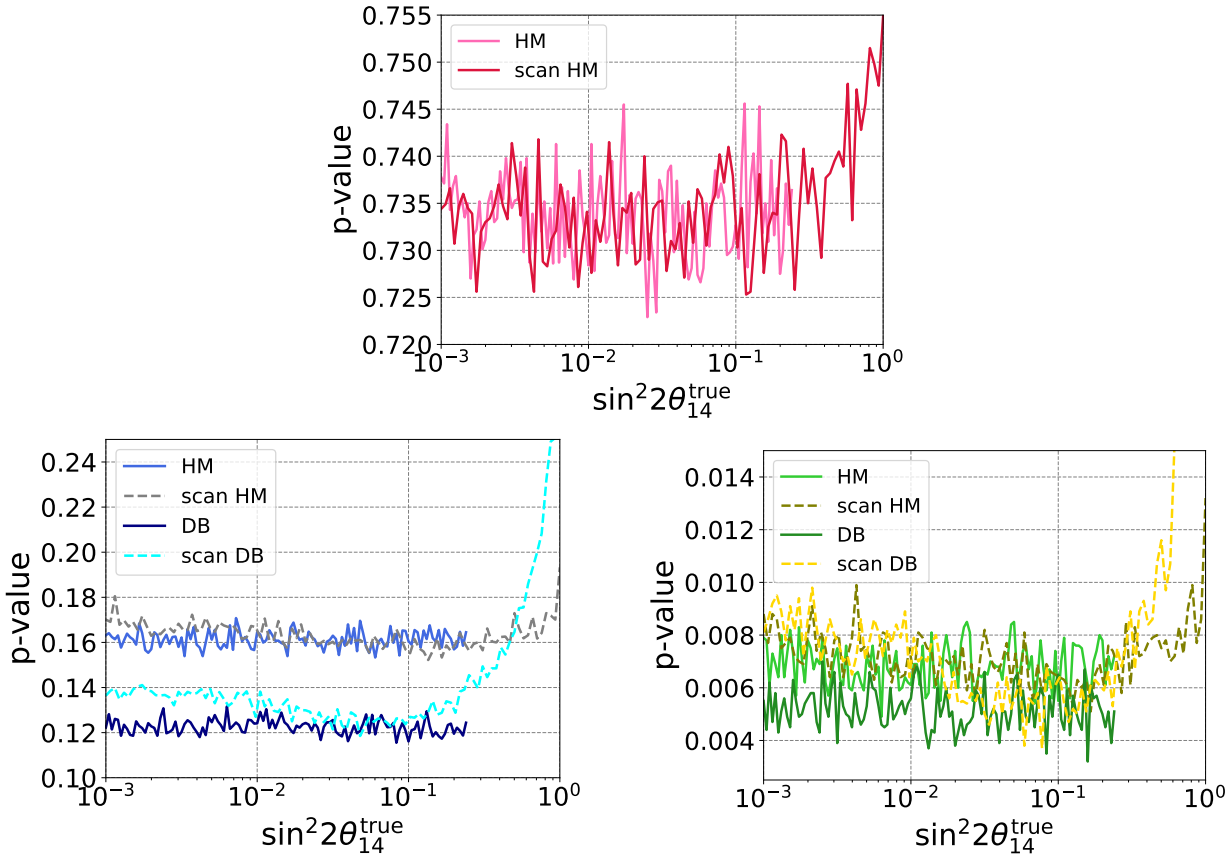


Figure B.0.2: $p$-values of the $H_0$ (lower left panel) and $H_1$ (upper middle panel) hypotheses, and of the test statistic $T$ (lower right panel) for the Daya Bay data [34] analysis. Different assumptions on the flux predictions, HM and DB cases, and different minimization methods, linearizing and scanning over the minimizing parameters, are shown. See text fro details.

physical range. With the other minimization method, when $\sigma_{\text{pred}}$ is linearized, the minimum in $P_{\text{osc}}$ is found solving the linear system of equations, so that the physical boundaries are

not imposed and thus the up-turn feature does not show up. Note that $\sin^2 2\theta_{14}$ has to be small so that the expansion (B.0.2) holds with good accuracy, in this case values up to $\sin^2 2\theta_{14}^{\text{true}} \sim 0.25$ are considered.

It is important to note that in order to get the correct goodness of fit for the $H_1$ hypothesis, the random generated data should be generated for every $\hat{\boldsymbol{\sigma}}^{\text{true}}$ combination, while here only the particular case in which all the IBD yields are rescaled with the same factor, $P_{\text{osc}}$, is considered. As can be seen in the upper middle panel of figure B.0.2, with the used method, the $p$-value is independent of the values of the common rescaling, $P_{\text{osc}}$, of $\hat{\boldsymbol{\sigma}}^{\text{HM}}$. So there is no need to generate the data for every $\hat{\boldsymbol{\sigma}}^{\text{true}}$ combination. Consequently this method is additionally much cheaper in computational time.

# Appendix C

# Heavy neutrino flux from meson induced $\nu$ flux

This appendix is an extended version of the appendix in reference [40].

Here it is described in detail how to derive a heavy neutrino flux from a light neutrino flux originated from meson decays, showing as a particular example the construction of the heavy neutrino flux in MiniBooNE given the kaon induced $\nu_\mu$ flux.

First, assuming that the light neutrino fluxes are produced from two body kaon decays, $K \to \ell\nu$, the kaon flux can be reconstructed relating by a Lorentz transformation the light neutrino momentum in the laboratory and in the kaon rest frames. Second, assuming that the kaons and the heavy neutrinos that are produced in kaon decays are parallel to the beam line, there are two contributions to the flux: the heavy neutrinos that go into the forward and backward directions in the kaon rest frame; which we called forward and backward flux contributions. The latter is important when the kaon momentum is large enough to boost the backward emitted neutrinos into the forward direction. Finally, a different weighting factor to account for the angular acceptance, given the geometry of the experiment, has to be included to both the backward and forward heavy neutrino flux contributions.

## C.1 Lorentz transformations

Given a laboratory frame $S$ and the kaon rest frame $S_0$ which moves with respect to the laboratory frame with a momentum $p_K$, the energy an momentum of other particles seen at each reference frame are related by the Lorentz transformations:

$$\begin{pmatrix} p_0 \\ E_0 \end{pmatrix} = \begin{pmatrix} \gamma & -\gamma\beta \\ -\gamma\beta & \gamma \end{pmatrix} \begin{pmatrix} p \\ E \end{pmatrix} ; \quad \begin{pmatrix} p \\ E \end{pmatrix} = \begin{pmatrix} \gamma & \gamma\beta \\ \gamma\beta & \gamma \end{pmatrix} \begin{pmatrix} p_0 \\ E_0 \end{pmatrix} ,$$

where $\gamma \equiv \frac{1}{\sqrt{1-\beta^2}}$, with $\beta = \frac{p_K}{E_K}$ and $\gamma = \frac{E_K}{m_K}$ .

## C.2 Kaon flux reconstruction

The light neutrino flux $\phi_{\nu_\mu}(p_{\nu_\mu})$ coming from kaon decays is taken from figs. 29 and 31 in reference [217], for the neutrino and anti-neutrino operation modes, respectively. Both $\nu_\mu$ from $K^+$ and $\bar{\nu}_\mu$ from $K^-$ fluxes are considered since both, $N$ and $\bar{N}$, equally contribute to the heavy neutrino flux. The signal at the MiniBooNE detector do not distinguish $N$ from $\bar{N}$, given the decay mechanism considered in section 4. Assuming that the $\nu_\mu$ flux coming

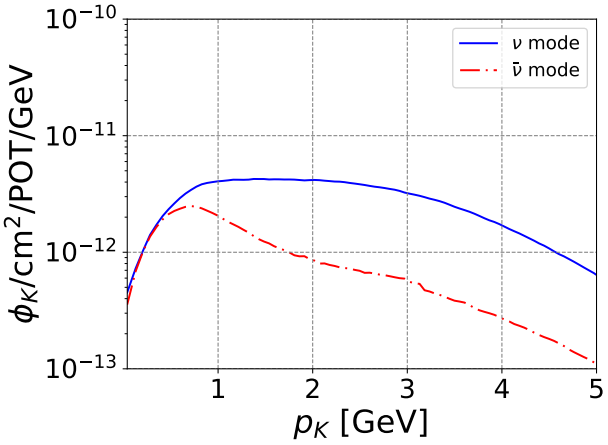


Figure C.2.1: Reconstructed kaon flux as a function of the kaon momentum, $\phi_K(p_K)$, for the neutrino mode (solid blue) and anti-neutrino mode (dashed red).

from kaon decays was produced by the two body decay $K \to \ell\nu$[1], the momentum of the neutrino in the kaon rest frame is fixed to

$$p_{\nu_0} = \frac{m_K^2 - m_\ell^2}{2m_K} ,$$

and can be related to their momentum in the lab frame, $p_\nu$, by the Lorentz transformation:

$$p_\nu = \frac{p_K}{m_K} E_{\nu_0} + \frac{E_K}{m_K} p_{\nu_0} .$$

Solving for $p_K$,

$$p_K = \frac{m_N}{2} \left( \frac{p_\nu}{p_{\nu_0}} - \frac{p_{\nu_0}}{p_\nu} \right) , \tag{C.2.1}$$

we find a one to one relation between the kaon and light neutrino momenta in the lab frame, $p_K$ and $p_\nu$. Then the kaon spectrum $\phi_K(p_K)$ can be reconstructed from the light neutrino flux in the laboratory frame $\phi_\nu(p_\nu)$, figure C.2.1

For the $\phi_\nu$ flux, both decays $K \to \mu^+\nu_\mu$ and $K \to \pi^0\mu^+\nu_\mu$, with branching ratios 63.44 % and 3.32 % respectively, are considered by the MiniBooNE collaboration, table I in reference [217]. That translates into a dominant contribution for the two body decay of 95 %, which means that under the assumption made here, a small error both in the normalization and shape of the kaon flux is introduced [2]. The light neutrino flux that has to be considered starts at $p_{\nu_0}$, for which the kaons decay at rest. At $p_{\nu_0}$ there is actually a peak feature, which corresponds to those neutrinos produced from stopped kaons, the ones that arrive at the end of the decay pipe and are stopped in the shield before decaying. That structure will be called the monochromatic peak from now on.

[1]Leptonic three body decays and other contributions from kaons to the light neutrino flux are not considered because there is not a one to one relation between the light and heavy neutrinos momenta generated in this processes, which is what the method described here is based on. This will introduce an uncertainty in the heavy neutrino reconstructed flux shape and normalization.

[2]Other contributions to the heavy neutrino flux, apart from the kaon decays, are not considered, which also introduces an uncertainty both in shape an normalization of the heavy neutrino flux.

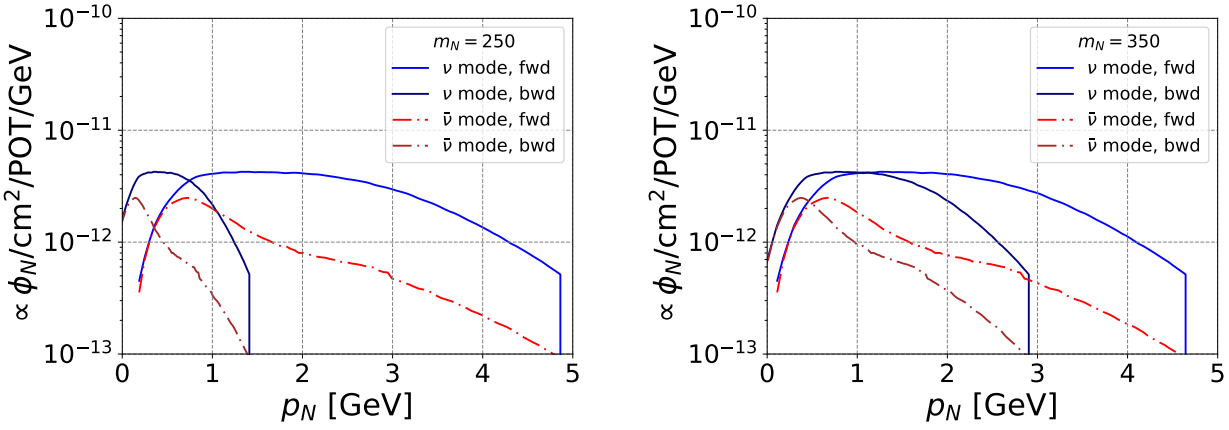


Figure C.3.1: Backward (purple and dashed brown) and forward (blue and dashed red) components of the heavy neutrino flux, for masses of 250 MeV (left panel) and 350 MeV right panel, assuming a parallel direction to the beam line, for the neutrino (solid lines) and anti-neutrino (dashed lines) modes. The forward component starts at $p_N = p_{N_0}$, while the backward component starts at $p_N = 0$. The spectra is neither normalized to the original light neutrino flux, nor the factor $\mathrm{Br}(K \to \ell N)/\mathrm{Br}(K \to \mu^+\nu_\mu)$ is included.

## C.3 Heavy neutrino flux

The kaons decay into heavy neutrinos together with a charged lepton, either muon or electron[3], $K \to \ell N$, producing a heavy neutrino flux. In the kaon rest frame the heavy neutrinos have a definite momentum

$$p_{N_0} = \frac{\sqrt{(m_K^2 - (m_N - m_\ell)^2)(m_K^2 - (m_N + m_\ell)^2)}}{2m_K} \,. \tag{C.3.1}$$

So, assuming that the heavy neutrino momenta in the lab frame is parallel to the beam line, it can be obtained via the Lorentz transformation:

$$p_N = \frac{p_K}{m_K} E_{N_0} \pm \frac{E_K}{m_K} p_{N_0} \,. \tag{C.3.2}$$

The $\pm$ sign corresponds to the forward and backward emitted neutrinos in the kaon rest frame, which give rise to two separate contributions to the heavy neutrino flux, called forward and backward. As can be seen in (C.3.2), given a heavy neutrino mass, for sufficiently large kaon momentum the heavy neutrinos produced in the backward direction in the kaon rest frame are boosted to the forward direction in the lab frame, i.e. $p_N$ is positive. Which for the light neutrinos can not happen, since $E_{\nu_0} \simeq p_{\nu_0}$, and then $p_N$, for those emitted in the backward direction in the kaon rest frame, is always negative.

The two components of the flux, backward and forward, have to be renormalized to the original light neutrino flux, since in both directions the same number of heavy neutrinos is emitted. Also the normalization factor $\mathrm{Br}(K \to \ell N)/\mathrm{Br}(K \to \mu^+\nu_\mu)$ (2.4.3), which accounts for the heavy neutrino mixing and the kinematical factors related to the helicity enhancement and phase space suppression with respect to the light neutrino case have to be taken into account.

In figure C.3.1, the two flux components, forward and backward, are shown for heavy neutrino masses $m_N = 250, 350\,\mathrm{MeV}$. They are not normalized to the original light neutrino flux, neither the factor $\mathrm{Br}(K \to \ell N)/\mathrm{Br}(K \to \mu^+\nu_\mu)$ is included. Note that the heavier is

[3]The kaons can not decay into a tau lepton because its mass is larger than the kaon mass.

the neutrino the larger are the momenta of the backward contribution to the flux, i.e. the heavier are the neutrinos the slower are emitted in the backward direction and the more they are boosted into the forward direction.

**Angular acceptance factor**

So far, the heavy neutrino flux components have been computed under the assumption that their momentum is parallel to the beam line. In reality, both light an heavy neutrinos are produced with an angle $\cos\theta$, and they will reach the detector provided it is smaller than the angular size of the detector $\theta_D = \arctan R/L \simeq R/L$, with $R$ the MiniBooNE detector radius and $L$ the baseline. The maximum decaying angle in the kaon rest frame, $\theta_N^{\rm rest}$, can be computed by solving:

$$\theta_D = \frac{p_{N,\perp}}{p_{N,\parallel}} = \frac{p_{N,0}\sin\theta_N^{\rm rest}}{\frac{p_K}{m_K}E_{N,0} \pm \frac{E_K}{m_K}p_{N,0}\cos\theta_N^{\rm rest}} \,. \tag{C.3.3}$$

here the parallel component of the momentum is boosted to the lab frame while the perpendicular component is unaffected. The + and − signs corresponds to the forward and backward decays. Approximating for small angles $\sin\theta \simeq \theta$, $\cos\theta \simeq 1$, equation (C.3.3) can be easily solved:

$$\theta_N^{\rm rest} = \frac{m_K}{p_{N,0}}\left(p_K E_{N,0} \pm E_K p_{N,0}\right)\theta_D \,. \tag{C.3.4}$$

The angular distribution in the kaon rest frame is isotropic, then the heavy neutrino flux components have to be corrected by adding a geometrical factor given by the ratio between the maximum acceptance angles for the heavy and light neutrinos, in the kaon rest frame:

$$f^{\rm fwd} = \frac{\theta_N^{\rm rest,\,fwd}}{\theta_\nu^{\rm rest}} \,; \quad f^{\rm bwd} = \frac{\theta_N^{\rm rest,\,bwd}}{\theta_\nu^{\rm rest}} \,. \tag{C.3.5}$$

Here it is assumed that the angular acceptance for light neutrinos is already included in the original flux $\phi_{\nu_\mu}$. For small angles, equation (C.3.5) have the form

$$f^{\rm fwd}(p_K) = \frac{\left(p_K E_{N,0} + E_K p_{N,0}\right)}{p_{N,0}\left(p_K + E_K\right)} \,; \quad f^{\rm bwd}(p_K) = \frac{\left(p_K E_{N,0} - E_K p_{N,0}\right)}{p_{N,0}\left(p_K + E_K\right)} \,. \tag{C.3.6}$$

Note that for the MiniBooNE proton beam energy, it might be considered that only the light neutrinos decaying in the forward direction reach the detector. Hence, the acceptance angle of the two components of the heavy neutrino, backward and forward, are compared to the light neutrino one in the forward direction.

These factors result in a different weight for the forward and backward contributions. For the same emission angle in the kaon rest frame, the backward and forward emitted neutrino face the detector with a different angle. This can be easily visualized in figure C.3.2, where the blue and red arrows corresponds to the forward and backward heavy neutrino momenta.

Rigorously, equation (C.3.3) has to be solved numerically for both light an heavy neutrinos, from which one can obtain the ratio of the two kaon rest frame angles, (C.3.5). The approximated expression (C.3.6) holds to good accuracy up to masses closed to $m_N \sim m_K + m_\mu$ and/or large kaon momenta. In the case of MiniBooNE, given the low kaon energies, up to 5 GeV, choosing not to be very close to the limiting heavy neutrino mass, the small angle approximation is very accurate. In figure C.3.3 the geometrical factors (C.3.5) and their approximation (C.3.6) are shown as a function of the kaon momentum, for the backward and

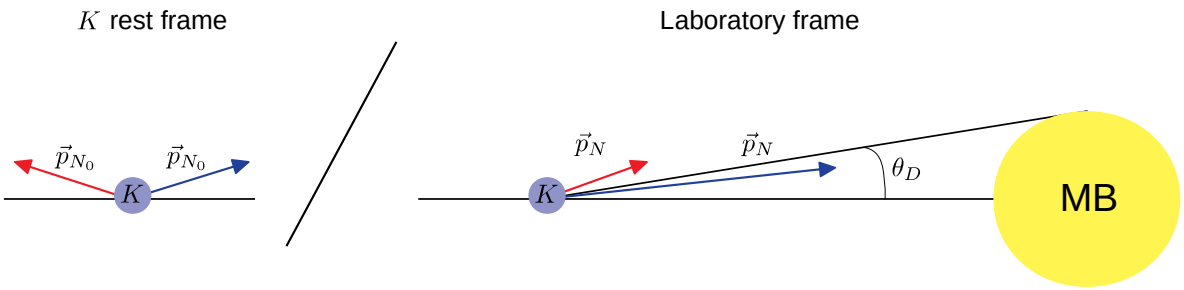


Figure C.3.2: Representations of the heavy neutrino momenta in the forward (blue) and backward (red) directions. In the kaon rest frame both are depicted decaying with the same angle and momentum (left panel). In the laboratory frame (right panel), after the Lorentz transformation is applied, they are different. $\theta_D$ is the angular size of the MiniBooNE detector, shown as a yellow disc.

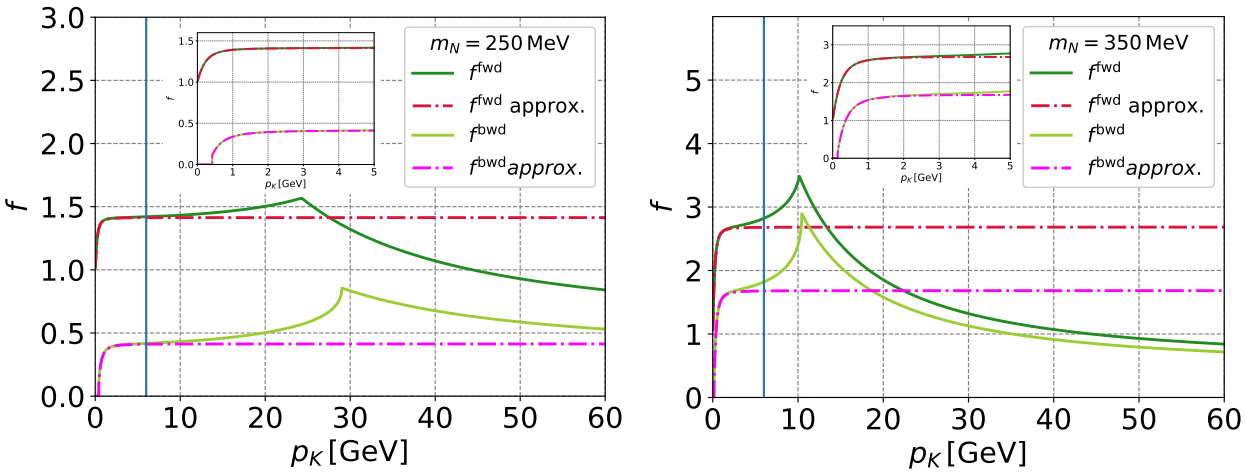


Figure C.3.3: Geometrical factors for the forward (green and red lines) and backward (light green and magenta lines) flux components as a function of the kaon momentum, for masses $m_N = 250\,\text{MeV}$ (left panel) and $m_N = 350\,\text{MeV}$ (right panel). Both the proper geometrical factors (solid lines) and their approximation are plotted (dotted-dashed). The blue vertical line, shows the maximum kaon momentum at MiniBooNE. A zoomed-in plot for the Kaon momentum at MiniBooNE is shown in each panel. The backward geometrical factor is zero utill the kaon momentum is large enough to forward boost the heavy neutrinos emitted in the backward direction.

forward flux components. The validity of the approximation for the MiniBooNE experiment can be seen in the zoomed-in plots in figure C.3.3.

In the whole range of kaon momentum the effect of the geometrical acceptance factors is that the low momentum part of the flux is suppressed with respect to the higher momenta. For larger kaon momenta the approximation starts to break down, and both forward and backward geometrical factors tend to a value close to 0.5. This can be understood, since for large enough kaon momentum even the light neutrinos emitted in a backward direction with an angle can be forward boosted, being the range of available angles $-1 < \cos\theta_\nu^{\text{rest}} < 1$, whereas the heavy neutrino flux components are considered separately, so that the angles can span only in half of the range, i.e. $0 < \cos\theta_N^{\text{rest}} < 1$, for both forward and backward components.

The geometrical factors (C.3.5), given as a function of the kaon momentum, $p_K$, can be expressed as a function of the heavy neutrino momentum, which can be computed perform-

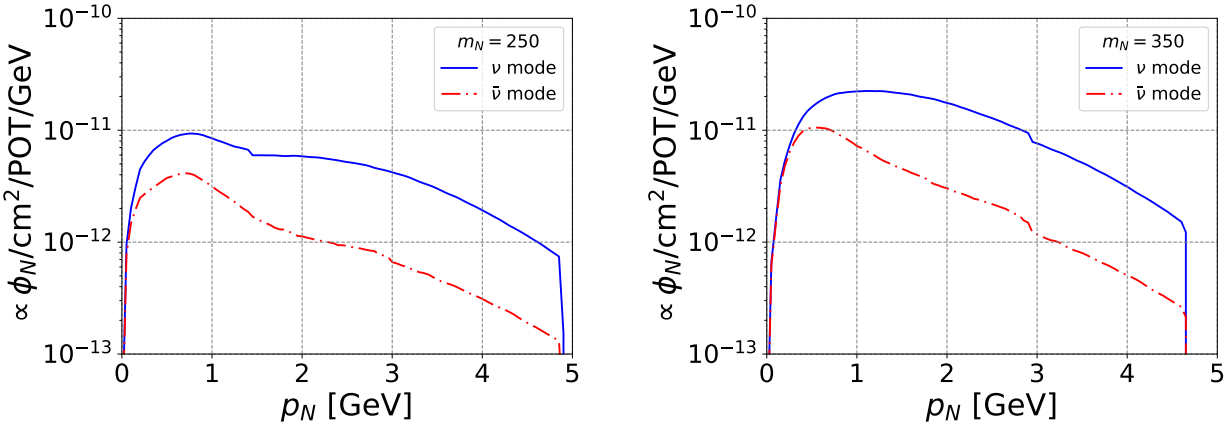


Figure C.3.4: Heavy neutrino flux, $\phi_N(p_N)$, for the neutrino (blue) and anti-neutrino (dashed red) modes, for masses $m_N = 250, 350\,\mathrm{MeV}$. The factor $\mathrm{Br}(K \to \ell N)/\mathrm{Br}(K \to \mu^+\nu_\mu)$ is not included.

ing the Lorentz transformation:

$$\frac{p_K}{m_K} E_N + \frac{E_N}{m_K} p_N = \pm p_{N,0}\,.$$

Solving for $p_K$:

$$p_K = \mp \frac{m_K}{m_N^2} E_N p_{N,0} + \frac{m_K}{m_N} \sqrt{\left(\frac{E_N\, p_{N,0}}{m_N}\right)^2 + p_N^2 - p_{N,0}^2}\,,$$

where upper (lower) signs apply to the forward (backward) geometrical factors. Note that in the forward decay case $p_N$ starts from $p_{N,0}$ and in the backward decay from 0.

The heavy neutrino flux is obtained summing both components weighted by the angular acceptance factors:

$$\Phi_N(p_N) = f^{\mathrm{fwd}}(p_N, m_N)\Phi_N^{\mathrm{fwd}}(p_N, m_N) + f^{\mathrm{bwd}}(p_N, m_N)\Phi_N^{\mathrm{bwd}}(p_N, m_N)\,.$$

In figure C.3.4 the final flux for the neutrino and anti-neutrino modes is shown, for masses $m_N = 250, 350\,\mathrm{MeV}$.

Finally, the monochromatic peak at $p_{N_0}$ is added by hand to the final flux, which for the original $\phi_\nu$ flux has a magnitude of $6.36(7.25) \times 10^{-13}\,\mathrm{cm}^{-2}/\mathrm{POT}$ in the neutrino (anti-neutrino) mode. Extracted from figs. 29 and 31 in reference [217].

# Appendix D

# 3+2 type-I seesaw parameterizations

In this appendix we derive in detail the seesaw parameterizations used in [76].

The objective of this appendix is to show a possible parameterization for a general type-I seesaw and the low-scale linear+inverse seesaw [228], both with only two extra neutrino species, ($(3+2)\nu$ seesaw).

These parameterizations were used in [76] in order to study the interplay between the $\beta$ and $0\nu\beta\beta$ decay for the discrimiation between different low-scale seesaw realizations [77–80] involving at least one heavy neutrino in the KeV range. The interest on these models arise from the fact that the KATRIN experiment future upgrade (TRISTAN) [229] can search for heavy neutrinos in the range $\sim [1, 18]$KeV, with a mixing $|U_{e4}|^2 \lesssim 10^{-6}$.

The parameterizations presented here are constructed such that they are compatible with the $3\nu$ standard measured parameters, cf. table 2.1.

## D.1 Low-scale seesaw realizations

For a general $(3+2)\nu$ seesaw, the mass matrix (2.3.4) have the form:

$$\mathcal{M} = \begin{pmatrix} 0 & m_D \\ m_D^T & M \end{pmatrix} , \tag{D.1.1}$$

where the Dirac, $m_D$, and Majorana $M$, matrices have dimensions $3 \times 2$ and $2 \times 2$, respectively. In the seesaw limit, the scale of $m_D$ is much smaller[1] than the scale of $M$. The mass matrix can be diagonalized by a unitary matrix $\mathcal{U}$:

$$\mathcal{U}^T M \mathcal{U} = \text{diag}\left\{m_1, m_2, m_3, m_4, m_5\right\} , \tag{D.1.2}$$

giving rise to the neutrino mass spectrum. $\mathcal{U}$ is the mixing matrix that relates the massive eigenstates to the active, $\nu_L$, and new sterile, $\nu_R$, neutrinos. $m_1$, $m_2$ and $m_3$ are the light and $m_4$ and $m_5$ the heavy neutrino masses. In this case, in which only two new neutrino species are added, the rank of the matrix (D.1.1) is four, so it follows that the lightest neutrino is massless[2].

The mass squared differences, measured in neutrino oscillations, tell us that at least two light neutrinos have non-zero mass, cf. table 2.1. Therefore, in order to give mass to the light neutrinos through the type-I seesaw mechanism, cf. (2.3.3), there must be at least

[1] A way of defining the scale of the matrix is by the square root of the determinant of the squared matrix: $\sqrt{\det\left\{m_D^\dagger m_D\right\}} \ll \sqrt{\det\left\{M^\dagger M\right\}}$.

[2] The rank of a matrix is invariant under the base choice.

two new neutrino species. This is so, because the mass matrix (D.1.1) with only one right-handed neutrino would have at most rank two. Hence, the neutrino mass spectrum would consist of two massive neutrinos and two massless, the latter corresponding to two of the light neutrinos. Adding three neutrino species instead, the matrix can have rank six and hence all the neutrinos can have non-zero mass.

**Linear and inverse seesaw**

The mass matrix (D.1.2) corresponds to a general type-I seesaw mechanism (2.3.3). Some particular realizations of this mechanism are based on an approximate lepton number symmetry, like the linear seesaw (LSS) [230,231] and the inverse seesaw (ISS) [232–234]. In these models, the neutrino masses are generated when the lepton number symmetry is broken. The smallness of the neutrino masses is achieved when the symmetry is broken perturbatively, by adding small lepton number violating parameters. The small parameters also break the degeneracy of the heavy neutrino masses, which constitute heavy pseudo-Dirac states [228, 235].

Adding two extra sterile neutrinos $\nu_{s,1}$ and $\nu_{s,2}$ with lepton numbers $L = 1, -1$, respectively, the conserving lepton number $\mathcal{L}$agrangian is given by:

$$\mathcal{L} = \mathcal{L}_{\rm SM} + i\bar{\nu}_{s,1}\partial\!\!\!/\nu_{s,1} + i\bar{\nu}_{s,2}\partial\!\!\!/\nu_{s,2} - \left(Y_{\nu 1}\overline{L_L}\tilde{\phi}\nu_{s,1} + Y_{12}\bar{\nu}_{s,1}\tilde{\phi}\nu_{s,2} + h.c.\right) . \tag{D.1.3}$$

After EWSB, analogous to (2.3.4), the neutrino mass matrix in the base $\left\{\nu_L, \nu^C_{s,1}, \nu^C_{s,2}\right\}$ is given by[3]:

$$\mathcal{M} = \begin{pmatrix} 0_{(3\times3)} & \eta & 0_{(3\times1)} \\ \eta^T & 0 & \Lambda \\ 0_{(1\times3)} & \Lambda & 0 \end{pmatrix} \tag{D.1.4}$$

where $\eta = Y_{\nu 1}\frac{v}{2}$ is a $3 \times 1$ matrix and $\Lambda = Y_{12}\frac{v}{2}$ is a scalar parameter, with $v$ the Higgs vacuum expectation value. To provide masses to the light neutrinos, the lepton number symmetry has to be broken. Two common ways of accomplishing this are adding either a $3 \times 1$ matrix, $\epsilon$, or a scalar parameter, $\mu$, as follows:

$$\mathcal{M}_{\rm LSS} = \begin{pmatrix} 0 & \eta & \epsilon \\ \eta^T & 0 & \Lambda \\ \epsilon^T & \Lambda & 0 \end{pmatrix} \quad ; \qquad \mathcal{M}_{\rm ISS} = \begin{pmatrix} 0 & \eta & 0 \\ \eta^T & 0 & \Lambda \\ 0 & \Lambda & \mu \end{pmatrix} , \tag{D.1.5}$$

where the scale of the parameters $\epsilon$ and $\mu$ is smaller than the scale of $\eta$ and $\Lambda$. Here the first matrix corresponds to the LSS and the second one to the ISS. A combination of both, linear and inverse, it is called linear+inverse seesaw (LISS) [76, 228], whose mass matrix is given by:

$$\mathcal{M}_{\rm LISS} = \begin{pmatrix} 0 & \eta & \epsilon \\ \eta^T & 0 & \Lambda \\ \epsilon^T & \Lambda & \mu \end{pmatrix} . \tag{D.1.6}$$

## D.2 Parameterization

In this section we show parameterizations of the mass matrix (D.1.1) constructed in such a way that after diagonalization the $3\nu$ standard parameters are recovered, cf. table 2.1, for the general type-I seesaw and LISS.

[3]Implicitly, $\nu_L$ has the three components corresponding to the three active flavors.

**Block diagonalization**

In order to get the parameterizations, we can start block-diagonalizing the mass matrix (D.1.1). According to what is done in [236], we write the diagonalization matrix $\mathcal{U}$ as a block-diagonalization, $U_B$, and two unitary matrices, $U$ and $X$:

$$\mathcal{U} = \underbrace{\begin{pmatrix} A_{(3\times3)} & B_{(3\times2)} \\ C_{(2\times3)} & D_{(2\times2)} \end{pmatrix}}_{\equiv U_B} \begin{pmatrix} U_{(3\times3)} & 0 \\ 0 & X_{(2\times2)} \end{pmatrix}, \tag{D.2.1}$$

such that

$$U_B^T \mathcal{M} U_B = \begin{pmatrix} m_{\text{light}} & 0 \\ 0 & m_{\text{heavy}} \end{pmatrix}, \tag{D.2.2}$$

where $m_{\text{light}}$ and $m_{\text{heavy}}$ are $3\times3$ and $2\times2$ matrices, respectively. $U$ diagonalizes $m_{\text{light}}$, so we identify it with the PMNS matrix (2.2.1). Since we are not interested in how the heavy neutrinos mix among each other, we can work directly in the heavy neutrino mass basis without loss of generality, setting $X = \mathbb{1}$ and $m_{\text{heavy}} = \text{diag}\{M_1, M_2\}$, with $M_1, M_2 \in \mathbb{R}^+$.

Since the deviations from unitarity of the PMNS matrix are expected to be small, we have that $A \cdot U = (\mathbb{1} - \zeta)U$, where $\zeta$ is a small quantity. From the unitarity condition of $\mathcal{U}$, it follows that $\mathbb{1} = AA^\dagger + BB^\dagger$. Hence, since $A$ is close to the identity, $B$ has to be a small scale matrix.

Anologously as it is done in [236], we write $U_B$ as the exponential of a small scale $3\times2$ matrix[4], $\Theta$:

$$U_B = \exp\begin{pmatrix} 0_{(3\times3)} & \Theta \\ -\Theta^\dagger & 0_{(2\times2)} \end{pmatrix} \simeq \begin{pmatrix} \mathbb{1}_{(3\times3)} - \frac{1}{2}\Theta\Theta^\dagger & \Theta \\ -\Theta^\dagger & \mathbb{1}_{(2\times2)} - \frac{1}{2}\Theta^\dagger\Theta \end{pmatrix}. \tag{D.2.3}$$

In this approximation the mixing matrix is given by

$$\mathcal{U} = \begin{pmatrix} \left(\mathbb{1} - \frac{1}{2}\Theta\Theta^\dagger\right) U & \Theta X \\ -\Theta^\dagger U & \left(\mathbb{1} - \frac{1}{2}\Theta^\dagger\Theta\right) X \end{pmatrix}.$$

Note that for the choice that we made here, $X = \mathbb{1}$, $\Theta$ is the mixing of the heavy neutrinos with the active ones.

Using (D.2.3), from the 0 entries of (D.2.2) follows:

$$0 = m_D - \Theta^* M + \mathcal{O}\left(\Theta^2\right).$$

Solving for $\Theta$ we obtain:

$$\Theta^* = m_D M^{-1}, \tag{D.2.4}$$

in analogy to the one neutrino generation case, cf. (2.3.6). Using (D.2.3) and (D.2.4), from the two diagonal entries in (D.2.2) and neglecting terms $\mathcal{O}(M^{-2})$ we get:

$$m_{\text{light}} = -m_D M^{-1} m_D^T, \tag{D.2.5}$$

$$m_{\text{heavy}} = M + \left(M^{-1}\right)^\dagger m_D^\dagger m_D - \frac{1}{2} m_D^T m_D^* \left(M^{-1}\right)^* - \frac{1}{2} M \left(M^{-1}\right)^* m_D^\dagger m_D M^{-1}. \tag{D.2.6}$$

Now that the matrix is block-diagonalized, we can find the parameterization for $m_D$. Note that $M$ is already parameterized:

$$M = m_{\text{heavy}} + \mathcal{O}\left(M^{-1}\right).$$

Which in the case considered here, i.e. $X = \mathbb{1}$: $M = \text{diag}\{M_1, M_2\}$.

[4]Note that in [236] $\Theta$ is a $3\times3$ matrix, while here we are using an analogous procedure with a $3\times2$ matrix.

### General type-I seesaw parameterization

For a general type-I seesaw, in which to first approximation $M = \text{diag}\{M_1, M_2\}$, the $m_D$ parameterization can be found as follows.

Using expression (D.2.5) and imposing that the PMNS matrix (2.2.1) diagonalizes $m_{\text{light}}$, we find:

$$-U^T m_D M^{-1} m_D^T U = \text{diag}\{0, m_2, m_3\}\ , \tag{D.2.7}$$

for NO and $\text{diag}\{m_1, m_2, 0\}$ for IO[5]. Where $m_1, m_2, m_3$ are the light neutrino masses that satisfy the two mass squared differences $\Delta m^2_{\text{sol}}$ and $\Delta m^2_{\text{atm}}$, cf. section 2.2.

Following the prodecure done in [237], we can parametrize the Dirac mass defining a complex matrix that satisfies $R^T R = \text{diag}\{0, m_2, m_3\}$:

$$R_{(\text{NO})} = \begin{pmatrix} 0 & \sqrt{m_2}\cos(a+ib) & \sqrt{m_3}\sin(a+ib) \\ 0 & \mp\sqrt{m_2}\sin(a+ib) & \pm\sqrt{m_3}\cos(a+ib) \end{pmatrix}\ , \tag{D.2.8}$$

for NO and

$$R_{(\text{IO})} = \begin{pmatrix} \sqrt{m_1}\cos(a+ib) & \sqrt{m_2}\sin(a+ib) & 0 \\ \mp\sqrt{m_1}\sin(a+ib) & \pm\sqrt{m_2}\cos(a+ib) & 0 \end{pmatrix}\ , \tag{D.2.9}$$

for IO. Where $a, b \in \mathbb{R}$.

Rewriting (D.2.7) as[6]:

$$R^T R = -U^T m_D \sqrt{M^{-1}}\sqrt{M^{-1}} m_D^T U\ ,$$

we can identify $R = -i\sqrt{M^{-1}} m_D^T U$ and solve for $m_D$:

$$m_D^T = i\sqrt{M} R U^\dagger\ . \tag{D.2.10}$$

With this parameterization, there are six free parameters: $a$, $b$, $M_1$, $M_2$, $\delta_{\text{CP}}$ and $\alpha$. $a$ and $b$ are the real parameters introduced in the $R$ parameterization (D.2.8). $M_1$ and $M_2$ are the heavy Majorana masses, i.e. the diagonal elements of $M$. From the PMNS matrix, we considered only the Dirac phase $\delta_{\text{CP}}$ and the Majorana phases. Given the parameterization (2.2.1) and the form of the $R$ matrix, $m_D$ only depends on one of the Majorana phases, $\alpha$. The rest of the parameters can be considered fixed: the mixing angles $\theta_{12}$, $\theta_{13}$ and $\theta_{23}$, and the light neutrinos masses $m_2$ and $m_3$ or $m_1$ and $m_2$, depending on the ordering.

### LISS parameterization

In the LISS model, the mass matrix is given by (D.1.6). Identifying the Dirac and Majorana matrices according to (D.1.1) we obtain:

$$m_{D\ (3\times 2)} = \begin{pmatrix} \eta_{(3\times 1)} & \epsilon_{(3\times 1)} \end{pmatrix} \quad ; \qquad M = \begin{pmatrix} 0 & \Lambda \\ \Lambda & \mu \end{pmatrix}\ .$$

In the seesaw limit, i.e. $M$ scale[7] is much larger than $m_D$ scale, we can use expressions (D.2.5) and (D.2.6), giving rise to:

$$m_{\text{light}} = \frac{1}{\Lambda}\left(\mu\frac{\eta\eta^T}{\Lambda} - \left(\eta\epsilon^T + \epsilon\eta^T\right)\right) + \mathcal{O}\left(1/\Lambda^2\right) \tag{D.2.11}$$

$$m_{\text{heavy}} = \begin{pmatrix} 0 & \Lambda \\ \Lambda & \mu \end{pmatrix} + \mathcal{O}\left(1/\Lambda\right) \tag{D.2.12}$$

[5]For IO, the lightest neutrino mass is $\nu_3$, hence $m_3 = 0$.

[6]Remember that without loss of generality $M = \text{diag}\{M_1, M_2\}$ with $M_1, M_2 \in \mathbb{R}^+$, hence $\sqrt{M^{-1}} = \text{diag}\left\{\sqrt{M_1}, \sqrt{M_2}\right\}$.

[7]Since $\mu$ is a small parameter, the scale of $M$ is dominated by $\Lambda$.

where we have used the inverse of $M$:

$$M^{-1} = \frac{1}{\Lambda}\begin{pmatrix} -\frac{\mu}{\Lambda} & 1 \\ 1 & 0 \end{pmatrix} .$$

Note that in this case $\Theta$ is no longer the mixing between the heavy mass neutrinos and the active ones, but $\Theta X$ is instead, where $X$ is the $2\times 2$ unitary matrix that diagonalizes $M$.

Defining $\epsilon' = \epsilon - \frac{\mu}{2\Lambda}$, $m_{\text{light}}$ takes the form

$$m_{\text{light}} = -\frac{\eta\epsilon'^T + \epsilon'\eta^T}{\Lambda} .$$

From the diagonalization of $m_{\text{light}}$ with the PMNS matrix we get: $m_{\text{light}} = U^*\text{diag}\{0, m_2, m_3\}\, U^\dagger$ for NO and $m_{\text{light}} = U^*\text{diag}\{m_1, m_2, 0\}\, U^\dagger$ for IO. Explicitly they read

$$\begin{aligned} \text{NO}: \quad & -\frac{\eta_i\epsilon'_j + \epsilon'_i\eta_j}{\Lambda} = m_2 U^*_{i2}U^*_{j2} + m_3 U^*_{i3}U^*_{j3} , \\ \text{IO}: \quad & -\frac{\eta_i\epsilon'_j + \epsilon'_i\eta_j}{\Lambda} = m_1 U^*_{i1}U^*_{j1} + m_2 U^*_{i2}U^*_{j2} , \end{aligned}$$

and their solutions are given by

$$\begin{aligned} \text{NO}: \quad & \eta_j = \xi\frac{\sqrt{\Lambda}}{\sqrt{2}}\left(\sqrt{m_3}U^*_{i3} + i\sqrt{m_2}U^*_{i2}\right) \;; \quad \epsilon'_j = \frac{1}{\xi}\frac{\sqrt{\Lambda}}{\sqrt{2}}\left(\sqrt{m_3}U^*_{i3} - i\sqrt{m_2}U^*_{i2}\right) . \\ \text{IO}: \quad & \eta_j = \xi\frac{\sqrt{\Lambda}}{\sqrt{2}}\left(\sqrt{m_2}U^*_{i2} + i\sqrt{m_1}U^*_{i1}\right) \;; \quad \epsilon'_j = \frac{1}{\xi}\frac{\sqrt{\Lambda}}{\sqrt{2}}\left(\sqrt{m_2}U^*_{i2} - i\sqrt{m_1}U^*_{i1}\right) . \end{aligned}$$

Here, $\xi$ is a real parameter that have to satisfy that the scale of the $\eta$ and $\epsilon$ matrices is much smaller than the scale of $M$, being the latter dominated by $\Lambda$.

Undoing the change of variables $\epsilon' = \epsilon - \frac{\mu}{2\Lambda}$, we reach the LISS parameterization:

$$\begin{aligned} \text{NO}: \quad & \eta_j = \xi\frac{\sqrt{\Lambda}}{\sqrt{2}}\left(\sqrt{m_3}U^*_{i3} + i\sqrt{m_2}U^*_{i2}\right) \;; \quad \epsilon_j = \frac{1}{\xi}\frac{\sqrt{\Lambda}}{\sqrt{2}}\left(\sqrt{m_3}U^*_{i3} - i\sqrt{m_2}U^*_{i2}\right) + \frac{\mu}{2\Lambda} \\ \text{IO}: \quad & \eta_j = \xi\frac{\sqrt{\Lambda}}{\sqrt{2}}\left(\sqrt{m_2}U^*_{i2} + i\sqrt{m_1}U^*_{i1}\right) \;; \quad \epsilon_j = \frac{1}{\xi}\frac{\sqrt{\Lambda}}{\sqrt{2}}\left(\sqrt{m_2}U^*_{i2} - i\sqrt{m_1}U^*_{i1}\right) + \frac{\mu}{2\Lambda} . \end{aligned} \tag{D.2.13}$$

In this parameterization, the free parameters are given by $\Lambda$, $\mu$ and $\xi$, and the $\delta_{\text{CP}}$ phase and one of the Majorana phases, $\alpha$, from the PMNS matrix. In [76] we chose, $\Lambda, \xi \in \mathbb{R}$ and $\mu \in \mathbb{C}$. Thus, there are six free parameters in total. As in the general type-I seesaw, the mixing angles $\theta_{12}$, $\theta_{13}$ and $\theta_{23}$, and the light neutrinos masses $m_2$ and $m_3$ or $m_1$ and $m_2$, depending on the ordering, are considered fixed.

The heavy mass spectrum in the LISS is obtained diagonalizing (D.2.12):

$$m_{4,5} = \Lambda \pm \frac{1}{2}|\mu| , \tag{D.2.14}$$

with the heavy mass splitting given by the lepton number violating parameter $\mu$, to leading order.

The parameterizations in (D.2.10) and (D.2.13) are such that in the outcome of the diagonalization of the mass matrix $\mathcal{M}$ (D.1.1), which is used in the studies performed in [76], one recovers the $3\nu$ standard neutrino parameter values, cf. table 2.1, regardless of the values chosen for the free parameters.

# Bibliography


[1] W. Pauli, *Dear radioactive ladies and gentlemen*, *Phys. Today* **31N9** (1978) 27.

[2] C. L. Cowan, F. Reines, F. B. Harrison, H. W. Kruse, and A. D. McGuire, *Detection of the free neutrino: A Confirmation*, *Science* **124** (1956) 103–104.

[3] B. Pontecorvo, *Mesonium and anti-mesonium*, *Sov. Phys. JETP* **6** (1957) 429. [Zh. Eksp. Teor. Fiz.33,549(1957)].

[4] B. Pontecorvo, *Neutrino Experiments and the Problem of Conservation of Leptonic Charge*, *Sov. Phys. JETP* **26** (1968) 984–988. [Zh. Eksp. Teor. Fiz.53,1717(1967)].

[5] R. Davis, Jr., D. S. Harmer, and K. C. Hoffman, *Search for neutrinos from the sun*, *Phys. Rev. Lett.* **20** (1968) 1205–1209.

[6] R. Becker-Szendy et al., *Neutrino measurements with the IMB detector*, *Nucl. Phys. Proc. Suppl.* **38** (1995) 331–336.

[7] **Kamiokande**, Y. Fukuda et al., *Atmospheric muon-neutrino / electron-neutrino ratio in the multiGeV energy range*, *Phys. Lett.* **B335** (1994) 237–245.

[8] **Super-Kamiokande**, Y. Fukuda et al., *Neutrino induced upward stopping muons in Super-Kamiokande*, *Phys. Lett.* **B467** (1999) 185–193, [hep-ex/9908049].

[9] S. L. Glashow, *Partial Symmetries of Weak Interactions*, *Nucl. Phys.* **22** (1961) 579–588.

[10] S. Weinberg, *A Model of Leptons*, *Phys. Rev. Lett.* **19** (1967) 1264–1266.

[11] P. Minkowski, $\mu \to e\gamma$ *at a Rate of One Out of* $10^9$ *Muon Decays?*, *Phys. Lett.* **67B** (1977) 421–428.

[12] R. N. Mohapatra and G. Senjanovic, *Neutrino Mass and Spontaneous Parity Nonconservation*, *Phys. Rev. Lett.* **44** (1980) 912. [,231(1979)].

[13] T. Yanagida, *Horizontal gauge symmetry and masses of neutrinos*, *Conf. Proc.* **C7902131** (1979) 95–99.

[14] M. Gell-Mann, P. Ramond, and R. Slansky, *Complex Spinors and Unified Theories*, *Conf. Proc.* **C790927** (1979) 315–321, [1306.4669].

[15] Z. Maki, M. Nakagawa, and S. Sakata, *Remarks on the unified model of elementary particles*, *Prog. Theor. Phys.* **28** (1962) 870–880. [,34(1962)].

[16] V. N. Gribov and B. Pontecorvo, *Neutrino astronomy and lepton charge*, *Phys. Lett.* **28B** (1969) 493.

[17] M. Fukugita and T. Yanagida, *Baryogenesis Without Grand Unification*, *Phys. Lett.* **B174** (1986) 45–47.

[18] E. K. Akhmedov, V. A. Rubakov, and A. Yu. Smirnov, *Baryogenesis via neutrino oscillations*, *Phys. Rev. Lett.* **81** (1998) 1359–1362, [hep-ph/9803255].

[19] L. Canetti, M. Drewes, and M. Shaposhnikov, *Matter and Antimatter in the Universe*, *New J. Phys.* **14** (2012) 095012, [1204.4186].

[20] S. Mele, *The Measurement of the Number of Light Neutrino Species at LEP*, *Adv. Ser. Direct. High Energy Phys.* **23** (2015) 89–106.

[21] S. Dodelson and L. M. Widrow, *Sterile-neutrinos as dark matter*, *Phys. Rev. Lett.* **72** (1994) 17–20, [hep-ph/9303287].

[22] S. Böser, C. Buck, C. Giunti, J. Lesgourgues, L. Ludhova, et al., *Status of Light Sterile Neutrino Searches*, 1906.01739.

[23] R. E. Shrock, *General Theory of Weak Leptonic and Semileptonic Decays. 1. Leptonic Pseudoscalar Meson Decays, with Associated Tests For, and Bounds on, Neutrino Masses and Lepton Mixing*, *Phys. Rev.* **D24** (1981) 1232.

[24] A. Atre, T. Han, S. Pascoli, and B. Zhang, *The Search for Heavy Majorana Neutrinos*, *JHEP* **05** (2009) 030, [0901.3589].

[25] S. Antusch, C. Biggio, E. Fernandez-Martinez, M. B. Gavela, and J. Lopez-Pavon, *Unitarity of the Leptonic Mixing Matrix*, *JHEP* **10** (2006) 084, [hep-ph/0607020].

[26] I. Esteban, M. C. Gonzalez-Garcia, A. Hernandez-Cabezudo, M. Maltoni, and T. Schwetz, *Global analysis of three-flavour neutrino oscillations: synergies and tensions in the determination of $\theta_2 3, \delta_C P$, and the mass ordering*, *JHEP* **01** (2019) 106, [1811.05487].

[27] "Nufit webpage." http://www.nu-fit.org.

[28] A. Hernandez-Cabezudo, S. J. Parke, and S.-H. Seo, *Constraint on the solar $\Delta m^2$ using 4,000 days of short baseline reactor neutrino data*, 1905.09479.

[29] **LSND**, A. Aguilar-Arevalo et al., *Evidence for neutrino oscillations from the observation of anti-neutrino(electron) appearance in a anti-neutrino(muon) beam*, *Phys. Rev.* **D64** (2001) 112007, [hep-ex/0104049].

[30] **MiniBooNE**, A. A. Aguilar-Arevalo et al., *Event Excess in the MiniBooNE Search for $\bar{\nu}_\mu \to \bar{\nu}_e$ Oscillations*, *Phys. Rev. Lett.* **105** (2010) 181801, [1007.1150].

[31] M. A. Acero, C. Giunti, and M. Laveder, *Limits on nu(e) and anti-nu(e) disappearance from Gallium and reactor experiments*, *Phys. Rev.* **D78** (2008) 073009, [0711.4222].

[32] C. Giunti and M. Laveder, *Statistical Significance of the Gallium Anomaly*, *Phys. Rev.* **C83** (2011) 065504, [1006.3244].

[33] G. Mention, M. Fechner, T. Lasserre, T. A. Mueller, D. Lhuillier, et al., *The Reactor Antineutrino Anomaly*, *Phys. Rev.* **D83** (2011) 073006, [1101.2755].

[34] **Daya Bay**, F. P. An et al., *Evolution of the Reactor Antineutrino Flux and Spectrum at Daya Bay*, *Phys. Rev. Lett.* **118** (2017), no. 25 251801, [1704.01082].

[35] **RENO**, G. Bak et al., *Fuel-composition dependent reactor antineutrino yield at RENO*, *Phys. Rev. Lett.* **122** (2019), no. 23 232501, [1806.00574].

[36] M. Dentler, A. Hernandez-Cabezudo, J. Kopp, M. Maltoni, and T. Schwetz, *Sterile neutrinos or flux uncertainties? — Status of the reactor anti-neutrino anomaly*, *JHEP* **11** (2017) 099, [1709.04294].

[37] M. Dentler, A. Hernandez-Cabezudo, J. Kopp, P. A. N. Machado, M. Maltoni, et al., *Updated Global Analysis of Neutrino Oscillations in the Presence of eV-Scale Sterile Neutrinos*, *JHEP* **08** (2018) 010, [1803.10661].

[38] **MiniBooNE**, A. Aguilar-Arevalo et al., *Improved Search for $\bar{\nu}_\mu \to \bar{\nu}_e$ Oscillations in the MiniBooNE Experiment*, *Phys.Rev.Lett.* **110** (2013) 161801, [1207.4809].

[39] **MiniBooNE**, A. A. Aguilar-Arevalo et al., *Significant Excess of ElectronLike Events in the MiniBooNE Short-Baseline Neutrino Experiment*, *Phys. Rev. Lett.* **121** (2018), no. 22 221801, [1805.12028].

[40] O. Fischer, A. Hernandez-Cabezudo, and T. Schwetz, *Explaining the MiniBooNE excess by a decaying sterile neutrino with mass in the 250 MeV range*, 1909.09561.

[41] S. M. Bilenky and S. T. Petcov, *Massive neutrinos and neutrino oscillations*, *Rev. Mod. Phys.* **59** (Jul, 1987) 671–754.

[42] C. Giunti and C. W. Kim, *Fundamentals of Neutrino Physics and Astrophysics*. 2007.

[43] **KATRIN**, M. Aker et al., *An improved upper limit on the neutrino mass from a direct kinematic method by KATRIN*, 1909.06048.

[44] E. Ma, *Pathways to naturally small neutrino masses*, *Phys. Rev. Lett.* **81** (1998) 1171–1174, [hep-ph/9805219].

[45] K. S. Babu, *Model of 'Calculable' Majorana Neutrino Masses*, *Phys. Lett.* **B203** (1988) 132–136.

[46] A. de Gouvêa and A. Kobach, *Global Constraints on a Heavy Neutrino*, *Phys. Rev.* **D93** (2016), no. 3 033005, [1511.00683].

[47] K. N. Abazajian, *Sterile neutrinos in cosmology*, *Phys. Rept.* **711-712** (2017) 1–28, [1705.01837].

[48] M. Drewes et al., *A White Paper on keV Sterile Neutrino Dark Matter*, *JCAP* **1701** (2017), no. 01 025, [1602.04816].

[49] K. N. Abazajian et al., *Light Sterile Neutrinos: A White Paper*, 1204.5379.

[50] S. Mertens, T. Lasserre, S. Groh, G. Drexlin, F. Glueck, et al., *Sensitivity of Next-Generation Tritium Beta-Decay Experiments for keV-Scale Sterile Neutrinos*, *JCAP* **1502** (2015), no. 02 020, [1409.0920].

[51] N. M. N. Steinbrink, J. D. Behrens, S. Mertens, P. C. O. Ranitzsch, and C. Weinheimer, *keV-Scale Sterile Neutrino Sensitivity Estimation with Time-Of-Flight Spectroscopy in KATRIN using Self-Consistent Approximate Monte Carlo*, *Eur. Phys. J.* **C78** (2018), no. 3 212, [1710.04939].

[52] D. A. Bryman and R. Shrock, *Constraints on Sterile Neutrinos in the MeV to GeV Mass Range*, 1909.11198.

[53] **NA62**, E. Cortina Gil et al., *Search for heavy neutral lepton production in $K^+$ decays*, *Phys. Lett.* **B778** (2018) 137–145, [1712.00297].

[54] **E949**, A. V. Artamonov et al., *Search for heavy neutrinos in $K^+ \to \mu^+ \nu_H$ decays*, *Phys. Rev.* **D91** (2015), no. 5 052001, [1411.3963]. [Erratum: Phys. Rev.D91,no.5,059903(2015)].

[55] **LHCb**, R. Aaij et al., *Searches for Majorana neutrinos in $B^-$ decays*, *Phys. Rev.* **D85** (2012) 112004, [1201.5600].

[56] **LHCb**, R. Aaij et al., *Search for Majorana neutrinos in $B^- \to \pi^+ \mu^- \mu^-$ decays*, *Phys. Rev. Lett.* **112** (2014), no. 13 131802, [1401.5361].

[57] B. Shuve and M. E. Peskin, *Revision of the LHCb Limit on Majorana Neutrinos*, *Phys. Rev.* **D94** (2016), no. 11 113007, [1607.04258].

[58] **Belle**, D. Liventsev et al., *Search for heavy neutrinos at Belle*, *Phys. Rev.* **D87** (2013), no. 7 071102, [1301.1105]. [Erratum: Phys. Rev.D95,no.9,099903(2017)].

[59] W.-Y. Keung and G. Senjanovic, *Majorana Neutrinos and the Production of the Right-handed Charged Gauge Boson*, *Phys. Rev. Lett.* **50** (1983) 1427.

[60] A. M. Gago, P. Hernández, J. Jones-Pérez, M. Losada, and A. Moreno Briceño, *Probing the Type I Seesaw Mechanism with Displaced Vertices at the LHC*, *Eur. Phys. J.* **C75** (2015), no. 10 470, [1505.05880].

[61] S. Antusch, E. Cazzato, and O. Fischer, *Sterile neutrino searches via displaced vertices at LHCb*, *Phys. Lett.* **B774** (2017) 114–118, [1706.05990].

[62] Y. Cai, T. Han, T. Li, and R. Ruiz, *Lepton Number Violation: Seesaw Models and Their Collider Tests*, *Front.in Phys.* **6** (2018) 40, [1711.02180].

[63] K. Bondarenko, A. Boyarsky, D. Gorbunov, and O. Ruchayskiy, *Phenomenology of GeV-scale Heavy Neutral Leptons*, *JHEP* **11** (2018) 032, [1805.08567].

[64] S. Antusch, E. Cazzato, and O. Fischer, *Sterile neutrino searches at future $e^-e^+$, $pp$, and $e^-p$ colliders*, *Int. J. Mod. Phys.* **A32** (2017), no. 14 1750078, [1612.02728].

[65] J. Hernandez-Garcia and J. Lopez-Pavon, *Non-Unitarity vs sterile neutrinos at DUNE*, in *Proceedings, Prospects in Neutrino Physics (NuPhys2016): London, UK, December 12-14, 2016*, 2017. 1705.01840.

[66] S. Antusch and O. Fischer, *Non-unitarity of the leptonic mixing matrix: Present bounds and future sensitivities*, *JHEP* **10** (2014) 094, [1407.6607].

[67] W. Rodejohann, *Neutrino-less Double Beta Decay and Particle Physics*, *Int. J. Mod. Phys.* **E20** (2011) 1833–1930, [1106.1334].

[68] F. F. Deppisch, M. Hirsch, and H. Pas, *Neutrinoless Double Beta Decay and Physics Beyond the Standard Model*, *J. Phys.* **G39** (2012) 124007, [1208.0727].

[69] S. M. Bilenky and C. Giunti, *Neutrinoless Double-Beta Decay: a Probe of Physics Beyond the Standard Model*, *Int. J. Mod. Phys.* **A30** (2015), no. 04n05 1530001, [1411.4791].

[70] H. Päs and W. Rodejohann, *Neutrinoless Double Beta Decay*, *New J. Phys.* **17** (2015), no. 11 115010, [1507.00170].

[71] S. Dell'Oro, S. Marcocci, M. Viel, and F. Vissani, *Neutrinoless double beta decay: 2015 review*, *Adv. High Energy Phys.* **2016** (2016) 2162659, [1601.07512].

[72] **GERDA**, M. Agostini et al., *Improved Limit on Neutrinoless Double-$\beta$ Decay of $^{76}$Ge from GERDA Phase II*, *Phys. Rev. Lett.* **120** (2018), no. 13 132503, [1803.11100].

[73] **KamLAND-Zen**, A. Gando et al., *Search for Majorana Neutrinos near the Inverted Mass Hierarchy Region with KamLAND-Zen*, *Phys. Rev. Lett.* **117** (2016), no. 8 082503, [1605.02889]. [Addendum: Phys. Rev. Lett.117,no.10,109903(2016)].

[74] P. Benes, A. Faessler, F. Simkovic, and S. Kovalenko, *Sterile neutrinos in neutrinoless double beta decay*, *Phys. Rev.* **D71** (2005) 077901, [hep-ph/0501295].

[75] M. Blennow, E. Fernandez-Martinez, J. Lopez-Pavon, and J. Menendez, *Neutrinoless double beta decay in seesaw models*, *JHEP* **07** (2010) 096, [1005.3240].

[76] A. Abada, A. Hernandez-Cabezudo, and X. Marcano, *Beta and Neutrinoless Double Beta Decays with KeV Sterile Fermions*, *JHEP* **01** (2019) 041, [1807.01331].

[77] M. B. Gavela, T. Hambye, D. Hernandez, and P. Hernandez, *Minimal Flavour Seesaw Models*, *JHEP* **09** (2009) 038, [0906.1461].

[78] A. Ibarra, E. Molinaro, and S. T. Petcov, *TeV Scale See-Saw Mechanisms of Neutrino Mass Generation, the Majorana Nature of the Heavy Singlet Neutrinos and $(\beta\beta)_{0\nu}$-Decay*, *JHEP* **09** (2010) 108, [1007.2378].

[79] A. Donini, P. Hernandez, J. Lopez-Pavon, and M. Maltoni, *Minimal models with light sterile neutrinos*, *JHEP* **07** (2011) 105, [1106.0064].

[80] A. Abada and M. Lucente, *Looking for the minimal inverse seesaw realisation*, *Nucl. Phys.* **B885** (2014) 651–678, [1401.1507].

[81] V. A. Rubakov and D. S. Gorbunov, *Introduction to the Theory of the Early Universe*. World Scientific, Singapore, 2017.

[82] R. H. Cyburt, B. D. Fields, K. A. Olive, and T.-H. Yeh, *Big Bang Nucleosynthesis: 2015*, *Rev. Mod. Phys.* **88** (2016) 015004, [1505.01076].

[83] **Planck**, N. Aghanim et al., *Planck 2018 results. VI. Cosmological parameters*, 1807.06209.

[84] Q.-G. Huang, K. Wang, and S. Wang, *Constraints on the neutrino mass and mass hierarchy from cosmological observations*, *Eur. Phys. J.* **C76** (2016), no. 9 489, [1512.05899].

[85] E. Giusarma, M. Gerbino, O. Mena, S. Vagnozzi, S. Ho, et al., *Improvement of cosmological neutrino mass bounds*, *Phys. Rev.* **D94** (2016), no. 8 083522, [1605.04320].

[86] S. Gariazzo, P. F. de Salas, and S. Pastor, *Thermalisation of sterile neutrinos in the early Universe in the 3+1 scheme with full mixing matrix*, *JCAP* **1907** (2019), no. 07 014, [1905.11290].

[87] J. Hamann, S. Hannestad, G. G. Raffelt, and Y. Y. Y. Wong, *Sterile neutrinos with eV masses in cosmology: How disfavoured exactly?*, *JCAP* **1109** (2011) 034, [1108.4136].

[88] X. Chu, B. Dasgupta, M. Dentler, J. Kopp, and N. Saviano, *Sterile neutrinos with secret interactions—cosmological discord?*, *JCAP* **1811** (2018), no. 11 049, [1806.10629].

[89] A. D. Dolgov, S. H. Hansen, G. Raffelt, and D. V. Semikoz, *Heavy sterile neutrinos: Bounds from big bang nucleosynthesis and SN1987A*, *Nucl. Phys.* **B590** (2000) 562–574, [hep-ph/0008138].

[90] O. Ruchayskiy and A. Ivashko, *Restrictions on the lifetime of sterile neutrinos from primordial nucleosynthesis*, *JCAP* **1210** (2012) 014, [1202.2841].

[91] C. Benso, V. Brdar, M. Lindner, and W. Rodejohann, *Prospects for Finding Sterile Neutrino Dark Matter at KATRIN*, 1911.00328.

[92] C. Giganti, S. Lavignac, and M. Zito, *Neutrino oscillations: the rise of the PMNS paradigm*, *Prog. Part. Nucl. Phys.* **98** (2018) 1–54, [1710.00715].

[93] C. Giunti, *Neutrino Flavor States and the Quantum Theory of Neutrino Oscillations*, *AIP Conf. Proc.* **1026** (2008), no. 1 3–19, [0801.0653].

[94] E. K. Akhmedov and A. Yu. Smirnov, *Neutrino oscillations: Entanglement, energy-momentum conservation and QFT*, *Found. Phys.* **41** (2011) 1279–1306, [1008.2077].

[95] S. P. Mikheev and A. Yu. Smirnov, *Resonance Amplification of Oscillations in Matter and Spectroscopy of Solar Neutrinos*, *Sov. J. Nucl. Phys.* **42** (1985) 913–917. [Yad. Fiz.42,1441(1985)].

[96] L. Wolfenstein, *Neutrino Oscillations in Matter*, *Phys. Rev.* **D17** (1978) 2369–2374.

[97] E. K. Akhmedov, *Neutrino physics*, in *Proceedings, Summer School in Particle Physics: Trieste, Italy, June 21-July 9, 1999*, pp. 103–164, 1999. hep-ph/0001264.

[98] K. Schreckenbach, G. Colvin, W. Gelletly, and F. Von Feilitzsch, *DETERMINATION OF THE ANTI-NEUTRINO SPECTRUM FROM U-235 THERMAL NEUTRON FISSION PRODUCTS UP TO 9.5-MEV*, *Phys. Lett.* **160B** (1985) 325–330.

[99] A. A. Hahn, K. Schreckenbach, G. Colvin, B. Krusche, W. Gelletly, et al., *Anti-neutrino Spectra From $^{241}$Pu and $^{239}$Pu Thermal Neutron Fission Products*, *Phys. Lett.* **B218** (1989) 365–368.

[100] F. Von Feilitzsch, A. A. Hahn, and K. Schreckenbach, *EXPERIMENTAL BETA SPECTRA FROM PU-239 AND U-235 THERMAL NEUTRON FISSION PRODUCTS AND THEIR CORRELATED ANTI-NEUTRINOS SPECTRA*, *Phys. Lett.* **118B** (1982) 162–166.

[101] P. Vogel, G. K. Schenter, F. M. Mann, and R. E. Schenter, *Reactor Anti-neutrino Spectra and Their Application to Anti-neutrino Induced Reactions. 2.*, *Phys. Rev.* **C24** (1981) 1543–1553.

[102] P. Huber, *On the determination of anti-neutrino spectra from nuclear reactors*, *Phys. Rev.* **C84** (2011) 024617, [1106.0687]. [Erratum: Phys. Rev.C85,029901(2012)].

[103] T. A. Mueller et al., *Improved Predictions of Reactor Antineutrino Spectra*, *Phys. Rev.* **C83** (2011) 054615, [1101.2663].

[104] J. Berryman and P. Huber, *Reevaluating Reactor Antineutrino Anomalies with Updated Flux Predictions*, 1909.09267.

[105] **KamLAND**, A. Gando et al., *Reactor On-Off Antineutrino Measurement with KamLAND*, *Phys. Rev.* **D88** (2013), no. 3 033001, [1303.4667].

[106] **Daya Bay**, D. Adey et al., *Measurement of the Electron Antineutrino Oscillation with 1958 Days of Operation at Daya Bay*, *Phys. Rev. Lett.* **121** (2018), no. 24 241805, [1809.02261].

[107] **RENO**, G. Bak et al., *Measurement of Reactor Antineutrino Oscillation Amplitude and Frequency at RENO*, *Phys. Rev. Lett.* **121** (2018), no. 20 201801, [1806.00248].

[108] **Double Chooz**, Y. Abe et al., *Improved measurements of the neutrino mixing angle $\theta_{13}$ with the Double Chooz detector*, *JHEP* **10** (2014) 086, [1406.7763]. [Erratum: JHEP02,074(2015)].

[109] **Daya Bay**, F. P. An et al., *Observation of electron-antineutrino disappearance at Daya Bay*, *Phys. Rev. Lett.* **108** (2012) 171803, [1203.1669].

[110] **Daya Bay**, F. P. An et al., *Improved Measurement of the Reactor Antineutrino Flux and Spectrum at Daya Bay*, *Chin. Phys.* **C41** (2017), no. 1 013002, [1607.05378].

[111] H. Kwon, F. Boehm, A. A. Hahn, H. E. Henrikson, J. L. Vuilleumier, et al., *Search for Neutrino Oscillations at a Fission Reactor*, *Phys. Rev.* **D24** (1981) 1097–1111.

[112] **CALTECH-SIN-TUM**, G. Zacek et al., *Neutrino Oscillation Experiments at the Gosgen Nuclear Power Reactor*, *Phys. Rev.* **D34** (1986) 2621–2636.

[113] G. S. Vidyakin, V. N. Vyrodov, I. I. Gurevich, Yu. V. Kozlov, V. P. Martemyanov, et al., *Detection of Anti-neutrinos in the Flux From Two Reactors*, *Sov. Phys. JETP* **66** (1987) 243–247. [Zh. Eksp. Teor. Fiz.93,424(1987)].

[114] G. S. Vidyakin et al., *Limitations on the characteristics of neutrino oscillations*, *JETP Lett.* **59** (1994) 390–393. [Pisma Zh. Eksp. Teor. Fiz.59,364(1994)].

[115] Yu. V. Kozlov et al., *Today and future neutrino experiments at Krasnoyarsk nuclear reactor*, *Nucl. Phys. Proc. Suppl.* **87** (2000) 514–516, [hep-ex/9912046]. [,514(1999)].

[116] A. I. Afonin, S. N. Ketov, V. I. Kopeikin, L. A. Mikaelyan, M. D. Skorokhvatov, et al., *A Study of the Reaction $\bar{\nu}_e + P \to e^+ + N$ on a Nuclear Reactor*, *Sov. Phys. JETP* **67** (1988) 213–221. [Zh. Eksp. Teor. Fiz.94N2,1(1988)].

[117] A. A. Kuvshinnikov, L. A. Mikaelyan, S. V. Nikolaev, M. D. Skorokhvatov, and A. V. Etenko, *Measuring the anti-electron-neutrino + p —> n + e+ cross-section and beta decay axial constant in a new experiment at Rovno NPP reactor. (In Russian)*, *JETP Lett.* **54** (1991) 253–257. [Sov. J. Nucl. Phys.52,300(1990)].

[118] Y. Declais et al., *Study of reactor anti-neutrino interaction with proton at Bugey nuclear power plant*, *Phys. Lett.* **B338** (1994) 383–389.

[119] Z. D. Greenwood, W. R. Kropp, M. A. Mandelkern, S. Nakamura, E. L. Pasierb-Love, et al., *Results of a two-position reactor neutrino-oscillation experiment*, *Phys. Rev. D* **53** (Jun, 1996) 6054–6064.

[120] **RENO**, S. H. Seo et al., *Spectral Measurement of the Electron Antineutrino Oscillation Amplitude and Frequency using 500 Live Days of RENO Data*, *Phys. Rev.* **D98** (2018), no. 1 012002, [1610.04326].

[121] **NEOS**, Y. J. Ko et al., *Sterile Neutrino Search at the NEOS Experiment*, *Phys. Rev. Lett.* **118** (2017), no. 12 121802, [1610.05134].

[122] G. Mention, M. Vivier, J. Gaffiot, T. Lasserre, A. Letourneau, et al., *Reactor antineutrino shoulder explained by energy scale nonlinearities?*, *Phys. Lett.* **B773** (2017) 307–312, [1705.09434].

[123] P. Huber, *NEOS Data and the Origin of the 5 MeV Bump in the Reactor Antineutrino Spectrum*, *Phys. Rev. Lett.* **118** (2017), no. 4 042502, [1609.03910].

[124] A. C. Hayes, J. L. Friar, G. T. Garvey, D. Ibeling, G. Jungman, et al., *Possible origins and implications of the shoulder in reactor neutrino spectra*, *Phys. Rev.* **D92** (2015), no. 3 033015, [1506.00583].

[125] I. Alekseev et al., *DANSS: Detector of the reactor AntiNeutrino based on Solid Scintillator*, *JINST* **11** (2016), no. 11 P11011, [1606.02896].

[126] **STEREO**, N. Allemandou et al., *The STEREO Experiment*, *JINST* **13** (2018), no. 07 P07009, [1804.09052].

[127] **PROSPECT**, J. Ashenfelter et al., *The PROSPECT Reactor Antineutrino Experiment*, *Nucl. Instrum. Meth.* **A922** (2019) 287–309, [1808.00097].

[128] **JUNO**, F. An et al., *Neutrino Physics with JUNO*, *J. Phys.* **G43** (2016), no. 3 030401, [1507.05613].

[129] P. Vogel and J. F. Beacom, *Angular distribution of neutron inverse beta decay, anti-neutrino(e) + p —> e+ + n*, *Phys. Rev.* **D60** (1999) 053003, [hep-ph/9903554].

[130] **Daya Bay**, F. P. An et al., *Measurement of electron antineutrino oscillation based on 1230 days of operation of the Daya Bay experiment*, *Phys. Rev.* **D95** (2017), no. 7 072006, [1610.04802].

[131] H. Nunokawa, S. J. Parke, and R. Zukanovich Funchal, *Another possible way to determine the neutrino mass hierarchy*, *Phys. Rev.* **D72** (2005) 013009, [hep-ph/0503283].

[132] S. Parke, *What is $\Delta m^2_{ee}$ ?*, *Phys. Rev.* **D93** (2016), no. 5 053008, [1601.07464].

[133] S.-H. Seo and S. J. Parke, *Constraints on the solar $\Delta m^2$ using Daya Bay and RENO data*, *Phys. Rev.* **D99** (2019), no. 3 033012, [1808.09150].

[134] A. Cabrera Serra, "Double Chooz Improved Multi-Detector Measurements." Talk given at the *CERN EP colloquium*, CERN, Switzerland, September 20, 2016.

[135] F. Kaether, W. Hampel, G. Heusser, J. Kiko, and T. Kirsten, *Reanalysis of the GALLEX solar neutrino flux and source experiments*, *Phys. Lett.* **B685** (2010) 47–54, [1001.2731].

[136] **SAGE**, J. N. Abdurashitov et al., *Measurement of the solar neutrino capture rate with gallium metal. III: Results for the 2002–2007 data-taking period*, *Phys. Rev.* **C80** (2009) 015807, [0901.2200].

[137] **Super-Kamiokande**, K. Abe et al., *Solar neutrino results in Super-Kamiokande-III*, *Phys. Rev.* **D83** (2011) 052010, [1010.0118].

[138] **SNO**, B. Aharmim et al., *Combined Analysis of all Three Phases of Solar Neutrino Data from the Sudbury Neutrino Observatory*, *Phys. Rev.* **C88** (2013) 025501, [1109.0763].

[139] G. Bellini et al., *Precision measurement of the 7Be solar neutrino interaction rate in Borexino*, *Phys. Rev. Lett.* **107** (2011) 141302, [1104.1816].

[140] **T2K**, K. Abe et al., *The T2K Experiment*, *Nucl. Instrum. Meth.* **A659** (2011) 106–135, [1106.1238].

[141] **NOvA**, D. S. Ayres et al., *NOvA: Proposal to Build a 30 Kiloton Off-Axis Detector to Study $\nu_\mu \to \nu_e$ Oscillations in the NuMI Beamline*, hep-ex/0503053.

[142] **MINOS**, P. Adamson et al., *Measurement of the Neutrino Mass Splitting and Flavor Mixing by MINOS*, *Phys. Rev. Lett.* **106** (2011) 181801, [1103.0340].

[143] **Super-Kamiokande**, Y. Fukuda et al., *The Super-Kamiokande detector*, *Nucl. Instrum. Meth.* **A501** (2003) 418–462.

[144] **SuperKamiokande**, "Atmospheric neutrino oscillation analysis with external constraints in Super-Kamiokande I-IV." link to data release: http://www-sk.icrr.u-tokyo.ac.jp/sk/publications/result-e.html#atmosci2018, 2018.

[145] **IceCube**, M. G. Aartsen et al., *Determining neutrino oscillation parameters from atmospheric muon neutrino disappearance with three years of IceCube DeepCore data*, *Phys. Rev.* **D91** (2015), no. 7 072004, [1410.7227].

[146] **IceCube**, J. P. Yañez et al., "IceCube Oscillations: 3 years muon neutrino disappearance data." http://icecube.wisc.edu/science/data/nu_osc.

[147] E. K. Akhmedov, R. Johansson, M. Lindner, T. Ohlsson, and T. Schwetz, *Series expansions for three flavor neutrino oscillation probabilities in matter*, *JHEP* **04** (2004) 078, [hep-ph/0402175].

[148] C. Jarlskog, *Commutator of the Quark Mass Matrices in the Standard Electroweak Model and a Measure of Maximal CP Violation*, *Phys. Rev. Lett.* **55** (1985) 1039.

[149] H. Minakata, H. Nunokawa, S. J. Parke, and R. Zukanovich Funchal, *Determining neutrino mass hierarchy by precision measurements in electron and muon neutrino disappearance experiments*, *Phys. Rev.* **D74** (2006) 053008, [hep-ph/0607284].

[150] **Hyper-Kamiokande Proto-Collaboration**, K. Abe et al., *Physics potential of a long-baseline neutrino oscillation experiment using a J-PARC neutrino beam and Hyper-Kamiokande*, *PTEP* **2015** (2015) 053C02, [1502.05199].

[151] **DUNE**, R. Acciarri et al., *Long-Baseline Neutrino Facility (LBNF) and Deep Underground Neutrino Experiment (DUNE)*, 1512.06148.

[152] **Hyper-Kamiokande**, K. Abe et al., *Physics potentials with the second Hyper-Kamiokande detector in Korea*, *PTEP* **2018** (2018), no. 6 063C01, [1611.06118].

[153] M. Maltoni and A. Yu. Smirnov, *Solar neutrinos and neutrino physics*, *Eur. Phys. J.* **A52** (2016), no. 4 87, [1507.05287].

[154] **Super-Kamiokande**, J. Hosaka et al., *Solar neutrino measurements in super-Kamiokande-I*, *Phys. Rev.* **D73** (2006) 112001, [hep-ex/0508053].

[155] **Super-Kamiokande**, J. P. Cravens et al., *Solar neutrino measurements in Super-Kamiokande-II*, *Phys. Rev.* **D78** (2008) 032002, [0803.4312].

[156] **Borexino**, G. Bellini et al., *Measurement of the solar 8B neutrino rate with a liquid scintillator target and 3 MeV energy threshold in the Borexino detector*, *Phys. Rev.* **D82** (2010) 033006, [0808.2868].

[157] Y. Nakano, *$^8$B solar neutrino spectrum measurement using Super-Kamiokande IV*. PhD thesis, Tokyo U., 2016-02.

[158] **Hyper-Kamiokande**, K. Abe et al., *Hyper-Kamiokande Design Report*, 1805.04163.

[159] F. Capozzi, S. W. Li, G. Zhu, and J. F. Beacom, *DUNE as the Next-Generation Solar Neutrino Experiment*, 1808.08232.

[160] S. Gariazzo, C. Giunti, M. Laveder, and Y. F. Li, *Updated Global 3+1 Analysis of Short-BaseLine Neutrino Oscillations*, *JHEP* **06** (2017) 135, [1703.00860].

[161] C. Giunti, *Precise determination of the $^{235}$U reactor antineutrino cross section per fission*, *Phys. Lett.* **B764** (2017) 145–149, [1608.04096].

[162] S.-H. Seo, 2017. talk given on behalf of the RENO Collaboration at the EPS conference on High Energy Physics, Venice, Italy, July 5–11, 2017.

[163] Y. Declais et al., *Search for neutrino oscillations at 15-meters, 40-meters, and 95-meters from a nuclear power reactor at Bugey*, *Nucl. Phys.* **B434** (1995) 503–534.

[164] S.-H. Seo, 2014. talk given on behalf of the RENO Collaboration at the XXVI International Conference on Neutrino Physics and Astrophysics, Boston, USA, June 2–7, 2014.

[165] **KamLAND**, A. Gando et al., *Constraints on $\theta_{13}$ from A Three-Flavor Oscillation Analysis of Reactor Antineutrinos at KamLAND*, *Phys. Rev.* **D83** (2011) 052002, [1009.4771].

[166] M. Danilov, 2017. talk given on behalf of the DANSS Collaboration at the Solvay Workshop 'Beyond the Standard model with Neutrinos and Nuclear Physics', 29 Nov.–1 Dec. 2017, Brussels, Belgium.

[167] J. Kopp, P. A. N. Machado, M. Maltoni, and T. Schwetz, *Sterile Neutrino Oscillations: The Global Picture*, *JHEP* **05** (2013) 050, [1303.3011].

[168] **Double Chooz**, Y. Abe et al., *Measurement of $\theta_{13}$ in Double Chooz using neutron captures on hydrogen with novel background rejection techniques*, *JHEP* **01** (2016) 163, [1510.08937].

[169] **DANSS**, M. Danilov, *Recent results of the DANSS experiment*, 1811.07354. [Nuovo Cim.C41,162(2019)].

[170] L. Bernard, 2019. talk given on behalf of the STEREO Collaboration at Rencontres de Moriond conference, March 21-28, 2019.

[171] **PROSPECT**, J. Ashenfelter et al., *First search for short-baseline neutrino oscillations at HFIR with PROSPECT*, *Phys. Rev. Lett.* **121** (2018), no. 25 251802, [1806.02784].

[172] **NEUTRINO-4**, A. P. Serebrov et al., *First Observation of the Oscillation Effect in the Neutrino-4 Experiment on the Search for the Sterile Neutrino*, *Pisma Zh. Eksp. Teor. Fiz.* **109** (2019), no. 4 209–218, [1809.10561]. [JETP Lett.109,no.4,213(2019)].

[173] **SoLid**, L. Manzanillas, *Performance of the SoLid Reactor Neutrino Detector*, *PoS* **ICHEP2018** (2019) 426, [1811.05694].

[174] B. T. Cleveland, T. Daily, R. Davis, Jr., J. R. Distel, K. Lande, et al., *Measurement of the solar electron neutrino flux with the Homestake chlorine detector*, *Astrophys. J.* **496** (1998) 505–526.

[175] **SNO**, B. Aharmim et al., *Determination of the $\nu_e$ and total $^8B$ solar neutrino fluxes with the Sudbury neutrino observatory phase I data set*, *Phys. Rev.* **C75** (2007) 045502, [nucl-ex/0610020].

[176] **SNO**, B. Aharmim et al., *Electron energy spectra, fluxes, and day-night asymmetries of B-8 solar neutrinos from measurements with NaCl dissolved in the heavy-water detector at the Sudbury Neutrino Observatory*, *Phys. Rev.* **C72** (2005) 055502, [nucl-ex/0502021].

[177] **SNO**, B. Aharmim et al., *An Independent Measurement of the Total Active B-8 Solar Neutrino Flux Using an Array of He-3 Proportional Counters at the Sudbury Neutrino Observatory*, *Phys. Rev. Lett.* **101** (2008) 111301, [0806.0989].

[178] **BOREXINO**, G. Bellini et al., *Neutrinos from the primary proton–proton fusion process in the Sun*, *Nature* **512** (2014), no. 7515 383–386.

[179] **GALLEX**, W. Hampel et al., *Final results of the Cr-51 neutrino source experiments in GALLEX*, *Phys. Lett.* **B420** (1998) 114–126.

[180] **SAGE**, J. N. Abdurashitov et al., *Measurement of the response of the Russian-American gallium experiment to neutrinos from a Cr-51 source*, *Phys. Rev.* **C59** (1999) 2246–2263, [hep-ph/9803418].

[181] J. N. Abdurashitov et al., *Measurement of the response of a Ga solar neutrino experiment to neutrinos from an Ar-37 source*, *Phys. Rev.* **C73** (2006) 045805, [nucl-ex/0512041].

[182] **LSND**, L. B. Auerbach et al., *Measurements of charged current reactions of nu(e) on 12-C*, *Phys. Rev.* **C64** (2001) 065501, [hep-ex/0105068].

[183] J. M. Conrad and M. H. Shaevitz, *Limits on Electron Neutrino Disappearance from the KARMEN and LSND $\nu_e$ - Carbon Cross Section Data*, *Phys. Rev.* **D85** (2012) 013017, [1106.5552].

[184] J. Reichenbacher, *Final KARMEN results on neutrino oscillations and neutrino nucleus interactions in the energy regime of supernovae*. PhD thesis, Karlsruhe U., 2005.

[185] B. Armbruster et al., *KARMEN limits on electron-neutrino —> tau-neutrino oscillations in two neutrino and three neutrino mixing schemes*, *Phys. Rev.* **C57** (1998) 3414–3424, [hep-ex/9801007].

[186] M. Maltoni and T. Schwetz, *Sterile neutrino oscillations after first MiniBooNE results*, *Phys. Rev.* **D76** (2007) 093005, [0705.0107].

[187] J. Kostensalo, J. Suhonen, C. Giunti, and P. C. Srivastava, *The gallium anomaly revisited*, *Phys. Lett.* **B795** (2019) 542–547, [1906.10980].

[188] M. Maltoni and T. Schwetz, *Testing the statistical compatibility of independent data sets*, *Phys. Rev.* **D68** (2003) 033020, [hep-ph/0304176].

[189] **MiniBooNE**, "Data release for arxiv:1207.4809." http://www-boone.fnal.gov/for_physicists/data_release/nue_nuebar_2012/combined.html#fit200.

[190] **KARMEN**, B. Armbruster et al., *Upper limits for neutrino oscillations muon-anti-neutrino —> electron-anti-neutrino from muon decay at rest*, *Phys. Rev.* **D65** (2002) 112001, [hep-ex/0203021].

[191] **NOMAD**, P. Astier et al., *Search for nu(mu) —> nu(e) oscillations in the NOMAD experiment*, *Phys. Lett.* **B570** (2003) 19–31, [hep-ex/0306037].

[192] L. Borodovsky et al., *Search for muon-neutrino oscillations muon-neutrino —> electron-neutrino (anti-muon-neutrino —> anti-electron-neutrino in a wide band neutrino beam*, *Phys. Rev. Lett.* **68** (1992) 274–277.

[193] M. Antonello et al., *Experimental search for the "LSND anomaly" with the ICARUS detector in the CNGS neutrino beam*, *Eur. Phys. J.* **C73** (2013), no. 3 2345, [1209.0122].

[194] C. Farnese, *Some recent results from ICARUS*, *AIP Conf. Proc.* **1666** (2015), no. 1 110002.

[195] **OPERA**, N. Agafonova et al., *Search for $\nu_\mu \to \nu_e$ oscillations with the OPERA experiment in the CNGS beam*, *JHEP* **07** (2013) 004, [1303.3953]. [Addendum: JHEP07,085(2013)].

[196] **IceCube**, M. G. Aartsen et al., *Searches for Sterile Neutrinos with the IceCube Detector*, *Phys. Rev. Lett.* **117** (2016), no. 7 071801, [1605.01990].

[197] B. J. P. Jones, *Sterile neutrinos in cold climates*. PhD thesis, Massachusetts Institute of Technology, 2015. available from http://hdl.handle.net/1721.1/101327.

[198] C. A. Argüelles, *New Physics with Atmospheric Neutrinos*. PhD thesis, University of Wisconsin, Madison, 2015. available from https://docushare.icecube.wisc.edu/dsweb/Get/Document-75669/tesis.pdf.

[199] **Super-Kamiokande**, R. Wendell, *Atmospheric Results from Super-Kamiokande*, *AIP Conf. Proc.* **1666** (2015), no. 1 100001, [1412.5234].

[200] **Super-Kamiokande**, R. Wendell et al., *Atmospheric neutrino oscillation analysis with sub-leading effects in Super-Kamiokande I, II, and III*, *Phys. Rev.* **D81** (2010) 092004, [1002.3471].

[201] **NOvA**, P. Adamson et al., *Search for active-sterile neutrino mixing using neutral-current interactions in NOvA*, *Phys. Rev.* **D96** (2017), no. 7 072006, [1706.04592].

[202] **MINOS+**, P. Adamson et al., *Search for sterile neutrinos in MINOS and MINOS+ using a two-detector fit*, *Phys. Rev. Lett.* **122** (2019), no. 9 091803, [1710.06488].

[203] F. Dydak et al., *A Search for Muon-neutrino Oscillations in the Delta m**2 Range 0.3-eV**2 to 90-eV**2*, *Phys. Lett.* **134B** (1984) 281.

[204] **MiniBooNE**, A. A. Aguilar-Arevalo et al., *A Search for muon neutrino and antineutrino disappearance in MiniBooNE*, *Phys. Rev. Lett.* **103** (2009) 061802, [0903.2465].

[205] **MiniBooNE, SciBooNE**, G. Cheng et al., *Dual baseline search for muon antineutrino disappearance at* $0.1\text{eV}^2 < \Delta m^2 < 100\text{eV}^2$, *Phys. Rev.* **D86** (2012) 052009, [1208.0322].

[206] **MiniBooNE**, "Data release for arxiv:0903.2465." http://www-boone.fnal.gov/for_physicists/data_release/numu_numubar/.

[207] S. N. Gninenko, *The MiniBooNE anomaly and heavy neutrino decay*, *Phys. Rev. Lett.* **103** (2009) 241802, [0902.3802].

[208] S. N. Gninenko, *A resolution of puzzles from the LSND, KARMEN, and MiniBooNE experiments*, *Phys. Rev.* **D83** (2011) 015015, [1009.5536].

[209] E. Bertuzzo, S. Jana, P. A. N. Machado, and R. Zukanovich Funchal, *Dark Neutrino Portal to Explain MiniBooNE excess*, *Phys. Rev. Lett.* **121** (2018), no. 24 241801, [1807.09877].

[210] P. Ballett, S. Pascoli, and M. Ross-Lonergan, *U(1)' mediated decays of heavy sterile neutrinos in MiniBooNE*, *Phys. Rev.* **D99** (2019) 071701, [1808.02915].

[211] M. Masip, P. Masjuan, and D. Meloni, *Heavy neutrino decays at MiniBooNE*, *JHEP* **01** (2013) 106, [1210.1519].

[212] G. Magill, R. Plestid, M. Pospelov, and Y.-D. Tsai, *Dipole Portal to Heavy Neutral Leptons*, *Phys. Rev.* **D98** (2018), no. 11 115015, [1803.03262].

[213] M. Dentler, I. Esteban, J. Kopp, and P. Machado, *Decaying Sterile Neutrinos and the Short Baseline Oscillation Anomalies*, 1911.01427.

[214] A. de Gouvêa, O. L. G. Peres, S. Prakash, and G. V. Stenico, *On The Decaying-Sterile Neutrino Solution to the Electron (Anti)Neutrino Appearance Anomalies*, 1911.01447.

[215] S. Palomares-Ruiz, S. Pascoli, and T. Schwetz, *Explaining LSND by a decaying sterile neutrino*, *JHEP* **09** (2005) 048, [hep-ph/0505216].

[216] J. R. Jordan, Y. Kahn, G. Krnjaic, M. Moschella, and J. Spitz, *Severe Constraints on New Physics Explanations of the MiniBooNE Excess*, *Phys. Rev. Lett.* **122** (2019), no. 8 081801, [1810.07185].

[217] **MiniBooNE**, A. A. Aguilar-Arevalo et al., *The Neutrino Flux prediction at MiniBooNE*, *Phys. Rev.* **D79** (2009) 072002, [0806.1449].

[218] P. Ballett, S. Pascoli, and M. Ross-Lonergan, *MeV-scale sterile neutrino decays at the Fermilab Short-Baseline Neutrino program*, *JHEP* **04** (2017) 102, [1610.08512].

[219] **NOMAD**, C. T. Kullenberg et al., *A search for single photon events in neutrino interactions*, *Phys. Lett.* **B706** (2012) 268–275, [1111.3713].

[220] **NOMAD**, P. Astier et al., *Prediction of neutrino fluxes in the NOMAD experiment*, *Nucl. Instrum. Meth.* **A515** (2003) 800–828, [hep-ex/0306022].

[221] H. K. Dreiner, C. Hanhart, U. Langenfeld, and D. R. Phillips, *Supernovae and light neutralinos: SN1987A bounds on supersymmetry revisited*, *Phys. Rev.* **D68** (2003) 055004, [hep-ph/0304289].

[222] **MINERvA**, L. Aliaga et al., *Design, Calibration, and Performance of the MINERvA Detector*, *Nucl. Instrum. Meth.* **A743** (2014) 130–159, [1305.5199].

[223] **MicroBooNE, LAr1-ND, ICARUS-WA104**, M. Antonello et al., *A Proposal for a Three Detector Short-Baseline Neutrino Oscillation Program in the Fermilab Booster Neutrino Beam*, 1503.01520.

[224] P. A. Machado, O. Palamara, and D. W. Schmitz, *The Short-Baseline Neutrino Program at Fermilab*, *Ann. Rev. Nucl. Part. Sci.* **69** (2019) [1903.04608].

[225] **T2K**, K. Abe et al., *Search for neutral-current induced single photon production at the ND280 near detector in T2K*, *J. Phys.* **G46** (2019), no. 8 08LT01, [1902.03848].

[226] **RENO**, J. K. Ahn et al., *RENO: An Experiment for Neutrino Oscillation Parameter $\theta_{13}$ Using Reactor Neutrinos at Yonggwang*, 1003.1391.

[227] **DANSS**, M. Danilov, *Sensitivity of DANSS detector to short range neutrino oscillations*, 1412.0817.

[228] A. Abada, G. Arcadi, V. Domcke, and M. Lucente, *Neutrino masses, leptogenesis and dark matter from small lepton number violation?*, *JCAP* **1712** (2017), no. 12 024, [1709.00415].

[229] **KATRIN**, S. Mertens et al., *A novel detector system for KATRIN to search for keV-scale sterile neutrinos*, *J. Phys.* **G46** (2019), no. 6 065203, [1810.06711].

[230] S. M. Barr, *A Different seesaw formula for neutrino masses*, *Phys. Rev. Lett.* **92** (2004) 101601, [hep-ph/0309152].

[231] M. Malinsky, J. C. Romao, and J. W. F. Valle, *Novel supersymmetric SO(10) seesaw mechanism*, *Phys. Rev. Lett.* **95** (2005) 161801, [hep-ph/0506296].

[232] D. Wyler and L. Wolfenstein, *Massless Neutrinos in Left-Right Symmetric Models*, *Nucl. Phys.* **B218** (1983) 205–214.

[233] R. N. Mohapatra and J. W. F. Valle, *Neutrino Mass and Baryon Number Nonconservation in Superstring Models*, *Phys. Rev.* **D34** (1986) 1642. [,235(1986)].

[234] M. C. Gonzalez-Garcia and J. W. F. Valle, *Fast Decaying Neutrinos and Observable Flavor Violation in a New Class of Majoron Models*, *Phys. Lett.* **B216** (1989) 360–366.

[235] M. Lucente, A. Abada, G. Arcadi, and V. Domcke, *Lepton number symmetry as a way to testable leptogenesis*, in *Proceedings, 51st Rencontres de Moriond on Electroweak Interactions and Unified Theories: La Thuile, Italy, March 12-19, 2016*, pp. 117–126, 2016. 1605.05328.

[236] S. Antusch, M. Blennow, E. Fernandez-Martinez, and J. Lopez-Pavon, *Probing non-unitary mixing and CP-violation at a Neutrino Factory*, *Phys. Rev.* **D80** (2009) 033002, [0903.3986].

[237] J. A. Casas and A. Ibarra, *Oscillating neutrinos and muon —¿ e, gamma*, *Nucl. Phys.* **B618** (2001) 171–204, [hep-ph/0103065].